

DISCONTINUOUS POTENTIAL SYSTEMS

A THESIS
SUBMITTED TO THE UNIVERSITY OF MANCHESTER
FOR THE DEGREE OF
DOCTOR OF PHILOSOPHY (PhD)
IN THE FACULTY OF ENGINEERING AND PHYSICAL SCIENCES

MARCUS N. CAMPBELL BANNERMAN

SCHOOL OF CHEMICAL ENGINEERING AND ANALYTICAL SCIENCE
2009

CONTENTS

List of Figures	7
List of Tables	9
Abstract	11
Declaration	13
Copyright	15
Acknowledgements	17
Nomenclature	19
1 Introduction	23
1.1 Motivation	23
1.2 Thesis Overview	25
1.3 References	26
2 Formalism	27
2.1 Basic Considerations	27
2.2 Distribution Function	28
2.3 Time Evolution Operators	29
2.4 Binary Interaction Expansion	30
2.5 BBGKY Hierarchy	31
2.6 Newtonian Dynamics	33
2.6.1 Inter-Particle Potential	34
2.7 Interaction Dynamics	36
2.7.1 Collision Conditions	36
2.7.2 Collision Dynamics	37
2.8 Determining the Interaction Operators	38
2.8.1 Overlap Function	38
2.8.2 p -Collision Operator	39
2.8.3 f -Collision Operator	41

Contents

2.8.4	<i>N</i> -body Dynamics	43
2.9	Conclusions	44
2.10	References	44
3	Direct Simulation Monte-Carlo	47
3.1	Introduction	47
3.2	Kinetic Theory	49
3.2.1	BBGKY Streaming Hierarchy	49
3.3	$f^{(2)}$ -DSMC	51
3.3.1	Limitations of the Approximate Velocity Distribution Function . .	52
3.3.2	Treatment of the Spatial Correlation Terms	53
3.4	Development of the $f^{(2)}$ -DSMC Algorithm	54
3.4.1	$f^{(2)}$ -DSMC Algorithm	55
3.5	Elastic Hard Sphere Systems	57
3.5.1	Phenomenological Estimation of the Re-collision Rates	58
3.6	Inelastic Hard Spheres Under Shear	61
3.7	Conclusions	63
3.8	References	64
4	An $O(N)$ General Event-Driven Simulator: DYNAMO	67
4.1	Introduction	67
4.2	Algorithm Details	69
4.3	Improvements to the Simulation Method	71
4.3.1	Particle Data	71
4.3.2	Over-Linking of Neighbor List Cells	72
4.3.3	Morton Ordered Neighbor Lists	72
4.3.4	Accuracy and Time Invariance	74
4.3.5	Summary	74
4.4	Program Design	75
4.5	Benchmarking	77
4.6	Conclusions	79
4.7	References	80
5	Hard Sphere Equations of State	85
5.1	Introduction	85
5.2	Equation of State	86
5.3	Simulation Details	88
5.4	Results and Discussion	89
5.5	Conclusions	92
5.6	References	93

6 Collision Statistics in Sheared Inelastic Hard Spheres	95
6.1 Introduction	95
6.2 Simulation Details	98
6.3 DSMC Simulations	101
6.4 Results and Discussion	102
6.4.1 Velocity Distribution	102
6.4.2 Stress Tensor	105
6.4.3 Collision Statistics	109
6.5 Conclusions	113
6.6 References	114
7 Transport Properties of Highly Asymmetric Hard Sphere Mixtures	119
7.1 Introduction	119
7.2 Theoretical Background	120
7.2.1 Static Properties	121
7.2.2 Calculation of Transport Coefficients	123
7.2.3 Einstein Forms of the Green-Kubo Relations	123
7.2.4 Enskog Theory Predictions for the Transport Coefficients	125
7.2.5 DSMC Solution of the Enskog Equation	126
7.3 Simulation Details	127
7.3.1 MD Simulations	127
7.3.2 DSMC Simulations	128
7.4 Results and Discussion	128
7.4.1 Static Properties	128
7.4.2 Thermal Conductivity	130
7.4.3 Shear Viscosity	132
7.4.4 Thermal Diffusion Coefficient	133
7.4.5 Mutual Diffusion Coefficient	134
7.5 Conclusions	135
7.6 References	136
8 Structure and Stability of Helices in Square-Well Homopolymers	141
8.1 Introduction	141
8.2 Simulation Details	143
8.3 Results and Discussion	145
8.3.1 Overview	145
8.3.2 Ratio of Monomer Size to Bond Length	147
8.3.3 Range of Attractive Interaction	150
8.3.4 Chain Length	152
8.4 Conclusions	155
8.5 References	156

Contents

9 Conclusions and Future Work	159
9.1 Conclusions	159
9.2 Future Work	161
9.2.1 Future Systems for Study	161
9.2.2 Event Driven Algorithms	162
9.3 References	163
A Reprint: Collision Statistics in Sheared Inelastic Hard Spheres	165
B Reprint: Transport Properties of Highly Asymmetric Hard-Sphere Mixtures	167
C Reprint: Structure and Stability of Helices in Square-Well Homopolymers	171
D Pre to Post Collision Jacobian	173
E Streaming Operator BBGKY Hierarchy	175

Final word count: 39484

LIST OF FIGURES

2.1	Collision variables.	36
3.1	Collision sequences accounted for in $f^{(2)}$ -DSMC.	53
3.2	$f^{(2)}$ -DSMC predictions for diffusion coefficients of hard spheres.	58
3.3	$f^{(2)}$ -DSMC predictions for viscosity and thermal conductivity of spheres.	59
3.4	Re-collision probabilities for elastic hard spheres.	60
3.5	Corrected $f^{(2)}$ -DSMC predictions for diffusion coefficients of hard spheres.	61
3.6	$f^{(2)}$ -DSMC predictions of the VACF for elastic hard spheres.	62
3.7	The distribution of kinetic energy in each dimension for sheared, inelastic, hard spheres versus ring DSMC.	63
3.8	Shear, in-plane, and out-plane viscosities of sheared, inelastic, hard spheres.	64
4.1	A stepped potential that approximates the Lennard-Jones potential.	68
4.2	Cells which enclose the neighborhood of a particle, for a cell length equal to and half of the maximum interaction distance.	72
4.3	A two dimensional 4×4 array stored in row major order and Morton order in memory.	73
4.4	The class hierarchy of DYNAMO.	75
4.5	The number of collision events processed per second as a function of the number of particles N and the number density ρ .	78
4.6	The number of events processed per second using linear and Morton ordered lists.	79
5.1	Reduced virial coefficients for the hard sphere fluid.	87
5.2	Hard sphere equation of state.	91
5.3	Comparison of EOS and MD results for the hard sphere fluid.	91
5.4	Comparison of EOS and MD results for the hard sphere solid.	92
6.1	System size dependence of the mean free time between collisions for sheared, inelastic hard-sphere systems.	100
6.2	Mean kinetic energy per particle with density for a sheared, inelastic, hard-sphere system.	104

6.3	The distribution of kinetic energy in each dimension for sheared, inelastic, hard spheres.	105
6.4	Peculiar velocity distribution of sheared, inelastic, hard spheres.	106
6.5	Pressure and compressibility factor for sheared, inelastic, hard spheres.	107
6.6	Shear, in-plane, and out-plane viscosities of sheared, inelastic, hard spheres.	109
6.7	Mean free time for sheared, inelastic, hard spheres.	110
6.8	Collision angle distribution for sheared, inelastic, hard spheres.	111
6.9	Kinetic energy change on collision for sheared, inelastic, hard-spheres.	112
6.10	Mean free time distributions of sheared, inelastic, hard spheres.	113
7.1	Sample Einstein correlation functions for the transport coefficients.	125
7.2	Pressure versus solid fraction for binary hard sphere mixtures.	129
7.3	Contact value of the pair correlation function for binary hard sphere mixtures.	130
7.4	Thermal conductivity for binary hard sphere mixtures.	131
7.5	Shear viscosity for binary hard sphere mixtures.	133
7.6	Thermal diffusivity for binary hard sphere mixtures.	134
7.7	Mutual diffusion coefficient for binary hard sphere mixtures.	135
8.1	Variables of the isolated homopolymer model.	143
8.2	Replica exchange simulations for an isolated square-well homopolymer. .	145
8.3	Heat capacity, optimal configuration RMSD, sample configurations, and contact maps at various temperatures of an isolated helix homopolymer. .	146
8.4	Average bond angle correlations for athermal overlapping chains.	148
8.5	Diagram of states for isolated square-well homopolymers with $N = 20$ and $\lambda = 1.5$	149
8.6	Diagram of states for isolated square-well homopolymers with $N = 20$ and $\sigma/l = 1.6$	151
8.7	Representative configurations at the state points indicated in Fig. 8.6. . . .	151
8.8	Diagram of states for isolated square-well homopolymers with $\sigma/l = 1.6$ and $\lambda = 1.5$ as a function of the chain length.	153
8.9	Samples of stable configurations for square-well homopolymers.	153
8.10	Diagram of states for isolated square-well homopolymers with $\sigma/l = 1.6$ and $\lambda = 1.32$ as a function of the chain length.	154
8.11	Diagram of states for isolated square-well homopolymers with $\sigma/l = 1.8$ and $\lambda = 1.5$ as a function of the chain length.	155

LIST OF TABLES

5.1	Virial coefficients for the hard sphere fluid.	87
5.2	Simulation conditions for the large hard-sphere systems.	89
5.3	Simulation results for the hard sphere equation of state.	90
6.1	Shear viscosities of sheared, inelastic, hard sphere systems.	108
7.1	Displacement functions for the Einstein form of the Green-Kubo relationships.	124
7.2	Transport coefficients and the corresponding displacement functions. . . .	125

ABSTRACT

This thesis is concerned with the theory and simulation of the static and dynamic properties of discrete-potential systems. Discrete potentials are a class of models used to describe the interactions between particles in many-body systems and have applications in many fields.

To investigate the dynamics of systems with discrete potentials, DYNAMO, a general event-driven molecular dynamics simulation package was developed. This software is one of the first event driven implementations to exhibit linear scaling of the computational cost with the system size, which is the theoretically optimal scaling. DYNAMO also implements stochastic interactions, including a novel extension of DSMC proposed to attempt to include pre-collision velocity correlations, which are significant in dense or complex fluids. Using a phenomenological correction for the dynamical spatial effects, the predictions for the self diffusion coefficient of the hard sphere fluid are improved over Enskog theory at low to moderate densities.

DYNAMO was used to examine a number of systems to determine their behaviour and to test theoretical predictions. Accurate simulations of large systems of hard spheres were used to test recent equations of state including a novel exponential closure of the virial series. This closure performs well in comparison to other theoretical equations of state for the fluid phase, and a revised semi-empirical equation of state is proposed for the solid phase. The collision statistics of sheared granular materials were studied to highlight the fundamental differences between elastic and inelastic systems and to critically compare Enskog theory and its approximate solutions. Overall, Enskog theory performs well; however, care must be taken with the predictions of the energy anisotropy and collision statistics. The effect of nano-colloids on the transport properties of a fluid were investigated using the binary hard sphere model. A “fines” effect in the viscosity and a strong thermal conductivity enhancement was observed in the simulations, which are absent from the Enskog theory predictions. Finally, a simple square-well homopolymer model is examined using constant temperature molecular dynamics, coupled with replica exchange techniques. This polymer forms helical structures, and the control parameters of the model (e.g., chain stiffness, range of the attractive interactions) were completely characterised to investigate the nature and stability of this surprising folding behaviour.

The results of all of these systems highlight the speed and versatility of both the DYNAMO simulation package and the underlying richness of discrete potential models.

DECLARATION

The University of Manchester
PhD by published work Candidate Declaration

Candidate Name: Marcus N. Campbell Bannerman

Faculty: Engineering and Physical Sciences

Thesis Title: Discontinuous Potential Systems

Declaration to be completed by the candidate:

I declare that no portion of this work referred to in this thesis has been submitted in support of an application for another degree or qualification of this or any other university or other institute of learning.

Signed: 

Date: 3rd September 2009

COPYRIGHT

The author of this thesis (including any appendices and/or schedules to this thesis) owns any copyright in it (the "Copyright")¹ and s/he has given The University of Manchester the right to use such Copyright for any administrative, promotional, educational and/or teaching purposes.

Copies of this thesis, either in full or in extracts, may be made only in accordance with the regulations of the John Rylands University Library of Manchester. Details of these regulations may be obtained from the Librarian. This page must form part of any such copies made.

The ownership of any patents, designs, trade marks and any and all other intellectual property rights except for the Copyright (the "Intellectual Property Rights") and any reproductions of copyright works, for example graphs and tables ("Reproductions"), which may be described in this thesis, may not be owned by the author and may be owned by third parties. Such Intellectual Property Rights and Reproductions cannot and must not be made available for use without the prior written permission of the owner(s) of the relevant Intellectual Property Rights and/or Reproductions.

Further information on the conditions under which disclosure, publication and exploitation of this thesis, the Copyright and any Intellectual Property Rights and/or Reproductions described in it may take place is available from the Head of School of Chemical Engineering and Analytical Science (or the Vice-President) and the Dean of the Faculty of Engineering and Physical Sciences, for Faculty of Engineering and Physical Sciences candidates.

¹This excludes material already printed in academic journals, for which the copyright belongs to said journal and publisher. Pages for which the author does not own the copyright are numbered differently from the rest of the thesis.

ACKNOWLEDGEMENTS

I'd like to thank everyone who has helped and supported me during my time at Manchester. A big thank you to my supervisor and friend Dr. Leo Lue, who managed to see some potential in a rather lazy student and instill in him a great enthusiasm for research and learning. I'd also like to thank Prof. Bill Hoover and Prof. Les Woodcock for the opportunity of working with them and for lending me their enthusiasm for cubes and spheres.

To all of my friends inside and outside of C19 (I haven't forgotten you Argyrios) I'd like to say thank you for making the work place a happy place. A special thanks goes to Ben for organising *everything* and for ensuring we go out and enjoy ourselves once in a while.

To my family, thank you for always looking after me and congratulations Mum and Dad on your retirement from parenting.

Finally, I'd like to give my greatest thanks to my girlfriend Miranda. She's encouraged, supported, cajoled, and listened patiently to me for these last 3 years and helped make them the happiest of my life. As a small token of gratitude and love, I'd like to dedicate this thesis to her.

NOMENCLATURE

Constants, Variables & Functions

α	Coefficient of restitution, 37
χ	Radial distribution function on contact, 50
$\chi^{(CS)}$	Carnahan-Starling contact value of the radial distribution function, 53
$\chi^{(n)}$	n -body correlation factor, 52
δ	Dirac delta function, 40
δN	Fraction of systems in phase space, 28
ΔE	Energy loss on collision, 99
Δp	Momentum change on collision, 37
Δt	Time to collision, 36
ΔZ	Relative deviation of compressibility, 89
ΔKE	Energy change on collision, 38
ε	Square-well depth, 35
η	Shear viscosity, 58
η_-	in-plane normal stress coefficient, 63
η_0	out-plane normal stress coefficient, 63
Γ	A Single particles phase variables, 27
Γ	Phase space co-ordinate, 27
$\dot{\gamma}$	Shear rate, 34
Λ	Phase space compressibility, 30
λ	Well/bond width parameter, 35
λ	Thermal conductivity, 58
μ	Relative mass, 37

$\nabla \mathbf{u}$	Shear rate tensor, 33
ϕ	Packing fraction, 53
ψ_j	Equation of motion for particle j , 27
ρ	Number density, 52
ρ_0	Close packing density, 86
ρ_*	Reduced density, 87
σ_j	Particle diameter, 34
σ_{jk}	Interaction diameter, 34
Θ	Heaviside step function, 39
$\hat{\mathbf{a}}$	Collision vector, 36
B_n	n th virial in the reduced density series, 86
b_n	n th virial coefficient, 85
$C(t)$	Velocity auto-correlation function, 61
D	Diffusion coefficient, 57
d	Dimensionality of the system, 41
D_{Pair}	Pair diffusion coefficient, 59
E	System energy, 102
erfc	Complimentary error function, 59
\mathbf{F}	Inter-particle force, 33
F	Normalised N -particle distribution function, 28
$f^{(n)}$	n -particle distribution function, 31
$f_{\text{pair}}^{(\text{MB})}$	Maxwell-Boltzmann distribution for the relative velocity of a pair of particles, 60
g_n	n -particle correlation function, 49
l	Initial separation/mean free length, 59

m	Particle mass, 28	\mathcal{B}	Hard sphere collision operator, 40
N	Number of particles in system, 27	\mathcal{B}^{-1}	Inverse HS collision operator, 42
N_s	DSMC sample count, 51	\mathcal{I}	Collisional streaming operator, 40
\mathbf{P}	Stress tensor, 105	$i\mathcal{L}$	f -Liouvillean operator, 29
\mathbf{p}	Particle momentum, 28	$i\mathcal{L}^\dagger$	p -Liouvillean operator, 29
p	Pressure, 85	$i\mathcal{L}^0$	Liouville free streaming operator, 30
$\bar{\mathbf{p}}$	Particle peculiar momentum, 33	\mathcal{P}	Permutation operator, 50
$P_{j3}^{(B)}$	Coupling collision probability, 57	\mathcal{S}_+	Forward time streaming operator, 43
$P_{max}^{(B)}$	Max observed value of $P_{j3}^{(B)}$, 57	\mathcal{S}_t^0	f -free streaming propagator, 32
$P_{12}^{(RR)}$	Correlated collision probability, 56	$\mathcal{S}_{\Delta t}^{(E)}$	Enskog streaming operator, 54
$P_{max}^{(C)}$	Max observed value of $P_{12}^{(C)}$, 56	\mathcal{S}_t^\dagger	p -streaming/propagator operator, 29
R	Fraction of interactions not leading to a recollision, 59	\mathcal{S}_t	f -streaming/propagator operator, 29
$\hat{\mathbf{r}}$	Randomly generated unit vector, 56	\mathcal{T}^\dagger	p -Binary interaction operator, 30
\mathbf{r}_{jk}	Relative position, 34	\mathcal{T}	f -Binary interaction operator, 30
$\text{sign}(x)$	Sign function, 38	\mathcal{T}_+	Forward time interaction operator, 41
t	Time, 27	\mathcal{T}_r	Real interaction operator piece, 42
t_{avg}	Mean free time, 54	\mathcal{T}_v	Virtual interaction operator piece, 42
$u_{jk}^{(HS)}$	Hard-sphere potential, 34		
$u_{jk}^{(SB)}$	Square-bond potential, 35		
$u_{jk}^{(SW)}$	Square-well potential, 35		
\mathbf{v}_{jk}	Relative velocity, 36		
$\bar{\mathbf{v}}$	Particle peculiar velocity, 33		
W	Overlap function, 39		
\mathbf{X}	Force on particle due to external field, 33		
Z	Compressibility factor, 85		
$Z_{[5,4]}, Z_{[4,5]}$	Pade approximant EOS, 87		
Z_{CS}	Carnahan-Starling EOS, 88		
Z_{KLM}	Fitted EOS of Kolafa et al., 88		
Z_{speedy}	Speedy's solid phase EOS, 92		
Z_{virial}	Truncated virial EOS, 85		
Z_{WC1}	Woodcock's linear EOS, 88		
Z_{WC2}	Woodcock's exponential EOS, 87		

Operators

$\Lambda(j, k)$	Phase space compression interaction operator, 31
∇	Laplace operator, 59
Ω_j	Enskog streaming operator, 55

Notation

$\hat{\mathbf{e}}_x$	Unit vector in the x dimension, 34
x'	Post-collision value, 38
x^*	Complex conjugate, 28
x^\dagger	Adjoint function, 29
$\langle x $	Bra, 28
$ x \rangle$	Ket, 28
$\langle x \rangle_\Gamma$	Ensemble average, 29
\dot{x}	Time derivative, 27
$\hat{\mathbf{x}}$	Unit vector, 34

Acronyms/Terminology

Γ -space	Phase space, 27
AIA	Adiabatic incompressibility of phase space, 30
BBGKY	Bogoliubov-Born-Green-Kirkwood-Yvon, 27

- DSMC Direct Simulation Monte Carlo,
47
- DYNAMO DYNAMics of discrete Ob-
jects, 68
- MD Molecular Dynamics, 24
- NTC Null Time Counter, 48
- VACF Velocity Auto-Correlation Func-
tion, 61

INTRODUCTION

THIS chapter outlines the motivation of the thesis and its structure. It begins with a discussion of the background to many-body systems before detailing the vital role discrete potentials have played in the modelling of many-body systems. Finally, the format and the content of the remainder of the thesis are outlined. First, the motivation behind a thesis on discrete potentials is presented.

1.1 Motivation

Particulate systems of all scales are at the heart of a wide range of natural phenomena. From the vibrations of atoms within a fluid to the swirlings of interstellar dust, the behaviour of these many-body systems is a rich field for study. In recent times the modelling of these systems has progressed rapidly thanks to large increases in computational power; however, our understanding of these systems and how the complex behaviour they exhibit arises is still quite limited.

Early attempts to describe many-body systems began with the successful application of hydrodynamics and thermodynamics [1]. These approximate the many-body system as a continuum fluid and only treat its behaviour at macroscopic length and time scales. These theories work remarkably well for many real fluids; however, hydrodynamics and thermodynamics were originally developed without a description of the smallest scales of the system (at the scale of a particle). As a result, these theories require, as input, phenomenological expressions relating the fundamental variables of the system (e.g., equations of state and constitutive relations). These must be obtained separately through experimental or theoretical work. In many-body systems, a hydrodynamic description may also be problematic as a time scale separation must exist between the dynamics of the particles and the macroscopic phenomena under consideration. For example, in granular flows (e.g., pouring of sand or grain), the particles are of the order of the system size and no such scale separation exists.

Kinetic theory or, more generally, statistical mechanics is a framework that attempts to take a model description of the interaction between particles and determine their bulk

behaviour. For molecular fluids, it is essentially an attempt to derive hydrodynamical balance equations and can provide the necessary expressions (e.g., constitutive relations) required to close the hydrodynamical theories. However, this treatment is complex, and the most successful applications to date are based on simple model fluids, such as the hard-sphere model [2].

Within the last fifty years, a new tool has arrived to aid in the study of many-body systems. Advances in computational power have allowed the equations of motion for a relatively large collection of particles to be directly solved using numerical methods. These molecular dynamics (MD) techniques provide a method to generate trajectories for a model system. These results can then be compared to theoretical predictions for the same model, providing feedback on the approximations taken and (hopefully) suggest improved methods of solution. Simulations, along with a suitable model, can also provide insight into complex behaviour observed experimentally, as there is complete control over the systems evolution and any property may be monitored.

Key to all of this analysis is the interaction model that is used to represent the particles of the many-body system. This model must be simple enough to allow theoretical analysis and simulation and yet be sophisticated enough to possess a sufficient amount of the underlying physics of the system studied.

Most interaction models that are used in molecular and mesoscale simulation work are based on continuous potentials. The focus of this thesis is on discrete potentials. Discrete potentials exhibit much of the complex behaviour of real systems and provide some of the most elegant minimal models which exhibit complex behaviour (e.g., see Chap. 8). Discrete potentials are also suitable for directly modelling real, complex systems, such as the thermodynamic properties of *n*-alkanes and aromatic fluids [3]. Theoretically, many calculations become tractable when using a discrete potential (e.g., see Chap. 3), and they are at the core of Enskog theory [2], the most successful kinetic theory to date. The hard-sphere model is the prototypical discrete potential and forms the basis of many successful perturbation theories [4, 5] for the properties of materials, such as the equation of state for polymers solutions.

Discrete potentials have also played a major role in the development of molecular dynamics simulation methods. The very first molecular dynamics simulations were performed using discrete potentials because of their relatively inexpensive computational cost [6]. Recent advances in the simulation of discrete potential systems have allowed the construction of molecular dynamics algorithms that scale linearly with the system size (see Chap. 4), allowing access to large system sizes and the long time scales required to extract the long time behaviour. Discrete potentials can even accurately approximate soft potentials, with possible savings in computational cost and time [7, 8].

Despite the extensive literature on discrete potentials, the software available for simulating discrete potentials are relatively limited and specialised when compared to what is available for continuous potential systems. The algorithms used to simulate discrete

potentials must be event driven to cope with the singularities in the interaction energies. These event-driven algorithms are significantly more complex than their time-stepping counterparts used for soft-potential simulations. This has hampered the development of a general simulation “tool” for discrete potentials, which in turn may have limited their uptake in the modelling community when compared with the adoption of continuous potentials.

In this work, we examine the properties of discrete potential systems and their use in modelling real systems. As part of this work, we develop a general event-driven simulation package tailored to simulating discrete potential systems. This performs both molecular dynamics simulations and Direct Simulation Monte Carlo (DSMC) of kinetic theories. These techniques are then applied to a wide range of systems to exhibit the implemented features and explore complex many-body dynamics.

1.2 Thesis Overview

This dissertation is presented in the alternate format, as allowed by The University of Manchester thesis submission guidelines¹. As such, certain chapters of this thesis are in a format suitable for submission to refereed journals. Each of these chapters is clearly marked and begins with a paragraph detailing the original contribution of the author to the work contained within. Reprints of published chapters are also included in the Appendices (see App. A–C).

The thesis is organised into two parts. The first part deals with the background theory and methods of studying discrete potential systems (Chap. 2–4). This is then followed by several applications of the novel methods to model systems (Chap. 5–8). Chapter 2 presents the formalism used in this work and describes the fundamental dynamics and interactions of all of the systems studied. This establishes the kinetic theory framework and focuses on the specifics for hard-sphere systems. In Chapter 3, a novel method of performing DSMC which includes pre-collision velocity correlations between particles is presented along with some benchmarking results. The following chapter (Chap. 4) concerns DYNAMO, the general event-driven simulation program developed for studying discrete potentials used throughout the remainder of the thesis. This concludes the first part of the thesis on methods of analysis and the later chapters are applications of the techniques.

Chapter 5 presents MD simulation results for very large systems of hard spheres. Using DYNAMO, calculations of the pressure for systems approaching the thermodynamic limit are compared against predictions from various equation of states. In Chap. 6, granular materials under shear are studied using the inelastic hard sphere model. The subsequent chapter (Chap. 7) studies the transport properties of nano-colloidal mixtures using a binary-hard sphere model. In the last chapter on applications (Chap. 8), the con-

¹<http://www.campus.manchester.ac.uk/researchoffice/graduate/ordinancesandregulations>

trol parameters for a simple model of helix formation are fully characterised. Finally, a summary of the dissertation work and directions for future work are outlined in Chap. 9.

1.3 References

- [1] S. de Groot and P. Mazur. *Non-Equilibrium Thermodynamics*. New York: Dover, 1984.
- [2] H. van Beijeren and M. H. Ernst, “Modified Enskog Equation”, *Physica*. 68, 437–456 (1973).
- [3] J. R. Elliott, “Optimized step potential models for *n*-alkanes and benzene”, *Fluid Phase Equilibria*. 194–197, 161–168 (2002).
- [4] W. G. Chapman, G. Jackson and K. E. Gubbins, “Phase equilibria of associating fluids: Chain molecules with multiple bonding sites”, *Mol. Phys.* 65, 1057–1079 (1988).
- [5] D. Ghonasgi and W. G. Chapman, “A new equation of state for hard chain molecules”, *J. Chem. Phys.* 100, 6633–6639 (1994).
- [6] B. J. Alder and T. E. Wainwright, “Phase transition for a hard sphere system”, *J. Chem. Phys.* 27, 1208–1209 (1957).
- [7] G. Chapela, L. E. Scriven and H. T. Davis, “Molecular dynamics for discontinuous potential. IV. Lennard-Jonesium”, *J. Chem. Phys.* 91, 4307–4313 (1989).
- [8] R. van Zon and J. Schofield, “Event-driven dynamics of rigid bodies interacting via discretized potentials”, *J. Chem. Phys.* 128, 154119 (2008).

CHAPTER
TWO

FORMALISM

THIS chapter reviews the general formalism for handling the dynamics of many-body systems and the specifics pertaining to the discrete potential models studied here. First, distribution functions are introduced to characterise the system. The dynamics of the distribution functions are governed by the Liouville equation. The relation of system variables to the distribution function and associated Liouvillean operators is then given. The Bogoliubov-Born-Green-Kirkwood-Yvon (BBGKY) hierarchy is then used to link the various “sub”-distribution functions to the full distribution using the binary interaction expansion.

These general results are then specialised to the case of a discrete potential system. This will begin by defining the equations of motion, which allow the definition of the free streaming operator. The potentials studied in this work are introduced and the dynamics of the possible two-particle events are outlined. Finally, the interaction operators for a hard sphere system are defined.

2.1 Basic Considerations

Consider a system of N particles. This system can be described by a set of dynamical variables $\Gamma_1, \Gamma_2, \dots$ (e.g., the position and velocity of every particle). If each of the dynamical variables are taken as the dimensions of a space, then what is commonly known as phase space (Γ -space) is constructed. The microscopic state of a system can then be represented by a point Γ in phase space. The systems evolution through time is then described by a curve in phase space. It is assumed that the dynamics of the system is governed by a set of differential equations:

$$\dot{\Gamma}_j = \psi_j(\Gamma, t) \quad (2.1.1)$$

where t is the time, Γ_i are the dynamical variables associated with particle j (e.g, its position and momentum), and $\dot{\Gamma}_j$ is the time derivative of Γ_j . Therefore we are dealing with a deterministic system, and if the initial conditions are known then the trajectory

through phase space is uniquely determined.

The Dirac notation is employed here for simplicity in dealing with these systems. Given a phase function A in Dirac form

$$A(\Gamma) \equiv \langle \Gamma | A \rangle \quad (2.1.2)$$

where each bra $\langle x |$ and ket $|x\rangle$ is the functional equivalent of a vector. The ket $|A\rangle$ is a representation free generalisation of a function to any co-ordinate or variable set. A simple example is kinetic energy, expressed in momentum form

$$\langle \mathbf{p} | E \rangle = \frac{\mathbf{p}^2}{2m} \quad (2.1.3)$$

where \mathbf{p} is the momentum of a particle and m is its mass. However this function could be rewritten in cylindrical co-ordinates and this is implied by a change of basis. For completeness, the bra is defined as the conjugate transpose of its complimentary ket. The inner product is also defined as

$$\langle A | B \rangle \equiv \int d\Gamma A^*(\Gamma) B(\Gamma) \quad (2.1.4)$$

where the asterisk denotes a complex conjugate. Typically it is assumed that the bra's and ket's presented here are entirely real.

In the following sections, several important tools for studying many-body theory are discussed, along with the exact equations of many-body theory and the foundations of previous kinetic theory work.

2.2 Distribution Function

Considering an ensemble, or infinite collection of systems that satisfy some restrictions (in this work a constant N and volume with the shear rate, temperature, or total energy held fixed is typical) and differ only in initial conditions allows the construction of a distribution function. The density of these systems in Γ -space is described using a distribution function:

$$\langle \Gamma | F(t) \rangle = \frac{\delta N(\Gamma, t)}{\delta \Gamma} \quad (2.2.1)$$

where δN is the fraction of systems contained within the infinitesimal phase space volume $\delta \Gamma$ about the point Γ , and F is the normalised N -particle phase space distribution function. The Liouville equation gives the equation of motion for the distribution function [1]

$$\left\langle \Gamma \left| \dot{F}(t) \right. \right\rangle = - \frac{\partial}{\partial \Gamma} \cdot (\dot{\Gamma} F(\Gamma, t)) = - \langle \Gamma | i\mathcal{L} | F(t) \rangle \quad (2.2.2)$$

where the f -Liouvillean operator $i\mathcal{L}$ is now defined. This equation is valid when the ensemble members cannot be destroyed or created and the distribution function is a continuous function. Although the distribution functions typically used in this work exclude unphysical configurations which results in discontinuities, the formalism is still valid given careful treatment of the overlap functions and evolution operators (See Sec. 2.8).

Using the distribution function, the expectation value of a property A (e.g., the pressure) can be determined

$$\langle A(t) \rangle_{\Gamma} = \int d\Gamma A(\Gamma) F(\Gamma, t) = \langle A | F(t) \rangle \quad (2.2.3)$$

where $\langle A \rangle_{\Gamma}$ is the ensemble average of A . Assuming the system is ergodic, the ensemble average (Eq. (2.2.3)) is equivalent to a time average over a (sufficiently long) single trajectory. This averaging is required as typically the initial state of the system is not exactly known (with the exception of simulations). Using Eqs. (2.2.3) and (2.2.2) the time derivative of any property can be determined if the evolution of f is known.

$$\left\langle \dot{A}(t) \right\rangle_{\Gamma} = \left\langle A \mid \dot{F}(t) \right\rangle = -\langle A | i\mathcal{L} | F(t) \rangle \quad (2.2.4)$$

The corresponding Liouvillean operator for the time evolution of a property, along with some of the properties of the operators are discussed in the next section.

2.3 Time Evolution Operators

The evolution of a phase function A can be obtained directly using the chain rule

$$\langle \Gamma | \dot{A} \rangle = \dot{\Gamma} \cdot \frac{\partial A(\Gamma)}{\partial \Gamma} = \langle \Gamma | i\mathcal{L}^{\dagger} | A \rangle \quad (2.3.1)$$

where the p -Liouvillean operator $i\mathcal{L}^{\dagger}$ is now defined. If there is no explicit dependence of $i\mathcal{L}$ (or $i\mathcal{L}^{\dagger}$) on time, the formal solution of Eqs. (2.2.2) and (2.3.1) is as follows

$$|f(t)\rangle = \exp(-i\mathcal{L}t) |f(0)\rangle = \mathcal{S}_t |f(0)\rangle \quad (2.3.2)$$

$$|A(t)\rangle = \exp(i\mathcal{L}^{\dagger}t) |A(0)\rangle = \mathcal{S}_t^{\dagger} |A(0)\rangle \quad (2.3.3)$$

where \mathcal{S}_t is the f -streaming operator or propagator, and \mathcal{S}_t^{\dagger} is the p -streaming operator or propagator. The symbol \dagger indicates that the operators are adjoint, which is easily proved through the equivalence

$$\langle A(t) \rangle = \langle A | \mathcal{S}_t | f(0) \rangle = \langle f(0) | \mathcal{S}_t^{\dagger} | A \rangle \quad (2.3.4)$$

It has again been assumed that both f and A are entirely real, which is the case in general for our system. This both proves the streaming operators are adjoint and defines

an adjoint operator. For future reference it should be remarked that Eq. (2.3.2) is in the Schrödinger picture, where the distribution function carries the time dependence. When the time dependence has been shifted to the property, as in Eq. (2.3.3), this is known as the Heisenberg picture.

The Liouvillean operators are adjoint, however a change of sign occurs when the adjoint is taken. From Eqs. (2.2.3) and (2.3.1)

$$\langle \dot{A} \rangle = -\langle A | i\mathcal{L} | f \rangle = \langle f | i\mathcal{L}^\dagger | A \rangle \quad (2.3.5)$$

Again the assumption that A , \mathcal{L} , and f are entirely real has been made. This adjoint property is indicated by prepending the operator with i .

For conservative, non-singular forces, the Liouville operators are self-adjoint and $i\mathcal{L} = i\mathcal{L}^\dagger$. This implies from the definition of the Liouville operators

Eqs. (2.2.2) and (2.3.1) that

$$\frac{\partial}{\partial \Gamma} \cdot \dot{\Gamma} = \langle \Gamma | \Lambda \rangle = 0 \quad (2.3.6)$$

where Λ is defined as the phase space compressibility. The phase space compressibility is in this case a phase function and not an operator. Typically, the equations of motion for the system are constructed such that $\Lambda = 0$, and this condition is known as the adiabatic incompressibility of phase space (AII). A sufficient requirement for a system to be AII is that the adiabatic (unthermostatted) equations of motion are derivable from a Hamiltonian [1].

2.4 Binary Interaction Expansion

With the definition of the Liouvillean and streaming operators the framework for developing kinetic theory is almost complete. However, an important simplification can be made to the Liouvillean operator for the case of discontinuous potentials.

The Liouvillean operator may be split into two pieces: one typically corresponding to the unperturbed motion of a particle in a field and another accounting for the inter-particle forces. Furthermore, only binary interactions (2-particle) need to be considered for discontinuous potentials. As interactions are instantaneous, three-particle interactions occur with measure zero. The Liouvillean operators can then be expanded as:

$$i\mathcal{L} = \sum_j^N \left[i\mathcal{L}_j^0 - \sum_{k>j}^N \mathcal{T}(j, k) \right] \quad (2.4.1)$$

$$i\mathcal{L}^\dagger = \sum_j^N \left[i\mathcal{L}_j^0 + \sum_{k>j}^N \mathcal{T}^\dagger(j, k) \right] \quad (2.4.2)$$

where $i\mathcal{L}_j^0$ is the free streaming operator for particle j , $\mathcal{T}(j, k)$ is the binary interaction

operator for particles j and k , and $\mathcal{T}^\dagger(j, k)$ is its adjoint. It has been assumed that the free streaming operators are self-adjoint

$$(i\mathcal{L}^0)^\dagger = -i\mathcal{L}^0 \quad (2.4.3)$$

Later this will be shown to be true for the systems studied. It should be noted now that the phase space compression Λ has been absorbed into the interaction term. So that from the definition of the Liouvillean operators and the assumption that the free streaming operator is self adjoint

$$\mathcal{T}(j, k) = -\mathcal{T}^\dagger(j, k) - \Lambda(j, k) \quad (2.4.4)$$

where $\Lambda(j, k)$ is now an operator that determines the phase space compression resulting from an interaction. If AII Γ is satisfied then the interaction operators are also self adjoint.

This binary interaction assumption now allows the development of the BBGKY hierarchy.

2.5 BBGKY Hierarchy

So far only the full N -particle distribution function F has been dealt with. Practically, the full distribution function contains an unnecessary level of information. Most physical properties (including the hydrodynamical variables) can be written in terms of the simpler single, or two particle distribution function. An n particle distribution function can be obtained from the full N particle distribution by integration

$$f^{(n)}(\Gamma_1, \dots, \Gamma_n, t) = \frac{N!}{(N-n)!} \int d\Gamma_{n+1} \cdots d\Gamma_N F(\Gamma_1, \dots, \Gamma_N, t) \quad (2.5.1)$$

where $f^{(n)}$ is the n particle distribution function for a system of N particles. The term in front of the integral arises from the fact that the distribution function is symmetric under interchange of particle numbering. It is the number of ways that a set of size n can be selected from a population of size N . The dynamics of this distribution function are determined using the Liouvillean equation. Using the binary collision expansion (see Eq. (2.4.1)) in Eq. (2.2.2) and inserting Eq. (2.5.1) leads to

$$\begin{aligned} & \left(\frac{\partial}{\partial t} + \sum_j^n \left[i\mathcal{L}_j^0 - \sum_{k>j}^n \mathcal{T}(j, k) \right] \right) f(\Gamma_1, \dots, \Gamma_n, t) \\ &= \sum_{j=1}^n \int d\Gamma_{n+1} \mathcal{T}(j, n+1) f(\Gamma_1, \dots, \Gamma_{n+1}, t) \end{aligned} \quad (2.5.2)$$

This is the BBGKY hierarchy that exactly links the n -distribution function to the $n+1$ -distribution function. The hierarchy is crucial in the formulation of kinetic theory as it

is exact (within the binary collision assumption) and forms the starting point for many derivations. The first two equations of the hierarchy are

$$\left(\frac{\partial}{\partial t} + i\mathcal{L}_1^0 \right) f(\Gamma_1, t) = \int d\Gamma_2 \mathcal{T}(1, 2) f(\Gamma_1, \Gamma_2, t) \quad (2.5.3a)$$

$$\left(\frac{\partial}{\partial t} + i\mathcal{L}_1^0 + i\mathcal{L}_2^0 - \mathcal{T}(1, 2) \right) f(\Gamma_1, \Gamma_2, t) = \int d\Gamma_3 [\mathcal{T}(1, 3) + \mathcal{T}(2, 3)] f(\Gamma_1, \Gamma_2, \Gamma_3, t) \quad (2.5.3b)$$

Typically the series is truncated at the second or first equation and the series closed by expressing the highest distribution function in terms of the lower distribution functions.

Another series in the spirit of the BBGKY hierarchy may be constructed using the streaming operators. Using the Dyson relations [2] and the binary interaction expansion (Sec. 2.4)

$$\mathcal{S}_t F = \mathcal{S}_t^0 F + \int_0^t dt' \mathcal{S}_{t-t'} \sum_{j,k>j}^N \mathcal{T}(j, k) \mathcal{S}_{t'}^0 F \quad (2.5.4a)$$

$$= \mathcal{S}_t^0 F + \int_0^t dt' \mathcal{S}_{t-t'}^0 \sum_{j,k>j}^N \mathcal{T}(j, k) \mathcal{S}_{t'} F \quad (2.5.4b)$$

where the free streaming propagator \mathcal{S}_t^0 has the following form and relations from free particle Liouville theory

$$\mathcal{S}_t^0 = \exp \left(t \sum_j^n i\mathcal{L}_j^0 \right) \quad (2.5.5)$$

$$(\mathcal{S}_t^0)^\dagger = \mathcal{S}_{-t}^0 \quad (2.5.6)$$

Applying this to the full distribution function and integrating over $N - n$ variables (see Appendix E) gives

$$\begin{aligned} f^{(n)}(t) &= \mathcal{S}_t^0 f^{(n)}(0) + \sum_j^n \sum_{k>j}^n \int_0^t dt' \mathcal{S}_{t-t'}^0 \mathcal{T}(j, k) f^{(n)}(t') \\ &\quad + \sum_j^n \int_0^t dt' \mathcal{S}_{t-t'}^0 \int d\Gamma_{n+1} \mathcal{T}(j, n+1) f^{(n+1)}(t') \end{aligned} \quad (2.5.7)$$

This expression is useful when attempting to numerically simulate the distribution functions using DSMC techniques (see Chap. 3). The Dyson equations (Eqs. (2.5.4)) also provide a formal starting point for the derivation of the interaction operators \mathcal{T} .

The BBGKY (Eq. (2.5.2)) and the streaming operator hierarchy (Eq. (2.5.7)) serve as an example of the restricted applicability of the full f -operators ($i\mathcal{L}$ and \mathcal{S}_t) to the N -particle distribution function F in generating the evolution in time; however, the components ($i\mathcal{L}^0$, \mathcal{S}_t^0 and \mathcal{T}) of these operators are still convenient when treating the $f^{(n)}$

distribution function.

The formalism developed so far in this chapter is, in general, applicable to all many-body classical systems and is exact within the binary interaction assumption. The BBGKY hierarchy (Eq. (2.5.2)) forms the starting point for many kinetic theory derivations and approximations. In the next sections, the Liouvillean operators are specialised for the simple granular gas system to complete the mathematical description of the system.

2.6 Newtonian Dynamics

To specialise the results of the previous sections to the systems studied in this work the dynamics of the models studied must first be defined. As this work contains two types of flow regimes the general equations of motion for a classical system of particles evolving adiabatically in a homogeneous flow field are used

$$\dot{\mathbf{r}}_j = \mathbf{v}_j = \frac{\bar{\mathbf{p}}_j}{m_j} + \mathbf{r}_j^T \cdot \nabla \mathbf{u} \quad (2.6.1a)$$

$$\dot{\bar{\mathbf{p}}}_j = \mathbf{X}_j(\mathbf{r}_j) + \sum_k \mathbf{F}_{jk} - \bar{\mathbf{p}}_j^T \cdot \nabla \mathbf{u} \quad (2.6.1b)$$

where $\mathbf{v}_j = m_j^{-1} \mathbf{p}_j$ is a particles “laboratory” velocity, \mathbf{F}_{jk} is the force exerted on particle j by particle k due to inter-particle interactions, and \mathbf{X}_j is the force on particle j due to an external field. The peculiar variants of the momentum $\bar{\mathbf{p}}$ and velocity ($\bar{\mathbf{v}}_j = \bar{\mathbf{p}}_j/m_j$) denoted by a bar, are defined by Eq. (2.6.1a). The peculiar variables are widely used with the assumption of a homogeneous flow. This is convenient as the distribution functions of a homogeneous flow are spatially invariant when expressed in the peculiar variables.

Equations (2.6.1) are the Sllod equations of motion [3], originally derived for the study of planar Couette shear flow. There exists a “generalised” Sllod (g-Sllod) [4] variant of the Sllod equations, created to study elongation flow. g-Sllod was later re-derived as the “proper”-Sllod or p-Sllod equations [5] by requiring Newtonian dynamics under time-independent flow.

$$\dot{\mathbf{v}}_j = m_j^{-1} \mathbf{X}_j(\mathbf{r}_j) + m_j^{-1} \sum_k \mathbf{F}_{jk} + \mathbf{r}_j^T \cdot \frac{\partial \nabla \mathbf{u}}{\partial t} \quad (2.6.2)$$

A somewhat heated discussion of the benefits of Sllod and g/p-Sllod algorithms has occurred in the literature [6, 7]. g-Sllod dynamics corresponds to the correct, physical description of the system in experiments, where time-independent flows are induced through boundary conditions; however, the Sllod equations present several algorithmic benefits in the treatment of boundary conditions of infinite, periodic systems. One point is agreed upon, the Sllod and g-Sllod equations collapse to the same expressions for planar Couette/simple shear flow.

In this work two types of flow are considered

$$\nabla \mathbf{u} = \begin{cases} 0 & \text{Stationary flow} \\ \dot{\gamma} \hat{\mathbf{e}}_y \hat{\mathbf{e}}_x & \text{Simple shear flow} \end{cases} \quad (2.6.3)$$

where $\hat{\mathbf{e}}_x$ is a unit vector in the x -dimension and $\dot{\gamma}$ is the shear rate. As the time derivative of these flow gradients are zero, $\partial \nabla \mathbf{u} / \partial t = 0$ (Eq. (2.6.2)), only Newtonian dynamics are considered here.

If the interaction term (\mathbf{F}) is deleted from the equations of motion it is apparent that the free streaming equations of motion do satisfy the AII condition, provided the diagonal terms of $\nabla \mathbf{u}$ are zero. This confirms the previous assumption of the free streaming Liouvillean operator being self-adjoint ($i\mathcal{L}_j^0 = -(i\mathcal{L}_j^0)^\dagger$). Taking \mathbf{r} and $\bar{\mathbf{p}}$ as the dynamical variables ($\Gamma_j = \{\mathbf{r}_j, \bar{\mathbf{p}}_j\}$), the definition of the dynamics allows the redefinition of the Liouvillean operators

$$\langle \Gamma_j | i\mathcal{L}_j^0 | \Gamma_j \rangle = \mathbf{v}_j \cdot \frac{\partial}{\partial \mathbf{r}_j} + (\mathbf{X}_j(\mathbf{r}_j) - \bar{\mathbf{p}}_j^T \cdot \nabla \mathbf{u}) \cdot \frac{\partial}{\partial \bar{\mathbf{p}}_j} \quad (2.6.4a)$$

$$\langle \Gamma_j, \Gamma_k | \mathcal{T}^\dagger(j, k) | \Gamma_j, \Gamma_k \rangle = \mathbf{F}_{jk} \cdot \left(\frac{\partial}{\partial \bar{\mathbf{p}}_j} - \frac{\partial}{\partial \bar{\mathbf{p}}_k} \right) \quad (2.6.4b)$$

$$\langle \Gamma_j, \Gamma_k | \mathcal{T}(j, k) | \Gamma_j, \Gamma_k \rangle = - \langle \Gamma_j, \Gamma_k | \mathcal{T}^\dagger(j, k) | \Gamma_j, \Gamma_k \rangle - \left(\frac{\partial}{\partial \bar{\mathbf{p}}_j} - \frac{\partial}{\partial \bar{\mathbf{p}}_k} \right) \cdot \mathbf{F}_{jk} \quad (2.6.4c)$$

This definition of the \mathcal{T} operators is not useful for discontinuous potentials as it contains derivatives of the inter-particle potential. The following sections derive the interaction operators for discontinuous potential systems and begins with a discussion of the studied potentials.

2.6.1 Inter-Particle Potential

In soft potential systems, the inter-particle force is typically defined through the derivative of the inter-particle potential. In discontinuous potentials, the singularities in the potential mean the force cannot be defined through the potential alone and conservation of mass and an energy balance must also be used. The simplest discrete potential used in this work is the prototypical hard-sphere potential, given by

$$u_{jk}^{(HS)}(\mathbf{r}_j, \mathbf{r}_k) = \begin{cases} 0 & \text{for } |\mathbf{r}_{jk}| > \sigma_{jk} \\ \infty & \text{for } |\mathbf{r}_{jk}| < \sigma_{jk} \end{cases} \quad (2.6.5)$$

where $\mathbf{r}_{jk} = \mathbf{r}_j - \mathbf{r}_k$ is the separation vector and $\sigma_{jk} = (\sigma_j + \sigma_k)/2$ is the interaction diameter, where σ_j is the particle j 's interaction diameter. The inter-particle potential is singular about the point of contact $\mathbf{r}_{jk} = \sigma_{jk}$ and the derivative is undefined. \mathcal{T} cannot be defined through the potential alone and more information on the possible interaction events must be specified. The hard-sphere potential results in a single class of event, the

collision or hard “core” interaction at $|\mathbf{r}_{jk}| = \sigma_{jk}$, which prevents particles overlapping. By examining the conditions upon which this event occurs and it’s effect, the corresponding interaction operator may be derived.

There are a further two other potentials used in this work, but only the hard sphere potential is treated using kinetic theory. The other two potentials and their interaction dynamics are described here for the purpose of simulation only. Beginning with the square-bond potential

$$u_{jk}^{(SB)}(\mathbf{r}_j, \mathbf{r}_k) = \begin{cases} \infty & \text{for } |\mathbf{r}_{jk}| > \lambda\sigma_{jk} \\ 0 & \text{for } \sigma_{jk} < |\mathbf{r}_{jk}| < \lambda\sigma_{jk} \\ \infty & \text{for } |\mathbf{r}_{jk}| < \sigma_{jk} \end{cases} \quad (2.6.6)$$

where λ is the well/bond width parameter. The square-bond potential contains a hard-core interaction and introduces a “bounce” event at the limit of the bond well $|\mathbf{r}_{jk}| = \lambda\sigma_{jk}$. This interaction is used to bond two particles together to form polymeric materials, as bonded particles must remain within a distance $\sigma_{jk} < |\mathbf{r}_{jk}| < \lambda\sigma_{jk}$. Finally, the square-well potential is used to simulate short range attraction forces

$$u_{jk}^{(SW)}(\mathbf{r}_j, \mathbf{r}_k) = \begin{cases} 0 & \text{for } |\mathbf{r}_{jk}| > \lambda\sigma_{jk} \\ -\varepsilon & \text{for } \sigma_{jk} < |\mathbf{r}_{jk}| < \lambda\sigma_{jk} \\ \infty & \text{for } |\mathbf{r}_{jk}| < \sigma_{jk} \end{cases} \quad (2.6.7)$$

where ε is the square well depth. The square-well expands upon the square-bond potential. At the limit of the bond $|\mathbf{r}_{ij}| = \lambda\sigma_{ij}$ a “bounce” event occurs; however, two receding particles with sufficient kinetic energy may escape the particle well and a “release” event will occur. Two approaching particles outside the limits of the square well will “capture” each other at a distance of $|\mathbf{r}_{jk}| = \lambda\sigma_{jk}$.

The treatment given below will focus on generating the interaction operators for the hard sphere system only. This is straightforward to extend to square-bond and square-well fluids by decomposing the interaction operator into the operators for each class of event

$$\mathcal{T}(j, k) \equiv \mathcal{T}_c(j, k) + \mathcal{T}_{wc}(j, k) + \mathcal{T}_{wr}(j, k) \quad (2.6.8)$$

where \mathcal{T}_c , \mathcal{T}_{wc} , and \mathcal{T}_{wr} are the “core”, “bond”, “well capture” and “well release”/“Bounce” operators respectively. In the following sections the dynamics of these potentials is discussed for the purpose of simulations and for defining \mathcal{T}_c .

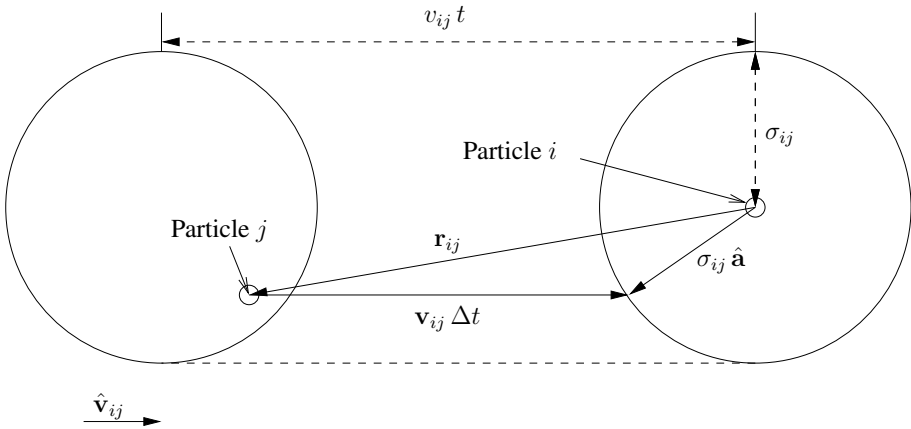


Figure 2.1: Collision variables rotated into the v_{ij} frame. The cylinder contains the volume in r_{ij} space that is swept out for a given v_{ij} and reference particle position. Any particles within this cylinder are on a collision course.

2.7 Interaction Dynamics

The conditions that preclude an interaction must be known to specify when the interaction operators should act. The dynamics of the collision is then used to determine the action of \mathcal{T} on functions of the phase variables.

2.7.1 Collision Conditions

To determine the necessary conditions for a pair of particles to interact, the free streaming equations of motion (Eq. (2.6.1a)) must be solved. The square-well, square-bond and hard sphere potential events can all be decomposed into tests on non-overlapping spheres approaching each other and overlapping spheres receding from each other.

For both tests, the distance between the particles is equal to the an interaction diameter σ_{jk} at the time of the event, giving

$$\mathbf{r}_{jk} + \Delta t \mathbf{v}_{jk} = \sigma_{jk} \hat{\mathbf{a}} \quad (2.7.1)$$

where $\mathbf{v}_{jk} = \mathbf{v}_j - \mathbf{v}_k$ is the relative velocity, $\hat{\mathbf{a}}$ is a unit vector along the line of contact, and Δt is the time till the interaction occurs (see Fig. (2.1)). Squaring the equation of motion and expanding the left hand side yields a quadratic in time

$$v_{jk}^2 \Delta t^2 + 2 \mathbf{r}_{jk} \cdot \mathbf{v}_{jk} \Delta t + r_{jk}^2 - \sigma_{jk}^2 = 0 \quad (2.7.2)$$

The interaction conditions can then be inferred from the conditions of finding roots to this equation. These conditions vary depending on the type of interaction tested for.

For a “collision” (two non-overlapping spheres to touch) to occur, the following must

be true

$$\mathbf{r}_{jk} \cdot \mathbf{v}_{jk} < 0 \quad (\text{Particles approaching}) \quad (2.7.3a)$$

$$(\mathbf{r}_{jk} \cdot \mathbf{v}_{jk})^2 - v_{jk}^2 (r_{jk}^2 - \sigma_{jk}^2) \geq 0 \quad (\text{Real roots/Collision course}) \quad (2.7.3b)$$

The time till a “collision” is then given by the smallest root of Eq. (2.7.2). For two overlapping spheres, the only exit condition is

$$v_{jk} > 0 \quad (\text{particles are in motion}) \quad (2.7.4)$$

The real roots condition is satisfied if this condition holds as $c \leq 0$ for the overlapping case. The correct root for this system is then the positive root.

A final collision condition, required only for the definition of the interaction operators, is used to ensure that the dynamics are valid by exclusively considering future events.

$$\Delta t \geq 0 \quad (2.7.5)$$

This condition is most conveniently expressed through the equation of motion for the particle separation (Eq. (2.7.1))

$$\Delta t = \frac{\sigma_{ij} - \mathbf{r}_{ij} \cdot \hat{\mathbf{a}}}{\mathbf{v}_{ij} \cdot \hat{\mathbf{a}}} \geq 0 \quad (2.7.6)$$

Equations (2.7.3), (2.7.4), and (2.7.6) form the collision conditions which are key to deriving the interaction operators.

2.7.2 Collision Dynamics

In determining the interaction operators and when performing simulations, the mechanics of the events are required. When a interaction occurs, the total momentum of the system is conserved. The “core” and “bounce” interactions use the same rule and is given for the simple granular gas by [8]

$$\Delta \mathbf{p}_j = -\mu_{jk} (1 + \alpha) (\hat{\mathbf{r}}_{jk} \cdot \mathbf{v}_{jk}) \hat{\mathbf{r}}_{jk} \quad (2.7.7)$$

where $\Delta \mathbf{p}$ is the momentum change of j on collision, $\mu_{jk} = m_j m_k / (m_j + m_k)$ and α is the coefficient of restitution. It is this coefficient of restitution that characterises the inelasticity of the system and in the limit of $\alpha \rightarrow 1$ the results for elastic hard spheres are recovered.

Theoretically, an inverse collision where the pre-collision values are obtained from post-collision variables [8] can be defined

$$-\Delta \mathbf{p}_j = -\mu_{jk} (1 + \alpha^{-1}) (\hat{\mathbf{r}}'_{jk} \cdot \mathbf{v}'_{jk}) \hat{\mathbf{r}}'_{jk} \quad (2.7.8)$$

where the primes denote post-collision values. This completes the description of the dynamics of hard-sphere and square-bond dynamics and is all that is required to specify \mathcal{T} for the hard-sphere system. The interaction rules for the other events are derived for the purpose of simulation.

Using an energy balance and conservation of momentum, the collision rule for an arbitrary event with a change in total kinetic energy of ΔKE is

$$\Delta \mathbf{p}_j = 2 \Delta KE \left[\mathbf{v}_{jk} \cdot \hat{\mathbf{r}}_{jk} + \text{sign}(\mathbf{v}_{jk} \cdot \hat{\mathbf{r}}_{jk}) \left\{ (\mathbf{v}_{jk} \cdot \hat{\mathbf{r}}_{jk})^2 + \frac{2 \Delta KE}{\mu_{jk}} \right\}^{1/2} \right]^{-1} \hat{\mathbf{r}}_{jk} \quad (2.7.9)$$

For a well capture event $\Delta KE = \varepsilon$ and for a release event $\Delta KE = -\varepsilon$. A test for these events arises from the real roots condition

$$\frac{\mu_{jk}}{2} (\hat{\mathbf{r}}_{ij} \cdot \mathbf{v}_{ij})^2 \geq -\Delta KE \quad (2.7.10)$$

Should this not hold true then a “bounce” event will occur and Eq. (2.7.7) is used. These equations are also valid for a square shoulder interaction by specifying a negative well depth. With the dynamics and conditions for the events specified the interaction operator \mathcal{T} for a system of hard spheres can now be determined.

2.8 Determining the Interaction Operators

Systems containing hard or discontinuous potentials present several difficulties when defining \mathcal{T} and \mathcal{T}^\dagger . An alternative approach to Eqs. (2.6.4) must be used, either taking the hard limit of an increasingly steep soft potential or, as will be done here, a more direct way by observing the action of \mathcal{T}^\dagger on a property [9]. This section is largely based on the works of Ernst et al. [10] and Dorfman and Ernst [11] for elastic hard spheres. The final results for granular interaction operators were first reported by van Noije et al. [8] and Brey et al. [9].

First, the overlapping configurations must be eliminated from the phase space integrations by the consideration of an overlap function theoretically contained within the distribution function. Then the action of \mathcal{T}^\dagger on a property is used to determine the form of \mathcal{T}^\dagger . Finally, using the adjoint relationship \mathcal{T} is determined from \mathcal{T}^\dagger .

2.8.1 Overlap Function

In determining the average values of properties, integrations are performed over all of phase space (Eq. (2.3.4)). In hard potentials there are physically impossible regions of phase space where an overlap occurs in the system. The system dynamics is also undefined in these regions and care must be taken to ensure that these portions of phase space are zero-weighted. In hard-sphere systems, this is achieved through the use of an

overlap function

$$W(\boldsymbol{\Gamma}) = \prod_{j>k} \Theta(|\mathbf{r}_{jk}|^2 - \sigma_{jk}^2) \quad (2.8.1)$$

where Θ is the Heaviside step function. The function W is equal to 1 for all allowed configurations and vanishes in the event of an overlap between two particles. The distribution function is proportional to this function and in the Heisenberg picture (Eq. (2.3.3)) the dynamics are well defined as the overlap function appears to the left of the streaming operator

$$\langle A(t) \rangle_\Gamma = \langle f(0) W | \mathcal{S}_t^\dagger | A \rangle \quad (2.8.2)$$

Therefore any overlapping regions of phase space will be eliminated from the ensemble average. In the Schrödinger picture the overlap function stands to the right of \mathcal{S}_t and the integration is not well defined. To retain the current formalism, the overlap function is included in the definition of the adjoint streaming operator

$$(W \mathcal{S}_t^\dagger)^\dagger = \mathcal{S}_t W \quad (2.8.3)$$

Therefore \mathcal{S}_t will give the correct behaviour if defined through this adjoint relationship.

The free streaming Liouvillean operators ($i\mathcal{L}_i^0$) are already defined for all of phase space and so it is natural to extend the collision operators for all of phase space. The actual definition of overlapped dynamics is unimportant provided the operators are defined correctly with the overlap function [10].

2.8.2 p -Collision Operator

To begin determining the interaction operators only two particle dynamics is considered. These results are then extended to N -particle systems. From this point on, the interaction operator is specialised to hard sphere systems ($\mathcal{T} \rightarrow \mathcal{T}_c$). Using the binary interaction expansion (Sec. (2.4)) the streaming operators may be decomposed into a free streaming operator and interaction operators. Using the Dyson equation (see Eq. (2.5.4)), the p -streaming propagator for a system of hard spheres can be written as

$$\mathcal{S}_t^\dagger = \mathcal{S}_t^0 + \sum_{j,k=j+1}^n \int_0^t d\tau \mathcal{S}_{t-\tau}^0 \mathcal{T}^\dagger(j, k) \mathcal{S}_\tau^\dagger \quad (2.8.4)$$

The following relation can also be defined

$$\mathcal{T}^\dagger(j, k) \mathcal{S}_t^0 \mathcal{T}^\dagger(j, k) = 0 \quad (2.8.5)$$

which specifies that a pair of particles cannot re-collide with only free streaming occurring between.

If the two particle form of Eq. (2.8.4) is iterated and Eq. (2.8.5) used, the following

equation is obtained

$$\mathcal{S}_t^\dagger = \mathcal{S}_t^0 + \int_0^t d\tau \mathcal{S}_{(t-\tau)}^0 \mathcal{T}^\dagger(j, k) \mathcal{S}_\tau^0 \quad (2.8.6)$$

This equation is the two particle hard-sphere Dyson equation for the p -propagator. In order to eliminate the free streaming parts of space, the operator \mathcal{I}_t is introduced

$$\mathcal{I}_t(j, k) = \mathcal{S}_t^\dagger - \mathcal{S}_t^0 = \int_0^t d\tau \mathcal{S}_{(t-\tau)}^0 \mathcal{T}^\dagger(j, k) \mathcal{S}_\tau^0 \quad (2.8.7)$$

The operator \mathcal{I}_t represents the difference between a system where two particles interact and a system where two particles do not interact. Equation (2.8.7) is only non-zero when a collision occurs between time 0 and a time t . Assuming a collision does occur, the collision conditions (Eqs. (2.7.3) and (2.7.5)) are used to write

$$\begin{aligned} & \langle \mathbf{x}_j'' \mathbf{x}_k'' | \mathcal{I}_t | \mathbf{x}_j' \mathbf{x}_k' \rangle \\ &= \int d\mathbf{x}_j d\mathbf{x}_k \int_0^t d\tau \langle \mathbf{x}_j'' \mathbf{x}_k'' | \mathcal{S}_{t-\tau}^0 (\mathcal{B} - 1) | \mathbf{x}_j \mathbf{x}_k \rangle \langle \mathbf{x}_j \mathbf{x}_k | \mathcal{S}_\tau^0 | \mathbf{x}_j' \mathbf{x}_k' \rangle \\ & \quad \Theta(-\mathbf{r}_{jk} \cdot \mathbf{v}_{jk}) \delta(-\Delta t) \end{aligned} \quad (2.8.8)$$

where the variables are to be evaluated as indicated by the absence of primes and \mathcal{B} is the collision variable operator. This replaces pre-collision variables to the right with post collision values. It can be defined with the use of Eq. (2.7.7)

$$\begin{aligned} \langle \mathbf{x}_i' \mathbf{x}_j' | \mathcal{B} | \mathbf{x}_i \mathbf{x}_j \rangle &= \delta(\mathbf{r}_i' - \mathbf{r}_i) \delta(\mathbf{r}_j' - \mathbf{r}_j) \\ & \times \delta(\mathbf{p}_i' - \mathbf{p}_i + (1 + \alpha) \mu (\hat{\mathbf{r}}_{ij} \cdot \mathbf{v}_{ij}) \hat{\mathbf{r}}_{ij}) \\ & \times \delta(\mathbf{p}_j' - \mathbf{p}_j - (1 + \alpha) \mu (\hat{\mathbf{r}}_{ij} \cdot \mathbf{v}_{ij}) \hat{\mathbf{r}}_{ij}) \end{aligned} \quad (2.8.9)$$

where δ is the Dirac delta function. At collision $\hat{\mathbf{r}}_{jk} = \hat{\mathbf{a}}$ and using Eq. (2.7.6) gives

$$\begin{aligned} \langle \mathbf{x}_j'' \mathbf{x}_k'' | \mathcal{I}_t | \mathbf{x}_j' \mathbf{x}_k' \rangle &= \int d\mathbf{x}_j d\mathbf{x}_k \int_0^t d\tau \langle \mathbf{x}_j'' \mathbf{x}_k'' | \mathcal{S}_{t-\tau}^0 (\mathcal{B} - 1) | \mathbf{x}_j \mathbf{x}_k \rangle \langle \mathbf{x}_j \mathbf{x}_k | \mathcal{S}_\tau^0 | \mathbf{x}_j' \mathbf{x}_k' \rangle \\ & \quad |\mathbf{v}_{jk}| \Theta(-\mathbf{r}_{jk} \cdot \mathbf{v}_{jk}) \delta(|\mathbf{r}_{jk}| - \sigma_{jk}) \end{aligned} \quad (2.8.10)$$

The second collision condition can now be dropped as the delta function fulfils the same restriction. This can now be transformed into the more typical collision integral over some vector $\hat{\mathbf{e}}$

$$\begin{aligned} \langle \mathbf{x}_j'' \mathbf{x}_k'' | \mathcal{I}_t | \mathbf{x}_j' \mathbf{x}_k' \rangle &= \int d\mathbf{x}_j d\mathbf{x}_k \int_0^t d\tau \langle \mathbf{x}_j'' \mathbf{x}_k'' | \mathcal{S}_{t-\tau}^0 (\mathcal{B} - 1) | \mathbf{x}_j \mathbf{x}_k \rangle \langle \mathbf{x}_j \mathbf{x}_k | \mathcal{S}_\tau^0 | \mathbf{x}_j' \mathbf{x}_k' \rangle \\ & \quad \int d\hat{\mathbf{e}} |\mathbf{v}_{jk} \cdot \hat{\mathbf{e}}| \Theta(-\mathbf{r}_{jk} \cdot \mathbf{v}_{jk}) \delta(|\mathbf{r}_{jk}| - \sigma_{jk}) \delta(\hat{\mathbf{r}}_{jk} - \hat{\mathbf{e}}) \end{aligned} \quad (2.8.11)$$

The last piece can be rewritten by changing from spherical to Cartesian co-ordinates

$$\delta(|\mathbf{r}_{jk}| - \sigma_{jk}) \delta(\hat{\mathbf{r}}_{jk} - \hat{\mathbf{e}}) = \sigma_{jk}^{d-1} \delta(\mathbf{r}_{jk} - \sigma_{jk} \hat{\mathbf{e}}) \quad (2.8.12)$$

The final equation can then be written

$$\langle \mathbf{x}_j'' \mathbf{x}_k'' | \mathcal{I}_t | \mathbf{x}_j' \mathbf{x}_k' \rangle = \int_0^t d\tau \langle \mathbf{x}_j'' \mathbf{x}_k'' | \mathcal{S}_{t-\tau}^0 \mathcal{T}_+^\dagger \mathcal{S}_\tau^0 | \mathbf{x}_j' \mathbf{x}_k' \rangle$$

where the p -interaction operator for dissipative hard sphere potentials has been defined as

$$\begin{aligned} & \langle \mathbf{x}_j' \mathbf{x}_k' | \mathcal{T}_{b+}^\dagger(j, k) | \mathbf{x}_j \mathbf{x}_k \rangle \\ &= \sigma_{jk}^{d-1} \int_{\mathbf{v}_{jk} \cdot \hat{\mathbf{a}} < 0} d\hat{\mathbf{a}} |\mathbf{v}_{jk} \cdot \hat{\mathbf{a}}| \delta(\mathbf{r}_{jk} - \sigma_{jk} \hat{\mathbf{a}}) \langle \mathbf{x}_j' \mathbf{x}_k' | (\mathcal{B} - 1) | \mathbf{x}_j \mathbf{x}_k \rangle \end{aligned} \quad (2.8.13)$$

where d is the dimensionality of the system. The subscript $+$ indicates that this operator is valid for forward progression in time only¹. This is a direct result of the collision conditions and the nature of the \mathcal{B} operator.

2.8.3 f -Collision Operator

To determine the f -interaction operator, the calculations proceed as before and the two particle Dyson equation for the f -propagator is used. The \mathcal{T} operators share a similar re-collision rule as the adjoint \mathcal{T}^\dagger

$$\mathcal{T}(j, k) \mathcal{S}_{-t}^0 \mathcal{T}(j, k) = 0 \quad (2.8.14)$$

Using this and free particle Liouville theory (Eq. (2.5.6)) yields the following Dyson equation for the f -propagator

$$\begin{aligned} \langle B | \mathcal{S}_t | A \rangle &= \langle B | \mathcal{S}_{-t}^0 | A \rangle + \int_0^t d\tau \langle B | \mathcal{S}_{-\tau}^0 \mathcal{T}(j, k) \mathcal{S}_{-(t-\tau)}^0 | A \rangle \\ &= \langle B | \mathcal{S}_{-t}^0 | A \rangle + \int_0^t d\tau \int d\mathbf{x}_j d\mathbf{x}_k \langle \mathbf{x}_j \mathbf{x}_k | \mathcal{T}^\dagger(j, k) \mathcal{S}_\tau^0 | B \rangle^* \langle \mathbf{x}_j \mathbf{x}_k | \mathcal{S}_{-(t-\tau)}^0 | A \rangle \end{aligned} \quad (2.8.15)$$

Using the adjoint identity of the streaming operator (Eq. (2.8.3)), the above equation can be derived from the p -Streaming operator Dyson equation (Eq. (2.8.4)). Defining the \mathcal{T} operator from the \mathcal{T}^\dagger operator is crucial to ensure the overlap dynamics are handled correctly.

¹The reverse time operators can be obtained using exactly the same arguments to give

$$\langle \mathbf{x}_j' \mathbf{x}_k' | \mathcal{T}_-^\dagger | \mathbf{x}_j \mathbf{x}_k \rangle = \sigma^{d-1} \int_{\mathbf{v}_{jk} \cdot \hat{\mathbf{a}} > 0} d\hat{\mathbf{a}} |\mathbf{v}_{jk} \cdot \hat{\mathbf{a}}| \delta(\mathbf{r}_{jk} - \sigma \hat{\mathbf{a}}) \langle \mathbf{x}_j' \mathbf{x}_k' | (\mathcal{B}^{-1} - 1) | \mathbf{x}_j \mathbf{x}_k \rangle$$

The interaction operators contain a “real” term with the B operator and a “virtual” interaction term

$$\mathcal{T} = \mathcal{T}_r + \mathcal{T}_v \quad (2.8.16)$$

Concerning ourselves with the real interaction term of the p -interaction operator (Eq. (2.8.15))

$$\begin{aligned} & \langle \mathbf{x}_j \mathbf{x}_k | \mathcal{T}_{r+}^\dagger(j, k) \mathcal{S}_{-\tau}^0 | B \rangle^* \\ &= \sigma^{d-1} \int d\mathbf{x}'_j d\mathbf{x}'_k \int_{\mathbf{v}'_{jk} \cdot \hat{\mathbf{a}} < 0} d\hat{\mathbf{a}} |\mathbf{v}'_{jk} \cdot \hat{\mathbf{a}}| \delta(\mathbf{r}'_{jk} - \sigma \hat{\mathbf{a}}) \langle \mathbf{x}_j \mathbf{x}_k | \mathcal{B} | \mathbf{x}'_j \mathbf{x}'_k \rangle^* \langle \mathbf{x}'_j \mathbf{x}'_k | \mathcal{S}_{\tau}^0 | B \rangle^* \\ &= \sigma^{d-1} \int d\mathbf{x}'_j d\mathbf{x}'_k \langle B | \mathcal{S}_{-\tau}^0 | \mathbf{x}'_j \mathbf{x}'_k \rangle \int_{\mathbf{v}'_{jk} \cdot \hat{\mathbf{a}} < 0} d\hat{\mathbf{a}} |\mathbf{v}'_{jk} \cdot \hat{\mathbf{a}}| \delta(\mathbf{r}'_{jk} - \sigma \hat{\mathbf{a}}) \langle \mathbf{x}'_j \mathbf{x}'_k | \mathcal{B}^\dagger | \mathbf{x}_j \mathbf{x}_k \rangle \end{aligned} \quad (2.8.17)$$

The adjoint \mathcal{B} operator is related to its inverse operator which is obtained from Eq. (2.7.8)

$$\begin{aligned} \langle \mathbf{x}_i \mathbf{x}_j | \mathcal{B}^{-1} | \mathbf{x}'_i \mathbf{x}'_j \rangle &= \delta(\mathbf{r}_i - \mathbf{r}'_i) \delta(\mathbf{r}_j - \mathbf{r}'_j) \\ &\times \delta(\mathbf{p}_i - \mathbf{p}'_i + (1 + \alpha^{-1}) \mu (\hat{\mathbf{r}}'_{ij} \cdot \mathbf{v}'_{ij}) \hat{\mathbf{r}}'_{ij}) \\ &\times \delta(\mathbf{p}_j - \mathbf{p}'_j - (1 + \alpha^{-1}) \mu (\hat{\mathbf{r}}'_{ij} \cdot \mathbf{v}'_{ij}) \hat{\mathbf{r}}'_{ij}) \end{aligned} \quad (2.8.18)$$

Given two functions, A and B , of the phase variables

$$\begin{aligned} \langle A | \mathcal{B} | B \rangle &= \int d\mathbf{x}_j d\mathbf{x}_k B(\mathbf{x}_j, \mathbf{x}_k) \langle \mathbf{x}'_j \mathbf{x}'_k | \mathcal{B} | \mathbf{x}_j \mathbf{x}_k \rangle A(\mathbf{x}_j, \mathbf{x}_k) \\ &= \frac{1}{\alpha} \int d\mathbf{x}'_j d\mathbf{x}'_k B(\mathbf{x}'_j, \mathbf{x}'_k) \langle \mathbf{x}_j \mathbf{x}_k | \mathcal{B}^{-1} | \mathbf{x}'_j \mathbf{x}'_k \rangle A(\mathbf{x}'_j, \mathbf{x}'_k) \\ &= \langle B | \frac{1}{\alpha} \mathcal{B}^{-1} | A \rangle \end{aligned} \quad (2.8.19)$$

The Jacobian for the pre- to post-collision variable change is given in Appendix D. This value of the Jacobian is only valid for constant coefficients of restitution. Examining Eq. (2.8.19), the following adjoint relationship has been obtained

$$\mathcal{B}^\dagger = \frac{1}{\alpha} \mathcal{B}^{-1} \quad (2.8.20)$$

Inserting this into Eq. (2.8.17) and changing the variables of integration gives

$$\begin{aligned} \langle B | \mathcal{S}_{-\tau}^0 \mathcal{T}_{r+} | \mathbf{x}_j \mathbf{x}_k \rangle &= \sigma^{d-1} \int d\mathbf{x}'_j d\mathbf{x}'_k \langle B | \mathcal{S}_{-\tau}^0 | \mathbf{x}'_j \mathbf{x}'_k \rangle \frac{1}{\alpha^2} \int_{\mathbf{v}_{jk} \cdot \hat{\mathbf{a}} > 0} d\hat{\mathbf{a}} \\ &\quad |\mathbf{v}_{jk} \cdot \hat{\mathbf{a}}| \delta(\mathbf{r}_{jk} - \sigma \hat{\mathbf{a}}) \langle \mathbf{x}'_j \mathbf{x}'_k | \mathcal{B}^{-1} | \mathbf{x}_j \mathbf{x}_k \rangle \end{aligned} \quad (2.8.21)$$

Now considering the virtual interaction term

$$\begin{aligned}
 & \langle \mathbf{x}_j \mathbf{x}_k | \mathcal{T}_{v+}^\dagger \mathcal{S}_\tau^0 | B \rangle^* \\
 &= \sigma^{d-1} \int d\mathbf{x}'_j d\mathbf{x}'_k \int_{\mathbf{v}'_{jk} \cdot \hat{\mathbf{a}} < 0} d\hat{\mathbf{a}} |\mathbf{v}'_{jk} \cdot \hat{\mathbf{a}}| \delta(\mathbf{r}'_{jk} - \sigma \hat{\mathbf{a}}) \langle \mathbf{x}_j \mathbf{x}_k | \mathbf{x}'_j \mathbf{x}'_k \rangle^* \langle \mathbf{x}'_j \mathbf{x}'_k | \mathcal{S}_\tau^0 | B \rangle^* \\
 &= \langle B | \mathcal{S}_{-\tau}^0 | \mathbf{x}_j \mathbf{x}_k \rangle \sigma^{d-1} \int_{\mathbf{v}_{jk} \cdot \hat{\mathbf{a}} < 0} d\hat{\mathbf{a}} |\mathbf{v}_{jk} \cdot \hat{\mathbf{a}}| \delta(\mathbf{r}_{jk} - \sigma \hat{\mathbf{a}}) \\
 &= \langle B | \mathcal{S}_{-\tau}^0 | \mathbf{x}_j \mathbf{x}_k \rangle \sigma^{d-1} \int_{\mathbf{v}_{jk} \cdot \hat{\mathbf{a}} > 0} d\hat{\mathbf{a}} |\mathbf{v}_{jk} \cdot \hat{\mathbf{a}}| \delta(\mathbf{r}_{jk} + \sigma \hat{\mathbf{a}}) \\
 &= \langle B | \mathcal{S}_{-\tau}^0 \mathcal{T}_{v+} | \mathbf{x}_j \mathbf{x}_k \rangle
 \end{aligned} \tag{2.8.22}$$

By combining the two expressions the full f -interaction operator is obtained

$$\begin{aligned}
 & \langle \mathbf{x}'_j \mathbf{x}'_k | \mathcal{T}_+ | \mathbf{x}_j \mathbf{x}_k \rangle \\
 &= \sigma^{d-1} \int_{\mathbf{v}_{jk} \cdot \hat{\mathbf{a}} > 0} d\hat{\mathbf{a}} |\mathbf{v}_{jk} \cdot \hat{\mathbf{a}}| \langle \mathbf{x}'_j \mathbf{x}'_k | \left(\frac{1}{\alpha^2} \delta(\mathbf{r}_{jk} - \sigma \hat{\mathbf{a}}) \mathcal{B}^{-1} - \delta(\mathbf{r}_{jk} + \sigma \hat{\mathbf{a}}) \right) | \mathbf{x}_j \mathbf{x}_k \rangle
 \end{aligned} \tag{2.8.23}$$

These results for inelastic hard sphere interaction operators were first obtained by Noije et al [8] and Brey et al [9]. This operator is only valid for the simple granular gas due to the Jacobian of the pre to post collision variables. This operator is only valid for forward time progression¹.

2.8.4 N -body Dynamics

The \mathcal{T} operators are determined for two particle systems and their applicability to N -particle dynamics must be confirmed. Defining the pseudo-streaming operators with the overlap function

$$\mathcal{S}_{+t} W = \exp \left(-t i \mathcal{L}_0 + t \sum_{j < k}^N \mathcal{T}_+(j, k) \right) W \tag{2.8.24}$$

$$W \mathcal{S}_{+t}^\dagger = W \exp \left(t i \mathcal{L}_0 + t \sum_{j < k}^N \mathcal{T}_+^\dagger(j, k) \right) \tag{2.8.25}$$

The propagators now must explicitly state the direction of the time evolution. Expanding the operators using the Dyson equations, the re-collision identities and for a set of

¹Following the same arguments as the construction of the forward time f-operator but using the reverse time p-operator gives

$$\langle \mathbf{x}'_j \mathbf{x}'_k | \mathcal{T}_{b-} | \mathbf{x}_j \mathbf{x}_k \rangle = \sigma^{d-1} \int_{\mathbf{v}_{jk} \cdot \hat{\mathbf{a}} < 0} d\hat{\mathbf{a}} |\mathbf{v}_{jk} \cdot \hat{\mathbf{a}}| \langle \mathbf{x}'_j \mathbf{x}'_k | (\alpha^2 \delta(\mathbf{r}_{jk} - \sigma \hat{\mathbf{a}}) \mathcal{B} - \delta(\mathbf{r}_{jk} + \sigma \hat{\mathbf{a}})) | \mathbf{x}_j \mathbf{x}_k \rangle$$

collisions

$$\mathcal{S}_t W = \mathcal{S}_{-\Delta t_1}^0 \mathcal{T}_{r+}(j_1, k_1) \mathcal{S}_{-\Delta t_2}^0 \mathcal{T}_{r+}(j_2, k_2) \cdots \mathcal{S}_{(t - \sum_a \Delta t_a)} W \quad (2.8.26a)$$

$$W \mathcal{S}_t^\dagger = W \mathcal{S}_{\Delta t_1}^0 \mathcal{T}_{r+}^\dagger(i_1, j_1) \mathcal{S}_{\Delta t_2}^0 \mathcal{T}_{r+}^\dagger(j_2, k_2) \cdots \mathcal{S}_{(t - \sum_a \Delta t_a)}^\dagger \quad (2.8.26b)$$

If the complete set of collision pairs j_n, k_n and times Δt_n are expanded, then the propagator terminates with a free streaming operator as expected. This proves the applicability of the pseudo-streaming operators for N particle systems.

2.9 Conclusions

Equations (2.6.4a), (2.8.13), and (2.8.23) are the major results of this section as they characterise the exact dynamics of the simple granular gas model. This completes the definition of the system; however, it is still too complex for analytical calculations and some approximation must be made. The next chapter describes the DSMC method of solving kinetic theory and its assumptions.

2.10 References

- [1] D. J. Evans and G. P. Morris. *Statistical Mechanics of Nonequilibrium Liquids*. London: Academic Press, 1990.
- [2] F.J. Dyson, “The Radiation Theories of Tomonaga, Schwinger, and Feynman”, *Phys. Rev.* 75, 486–502 (1949).
- [3] D. J. Evans and G. P. Morris, “Nonlinear-Response theory for steady planar Couette-flow”, *Phys. Rev. A*. 30, 1528–1530 (1984).
- [4] M. E. Tuckerman et al., “Modified nonequilibrium molecular dynamics for fluid flows with energy conservation”, *J. Chem. Phys.* 106, 5615–5621 (1997).
- [5] B. J. Edwards, B. Chunggi and D. J. Keffer, “An examination of the validity of nonequilibrium molecular-dynamics simulation algorithms for arbitrary steady-state flows”, *J. Chem. Phys.* 123, 114106 (2005).
- [6] P. J. Daivis and B. D. Todd, “A simple, direct derivation and proof of the validity of the SLLOD equations of motion for generalized homogeneous flows”, *J. Chem. Phys.* 124, 194103 (2006).
- [7] B. J. Edwards, C. Baig and D. J. Keffer, “A validation of the p-SLLOD equations of motion for homogeneous steady-state flows”, *J. Chem. Phys.* 124, 194104 (2006).
- [8] T. P. C. van Noije, M. H. Ernst and R. Brito, “Ring kinetic theory for an idealized granular gas”, *Physica A*. 251, 266–283 (1998).

- [9] J. J. Brey, J. W. Dufty and A. Santos, “Dissipative Dynamics for Hard Spheres”, *J. Stat. Phys.* 87, 1051–1066 (1997).
- [10] M. H. Ernst et al., “Hard-Sphere Dynamics and Binary-Collision Operators”, *Physica*. 45, 127–146 (1969).
- [11] J. R. Dorfman and M. H. Ernst, “Hard-Sphere Binary-Collision Operators”, *J. Stat. Phys.* 57, 581–593 (1989).

CHAPTER
THREE

DIRECT SIMULATION MONTE-CARLO

IN this chapter, a direct simulation Monte Carlo (DSMC) method is developed for solving kinetic theories. In this approach, the n -body distribution function $f^{(n)}$ is represented using a set of samples, and the corresponding member of the BBGKY hierarchy is then used to evolve the samples forward in time. The properties of the system are extracted in the same manner as in molecular dynamics simulations; however, DSMC simulations are generally faster and equilibrate more rapidly due to the approximations made in the particle-particle correlations. Here, a general method capable of simulating any level of the BBGKY hierarchy, provided some specific approximations are made for the dynamic spacial correlations of the system, is developed. This method is then applied to numerically solve the second member of the BBGKY hierarchy for equilibrium elastic hard sphere systems and sheared inelastic hard sphere systems. The results are compared against MD simulations and predictions of Enskog theory. The approximation of the dynamic spatial correlations is found to be quite severe, and the re-collisions observed in simulations are analysed to attempt to discover a phenomenological expression to recover the low density limit for the self-diffusion coefficient. The method is found to only slightly improve the predictions of the other transport properties.

3.1 Introduction

Direct simulations of the Boltzmann kinetic equation using Monte Carlo techniques were originally devised by Bird [1] as a method to overcome computational limits on the number of particles in a simulation. Since then, the DSMC technique has been applied in a wide range of fields including the modelling of supersonic flows and, in particular, rarefied flows with applications in the space program [2]. The success of the technique is due to its ability to simulate hydrodynamic scales while retaining a sufficient level of detail of the particle dynamics. DSMC can also provide a cost-effective method for modeling the solvent-solvent interactions within event-driven simulations [3].

Homogeneous DSMC provides a tool for rapidly solving kinetic theories numerically. This can be used to test the inherent approximations of the kinetic theory against MD

results or to test an approximate solution of the kinetic theory. For example, the extension of DSMC to Enskog kinetic theory [4] is widely used for this purpose (e.g., granular materials [5–7]). The Enskog DSMC method is also used here in two later chapters to study shear flows of granular materials (Chap. 6) and the dynamics of nano-colloidal mixtures (Chap. 7).

There have been several advances in homogeneous DSMC techniques over the years. The basic DSMC algorithm [8] consists of two stages, a free streaming and an interaction testing step. An efficient DSMC algorithm must have two key properties. First, it must perform the minimum number of interaction tests to avoid wasted CPU cycles. In a naive algorithm, all interaction operators must be applied on all velocity samples at each time step. Bird’s [8] Null Time Counter (NTC) method calculates an estimate for the maximum possible number of events occurring in a time step, performs only that number of tests and re-weights the event probability accordingly. This results in a much higher acceptance rate for the tests and a computational cost which scales linearly in the number of samples. Secondly, the algorithm should preserve the conserved quantities (i.e., momentum, mass and, with the exception of granular flows, energy) which are eigenfunctions of the collision operators \mathcal{T} with a zero eigenvalue. The popular method proposed by Nanbu [9] does not exactly conserve these properties, and errors of magnitude $O(1/N)$ cause the total energy to continually decrease [10]. This was corrected by Montanero and Santos [7] by executing symmetric parts of the collision operators together in the spirit of Bird’s original algorithm.

In the following sections, the homogeneous DSMC method is generalised to include n -body velocity correlations. This is then applied to the $f^{(2)}$ -DSMC or “repeated ring” kinetic theory level. Enskog theory and Enskog DSMC are only concerned with the first member of the BBGKY hierarchy (Eq. (2.5.3a)) and ignore all pre-collision correlations, save for a single, static structural factor. Therefore, the extension of the DSMC technique to higher levels of the BBGKY hierarchy, which include pre-collision correlations, is a natural progression of the work so far. The approximations taken here in $f^{(2)}$ -DSMC are quite severe when compared to the typical theoretical solutions of kinetic theory with pre-collision correlations [11]. Only dynamical correlations in the velocity space are considered, and correlations in the configurational space are truncated, save for a single static correlation factor. This static structural factor is then obtained from an equation of state for the system studied. This truncation of the static portion of the configurational space is acceptable as ring theory is relatively poor at predicting the equation of state. Piasecki and Soto [12] ascertain that structural ring theory is only suitable for calculating up to the second virial coefficient. In contrast, many excellent empirical equations of state exist for hard sphere systems (e.g., see Chap. 5).

In the following section, the development of kinetic theories beyond the Enskog approximation is presented. In particular, the repeated ring theory is discussed. Then, a general approach to generating a $f^{(2)}$ -DSMC algorithm is developed in Sections 3.3 and

3.4. This DSMC algorithm is then used to study elastic hard sphere systems in Sec. 3.5 and sheared inelastic hard sphere systems in Sec. 3.6. Finally, the main conclusions of this chapter are summarized in Sec. 3.7.

3.2 Kinetic Theory

Homogeneous DSMC is, as its name suggests, an algorithm to directly simulate a kinetic equation using Monte Carlo techniques. The typical starting point of kinetic theory and the derivation of a general $f^{(n)}$ -DSMC technique is the first member of the BBGKY hierarchy (see Eq. (2.5.3a)). As $f^{(n)}$ -DSMC attempts to include pre-collision correlations, higher members of the hierarchy must be used. In the next subsection, the first two levels of the BBGKY hierarchy and the corresponding kinetic theories are discussed.

3.2.1 BBGKY Streaming Hierarchy

The starting point for deriving the $f^{(n)}$ -DSMC algorithm is the streaming operator hierarchy (Sec. 2.5). The streaming BBGKY hierarchy is preferred to the original hierarchy as it is a more appropriate form for developing time stepping algorithms. Recall that the n th member of the streaming operator hierarchy (see Eq. (2.5.7)) is given by

$$f^{(n)}(t) = \mathcal{S}_t^0 f^{(n)}(0) + \sum_{j=1}^{n-1} \sum_{k=j+1}^n \int_0^t dt' \mathcal{S}_{t-t'}^0 \mathcal{T}(j, k) f^{(n)}(t') \\ + \sum_{j=1}^n \int_0^t dt' \mathcal{S}_{t-t'}^0 \int d\Gamma_{n+1} \mathcal{T}(j, n+1) f^{(n+1)}(t') \quad (3.2.1)$$

The first term is the free motion of the system without interactions. The second term includes correlated interactions between a cluster of n particles, and the third term couples to higher correlated interactions. The first difficulty with using the hierarchy is that the distributions are all coupled upwards to the $f^{(N)}$ distribution. This is typically broken by performing a cluster expansion in the particle correlations

$$f^{(2)}(\Gamma_1, \Gamma_2) = f^{(1)}(\Gamma_1)f^{(1)}(\Gamma_2) + g_2(\Gamma_1, \Gamma_2) \\ f^{(3)}(\Gamma_1, \Gamma_2, \Gamma_3) = f^{(1)}(\Gamma_1)g_2(\Gamma_2, \Gamma_3) + f^{(1)}(\Gamma_2)g_2(\Gamma_1, \Gamma_3) + f^{(1)}(\Gamma_3)g_2(\Gamma_1, \Gamma_2) \\ + f^{(1)}(\Gamma_1)f^{(1)}(\Gamma_2)f^{(1)}(\Gamma_3) + g_3(\Gamma_1, \Gamma_2, \Gamma_3) \quad (3.2.2) \\ \vdots$$

where g_n is a function that accounts for correlations between n particles.

In the Boltzmann approximation, the BBGKY hierarchy is truncated at first order ($n = 1$), closed by neglecting two-body correlations (i.e., $g_2 = 0$), and simplified by assuming that the distance over which particles interact with each other is negligible.

The resulting Boltzmann equation is exact in the low density limit, but it rapidly becomes inaccurate at higher densities.

The predictions of the Boltzmann equation can be improved by including static spatial two-body correlations, through an approximation such as

$$g_2 = (\chi - 1)f^{(1)}(\Gamma_1)f^{(1)}(\Gamma_2),$$

where χ is the radial distribution function at contact), and introducing a finite interaction distance into the theory. This approach still neglects dynamical pre-collision correlations between the particles, and leads to Enskog theory. Enskog theory provides fair predictions up to moderate densities, and for hard sphere fluids it yields reasonable predictions even for dense systems. Enskog theory is remarkably successful and has also been extended to inelastic systems with great success (e.g., see Chap. 6).

Both the Enskog and Boltzmann kinetic theories predict exponential decays of the time correlation functions at long times. This was proven to be incorrect when a long time algebraic decay, first observed in simulations by Alder and coworkers [13], was discovered in the velocity auto-correlation function. The long time tails present in the time correlation functions result from correlated interactions between localised clusters of particles and are related to the hydrodynamic behaviour [13] of the system. The Boltzmann and Enskog kinetic theories also yield poor predictions at much lower densities for fluids with an attractive interaction, such as the square well fluid [14]. Correlated collisions/events are important in these systems, even for fairly low densities, due to bound state contributions from particles within each others' attractive well [15]. These effects have led to the development of more sophisticated kinetic theories, derived from the second member of the BBGKY, to include the pre-collision correlations, which are vital in all of these systems.

Truncating the BBGKY hierarchy at second order ($n = 2$) and neglecting three-body correlations (i.e., setting $g_3 = 0$) leads to the repeated ring kinetic theory [11]. The first and second members of the BBGKY are typically rearranged in terms of the two particle correlation function, g_2 , to give [16]

$$\left(\frac{\partial}{\partial t} + \mathcal{L}_1^0 \right) f^{(1)}(\Gamma_1, t) = \int d\Gamma_2 \mathcal{T}(1, 2) \left(f^{(1)}(\Gamma_1, t) f^{(1)}(\Gamma_2, t) - g_2(\Gamma_1, \Gamma_2, t) \right) \quad (3.2.3)$$

$$\begin{aligned} \left(\frac{\partial}{\partial t} + \mathcal{L}_1^0 + \mathcal{L}_2^0 - \mathcal{T}(1, 2) - \mathcal{P}_{12} \int d\Gamma_3 \mathcal{T}(1, 3) \mathcal{P}_{13} f^{(1)}(\Gamma_3, t) \right) g_2(\Gamma_1, \Gamma_2, t) \\ = \mathcal{T}(1, 2) f^{(1)}(\Gamma_1, t) f^{(1)}(\Gamma_2, t) \end{aligned} \quad (3.2.4)$$

where \mathcal{P} is a permutation operator that sums over all permutations of its indices. If the $\mathcal{T}(1, 2)$ term on the left of Eq. (3.2.4) is deleted, then ring theory is obtained. The solutionx of these coupled equations is complex [11] and requires further approximations to make tractable. For example, structural ring theory [12] only considers static spatial correlations, and the results of van Noije's ring theory for granular gases [16] were

obtained in the limit of low density. Despite this, there have been many successful applications of ring/repeated ring theory (e.g., Refs. [12, 14–17]) and generalisations, such as the fully re-normalised kinetic theory of Mazenko [18]. However, DSMC is successful as it is simple to implement, rapidly generalises to a wide range of systems, and, within the approximations of Enskog theory, provides numerically exact results without requiring further approximation or the use of polynomial expansions. Here, it is proposed to develop a DSMC algorithm which includes correlation effects present at the second level of the BBGKY hierarchy without requiring the complex theoretical treatment of repeated ring theory.

Formally, Eq. (3.2.4) can be solved to express g_2 in terms of $f^{(1)}$ and then used to close Eq. (3.2.3). Rather than attempt to solve for the correlation function g_2 , in this work the two particle distribution function $f^{(2)}$ will be directly simulated. Only the second member of the BBGKY hierarchy is required

$$f^{(2)}(\Gamma_1, \Gamma_2, t) = \mathcal{S}_t^0 f^{(2)}(\Gamma_1, \Gamma_2, 0) + \int_0^t dt' \mathcal{S}_{t-t'}^0 \mathcal{T}(1, 2) f^{(2)}(\Gamma_1, \Gamma_2, t') + \sum_j^2 \int_0^t dt' \mathcal{S}_{t-t'}^0 \int d\Gamma_3 \mathcal{T}(j, 3) f^{(3)}(\Gamma_1, \Gamma_2, \Gamma_3, t') \quad (3.2.5)$$

where $f^{(3)}$ can be rewritten using the cluster expansion (see Eq. (3.2.2)) provided the three particle correlation terms are truncated ($g_3 = 0$)

$$f^{(3)}(\Gamma_1, \Gamma_2, \Gamma_3) \approx f^{(1)}(\Gamma_1) f^{(2)}(\Gamma_2, \Gamma_3) + f^{(1)}(\Gamma_2) f^{(2)}(\Gamma_1, \Gamma_3) + f^{(1)}(\Gamma_3) f^{(2)}(\Gamma_1, \Gamma_2) - 2 f^{(1)}(\Gamma_1) f^{(1)}(\Gamma_2) f^{(1)}(\Gamma_3) \quad (3.2.6)$$

The one particle distribution function can be obtained from the $f^{(n)}$ distribution using Eq. (2.5.1). Thus, Eqs. (2.5.1), (3.2.5), and (3.2.6) formally describe the evolution of a $f^{(2)}$ distribution function, neglecting three body contributions. Further approximations must be made in the DSMC technique and in the following section the DSMC method is derived for the two particle distribution function $f^{(2)}$.

3.3 $f^{(2)}$ -DSMC

The crucial first step in developing a $f^{(2)}$ -DSMC algorithm to simulate the second BBGKY streaming hierarchy equation is the approximation of the n -particle distribution function using a set of N_s velocity samples. Unlike the lattice Boltzmann methods, the samples are not restricted to discrete values, but can explore the full continuous values of the velocity Γ -space. Assuming the velocity-velocity correlations can factor out of the

distribution function, the $f^{(n)}$ distribution function can then be expressed as

$$\begin{aligned} f^{(n)}(\Gamma_1, \dots, \Gamma_n, t) &\approx \chi^{(n)}(\Gamma_1, \dots, \Gamma_n) f^{(n)}(\mathbf{v}_1, \dots, \mathbf{v}_n, t) \\ &\approx \frac{\rho^n \chi^{(n)}(\Gamma_1, \dots, \Gamma_n)}{n!} \sum_s^{N_s} \mathcal{P}_{1,\dots,n} \prod_j^n \delta(\mathbf{v}_j - \mathbf{v}_{sj}) \end{aligned} \quad (3.3.1)$$

where ρ is the number density of the system, \mathbf{v}_{sj} is the velocity of “bin” j of the distribution sample s , and $\chi^{(n)}$ is a factor including velocity-spatial and spatial-spatial correlations. This approximate velocity distribution function approaches the real distribution as $N_s \rightarrow \infty$; however, excellent results can be achieved with only a few hundred samples [1]. The approximate distribution function of Eq. (3.3.1) is problematic in the coupling term of the $f^{(n)}$ -DSMC algorithm and this is discussed in the next section.

3.3.1 Limitations of the Approximate Velocity Distribution Function

The approximate distribution function of Eq. (3.3.1) has a severe limitation within $f^{(n)}$ -DSMC. Taking moments or averages of the distribution function of Eq. (3.3.1) generates the correct approximate description of the $f^{(n)}$ distribution, but the distribution function cannot be sampled directly for two specified velocities. As the velocity coordinates of the distribution samples are continuous, there is a measure zero chance of selecting a sample for finite N_s . The approximation of $f^{(3)}$ using Eq. (3.2.6) is therefore no longer applicable, as with an existing velocity sample $f^{(2)}(\Gamma_1, \Gamma_2)$, there is no way of sampling $f^{(2)}(\Gamma_1, \Gamma_3)$ or $f^{(2)}(\Gamma_2, \Gamma_3)$ for an arbitrary particle 3. Thus, the velocity correlations involving particle 3 on the right hand side of Eq. (3.2.5) must be truncated ($f^{(3)}(\mathbf{v}_1, \mathbf{v}_2, \mathbf{v}_3, t) \rightarrow f^{(2)}(\mathbf{v}_1, \mathbf{v}_2, t) f^{(1)}(\mathbf{v}_3, t)$), to allow a sample approximation of the distribution using Eq. (3.3.1) and Eq. (2.5.1). This leads to the following approximation in the n th BBGKY streaming hierarchy member

$$f^{(n+1)}(\Gamma_1, \dots, \Gamma_n, t) \approx \chi^{(n+1)}(\Gamma_1, \dots, \Gamma_n) f^{(n)}(\mathbf{v}_1, \dots, \mathbf{v}_n, t) f^{(n)}(\mathbf{v}_{n+1}, t) \quad (3.3.2)$$

This has the result that $f^{(2)}$ -DSMC only takes into account the velocity-correlated collision sequences described in Fig. 3.1. Two particles can undergo repeated re-collisions, interspersed between sequences of uncorrelated events. The collision sequences included here are not as complete as the sequences of repeated ring theory but are a subset. Nevertheless, these contributions are an improvement over Enskog theory’s assumption of completely uncorrelated events. More complex collision diagrams can also be accounted for by simply increasing the level of the BBGKY hierarchy simulated. In the following subsection the spatial correlations are discussed and treated to allow a $f^{(2)}$ -DSMC algorithm to be developed.

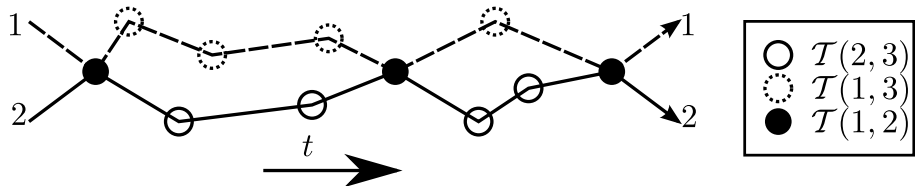


Figure 3.1: Collision sequences accounted for in $f^{(2)}$ -DSMC for a pair of velocity bins 1 and 2 in a distribution sample. Time is progressing from left to right and the velocity-correlated $T(1, 2)$ and uncorrelated $T(j, 3)$ events occurring to each sample are labelled using circles.

3.3.2 Treatment of the Spatial Correlation Terms

The spatial correlations within $\chi^{(n)}$ and $\chi^{(n+1)}$ are also problematic within a $f^{(2)}$ -DSMC algorithm. A sample based approach, used for the velocity correlations (see Eq. (3.3.1)), is essentially the task of MD simulation but due to the low order of truncation of the BBGKY hierarchy it is unclear how to develop this method. In the simplest workable approximation the spatial correlations could be truncated altogether ($\chi^{(n)} \rightarrow 1$) in the spirit of Boltzmann's original kinetic theory; however, this would yield poor estimates for the equation of state. A better approximation would be to include the static spatial correlations *à la* Enskog and wherever $\chi^{(n)}$ and $\chi^{(n+1)}$ appears to the right of an interaction operator it is replaced by the value of the radial distribution function on contact. Here it is assumed that this is a function of the density only. This value can then be obtained from one of the many equations of state available for hard sphere fluids (see Chap. 5). Here the Carnahan-Starling [19] equation of state will be used

$$\chi^{(CS)} = \frac{1 - \phi/2}{(1 - \phi)^3} \quad (3.3.3)$$

where $\phi = \pi \sigma^3 \rho / 6$ is the packing fraction.

Although this Enskog-like approximation recovers the correct equation of state, this approximation is very severe. The ratio of the correlated ($T(1, 2)$) and uncorrelated ($T(j, 3)$) interactions in this approximation is now independent of density. In a low density system, two particles which have become correlated through an interaction are unlikely to re-collide. This is because the mean free length is large compared to a particle diameter and the next interactions of each of the two particles will be at remote locations to the original collision. Thus the ratio of the $T(1, 2)$ to $T(j, 3) + T(1, 2)$ events will approach zero at low densities. At high densities this ratio will approach a value near 1 as particles are always re-colliding within a localised cluster of particles due to caging. Without exhibiting this limiting behaviour, the low density limit of properties solely dependent on velocity correlations (i.e., the self diffusion coefficient) will not be recovered. The truncation of the spatial-velocity and spatial-spatial correlations also removes any possibility of approximating the higher density behaviour, as effects such as caging are

also discarded.

Despite these limitations the results obtained are still useful as at low densities collisional contributions to most system properties are small and the correct limiting behaviour will be recovered in these cases. Thus this truncation of the dynamical spatial correlations will be used in preliminary results to determine the magnitude of the approximation, before attempting to correct the limiting behaviour of the theory. In the following subsection, the general approach to simulating the time evolution of this approximate distribution function is determined.

3.4 Development of the $f^{(2)}$ -DSMC Algorithm

In Eq. (3.2.1), the distribution function is intimately linked to all of its previous values in time. This dependency must be broken before deriving the DSMC algorithm. If only small time steps $\Delta t \ll t_{\text{avg}}$ are performed where t_{avg} is the mean free time, Eq. (3.2.1) may be approximated as

$$f^{(n)}(\Delta t) = \mathcal{S}_{\Delta t}^0 f^{(n)}(0) + \Delta t \sum_j^n \sum_{k>j}^n \mathcal{T}(j, k) \mathcal{S}_{\Delta t}^0 f^{(n)}(0) + \Delta t \sum_j^n \int d\Gamma_{n+1} \mathcal{T}(j, n+1) \mathcal{S}_{\Delta t}^0 f^{(n+1)}(0) \quad (3.4.1)$$

where we assume that the probability of an interaction of a single sample in the time step Δt is small enough to ignore repeated interaction terms ($\mathcal{T} \mathcal{S}_{t \leq \Delta t} \mathcal{T} = 0$). The collision operators are then extracted to the end of the streaming interval by assuming the action of \mathcal{T} does not change significantly during the time interval Δt . The size of the time step Δt used in simulations of large systems is typically long enough to allow for a few interactions within the system to occur per time step. With these assumptions, the evolution of $f^{(n)}$ now resembles a time stepping algorithm and is only linked to $f^{(n)}$ and $f^{(n+1)}$ at the previous time step.

A brief note is made here on the uncorrelated interaction terms of Eq. (3.4.1). In solutions of “repeated ring” kinetic theory [14], uncorrelated Enskog interaction terms are often grouped and inserted into the streaming operators

$$\mathcal{S}_{\Delta t}^{(E)} = \exp \left(-\Delta t \sum_j^N [i\mathcal{L}_j^0 + \Omega_j] \right) \quad (3.4.2)$$

where here $\mathcal{S}^{(E)}$ is the Enskog streaming operator and Ω_j is the Enskog collision operator for particle j defined by

$$\Omega_j = \int d\Gamma_\alpha \mathcal{T}(j, \alpha) f(\Gamma_\alpha, t) \quad (3.4.3)$$

This is done to make the exponential decay terms in the ring theory calculations of the correlation functions obvious in the formalism. However, as the $f^{(n)}$ -DSMC algorithm treats correlated and uncorrelated interactions in the same way, Eq. (3.4.1) is a more straightforward starting point to write the $f^{(n)}$ -DSMC algorithm. With the hierarchy closed and in the form of a time stepping algorithm the steps of the $f^{(2)}$ -DSMC algorithm can be outlined.

3.4.1 $f^{(2)}$ -DSMC Algorithm

The interaction operators contain both a real (\mathcal{T}_r) and a virtual (\mathcal{T}_v) interaction piece (see Sec. 2.8.3), and the unfolded action of Eq. (3.4.1) results in an expression of the form of Eq. (2.8.26). If a stochastic interpretation of the interaction operators is assumed, it can be stated that the interaction operators replace the pre-collision values of samples of the distribution function with post-collision values according to a calculated interaction probability. The algorithmic interpretation of Eq. (3.4.1) acting on the approximate distribution (Eq. (3.3.1)) is then

1. Generate a set of velocity samples to initialise the $f^{(2)}$ distribution.
2. $t = t + \Delta t$
3. Apply the free streaming operator $S_{\Delta t}^0$ to the distribution function, free streaming each sample to the current time.
4. Interaction stage:
 - (a) For each sample, apply the $\mathcal{T}(1, 2)$ operators for all $n!/2(n - 2)!$ pairings, calculating transition probabilities and evaluating post collision values.
 - (b) For each of the $n N_s$ velocity bins, the $\mathcal{T}(j, 3)$ operators are applied by randomly selecting another velocity bin from the $f^{(2)}$ distribution as $f^{(1)}$. The operators, according to a calculated probability, replace the velocity bin j with its post collision value.
5. Return to step 2.

The order in which steps 4a and 4b are processed is unimportant if the time step Δt is small and there is a very small probability of a multiple collision of a single sample. The probability of each operator resulting in an interaction is determined by examining each interaction term individually.

The collision rate per unit volume in a system of hard spheres [5] can be written as

$$\frac{1}{2} \sigma^{d-1} \rho^2 \chi^{(2)} \int d\mathbf{v}_1 d\mathbf{v}_2 d\hat{\mathbf{r}}_{12} f(\mathbf{v}_1, \mathbf{v}_2, t) |\mathbf{v}_{12} \cdot \hat{\mathbf{r}}_{12}| \Theta(-\mathbf{v}_{12} \cdot \hat{\mathbf{r}}_{12}) \quad (3.4.4)$$

Integrating over the system volume and dividing by the number of particles results in the collision rate per particle. Equation 3.4.4 is used to normalise the collision rates of the system to that of a fluid of $n N_s$ particles. This is effectively selecting the number of particles a single distribution sample represents and, for ease of integration with DYNAMO

(see Chap. 4), this is chosen to be one velocity bin per particle. This will result in an extra factor of $\rho/2$ appearing in the following interaction probabilities. In the next two subsections, these probabilities are determined for the hard sphere system.

Step 4a Application of the $\mathcal{T}(1, 2)$ operator

Expanding the hard sphere collision operator (Eq. (2.8.23)), the $\mathcal{T}(1, 2)$ term of Eq. (3.4.1) becomes

$$\Delta t \mathcal{T}(1, 2) f^{(2)}(t) = \Delta t \sigma^{d-1} \int_{\mathbf{v}_{12} \cdot \hat{\mathbf{a}} > 0} d\hat{\mathbf{a}} |\mathbf{v}_{12} \cdot \hat{\mathbf{a}}| \left(\frac{1}{\alpha^2} \delta(\mathbf{r}_{12} - \sigma \hat{\mathbf{a}}) \mathcal{B}^{-1} - \delta(\mathbf{r}_{12} + \sigma \hat{\mathbf{a}}) \right) \chi^{(CS)} f(\mathbf{v}_1, \mathbf{v}_2, t) \quad (3.4.5)$$

The $\mathcal{B}^{-1}/\alpha^2$ term is concerned with collisions entering this sample of the distribution function and the second term is the collisional loss of samples. By using Monte Carlo integration, the probability of the velocities 1 and 2 from a sample undergoing this type of collision can be written as

$$P_{12}^{(C)} = 4\pi \Delta t \sigma^{d-1} \frac{\rho}{2} \chi^{(CS)} \Theta(\mathbf{v}_{12} \cdot \hat{\mathbf{r}}) |\mathbf{v}_{12} \cdot \hat{\mathbf{r}}| \quad (3.4.6)$$

where $\hat{\mathbf{r}}$ is a randomly generated unit vector, $P_{12}^{(C)}$ is the correlated collision probability, and the factor of 4π arises from the area of the collision angle integral.

To process this event, at each time step all $N_s n!/2(n-2)!$ velocity sample pairings must be tested with a probability of occurrence of $P_{12}^{(C)}$. To reduce this cost, Birds NTC method [8] is used and only $P_{max}^{(C)} N_s n!/2(n-2)!$ sample pairs are selected where $P_{max}^{(C)}$ is the maximum observed value of $P_{12}^{(C)}$ updated dynamically during a simulation. The selected pairs are then accepted and the interaction operator applied with a probability of $P_{12}^{(C)}/P_{max}^{(C)}$. In applying the collision operator, the values of the 1 and 2 velocity bins are changed to their post collision values. This satisfies the \mathcal{B}^{-1} term in Eq. (3.4.6) and completes the treatment of this term. The treatment of the $\mathcal{T}(j, 3)$ terms is almost identical; however, unless handled with care, these terms will not conserve the zero eigenfunctions of the collision operators, such as the momentum and the kinetic energy.

Step 4b Application of the $\mathcal{T}(j, 3)$ operator

Expanding the $\mathcal{T}(j, 3)$ collision operator in Eq. (3.4.1) gives

$$\begin{aligned} \Delta t \int d\Gamma_{n+1} \mathcal{T}(j, 3) f^{(2)}(t) f^{(1)}(t) \\ = \Delta t \sigma^{d-1} \int d\Gamma_3 \int_{\mathbf{v}_{j,3} \cdot \hat{\mathbf{a}} > 0} d\hat{\mathbf{a}} |\mathbf{v}_{j,3} \cdot \hat{\mathbf{a}}| \\ \left(\frac{1}{\alpha^2} \delta(\mathbf{r}_{j,3} - \sigma \hat{\mathbf{a}}) \mathcal{B}^{-1} - \delta(\mathbf{r}_{j,3} + \sigma \hat{\mathbf{a}}) \right) \chi^{(CS)} f(\mathbf{v}_1, \mathbf{v}_2, t) f(\mathbf{v}_3, t) \end{aligned} \quad (3.4.7)$$

Using Monte-Carlo integration techniques, the probability of executing this event for a velocity j in sample s in a time step Δt is

$$P_{j3}^{(B)} = 4\pi \Delta t \sigma^{d-1} \frac{\rho}{2} \chi^{(CS)} \Theta(\mathbf{v}_{j3} \cdot \hat{\mathbf{r}}) |\mathbf{v}_{j3} \cdot \hat{\mathbf{r}}| \quad (3.4.8)$$

where \mathbf{v}_3 is the velocity of a randomly selected bin and sample, $\mathbf{v}_{j3} = \mathbf{v}_j - \mathbf{v}_3$, and $P_{j3}^{(B)}$ is the coupling collision probability. To conserve energy and momentum during the simulation, the $\mathcal{T}(j, 3)$ events are executed in twos [7]. Thus, two velocity bins are selected and both bins $\mathcal{T}(j, 3)$ operators are performed simultaneously with half the probability. If the event occurs then the samples undergo an interaction with each other. The selection of velocity bin pairs is also optimised in the same manner as for the $\mathcal{T}(1, 2)$. Therefore, $n N_s P_{max}^{(B)}/2$ random pairs of velocity bins 1 and 2 from separate samples are selected and interactions are executed with a probability of $P_{12}^{(B)}/P_{max}^{(B)}$ where $P_{max}^{(B)}$ is the maximum observed value of $P_{j3}^{(B)}$ updated dynamically during a simulation. This method [7] conserves the ensemble averages of the Eigenfunctions of the collision operators but will introduce N_s -body correlations between the distribution samples; however, the effect of these correlations are small provided the number of samples N_s is sufficiently high.

To determine the effect of including correlations in the predictions of dynamical properties, simulations were performed on a mono-component hard sphere fluid using $f^{(2)}$ -DSMC, Enskog DSMC and molecular dynamics simulations. Fluids of $N = 2 N_s = 4000$ spheres were equilibrated for 10^6 collisions and data collected over 5 runs of 10^7 collisions. Both elastic hard sphere systems, and inelastic hard sphere systems under shear were simulated. First the results for the elastic hard sphere system are presented.

3.5 Elastic Hard Sphere Systems

For elastic hard sphere systems, the most straightforward dynamical property to measure is the self-diffusion coefficient D . This can be evaluated through the mean-square displacement of a particle [20]

$$D = \lim_{t \rightarrow \infty} \frac{\langle [\mathbf{r}(t) - \mathbf{r}(0)]^2 \rangle}{2 dt} \quad (3.5.1)$$

The results for $f^{(2)}$ and Enskog DSMC, reduced by the MD simulation values are presented in Fig. 3.2. $f^{(2)}$ -DSMC is improved over Enskog theory for intermediate densities ($0.15 \leq \rho \sigma^3 \leq 0.75$); however, as expected the $f^{(2)}$ -DSMC overpredicts the diffusion coefficient at low densities. Particles can only become de-correlated through $\mathcal{T}(j, 3)$ events, and thus correlations persist at low densities with the result that $f^{(2)}$ -DSMC does not recover the low-density Boltzmann limit. At high densities, the diffusion coefficient is lower than predicted as caging effects are missing from $f^{(2)}$ -DSMC. A mechanism within $f^{(2)}$ -DSMC is required to remove the correlated collisions at low densities.

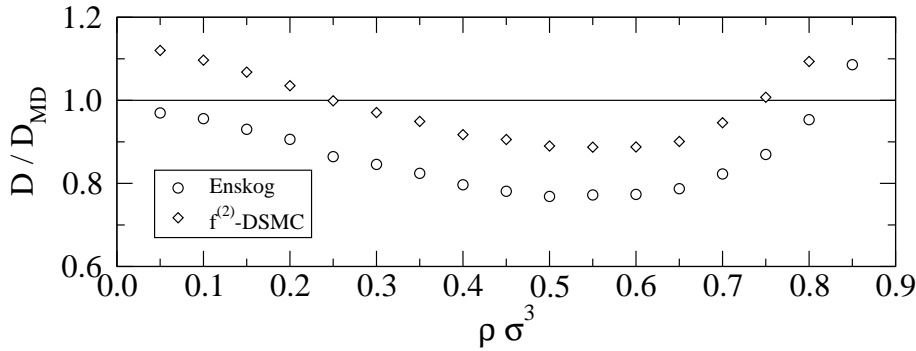


Figure 3.2: $f^{(2)}$ -DSMC and Enskog theory predictions for hard-sphere diffusion coefficients for hard spheres reduced by molecular dynamics values. Errors in the MD data are at most 1%, with errors in the ring DSMC results significantly smaller.

Figure 3.2 also highlights the trivial density dependence that occurs from the truncation of the dynamic spatial correlations, as the Enskog and $f^{(2)}$ -DSMC predictions have the same form. Enskog theory predicts a remarkably simple expression of $D_{\text{Enskog}} = 1.5 t_{\text{avg}}$ for the reduced diffusion coefficient [21]. By comparing the ratio of the $f^{(2)}$ -DSMC and Enskog values for the diffusion in Fig. 3.2 the ratio $D_{f^2\text{-DSMC}}/D_{\text{Enskog}} = 1.15 \pm 0.005$ is calculated, where the uncertainty is the standard deviation of the averaged values.

The contributions of the velocity correlations are not as significant in other transport properties when compared to the diffusion coefficient results. Figure 3.3 compares the predictions for the shear viscosity η and thermal conductivity λ against MD results evaluated using the Einstein forms of the Green-Kubo expressions (see Sec. 7.2.3). These transport coefficients are more difficult to evaluate to the same level of numerical precision as the diffusion coefficient but, within error, $f^{(2)}$ -DSMC performs equally well as Enskog theory. The low density limit, while missing from the diffusion predictions, is correct for both the viscosity and thermal conductivity. At low densities the collisional contribution (correlated or uncorrelated) is small compared to the contribution from the free motion of the particles. Thus the limiting behaviour is unaffected by the truncation of the spatial correlations. In the following subsection, a phenomenological expression is used to correct the description of the diffusion coefficient at low densities.

3.5.1 Phenomenological Estimation of the Re-collision Rates

To correct the predicted diffusion coefficient of $f^{(2)}$ -DSMC at low densities, we must examine the rate at which re-collision events are expected to occur between two spheres. Assuming that the spheres can be considered to randomly diffuse after collision, the distribution of the separation between the spheres is governed by the diffusion equation:

$$\frac{\partial c}{\partial t} = D_{\text{pair}} \nabla^2 c \quad (3.5.2)$$

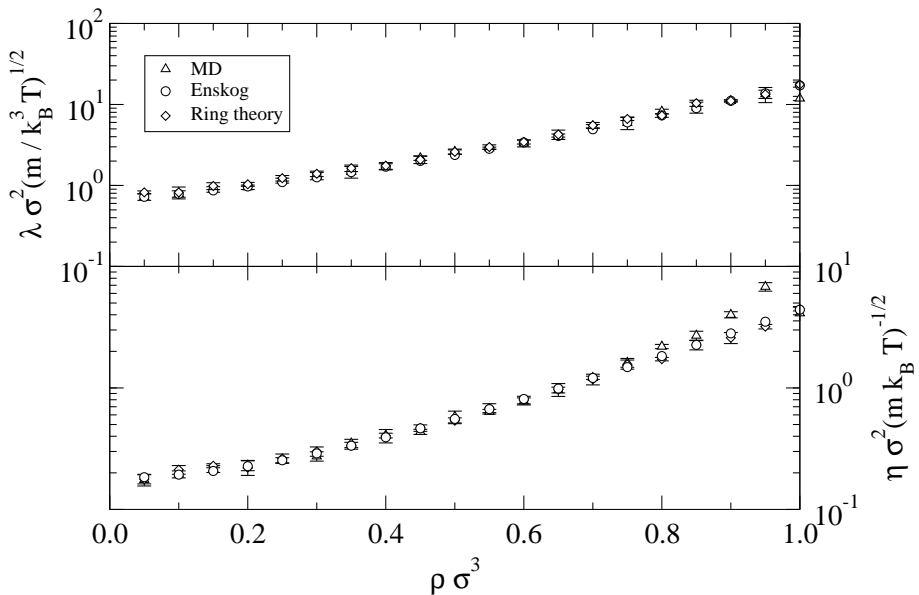


Figure 3.3: $f^{(2)}$ -DSMC, Enskog, and MD results for the thermal conductivity λ and viscosity η for hard spheres. Error bars are the standard deviations of the values for each run.

where ∇ is the Laplace operator, c is the probability that the particles are separated by \mathbf{r} at time t , D_{pair} is the diffusion coefficient of one particle given a coordinate system centred on another particle and will be approximately twice the diffusion coefficient of a single particle $D_{\text{pair}} \approx 2 D$. The associated boundary conditions are $c(\mathbf{r}, t) = 0$ for $|\mathbf{r}| \rightarrow \sigma$, the diameter of the spheres, and $|\mathbf{r}| \rightarrow \infty$.

Given a pair of particles initially at a separation $\sigma + l$, the solution to Eq. (3.5.2) for the fraction that *do not* diffuse to a distance σ within a time t is given by

$$R(t, l) = 1 - \frac{\sigma}{\sigma + l} \operatorname{erfc} \left(\frac{l}{2\sqrt{D_{\text{pair}} t}} \right) \quad (3.5.3)$$

where erfc is the complimentary error function. The initial separation l will be related to the mean free separation generated by the short time ballistic trajectory of the particles after a collision. This quantity is difficult to estimate precisely as this must also be the distance at which the motion of the two particles becomes de-correlated and diffusive. We approximate the mean free separation l as

$$l \approx A v t_{\text{avg}} \quad (3.5.4)$$

where v is the relative velocity of the pair and $A \approx 2.25$ is a fitting parameter. For simplicity, we also assume a Maxwell-Boltzmann distribution of the relative velocities after collision and write

$$R(t) = \int_0^\infty dv R(t, l) f_{\text{pair}}^{(\text{MB})}(v) \quad (3.5.5)$$

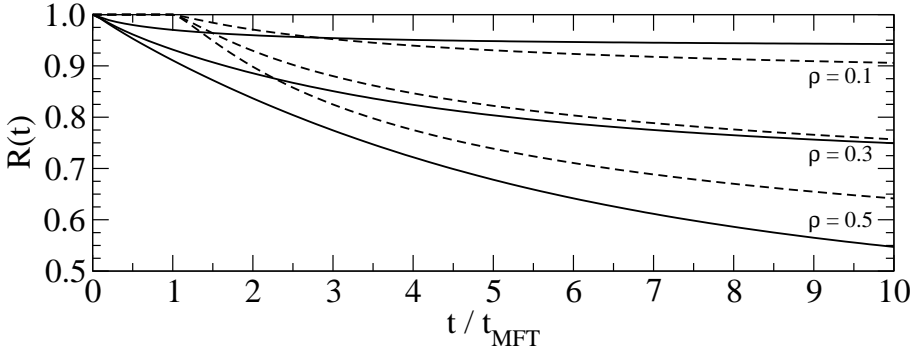


Figure 3.4: The fraction of pairs of particles that, having undergone a collision at $t = 0$, have not undergone a re-collision at a time t . The solid lines are molecular dynamics results and the dashed lines are the predictions of Eq. (3.5.5).

with $f_{pair}^{(\text{MB})}$ the Maxwell-Boltzmann distribution for relative velocities of a pair of particles given by

$$f_{pair}^{(\text{MB})}(v) = 4\pi v^2 \left(\frac{\beta\mu}{2\pi}\right)^{3/2} \exp(-\beta\mu v^2/2) \quad (3.5.6)$$

where $\mu = m/2$ is the relative mass of the two particles. The re-collision probabilities predicted by Eq. (3.5.5) are compared against simulation results for elastic hard spheres in Fig. 3.4. From Fig. 3.4, it is apparent that the value of A was selected to attempt to match the long time limit of the density of $\rho\sigma^3 = 0.3$. The predictions of Eq. (3.5.5) are incorrect at short times but a complete analysis would require knowledge of the velocity auto-correlation function and collision statistics. The long time limit is also incorrect for densities other than $\rho = 0.3$ but can be made to match by adjusting both A and the pair diffusion coefficient. Here, $\rho\sigma^3 = 0.3$ has been selected as a fitting point as it is in the middle of the predicted density range of applicability of $f^{(2)}$ -DSMC and no adjustment of the pair diffusion coefficient is required. The long time limit of Eq. (3.5.5) is given by

$$\lim_{t \rightarrow \infty} R(t) \rightarrow \int_0^\infty dv \frac{\sigma f_{pair}^{(\text{MB})}(v)}{\sigma + Av t_{\text{avg}}} \quad (3.5.7)$$

This equation predicts that, at low densities, the re-collision rate approaches zero. Using this expression to set the ratio of $\mathcal{T}(1, 2)$ to $\mathcal{T}(1, 2) + \mathcal{T}(j, 3)$ events inside a $f^{(2)}$ -DSMC simulation would therefore recover the low density diffusion limit. Further $f^{(2)}$ -DSMC simulations were performed to test this correction in predictions for the hard sphere diffusion coefficient (see Fig. 3.5). The low density result is now recovered and the predictions for the diffusion coefficient are greatly improved over Enskog theory up to a density of $\rho\sigma^3 = 0.5$. Above this density, caging effects begin to appear and re-collisions constrain a particle to its local neighbourhood rather than enhance particle motion.

Despite this ‘‘correction’’ to $f^{(2)}$ -DSMC lacking a formal derivation within the kinetic theory framework the results are surprisingly good given the simple form and single fitting

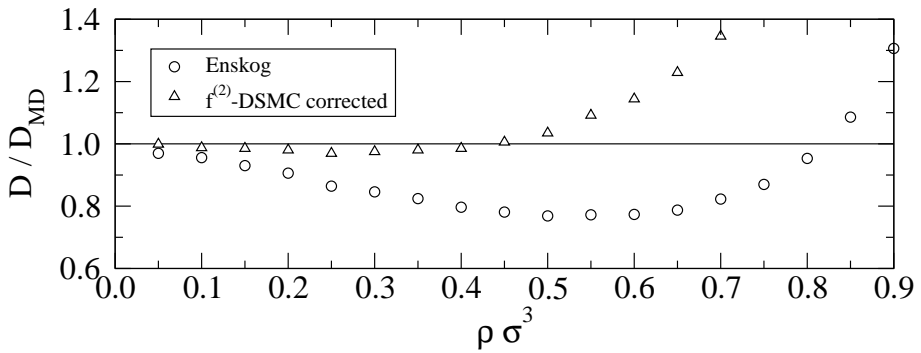


Figure 3.5: Corrected $f^{(2)}$ -DSMC and Enskog theory predictions for hard-sphere diffusion coefficients reduced by molecular dynamics values. Errors in the MD data are at most 1%, with errors in the $f^{(2)}$ -DSMC results significantly smaller.

parameter A . To study this surprising result, an alternative method of obtaining the self diffusion coefficient is examined.

The diffusion coefficient can also be calculated through the integral of the velocity auto-correlation function (VACF) [20]

$$D = \int_0^\infty dt C(t)$$

$$C(t) = \langle \mathbf{v}(t) \cdot \mathbf{v}(0) \rangle \quad (3.5.8)$$

where $C(t)$ is the VACF. The VACF was calculated using corrected $f^{(2)}$ -DSMC and is compared against results from MD simulations in Fig. 3.6. At low densities ($\rho \sigma^3 = 0.1$), the corrected $f^{(2)}$ -DSMC reduces to the Enskog limit and accurately predicts the VACF. At $\rho \sigma^3 = 0.5$, the long-time tail is missing from the corrected $f^{(2)}$ -DSMC, but this is compensated for by an over-prediction of the correlations at short times. At higher densities, caging causes the VACF to go negative and this leads to the large over-predictions of the diffusion coefficient. It appears that a fortuitous cancellation of errors results in improved predictions of the diffusion coefficient at moderate densities ($\rho \sigma^3 = 0.5$). However, this is also true of Enskog theory and predictions of the VACF using $f^{(2)}$ -DSMC are excellent up to a density of $\rho \sigma^3 = 0.3$. In the next section the $f^{(2)}$ -DSMC method is applied to sheared granular materials.

3.6 Inelastic Hard Spheres Under Shear

This section is to be read as an addendum to Chap. 6.

Chapter 6 on “Collision Statistics in Sheared Inelastic Hard Spheres” was written, submitted and published before the $f^{(2)}$ -DSMC simulation technique of this chapter was developed. As such, a few of the simulation results may be revisited using $f^{(2)}$ -DSMC

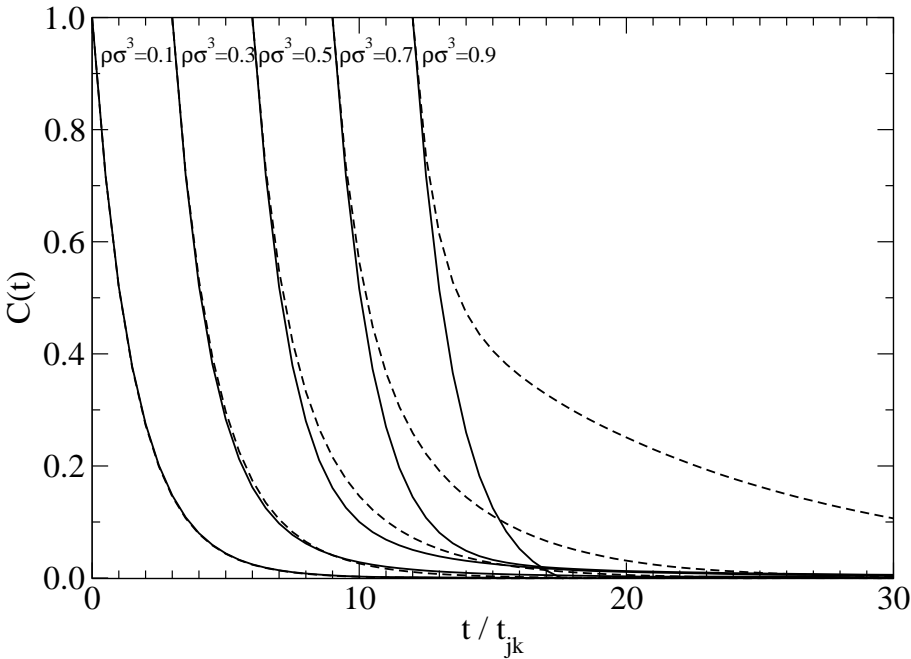


Figure 3.6: The velocity auto-correlation function calculated using (solid) MD simulations and (dashed) corrected $f^{(2)}$ -DSMC simulations.

simulation to analyse the role of velocity correlations. This section reviews some of the more interesting results provided by the $f^{(2)}$ -DSMC calculations.

Velocity correlations in sheared granular materials have already been analysed by Mitarai and Nakanishi [22] using the concept of a separate collision temperature to fit to simulation results. The analysis was successful and indicated that pre-collision correlations are significant in inelastic systems due to clustering effects. Ring kinetic theory has also been solved for homogeneously cooling inelastic materials by van Noije [16], in the limit of low density. Van Noije found that dynamical spatial correlations in the velocity led to vortex formation and reported excellent agreement with MD results for sheared inelastic disks. This theory included spatial correlations which are missing here but the effect of velocity correlations should still be significant.

The $f^{(2)}$ -DSMC mean free time and pressure (not shown) when compared against the Enskog DSMC results did not change significantly; however, the temperature (Enskog and MD data in Fig. 6.2) increased slightly (3-5%) over the Enskog predictions and in the direction of the MD results at low densities. The predictions for the distribution of the kinetic energy between each dimension (see Fig. 3.7) are improved over Enskog theory. The $f^{(2)}$ -DSMC simulations display a greater anisotropy in the distribution of energy between each dimension at low densities. Re-collisions appear to increase anisotropy and it is likely that clustering effects, which are missing from $f^{(2)}$ -DSMC, would increase the re-collision rate and anisotropy further to match the simulation values.

The viscosity η (see Fig. 3.8), which is directly related to the collisional energy loss rate, is almost unaffected using $f^{(2)}$ -DSMC, as can be expected from the small change in the steady state granular temperature. Although the predictions for the distribution of

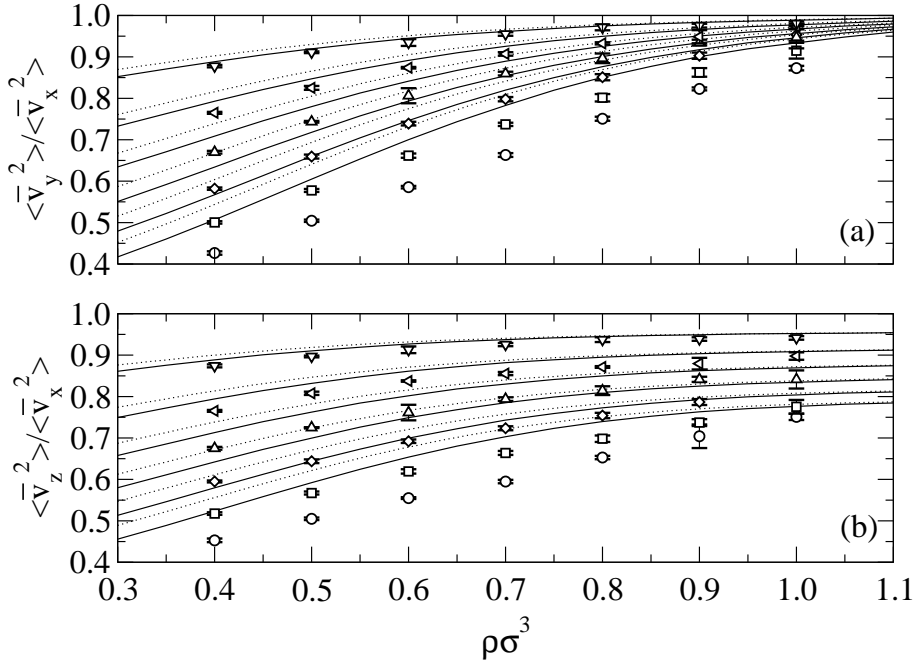


Figure 3.7: The ratio of the mean-squared-velocity (a) in the y - and x -directions and (b) in the z - and x -directions for sheared inelastic hard sphere systems with (i) $\alpha = 0.4$ (circles), (ii) $\alpha = 0.5$ (squares), (iii) $\alpha = 0.6$ (diamonds), (iv) $\alpha = 0.7$ (triangles-up), (v) $\alpha = 0.8$ (triangles-left), and (vi) $\alpha = 0.9$ (triangles-down). The dotted lines are the Enskog DSMC results and the solid lines are the $f^{(2)}$ -DSMC results.

kinetic energy between each dimension is improved, only a small improvement is noted in the normal stress coefficient predictions. It appears that although the energy anisotropy predictions are improved, the collisional terms of the pressure are dominant for the in η_- and out-plane η_0 normal stress coefficients. The deviations in the out-plane normal stress are likely due to the clustering of the particles in the shear plane at high densities.

The predictions for the collisional properties of sheared inelastic hard sphere system are relatively unaffected by including velocity correlations. Although the kinetic energy anisotropy predictions are improved, the deviations of Enskog theory and molecular are likely due to spatial clustering effects.

The phenomenological analysis used for the elastic systems (see Sec. 3.5.1) cannot be directly extended to inelastic systems. Granular systems are prone to clustering at all densities and velocity distributions between particles are unknown *a priori*. The re-collision rate is then difficult to calculate using a only a diffusive model for particle motion as key parameters cannot be approximated.

3.7 Conclusions

The direct simulation Monte Carlo method has been extended to any level of the BBGKY hierarchy, provided severe approximations are made in the spatial correlations. This method was then applied to the $f^{(2)}$ or “repeated ring” level of kinetic theory for hard

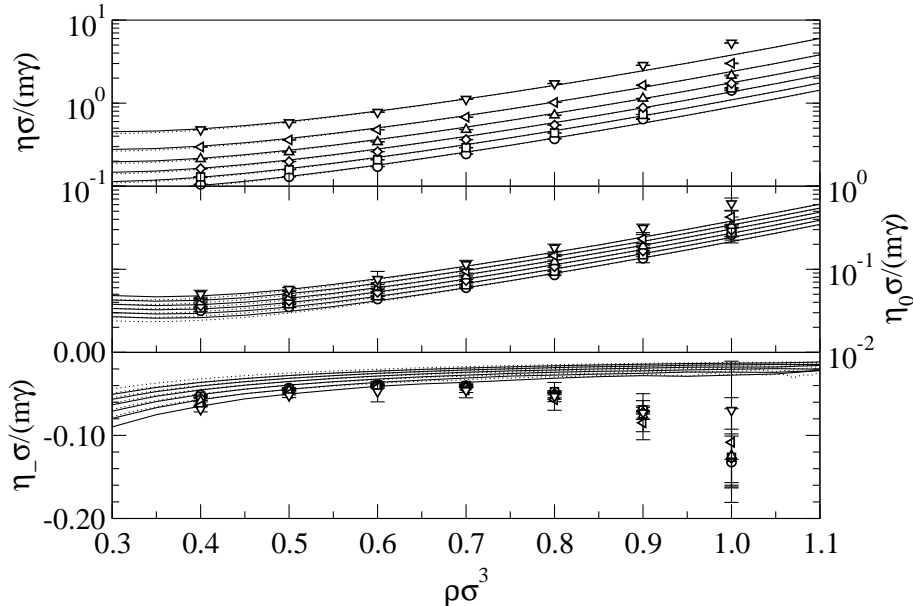


Figure 3.8: The viscosity for a homogeneously sheared inelastic-hard-sphere system with (i) $\alpha = 0.4$ (circles), (ii) $\alpha = 0.5$ (squares), (iii) $\alpha = 0.6$ (diamonds), (iv) $\alpha = 0.7$ (triangles-up), (v) $\alpha = 0.8$ (triangles-left), and (vi) $\alpha = 0.9$ (triangles-down). The dotted lines are the Enskog DSMC results and the solid lines are the $f^{(2)}$ -DSMC results.

spheres. The predictions of $f^{(2)}$ -DSMC are in general very similar to the predictions of Enskog theory for the elastic hard sphere fluid except in the diffusion coefficient where velocity correlations are most significant. A phenomenological correction is suggested that significantly improves the predictions over Enskog theory. For sheared inelastic systems, velocity correlations play a significant role in the energy anisotropy but most discrepancies between Enskog theory and MD results are due to spatial correlations. These may be included by performing a thorough comparison of each term in $f^{(2)}$ -DSMC with its counterpart in repeated ring theory or by further phenomenological analysis.

3.8 References

- [1] G. A. Bird, “Approach to Translational Equilibrium in a Rigid Sphere Gas”, *Phys. Fluids.* 6, 1518–1519 (1963).
- [2] G. J. LeBeau and F. E. Lumpkin III, “Application highlights of the DSMC Analysis Code (DAC) software for simulating rarefied flows”. 191, 595–609 (2001).
- [3] A. Donev, “Asynchronous Event-Driven Particle Algorithms”, *Simulation.* 85, 229–242 (2009).
- [4] F. J. Alexander, A. L. Garcia and B. J. Alder, “A consistent Boltzmann algorithm”, *Phys. Rev. Lett.* 74, 5212–5215 (1995).

- [5] M. A. Hopkins and H. H. Shen, “A Monte Carlo solution for rapidly shearing granular flows based on the kinetic theory of dense gases”, *J. Fluid Mech.* 244, 477–491 (1992).
- [6] J. M. Montanero and A. Santos, “Monte Carlo simulation method for the Enskog equation”, *Phys. Rev. E.* 54, 438–444 (1996).
- [7] J. M. Montanero and A. Santos, “Simulation of the Enskog equation a la Bird”, *Phys. Fluids.* 9, 2057–2060 (1997).
- [8] G. A. Bird. *Molecular gas dynamics and the direct simulation of gas flows*. Oxford: Oxford University Press, 1994.
- [9] K. Nanbu, “Direct Simulation Scheme Derived from the Boltzmann Equation. I. Monocomponent Gases”, *J. Phys. Soc. Jpn.* 49, 2042–2049 (1980).
- [10] C. Greengard and L. G. Reyna, “Conservation of expected momentum and energy in Monte Carlo particle simulation”, *Phys. Fluids A.* 4, 849–852 (1992).
- [11] M. H. Ernst and J. R. Dorfman, “Nonanalytic dispersion relations in classical fluids”, *Physica*. 61, 157–181 (1972).
- [12] J. Piasecki and R. Soto, “Ring approximation at equilibrium: The hard sphere pair correlation function”, *Physica A.* 379, 409–416 (2007).
- [13] B. J. Alder and T. E. Wainwright, “Decay of the Velocity Autocorrelation Function”, *Phys. Rev. A.* 1, 18–21 (1970).
- [14] J. W. Dufty, K. C. Mo and K. E. Gubbins, “Models for self-diffusion in the square well fluid”, *J. Chem. Phys.* 94, 3132–3140 (1991).
- [15] G. E. Garland and J. W. Dufty, “Bound state contributions to transport coefficients”, *J. Chem. Phys.* 95, 2702–2716 (1991).
- [16] T. P. C. van Noije, M. H. Ernst and R. Brito, “Ring kinetic theory for an idealized granular gas”, *Physica A.* 251, 266–283 (1998).
- [17] A. J. Masters and T. Keyes, “An Enskog repeated-ring kinetic equation; Long time tails and the Brownian limit”, *J. Stat. Phys.* 33, 149–180 (1983).
- [18] G. F. Mazenko, “Fully renormalized kinetic theory. I. Self diffusion”, *Phys. Rev. A.* 7, 209–222 (1973).
- [19] N. F. Carnahan and K. E. Starling, “Equation of state for nonattracting rigid spheres”, *J. Chem. Phys.* 51, 635–636 (1969).
- [20] J. M. Haile. *Molecular Dynamics Simulation - Elementary Methods*. New York: Wiley-Interscience, 1997.
- [21] L. Lue, “Collision statistics, thermodynamics, and transport coefficients of hard hyperspheres in three, four, and five dimensions”, *J. Chem. Phys.* 122, 044513 (2005).

- [22] N. Mitarai and H. Nakanishi, “Velocity correlations in dense granular shear flows: Effects on energy dissipation and normal stress”, *Phys. Rev. E.* 75, 031305 (2007).

CHAPTER
FOUR

AN $O(N)$ GENERAL EVENT-DRIVEN SIMULATOR: DYNAMO

This chapter has been submitted to the Journal of Computational Physics.
Authors: M. Bannerman, R. Sargent, L. Lue

THIS chapter is primarily the work of M. Bannerman. R. Sargent implemented assymetric potentials into DYNAMO and assisted in proof reading the submitted paper.

4.1 Introduction

“There is another way, that of brute force and ignorance!”

L. V. Woodcock, introducing the talk on DYNAMO at the Hoover colloquium.

Molecular-dynamics simulations have become an indispensable tool in the engineering of materials, such as in the development of novel nanomaterials and drug design. They play an important role in bioinformatics, nanotechnology, and materials engineering in the estimation of thermophysical properties and phase behavior of complex solutions. Molecular dynamics not only allows the exploration of the link between intermolecular interactions and macroscopic structure and dynamics, but it is also capable of providing quantitative predictions for real materials. Molecular-dynamics simulations have been dominated by time driven methods on systems that interact with continuous potentials. This method was first used by Rahman [1] in 1964, and later popularized by Verlet [2]. Since then, many sophisticated software packages have been developed, such as LAMMPS (Large-scale Atomic/Molecular Massively Parallel Simulator) [3], GROMACS (Groningen Machine for Chemical Simulation) [4], and ESPResSo (Extensible Simulation Package for Research on Soft Matter) [5], which are freely available software and allow the simulation of complex systems. In addition, a wealth of force fields based on continuous potentials have been developed to describe real materials, such as small organic and inorganic molecules, polypeptides, proteins, and DNA. Among these force fields are AMBER (Assisted Model Building and Energy Refinement) [6, 7], CHARMM (Chemistry at HARvard Molecular Mechanics) [8], OLPS (Optimized Potential for Liquid Simulations) [9, 10], ECEPP/2 [11, 12], etc. Coarse grained potentials have also been developed to describe systems on larger scales.

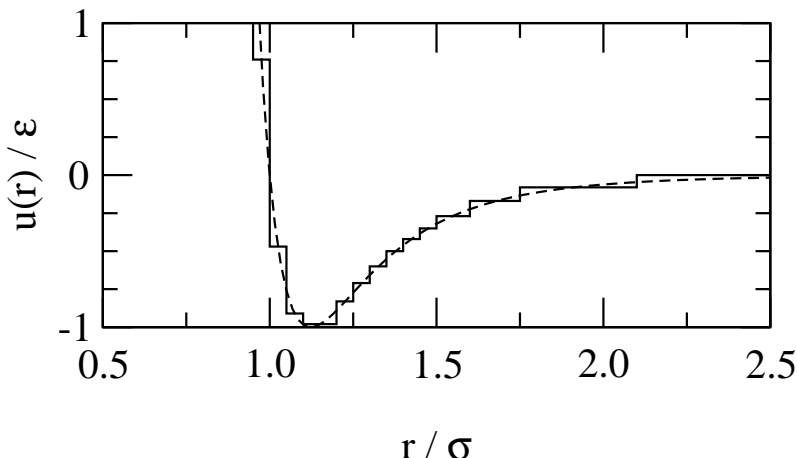


Figure 4.1: A stepped potential (solid line) that approximates the Lennard-Jones potential (dashed line) [13].

An alternative approach to modeling many-body systems is through the use of discrete interaction potentials, such as the hard-sphere or square-well potentials. These potentials contain only distinct energy level changes; however, they can be stepped to either approximate soft potentials, such as the Lennard-Jones potential [13] (see Fig. 4.1), or directly reproduce thermodynamic data [14]. In many cases, they offer a significant increase in the computational speed of the simulation. Standard numerical methods developed for integrating systems interacting through soft potentials are inefficient for systems with discrete potentials due to the presence of discontinuities in the potential. A time-driven algorithm, where changes in the interaction energies are detected after the time step is taken, is still feasible [15]; however, this method is necessarily approximate, and high accuracy requires a small computationally-expensive time-step.

In principle, event-driven algorithms provide an exact method for performing molecular-dynamics simulations for discrete potential systems, where the dynamics can be decomposed into a sequence of events. Although simulations for discrete potential systems are not as prevalent as for continuous potential systems, the literature for classical systems of particles with discontinuous potentials is quite extensive. Indeed, Alder et al. [16] reported molecular-dynamics simulations for systems of hard spheres using an event-driven algorithm in 1957, seven years before Rahman’s soft potential simulations. Since then, discrete potential models have found application in granular materials [17], polypeptide and protein simulations (e.g., PRIME [18]), vapor-liquid equilibrium (e.g., SPEADMD [19]), and more.

There are numerous review papers on the subject of algorithms for event-driven molecular dynamics [15, 20–25]; however, it is difficult to find reference implementations. Modern algorithms are complex and contain many subtle difficulties which, if poorly implemented, can severely restrict the generality and speed of the code. In this article, we present DYNAMO (DYNAMics of discrete Objects), a free source molecular-dynamics package that is optimized for event-driven dynamics. DYNAMO is capable of simulat-

ing large ($\gtrsim 10^6$ particles) and complex systems for extremely long simulation times. This package has already been used to study sheared granular materials [26], binary mixtures [27], and helix forming polymers [28].

The remainder of this article is organized as follows. In Section 4.2, we begin with an overview of the basic elements of event-driven molecular-dynamics simulations. This section briefly reviews some of the recent algorithmic advances. Some improvements that we have developed to the simulation algorithm are presented in Section 4.3. These include novel approaches to access particle information, optimize neighbor lists, and minimize numerical inaccuracy. Section 4.4 outlines the general structure of DYNAMO and details various aspects of its implementation, as well as lists its currently implemented features. Section 4.5 provides benchmark simulations for DYNAMO on systems of single component hard spheres. These simulations provide timing results and information on the scaling of the calculation times with system size. Finally, the conclusions of the paper are presented in Section 4.6, along with a discussion of possible directions for future improvements to DYNAMO.

4.2 Algorithm Details

A molecular-dynamics simulation calculates the trajectory of a collection of a large number of interacting particles. When the particles interact with each other through a discrete potential, the dynamics of the system are governed by a series of distinct events (e.g., collisions between particles). These events may alter the properties of the particles, such as their velocities. Between these events, the particles move freely, and the dynamics of the system is known analytically.

In an event-driven simulation, there are three major tasks which occupy most of the computational time: (i) search for events (event detection), (ii) maintenance of the event list, and (iii) execution of events. An outline of a basic event-driven simulation algorithm is given below, including the computational cost scaling with system size N of each step :

1. Event testing $O(N^2)$: All particles and pairs of particles are tested to determine if/when the next interaction occurs. The times of these events are inserted into the Future Event List (FEL).
2. Event sorting $O(N)$: The events in the FEL are sorted to determine the next event to occur.
3. Motion of the system $O(N)$: The system is evolved, or free streamed, to the time of the next event.
4. Execution of the event $O(1)$: Particles involved in the event are updated with new velocities.

5. Update events in FEL $O(N)$: Events in the FEL that involve particles that have just undergone the executed event are now invalid. New events for these particles are possible and must be tested for. The future event list may be cleared and rebuilt ($O(N^2)$), or only the affected events can be updated ($O(N)$).
6. End condition: Continue to step 2 unless sufficient collisions have been executed or the maximum simulation time has elapsed.

Alder and coworkers [16] proposed the first algorithm for event-driven molecular-dynamics simulations. Since their pioneering work, there have been significant advances in the development of this initial algorithm. We will briefly cover the advances in event detection/execution before detailing improvements in the maintenance of the list of all possible future events.

Alder and Wainwright [20] were the first to suggest the use of a “neighbor list” technique to improve the efficiency of the search for future events. In this method, only localized pairs of particles are tested for possible collisions by dividing the simulation box into smaller cells. This significantly reduces the number of pairs of particles that need to be tested for interactions. An additional event is introduced to track the motion of the particles between these cells. The resulting computational scaling of steps 1 and 5 reduces to $O(1)$. This “neighbor list” technique has since been extended to infinite systems [29], overlapping cells [30], hybrid methods [31], and asymmetric particle shapes [32].

In asynchronous [22, 33] or “delayed states” [23] algorithms, only particles involved in or in the neighborhood of an event are updated when an event occurs (step 3). Each particle stores the time at which it was last updated and is only evolved to the current time when it is tested for or undergoes an event. As particles which are not involved in an event incur no overhead, step 3 is reduced to $O(1)$.

In most modern implementations of event-driven algorithms, the system size scaling of the event computational cost arises from the maintenance [21] of a list of all possible future events (step 2). This list needs to be sorted to determine the next event to occur, and after an event is executed the list must be updated. Improvements in sorting began with the use of many variants of binary trees [21] before complete binary trees were found to be optimal [34]. Complete binary trees exhibit an $O(\log_2 N_{\text{event}})$ scaling in the number of events N_{event} contained in the tree. It has been previously suggested [21, 22] that an $O(\log_2 N_{\text{event}})$ scaling of sorting the event list is the asymptotic minimum; however, a recent advance in event sorting using calendar event queues [35] now enables $O(1)$ scaling. This is achieved by presorting events into a calendar before sequentially processing the “dates” in the calendar using a complete binary tree. The length of the calendar is scaled linearly with the system size, resulting in a fixed average size of the complete binary tree. This ensures that the deletion, insertion, and updating operations all remain of order $O(1)$.

With these methods, the overall computational cost of executing a single event is now independent of the system size, which is the theoretical optimum. The number of events

per particle is typically proportional to the total time simulated, thus the computational cost of simulating a unit of time scales as $O(N)$ with the system size.

Other algorithmic improvements, which do not affect the system size scaling of the computational cost, have been made to the deletion of events from the calendar. The local minima algorithm [23] relies on each event being associated with at least one particle. Only the shortest event time for each particle is entered into the global event list, as this is the most likely event to occur. Here, we use a priority queue called a particle event list (PEL) to sort the events associated with a particle. Priority queues allow only insertion, access to the shortest time event, and clearing; they are optimal for the access patterns of the PEL [36]. When a particle undergoes an event, at least half of the invalidated events associated with it can be deleted simply by erasing the corresponding PEL. The remainder of the invalidated events are left in the FEL and are deleted if they reach the top of the FEL. This is achieved by tracking the number of events each particle has undergone in total and the value of this when the event was tested [23].

4.3 Improvements to the Simulation Method

In this section, we present some additional improvements to the event-driven simulation algorithm that we have developed and implemented within DYNAMO. These methods are primarily concerned with the storage of data and increasing simulation accuracy.

4.3.1 Particle Data

In DYNAMO, a minimal approach is taken to the storage of particle data. Each particle class contains only a particle's position, velocity, ID number, and the time the particle was last updated. Other data dependent on the system (e.g., mass/inertia, orientation, species) are defined separately and accessed using the particle's ID number if required. This implies that a functional definition of a property (e.g., a distribution of particle masses) is possible using the particle ID numbers.

A design feature of DYNAMO is the use of functions, as opposed to look-up tables, when specifying the particles described by a property. These functions are pseudo containers and map to sets of particle ID numbers. They provide a mechanism to test for membership of the set and a method for iterating over all members of the set. This is used in defining molecular topology, species, mass, and in defining how particles interact (e.g., to create mixtures of particles). This approach conserves memory as a minimal number of entries are required and is faster than a look-up table when iterating over all members of a given property.

For dynamical properties of particles (e.g., if two particles have captured each other in an attractive well), we make use of unordered sets and maps. These hashed containers still provide $O(1)$ operations when using a suitable hash function but conserve memory when compared to look-up tables.

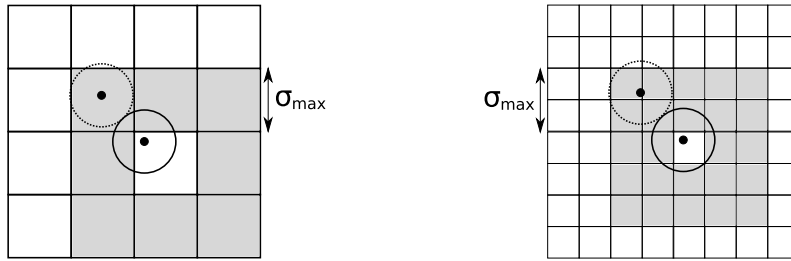


Figure 4.2: Cells (gray) which enclose the neighborhood of a particle (solid circle), for a cell length equal to (left) and half of (right) the maximum interaction distance σ_{max} .

4.3.2 Over-Linking of Neighbor List Cells

The speed of event-driven simulations is dependent on the effective use of neighbor lists. They must be inexpensive to maintain while providing the minimal neighborhood around each particle to reduce the number of interaction tests. The neighborhood must be large enough to include all possible interaction partners. For soft or asymmetric potentials (e.g., stepped Lennard-Jones or highly elongated particles) and high densities, a particle’s neighborhood can contain hundreds of particles, which significantly reduces the calculation speed.

Ideally, a particle’s neighbor cells should only encompass up to the maximum interaction distance. Typically, the cells are constructed by gridding the space of the simulation into cubes with a width equal to the maximum interaction distance σ_{max} . Each particle must then check its neighboring cells (26 in 3 dimensions) for interactions resulting in a neighborhood volume of $V_{nbh} = (3\sigma_{max})^d$ (see Fig. 4.2); however, the optimal volume for a cubic cell is equal to $V_{nbh} = (2\sigma_{max})^d$. This discrepancy arises from the finite width of the cell containing the particle. We can counteract this effect by shrinking the cell width and over-linking the cells to ensure the same maximum interaction distance is still contained (see Fig 4.2). This is beneficial at high density where the cost of the extra neighbor list maintenance, typically cheap compared to the interaction calculations, is offset by the reduced volume of the neighborhood. In three dimensions, halving the cell width results in a neighborhood volume $2.5^3/3^3 \approx 58\%$ of the original. In preliminary simulations of the stepped Lennard-Jones fluid (see Fig. 4.1), we observe a threefold increase in computational speed at liquid densities ($\rho\sigma^3 = 0.85$) using half size cells. Smaller cells are more expensive due to the increased number of cell transitions. In the next subsection, we discuss the storage of the neighbor list data.

4.3.3 Morton Ordered Neighbor Lists

The algorithms discussed in Sec. 4.2 result in a theoretical system size scaling of $O(1)$ in the cost of processing a single event. In practice, the computational cost will also be affected by the memory architecture of the computer that runs the simulation. If the events are relatively inexpensive to test for, the bulk of the simulation time will be spent on memory accesses to retrieve particle, event, and neighbor list data.

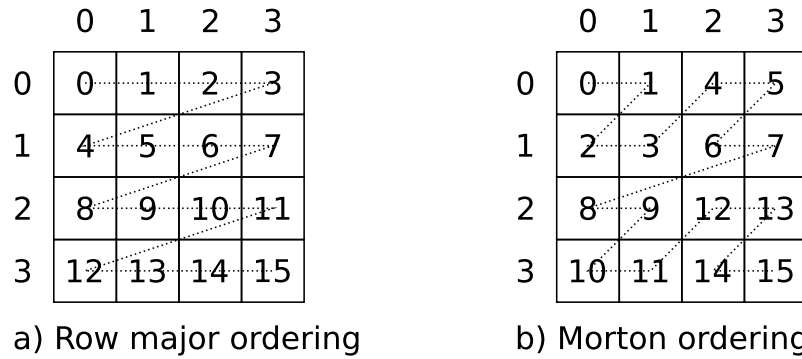


Figure 4.3: A two dimensional 4×4 array stored in row major order and Morton order in memory.

A fundamental aspect of modern processors is the use of a CPU cache, into which data are “fetched” before becoming available to the running process. A cache “miss” occurs when data to be accessed are not already available in the cache. The cost of a cache “miss” is typically quite severe, requiring several computational cycles to fetch the data from main memory and load it into the CPU cache. Data are typically fetched in blocks of the order of 10 bytes; therefore, data localized in memory are typically fetched at the same time. Thus, if the location of data in memory is strongly correlated to the data access pattern, then the number of cache misses can be reduced.

The particle and event data accesses are effectively random, which renders any attempt to optimize the access patterns futile; however, accesses to the neighbor list data are strongly correlated. Whenever a particles local space is to be inspected for possible events, the cells of the neighbor list which surround the particle are checked for event partners. Thus, accesses to the neighbor list cell contents are typically strongly correlated in the spatial coordinates of the cell. If the cell content data are arranged such that spatially localized data are also localized in memory, then the number of cache misses will be reduced.

Arrays are typically stored linearly (row major in C++) in computer memory, where each successive row of data in the lowest spatial dimension is appended to the previous row (see Fig. 4.3a). An alternative space filling curve which retains a high level of spatial locality is the Morton-order or “Z-order” curve (see Fig. 4.3b). Recently, fast methods for dilating integers used in Morton ordering [37] and methods for directly carrying out mathematical operations on the dilated integers [38] have become available. The overhead of calculating a three dimensional Morton number is now less than the cost of a cache miss in many applications. In DYNAMO, we have implemented Morton ordering in the neighbor list, and a comparison between linear and Morton order is presented in the timing results section (see Section 4.5).

The algorithms described thus far are primarily concerned with increasing the speed of the calculations; however, the numerical accuracy of the simulation is crucial. The methods employed to ensure precision is maintained are detailed in the following section.

4.3.4 Accuracy and Time Invariance

Molecular-dynamics simulations require a high level of accuracy. This is especially true “for hard core systems”, where configurations with overlapping hard cores resulting from numerical inaccuracies are unphysical and impossible to resolve. Accuracy is particularly important in inelastic, granular systems due to clustering of the particles; small errors in the movement of particles, resulting in overlaps, are increasingly probable.

Several improvements have been made to the algorithm used in DYNAMO to maintain the numerical precision of the simulation. The use of the “delayed states” [23] algorithm already reduces the number of times a particle is free-streamed between events. Also, when an event is scheduled to occur, events are retested to determine the exact time at which it occurs [36]. This reduces the likelihood of overlaps occurring due to inaccuracies in the free streaming. Furthermore, the dynamics of the system is tracked to ensure invalid events cannot occur (e.g., particles must be approaching to be tested for a collision, square-well molecules must have been captured to test for a release event). This implies that the dynamics of the system must always be deterministic; however, random events, such as those that occur in the Andersen thermostat [39], are possible by randomly assigning a time after each random event and scheduling this fixed time in the event list.

Another inaccuracy arises from the storage of absolute times in the simulation. Events occur at an absolute time t_e , and within the asynchronous algorithms the particle data are stored at a certain absolute simulation time t_p . As the absolute simulation time t_{sim} increases in magnitude, round-off error will accumulate in these stored absolute times. To avoid this, only time differences $\Delta t_{e/p}$, recording the time relative to the current absolute simulation time $t_{e/p} = t_{\text{sim}} + \Delta t_{e/p}$, must be stored. This does, however, introduce an $O(N)$ computational cost per event in maintaining these time differences. This is alleviated by storing time differences relative to a reference time difference $\Delta t_{e/p} = \Delta t_{\text{ref}} + \Delta t_{e/p}^{(\text{stored})}$. This reference time difference Δt_{ref} is updated at every event without incurring significant cost. Periodically all time differences and reference time differences must be synchronized to prevent round-off error, and the interval at which this synchronization occurs is proportional to the system size. This leads to a time invariant simulation algorithm with a fixed upper bound of round-off error *without* affecting the scaling of the computational cost.

4.3.5 Summary

In this section, we have discussed some of the new methods we have developed to improve the computational efficiency of DYNAMO. In the next section, the object orientated design of DYNAMO and its currently implemented features are described.

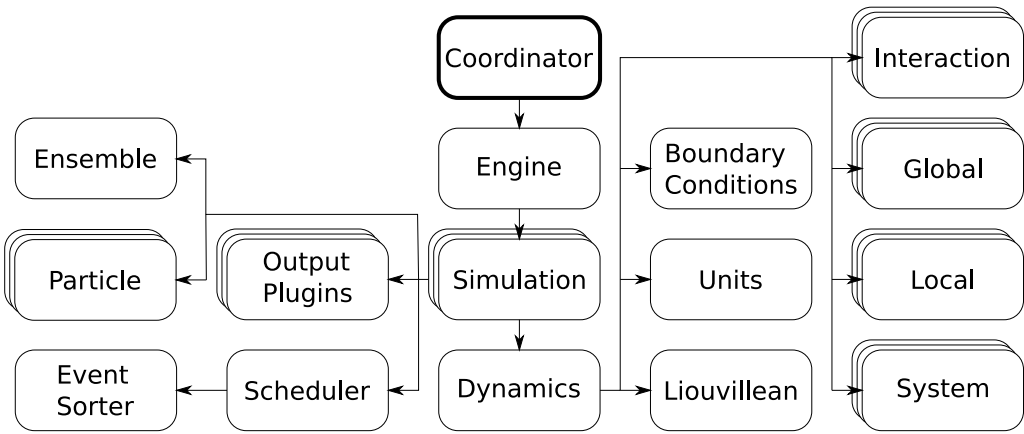


Figure 4.4: The class hierarchy of DYNAMO. Only the classes key to the algorithm are displayed. Arrows indicate the nesting of classes, and stacked boxes indicate multiple instances of the class may occur.

4.4 Program Design

The development of DYNAMO has focused on generating a flexible, modular simulator where systems can be constructed from an array of available interactions, conditions, and dynamics. DYNAMO is written in C++ using an object orientated design. This ensures the code is both extensible and maintainable, provided the classes have well defined interfaces and tasks. All input and output files are in XML to allow easy generation and alteration of system conditions. The implementation of DYNAMO utilizes only free, open source libraries, including the BOOST (www.boost.org) and GSL (www.gnu.org/software/gsl) libraries.

DYNAMO was originally written to perform NVE molecular-dynamics simulations of particles interacting through spherically symmetric, discrete potentials. However, because of its flexible design, DYNAMO has been extended to perform a wide variety of calculations for several different types of systems. The dynamics of infinitely thin lines [40] has already been incorporated within DYNAMO, and other shapes can also be included. Constant temperature simulations are performed through the use of the Andersen thermostat [39]. Multiple simulations can be executed concurrently and combined with the replica exchange method [41] to expedite the equilibration of systems with rough energy landscapes. Umbrella potentials can also be applied to sample specific regions of the phase space of a system. Finally, stepped potentials can be used to approximate rotationally symmetric soft potentials.

Alternate dynamics can also be easily implemented within DYNAMO. For example, compression dynamics, where the particles in the system grow with time, is already implemented. DYNAMO is also used [26, 27] as a framework to perform direct simulation Monte Carlo calculations for the Enskog equation.

Simple code hierarchies have been suggested previously [42]; however, the level of complexity of modern simulations requires a finer grained class structure than previously outlined.

The class hierarchy of DYNAMO is presented in Fig. 4.4. Typically each class has several implementations which are selected at run time through the input files. Below, we detail the scope of each class, along with the currently implemented features:

Coordinator: *Abstracts the user interface and system calls.*

This class encapsulates the entire program and provides the user interface. The initialization of operating system features, such as threading, is also performed here.

Engine: *Organizes a collection of simulations to achieve a task.*

In its simplest form, a single simulation is run to obtain output; however, replica exchange techniques [41] and a method to perform isotropic compression of configurations [43] is also available. The replica exchange technique runs several simulations in parallel with a Monte Carlo move to increase the ergodicity of low temperature trajectories.

Simulation: *Encapsulates a single simulation.*

This class represents a single simulation, containing an array of particles, classes describing the dynamics, and data collection classes. The primary function of the simulation class is to initialise and maintain these classes in evolving the system through time.

Scheduler: *Maintains the list of future events.*

This class is responsible for executing events and maintaining the FEL. Two variants exist, a “dumb” scheduler and a scheduler capable of interfacing with a specialized Global that implements a neighbor list.

Event Sorter: *Sorts events in the FEL.*

Provides a method of sorting the FEL, which contains an array of PELs. A complete binary tree [34] and a bounded priority queue [35] are implemented.

Particle: *Container for single particle data.*

This class encapsulates the minimal single particle data. This includes the particle ID number, position, velocity, and local time.

Output Plugins: *Data collection routines.*

A wide range of plugins are available, including radial distribution functions, the complete set of Green-Kubo expressions for mixtures, and visualization plugins for VMD (www.ks.uiuc.edu/Research/vmd), Povray (www.povray.org), and Geomview (www.geomview.org).

Ensemble: *Describes the ensemble of the simulation.*

This is used to ensure the simulation ensemble is valid for certain output plugins and for replica exchange.

Dynamics: *Encapsulates the dynamics methods of the system.*

The dynamics class initialises and maintains classes relating to the dynamics of the system. The actual dynamics are implemented in classes contained within this class.

Units: *Provides functions to scale between simulation and input units.*

Simulations are typically optimal in a unit set other than the input settings. For example,

if the dimensions of the simulation box are scaled to one then the enforcement of the periodic boundary conditions reduces to a rounding operation [44].

Liouvillean: *Contains simple functions to describe the evolution of the system.*

This class implements event testing for basic shapes (e.g., spheres, lines, planes), particle evolution and event dynamics. These are then used by interactions, locals and globals to implement an event. Several implementations exist, including Newtonian, isotropic compression, Enskog direct simulation Monte Carlo (DSMC) in Sllod coordinates [45], and axisymmetric rotational dynamics.

Boundary Conditions: *Specifies the limits of the simulation box.*

Square, rectangular, periodic, sliding brick shearing [46], and infinite boundary conditions are currently implemented.

Interaction: *Two particle events.*

Interactions between two particles are derived from this class. Many interactions have already been implemented (e.g., stepped potentials, hard spheres, parallel cubes, square wells, square-well bonds [47], thin needles [40], and an optimized square-well sequenced-polymer interaction).

Global: *Single particle events.*

Events which affect only one particle, regardless of its position in the simulation are derived from this class. This is primarily used for neighbor lists, specializations include overlapping cells [30], mixed methods [31], cells in shearing, Morton ordered neighbor lists, and a sentinel event to ensure the nearest image condition does not result in invalid dynamics at low density/small system size [40].

Local: *Single particle event, localized in space.*

These events only effect a region of space and are inserted into the neighbor lists when available. This is to reduce the number of event tests required. Solid and thermostatted walls [36] are implemented here.

System: *Simulation and multiple-particle events.*

Any type of event which is not compatible with the definition of a Local, Global or Interaction is implemented here. Includes DSMC interactions [48], Andersen thermostats [39], and simulation termination conditions. Umbrella potentials are also implemented here as they are many-body interactions.

The next section provides some benchmarking simulations for DYNAMO and tests the system size scaling of the code.

4.5 Benchmarking

In order to benchmark the speed of DYNAMO and test that the optimal scaling is achieved, we perform molecular-dynamics simulations on systems composed of elastic

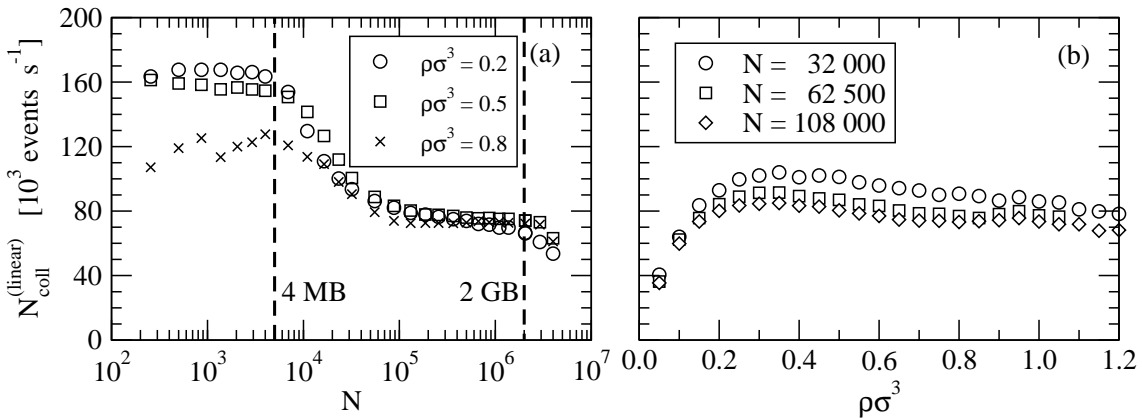


Figure 4.5: The number of collision events processed per second using linear neighbor lists $N_{\text{coll}}^{(\text{linear})}$ as a function of (a) the number of particles N and (b) the number density ρ . Lines indicating the memory boundaries are approximate as different densities incur slightly different memory requirements. The results are for a monodisperse system of elastic hard spheres simulated on an Intel®Core™2 Duo 6600.

hard spheres. This interaction is relatively inexpensive and as such is useful in testing the performance of the simulation framework. Each sphere has a diameter σ , and the system is bounded by standard periodic boundary conditions. The simulations were performed on a desktop computer with an Intel®Core™2 Duo 6600 processor with 2 GB of RAM. The simulations utilized a single core of the processor and are averaged over 3 runs of 2×10^7 collisions.

The average number of collisions per second is plotted in Fig. 4.5a as a function of system size and density. It is apparent that the memory architecture plays a large role in the speed of the simulation. The rate of collision maintains a relatively constant value when the program fits inside the CPU cache (≤ 4 MB boundary), and for very large systems ($N \gtrsim 10^5$) where the cache effects are proportionally small. Accounting for these memory size effects, the algorithm appears to exhibit $O(1)$ scaling of the collision cost. Inside the cache, the simulation reaches a maximum of roughly 1.7×10^5 events per second, compared to a minimum of approximately 7×10^4 events per second outside of the cache. Beyond the 2 GB memory limit disk swapping begins to occur and the performance is substantially degraded.

The event processing rate is relatively insensitive to density (see Fig. 4.5b), with the exception of low density. The low density effect is due to the overhead of the neighbor list becoming large as the number of neighbor list cells increases. This is because the simulation defaults to selecting the smallest possible cell size; however, this can be partly compensated for by optimizing the cell size. A slight decrease in the event processing rate is expected at higher densities as local neighbor lists contain more entries (neighbors). Over linking the cells does not become favourable for hard spheres before maximum packing is reached as the interaction calculation is cheap.

The large effect of caching on the performance of the simulation indicates at least

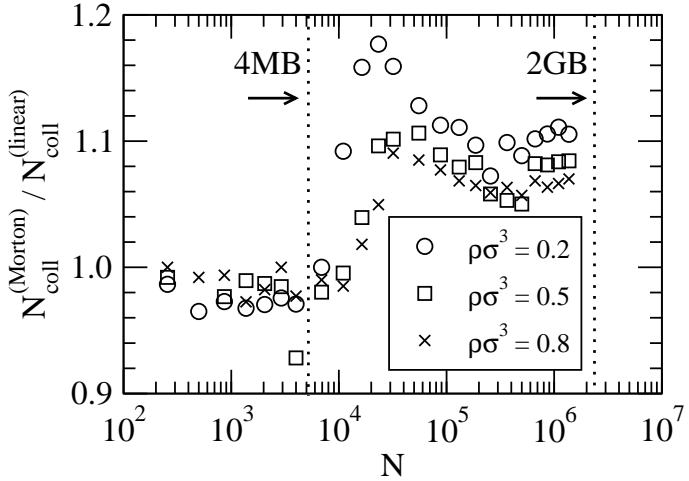


Figure 4.6: The number of events processed per second using linear and Morton ordered lists, $N_{\text{coll}}^{(\text{linear})}$ and $N_{\text{coll}}^{(\text{Morton})}$, respectively. The dashed lines and system are described in Fig. 4.5.

half the time of simulations outside the cache boundary are spent waiting on memory accesses. Cache simulations have been performed using Callgrind [49], and for a density of $\rho\sigma^3 = 0.5$, approximately half of the cache misses result from accesses to the contents of the neighbor lists. The remaining cache misses are associated with accesses to particle and event data.

A comparison between Morton ordering and the typical linear ordering is presented in Fig. 4.6. Inside the 4 MB cache limit, the Morton ordering has no positive effect; however, the overhead is typically small (ca. 2–4%). Outside the cache, Morton ordering offers a 6–18% increase in event processing speed. At higher densities the Morton ordering has a reduced effect as the ratio of particle to neighbor list memory accesses is increased. Overall, Morton ordering appears to be an effective method of increasing the computational speed by reducing the number of cache misses within a simulation.

4.6 Conclusions

We have detailed the fundamental components of DYNAMO, a modern event-driven molecular-dynamics simulation package. The program is distributed under the GNU General Public License. The full source code and documentation to reference implementations are freely available online at

<http://www.marcusbannerman.co.uk/dynamo>. The program includes several new techniques for mitigating round-off error, improving speed, and optimizing memory access patterns. The latter was achieved by preserving cache locality through using Morton ordering to store neighbor entries in spatially localized clusters. The speed of the memory appears to be a significant bottleneck in simulating systems with simple potentials. Through benchmark simulations on single component elastic-hard-sphere systems,

we have demonstrated that DYNAMO exhibits an $O(1)$ scaling with system size of the computational cost of executing events. This leads to an overall scaling of $O(N)$ for a set duration of simulation time. This allows the rapid simulation of both complex and large (10^6 particle/atom) systems while extracting the long-time behavior.

Many systems can be explored with the package in its current state; however, there are a few planned improvements which will bring the package to the level of generality of modern soft potential packages.

Asymmetric potential dynamics are complex, especially in the case of hard particles [32]. The determination of the time to collision requires considerable care and these algorithms are typically specialised to the underlying potential. Soft potential dynamics are widely used for modelling due to the relative ease with which new potentials can be implemented. A natural step forward for event-driven dynamics is the implementation of a framework developed by van Zon and Schofield [50] to approximate asymmetric soft potentials using terraced potentials. This will facilitate rapid implementation of asymmetric models and the direct comparison of event-driven and time-driven integration techniques.

Long-ranged potentials, such as those due to electrostatic interactions, do not yet have an event-driven equivalent. The implementation of a stepped force field is not difficult; however, coupling the particle positions to the field is not trivial [24]. In the limit of a weak and long-ranged field within a large system, this coupling may be implemented as a boundary condition of the stepped potential grid. These techniques must be developed before event-driven dynamics can be utilized in modelling charged systems.

Event-driven simulations are serial by nature; however, attempts have been made to develop parallel algorithms [51, 52]. Simulations are split into computational cells and divided among a collection of processors. Each cell is then run independently of all others until an event occurs in the boundaries of the cells, forcing a synchronization. This would require considerable work to implement, yet this will be required as the complexity of the underlying potentials increases.

4.7 References

- [1] A. Rahman, “Correlations in the Motion of Atoms in Liquid Argon”, *Phys. Rev.* 136, A405–A411 (1964).
- [2] L. Verlet, “Computer experiments on classical fluids. I. Thermodynamical properties of Lennard-Jones molecules”, *Phys. Rev.* 159, 98–103 (1967).
- [3] Steve Plimpton, “Fast parallel algorithms for short-range molecular dynamics”, *J. Comp. Phys.* 117, 1–19 (1995).
- [4] D. Van Der Spoel et al., “GROMACS: Fast, flexible, and free”, *J. Comput. Chem.* 26, 1701–1718 (2005).

- [5] Hans-Jörg Limbach et al., “ESPResSo – An Extensible Simulation Package for Research on Soft Matter Systems”, *Comput. Phys. Commun.* 174, 704–727 (2006).
- [6] T. E. Cheatham III and M.A. Young, “Molecular dynamics simulation of nucleic acids: Successes, limitations and promise”, *Biopolymers.* 56, 232–256 (2001).
- [7] J.W. Ponder and D.A. Case, “Force fields for protein simulations”, *Adv. Prot. Chem.* 66, 27–85 (2003).
- [8] A.D. MacKerel Jr. et al. “CHARMM: The Energy Function and Its Parameterization with an Overview of the Program ”. In: ed. by P. v. R. Schleyer et al. Vol. 1. The Encyclopedia of Computational Chemistry. John Wiley & Sons: Chichester, 1998, pp. 271–277.
- [9] W. L. Jorgensen and J. Tirado-Rives, “The OPLS Force Field for Proteins. Energy Minimizations for Crystals of Cyclic Peptides and Crambin”, *J. Am. Chem. Soc.* 110, 1657–1666 (1988).
- [10] W. L. Jorgensen, D. S. Maxwell and J. Tirado-Rives, “Development and Testing of the OPLS All-Atom Force Field on Conformational Energetics and Properties of Organic Liquids”, *J. Am. Chem. Soc.* 118, 11225–11236 (1996).
- [11] G. Nemethy, M. S. Pottle and H. A. Scheraga, “Energy parameters in polypeptides. 9. Updating of geometrical parameters, nonbonded interactions, and hydrogen bond interactions for the naturally occurring amino acids”, *J. Phys. Chem.* 87, 1883–1887 (1983).
- [12] M. J. Sippl, G. Nemethy and H. A. Scheraga, “Intermolecular potentials from crystal data. 6. Determination of empirical potentials for O-H · · · O=C hydrogen bonds from packing configurations”, *J. Phys. Chem.* 88, 6231–6233 (1984).
- [13] G. Chapela, L. E. Scriven and H. T. Davis, “Molecular dynamics for discontinuous potential. IV. Lennard-Jonesium”, *J. Chem. Phys.* 91, 4307–4313 (1989).
- [14] J. R. Elliott, “Optimized step potential models for *n*-alkanes and benzene”, *Fluid Phase Equilibria.* 194–197, 161–168 (2002).
- [15] M. P. Allen, D. Frenkel and J. Talbot, “Molecular dynamics simulation using hard particles”, *Comp. Phys. Rep.* 9, 302–353 (1989).
- [16] B. J. Alder and T. E. Wainwright, “Phase transition for a hard sphere system”, *J. Chem. Phys.* 27, 1208–1209 (1957).
- [17] I. Goldhirsch, “Rapid Granular Flows”, *Annu. Rev. Fluid Mech.* 35, 267–293 (2003).
- [18] H. D. Nguyen and C. K. Hall, “Phase diagrams describing fibrillization by polyalanine peptides”, *Biophys. J.* 87, 4122–4134 (2004).

- [19] O. Unlu et al., “Transferable Step Potentials for the Straight-Chain Alkanes, Alkenes, Alkynes, Ethers, and Alcohols”, *Ind. Eng. Chem. Res.* 43, 1788–1793 (2004).
- [20] B. J. Alder and T. E. Wainwright, “Studies in molecular dynamics. 1. General method”, *J. Chem. Phys.* 31, 459–466 (1959).
- [21] D. C. Rapaport, “Event Scheduling Problem in Molecular Dynamics Simulation”, *J. Comp. Phys.* 34, 184–201 (1980).
- [22] B. D. Lubachevsky, “How to simulate billiards and similar systems”, *Int. J. Comput. Phys.* 94, 255–283 (1991).
- [23] M. Marin, D. Risso and P. Cordero, “Efficient Algorithms for Many-Body Hard Particle Molecular Dynamics”, *J. Comp. Phys.* 109, 306–317 (1993).
- [24] H. Sigurgeirsson, A. Stuart and W.-L. Wan, “Algorithms for Particle-Field Simulations with Collisions”, *J. Comp. Phys.* 172, 766–807 (2001).
- [25] A. Donev, “Asynchronous Event-Driven Particle Algorithms”, *Simulation.* 85, 229–242 (2009).
- [26] Marcus N. Bannerman et al., “Collision statistics in sheared inelastic hard spheres”, *Phys. Rev. E.* 79, 041308 (2009).
- [27] Marcus N. Bannerman and Leo Lue, “Transport properties of highly asymmetric hard sphere mixtures”, *J. Chem. Phys.* 130, 164507 (2009).
- [28] M. N. Bannerman, J.E. Magee and L. Lue, “Structure and stability of helices in square-well homopolymers”, *Phys. Rev. E.* 80, 021801 (2009).
- [29] M. Marin and P. Cordero. “Hashing-Cell Combination for Boundless Space Event-Driven Molecular Dynamics ”. In: *8th Joint EPS-APS International Conference on Physics Computing*. Ed. by P. Borcherds and M. Bubak. World Scientific, 1996, pp. 315–318.
- [30] Alan T. Krantz, “Analysis of an efficient algorithm for the hard-sphere problem”, *TOMACS.* 6, 185–209 (1996).
- [31] A. Vrabecz and G. Tóth, “Simulation of binary hard-sphere systems with 1 : 5 and 1 : 10 size ratios”, *Mol. Phys.* 104, 1843–1853 (2006).
- [32] A. Donev, S. Torquato and F. Stillinger, “Neighbor list collision-driven molecular dynamics simulation for nonspherical hard particles. I. Algorithmic details”, *J. Comp. Phys.* 202, 737–764 (2005).
- [33] D. R. Jefferson, “Virtual time”, *TOPLAS.* 7, 404–425 (1985).
- [34] M. Marin and P. Cordero, “An empirical assessment of priority queues in event-driven molecular dynamics simulation”, *Comp. Phys. Comm.* 92, 214–224 (1995).
- [35] G. Paul, “A Complexity $O(1)$ priority queue for event driven molecular dynamics simulations”, *J. Comp. Phys.* 221, 615–625 (2007).

- [36] T. Pöschel and T. Schwager. *Computational Granular Dynamics*. New York: Springer, 2005.
- [37] R. Raman and D. S. Wise, “Converting to and from Dilated Integers”, *IEEE Trans. Comp.* 57, 567–573 (2008).
- [38] M. D. Adams and D. S. Wise, “Fast Additions on Masked Integers”, *ACM SIGPLAN Notices*. 41, 39–45 (2006).
- [39] H. C. Andersen, “Molecular dynamics simulations at constant pressure and/or temperature”, *J. Chem. Phys.* 72, 2384–2393 (1980).
- [40] D. Frenkel and J. F. Maguire, “Molecular dynamics study of the dynamical properties of an assembly of infinitely thin hard rods”, *Mol. Phys.* 49, 503–541 (1983).
- [41] R. H. Swendsen and J. Wang, “Replica Monte Carlo Simulation of Spin-Glasses”, *Phys. Rev. Lett.* 57, 2607–2609 (1986).
- [42] K. Erleben. *Module Based Design for Rigid Body Simulators*. Tech. rep. University of Copenhagen, 2002.
- [43] L. V. Woodcock, “Glass-Transistion in the Hard-Sphere Model and Kauzmann Paradox”, *Ann. N. Y. Acad. Sci.* 371, 274–298 (1981).
- [44] J. M. Haile. *Molecular Dynamics Simulation - Elementary Methods*. New York: Wiley-Interscience, 1997.
- [45] M. A. Hopkins and H. H. Shen, “A Monte Carlo solution for rapidly shearing granular flows based on the kinetic theory of dense gases”, *J. Fluid Mech.* 244, 477–491 (1992).
- [46] A. W. Lees and S. F. Edwards, “The Computer Study of Transport Processes Under Extreme Conditions”, *J. Phys. C.* 5, 1921–1929 (1972).
- [47] S. W. Smith, C. K. Hall and B. D. Freeman, “Molecular dynamics for polymeric fluids using discontinuous potentials”, *J. Comp. Phys.* 134, 16–30 (1997).
- [48] G. A. Bird. *Molecular gas dynamics and the direct simulation of gas flows*. Oxford: Oxford University Press, 1994.
- [49] J. Weidendorfer, M. Kowarschik and C. Trinitis. “Computational Science - ICCS 2004”. In: vol. 3038. Berlin: Springer-Verlag, 2004, pp. 440–447.
- [50] R. van Zon and J. Schofield, “Event-driven dynamics of rigid bodies interacting via discretized potentials”, *J. Chem. Phys.* 128, 154119 (2008).
- [51] M. Marin, “Event-driven hard-particle molecular dynamics using bulk-synchronous parallelism”, *Comp. Phys. Comm.* 102, 81–96 (1997).
- [52] S. Miller and S. Luding, “Event-driven molecular dynamics in parallel”, *J. Comput. Phys.* 193, 306–316 (2004).

CHAPTER
FIVE

HARD SPHERE EQUATIONS OF STATE

This chapter is in preparation for submission
Authors: M. Bannerman, L. Lue, L. V. Woodcock

THIS chapter was written in collaboration with Prof. Woodcock. Specifically, the WC1 equation of state presented here was originally proposed by Woodcock [1] before being revised upon in this work.

5.1 Introduction

Since van der Waals first modified the ideal gas equation to obtain his “second-virial” equation-of-state for the dilute gas of hard spheres (HS) [2], there have been many predictions of the hard-sphere equation-of-state. Theoretical equations, while yielding some physical insight into the origin, have all proven to be inaccurate when tested against computer simulation data. An essential starting point for an ultimate equation-of-state of the hard-sphere fluid is the known virial series. The expansion in powers of density for the fluid equation of state of hard spheres is

$$Z_{virial} = 1 + \sum_n b_n \rho^{n-1} \quad (5.1.1)$$

where $Z = p / \rho k_B T$ is the compressibility factor, p is the pressure, k_B is the Boltzmann constant, ρ is the number density, and b_n is the n th virial coefficient. Exact expressions for the third and fourth virial coefficients were derived analytically by Boltzmann, and values for the higher virial coefficients have now been computed numerically up to the tenth [2–14].

Despite these efforts, the virial expansion truncated at the tenth coefficient is still not sufficient for estimates of the pressure when approaching the freezing transition. Many methods have been used to attempt to estimate contributions from higher virials and Padé approximants [3] are by far the most common method. Padé approximants utilise a rational polynomial function to reproduce the known virials exactly and provide a closed

estimate for the remaining terms. Several types of approximants, including a recent attempt which includes all ten calculated virials [14], have also been used to attempt to determine the radius of convergence of the virial series. A Padé approximant was also at the heart of the original derivation of the ubiquitous Carnahan-Starling [15] equation of state.

The predictions of these approximate methods cannot be tested without comparing to molecular dynamics (MD) simulation results of very large systems [16–18]. Recently, Kolafa et al. [12] performed a comparison using simulations of 13 500 spheres and studied the errors introduced by the periodic boundary conditions and simulation ensemble.

The recent determination of the virial coefficients to higher accuracy and the calculation of the tenth virial by Clisby and McCoy [14] have prompted further developments on the equations of state (e.g., see Ref. [19]), and there is a need for new, higher accuracy (MD) data to test these approximate equations of state. Recently, a new event-driven molecular dynamics package called DYNAMO (see Chapter 4) has been developed. This package allows the simulation of previously unattainable system sizes with high accuracy. Results obtained from molecular dynamics simulations of hard spheres will be used to compare predictions from several equations of state including methods which avoid approximant methods. In Section 5.2 the virial series results are discussed before outlining several equations of state for testing. Section 5.3 details the simulation method and the systems studied, Section 5.4 presents and discusses the results of the simulations. Finally, the main findings of this work are summarized in Section 5.5.

5.2 Equation of State

Computed numerical values of the virial coefficients are often presented as a dimensionless ratio of $b_n/b_2^{(n-1)}$ where b_2 is the second virial coefficient, first determined by van der Waals to be $b_2 = 2\pi\sigma^3/3$ where σ is the hard-sphere diameter. Values for all the known virial coefficients from Clisby and McCoy [13, 14] are given in Table 5.1. Also given in Table 5.1 are the values of the known virial coefficients when expressed in powers of the density relative to crystal close packing $\rho_0 = 2^{-1/2}\sigma^{-3}$ (i.e., $B_n = b_n \rho_0^{n-1}$). Plotting the difference between the virials (see Fig. 5.1), it was found that the last three differences conform to an exponential form. The fitted linear expression of Fig. 5.1 has a correlation of 0.99999 with the virial data. Assuming that this expression can be extrapolated to infinite n , the virial series may be closed as follows

$$Z_{WC2} = 1 + \sum_{n=2}^m B_n (\rho/\rho_0)^{n-1} + (\rho/\rho_0)^m \left[\frac{B_m}{1 - \rho/\rho_0} - \frac{e(B_{m+1} - B_m) - (\rho/\rho_0)(B_m - B_{m-1})}{(\rho/\rho_0 - e)(1 - \rho/\rho_0)^2} \right] \quad (5.2.1)$$

Table 5.1: Known virial coefficients of the hard sphere fluid [13, 14]

n	b_n/b_2^{n-1}	B_n	$B_n - B_{n-1}$
2	1	2.961921	—
3	0.625	5.483111	2.52119
4	0.28694950	7.456345	1.973234
5	0.11025210	8.485568	1.029223
6	0.03888198	8.863719	0.378151
7	0.01302354	8.793670	-0.070049
8	0.00418320	8.366104	-0.427566
9	0.00130940	7.756405	-0.609699
10	0.00040350	7.079543	-0.676862

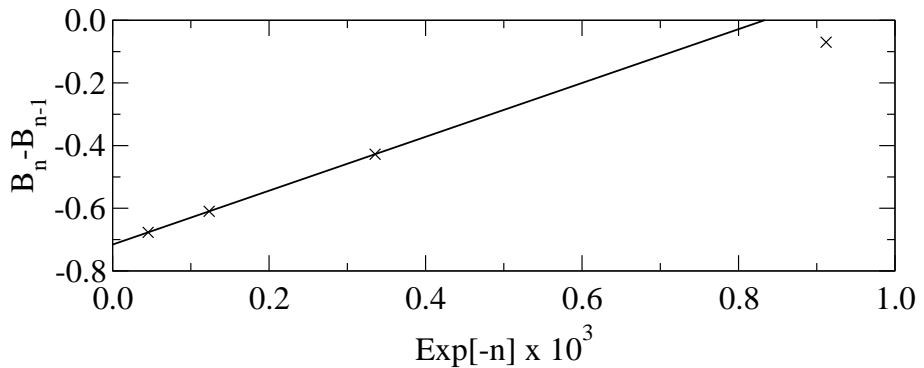


Figure 5.1: The differences between the reduced virial coefficients for a hard sphere fluid against the virial number. The solid line is a linear fit to the last 3 data points.

With this form of the closure the highest required virial is B_9 ($m = 8$), and the results are identical to the $m = 9$ values. Equation (5.2.1) also predicts that the virial coefficients will eventually go negative as postured by Clisby and McCoy [14]; however, there are no terms oscillating in sign which are significant in higher dimensions. Following the extrapolation of Eq. (5.2.1), the virial coefficients beyond the 19th virial are all negative. The virial coefficients predicted by Eq. (5.2.1) are remarkably close to the predictions of the Padé approximants suggested by Clisby and McCoy [14]. These Padé approximants were fitted to the first ten virials and are given by

$$Z_{[5,4]} = \frac{1 + 1.68408 \rho_* + 2.04682 \rho_*^2 + 1.30438 \rho_*^3 + 0.572217 \rho_*^4 + 0.113611 \rho_*^5}{1 - 0.410313 \rho_* + 0.164643 \rho_*^2 - 0.551756 \rho_*^3 + 0.236726 \rho_*^4} \quad (5.2.2a)$$

$$Z_{[4,5]} = \frac{1 + 1.06812 \rho_* + 0.91568 \rho_*^2 + 0.334868 \rho_*^3 + 0.0676832 \rho_*^4}{1 - 1.02627 \rho_* + 0.323543 \rho_*^2 - 0.165385 \rho_*^3 + 0.111142 \rho_*^4 - 0.0220673 \rho_*^5} \quad (5.2.2b)$$

where $\rho_* = \rho \sigma^3$ is the reduced density. The closure of Eq. (5.2.1) will also be contrasted against its predecessor [1], which assumed a limiting linear form of $B_n - B_{n-1}$ above $n > 9$ and utilised the Padé data of Eqs. (5.2.2) for the higher virials, resulting in a

closure of

$$Z_{WC1} = 1 + \sum_{n=2}^m B_n (\rho/\rho_0)^{n-1} + (\rho/\rho_0)^m \left[\frac{B_m}{1 - \rho/\rho_0} - \frac{A_2}{(1 - \rho/\rho_0)^2} \right] \quad (5.2.3)$$

where the parameter $A_2 = 0.68219$ was the fitted intercept and $m = 10$. This equation-of-state is a more convenient form of Eq. (4) in Ref. [1]; a simple derivation of this equation is also given in Ref. [20].

We will also compare against the equations of state determined by Kolafa et al. [12] by fitting to both the known virials and their accurate MD data, given by

$$\begin{aligned} Z_{KLM\ low} = & 1 + 4x + 6x^2 + 2.3647684x^3 - 0.8698551x^4 + 1.1062803x^5 \\ & - 1.2105096x^6 + 1.1356305x^7 - 0.5947886x^8 + 0.0849805x^{12} \end{aligned} \quad (5.2.4a)$$

$$\begin{aligned} Z_{KLM\ high} = & 1 + 4x + 6x^2 + 2.3647684x^3 - 0.8698551x^4 + 1.1062803x^5 \\ & - 1.095049x^6 + 0.637614x^7 - 0.2279397x^{10} + 0.1098948x^{14} \\ & - 0.00906797x^{22} \end{aligned} \quad (5.2.4b)$$

where $x = \phi/(1 - \phi)$ and $\phi = \rho \sigma^3 \pi/6$ is the packing fraction. Finally, for historical reasons we will also compare against the ubiquitous Carnahan-Starling equation of state [15], given by

$$Z_{CS} = \frac{1 + \phi + \phi^2 - \phi^3}{(1 - \phi)^3} \quad (5.2.5)$$

This simple expression is extremely popular and provides excellent predictions with little complexity. In the next section, the details of the simulations are outlined.

5.3 Simulation Details

Molecular dynamics simulations of collections of hard spheres were performed to generate pressure data for comparison. The algorithm used is discussed in detail in Chap. 4, and only the specifics of the simulations will be related here. The pressure was calculated using the collision rate formula [16]

$$Z_{MD} = 1 + \frac{\gamma(N) \sqrt{m \sigma^2 \pi \beta}}{dN} \frac{N_{coll}}{t} \quad (5.3.1)$$

where γ is a correction factor to convert the pressure calculated in the *NVEM* ensemble, where M is the total momentum in the system, to the value for the *NVT* ensemble. The factor γ is given by

$$\gamma(N) = \frac{\Gamma[(3(N-1)+1)/2]}{\Gamma[3(N-1)/2](3N/2)^{1/2}} \quad (5.3.2)$$

Table 5.2: Simulation conditions including the number of particles in Face Centred Cubic (N_{FCC}) and Simple Cubic (N_{SC}) starting configurations, number of simulations performed (N_{run}), number of collisions executed per simulation ($N_{coll}^{(R)}$), and the length of equilibration run ($N_{coll}^{(E)}$).

System	N_{FCC}	N_{SC}	N_{run}	$N_{coll}^{(R)}$	$N_{coll}^{(E)}$
1	1 098 500	1 124 864	5	$800 N$	$200 N$
2	108 000	125 000	5	10^9	10^8

where Γ is the Gamma function. There are a further two sources of error which will cause the MD results to differ from the theoretical equation of states. There is the ensemble error caused by the microcanonical ensemble suppressing fluctuations possible in the grand canonical ensemble. Secondly, the error arising from the periodic boundary conditions, necessary to simulate a bulk fluid element. Kolafa et al. [12] discusses both of these terms for their systems of $N = 13\,500$ hard spheres. The ensemble error, to leading order in the system size, requires derivatives of the equation of state to compute. The error introduced by the use of periodic boundary conditions can be estimated using radial distribution data. Following the analysis of Kolafa et al. [12] these errors are found to be overshadowed by the uncertainty in the simulation results and are very small for the largest system studied here.

To generate accurate values for the equation of state of hard sphere fluids, a recently developed simulation package called DYNAMO was utilised (see Chap. 4). Two separate runs were performed and the details of each are provided in Table 5.2. Error estimates are provided by the standard deviation of the reported values between each simulation run. The simulation results will be discussed in the following section.

5.4 Results and Discussion

The complete molecular dynamics results are summarised in Table 5.3 including estimates for the error. All systems in the metastable fluid branch between the fluid-solid transition densities [21] $0.943 \geq \rho \sigma^3 \geq 1.04$ were stable and showed no indications of freezing over the full timescale of the simulation. This is remarkable given the system size studied and the proximity of the $\rho \sigma^3 = 0.995$ to the stable solid.

The predictions of the truncated virial series and the Carnahan-Starling equations of state are remarkably good when directly compared against the MD data (see Fig. 5.2). The only apparent deviations are in the truncated virial series in the metastable branch. To allow accurate comparisons of the equations of state for the fluid and metastable branch the results are replotted in Fig. 5.3. The parameter plotted is the relative deviation of the compressibility from the MD results given by $\Delta Z = (Z_{MD} - Z)/Z_{MD}$. The truncated virial series begins to noticeably deviate from the MD results at a density of $\rho \sigma^3 = 0.5$ where it consistently under-predicts the compressibility. The Carnahan-Starling EOS is

Table 5.3: Simulation values for the hard sphere equation of state. Superscripts indicate the initial condition ((F)CC or (S)C) and system (see Table 5.2). Values in parenthesis are the standard deviations of the last two digits. State points between horizontal lines are in the metastable fluid section and the $\rho \sigma^3 = 1$ state point is in the metastable solid.

$\rho \sigma^3$	Z_{MD}	$\rho \sigma^3$	Z_{MD}
0.100^{F1}	1.2397243(69)	0.850^{S2}	9.11856(14)
0.150^{F1}	1.3859499(44)	0.875^{S2}	9.89890(38)
0.200^{F1}	1.5536109(77)	0.900^{F1}	10.76295(36)
0.250^{F1}	1.746288(31)	0.900^{S2}	10.76250(29)
0.300^{F1}	1.968242(26)	0.910^{S1}	11.13401(21)
0.350^{F1}	2.224609(29)	0.920^{S1}	11.52173(17)
0.400^{F1}	2.521648(39)	0.925^{S2}	11.721837(60)
0.450^{F1}	2.866821(48)	0.930^{S1}	11.92585(24)
0.500^{F1}	3.269361(52)	0.940^{S1}	12.34879(59)
0.550^{F1}	3.740700(47)	0.950^{S2}	12.79055(27)
0.600^{F1}	4.29494(10)	0.950^{S1}	12.79133(40)
0.650^{F1}	4.949678(25)	0.960^{S1}	13.25395(94)
0.675^{S2}	5.32149(16)	0.970^{S1}	13.73966(88)
0.700^{F1}	5.72686(15)	0.975^{S2}	13.9912(16)
0.700^{S2}	5.727007(39)	0.980^{S1}	14.24832(74)
0.725^{S2}	6.17006(17)	0.990^{S1}	14.7843(12)
0.750^{F1}	6.65521(25)	0.995^{S1}	15.06266(92)
0.750^{S2}	6.655057(70)	1.000^{F2}	10.24903(56)
0.775^{S2}	7.18656(33)	1.100^{F2}	13.26711(23)
0.800^{F1}	7.76997(27)	1.200^{F2}	19.46835(24)
0.800^{S2}	7.76975(24)	1.300^{F2}	36.75166(44)
0.825^{S2}	8.41188(18)	1.400^{F2}	298.0576(80)
0.850^{F1}	9.11867(26)	1.410^{F2}	1006.4503(96)

accurate (within 0.3%) and under-predicts the compressibility for all densities studied. The deviation of the Carnahan-Starling EOS also displays a minimum around the freezing density of the fluid. The Padé approximants of Clisby and McCoy [14] both perform significantly better but the $Z_{[5,4]}$ predictions are by far the superior of the two. The Z_{WC2} EOS is an improvement on its predecessor, Z_{WC1} , but the $Z_{[5,4]}$ Padé approximant fares better with roughly the same complexity. Interestingly the $Z_{[5,4]}$ and Z_{WC2} EOS appear to limit to the same form at higher densities. Finally, the EOS of Kolafa et al. [12] gives superb predictions which agree with the simulation results within the estimated errors. As this EOS is a semi-empirical expression, it serves as a comparison of the present MD simulation results against the accurate simulations of Kolafa et al. and highlights the small system size dependency at these state points.

The results for the solid branch were compared against the EOS of Speedy [17] for hard sphere FCC solids, given by

$$Z_{Speedy} = \frac{3}{1 - \rho/\rho_0} - A \frac{\rho/\rho_0 - B}{\rho/\rho_0 - C} \quad (5.4.1)$$

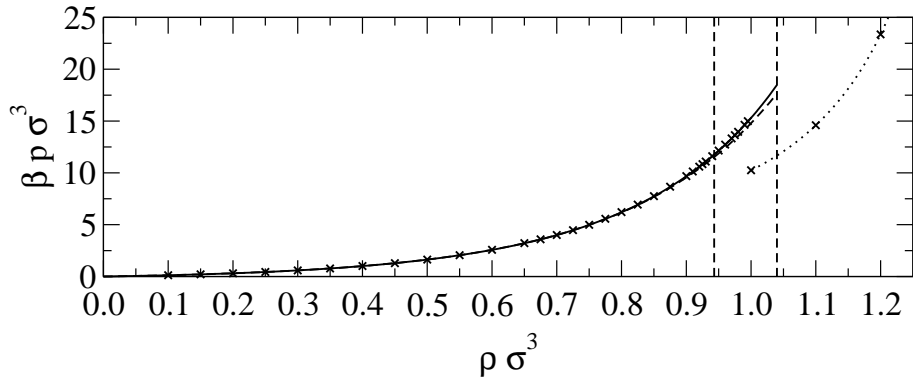


Figure 5.2: Pressure versus density for the hard sphere system. The dashed vertical lines are at the approximate freezing and melting points. The solid line are the predictions of the Carnahan-Starling EOS (see Eq. (5.2.5)), the dashed line is the truncated virial series (see Eq. (5.1.1)) and the dotted line is Speedy's EOS for the solid (see Eq. (5.4.1)).

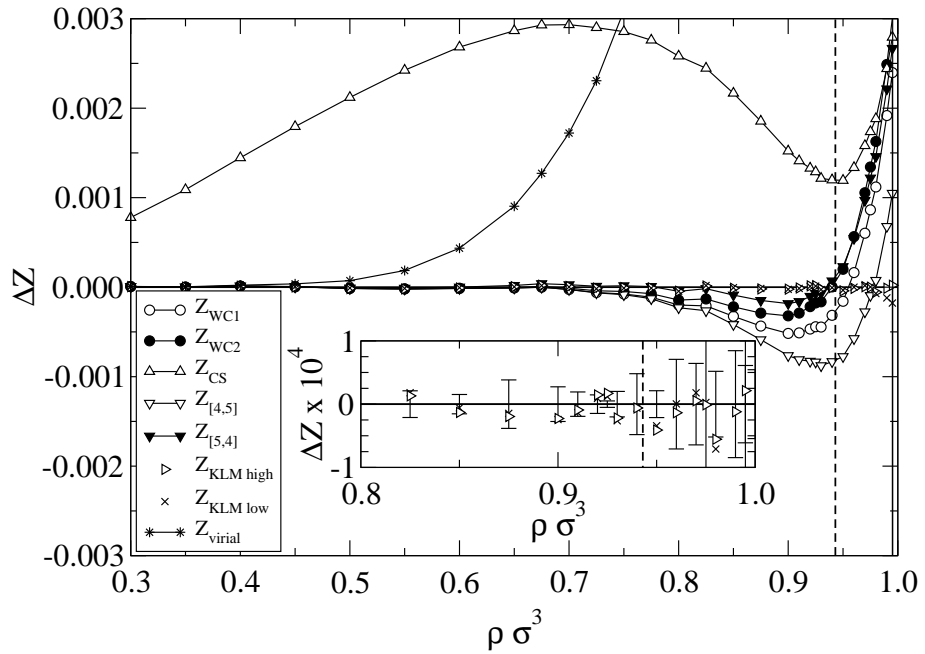


Figure 5.3: The difference between the simulation results for the compressibility and the predictions of the equations of state (Eqs. (5.2.1), (5.2.2), (5.2.3) and (5.2.5)) for the hard sphere fluid and metastable fluid region. Inset is a close-up of the high density for the Kolafa et al. [12] EOS (Eqs. (5.2.4)) including errors in the molecular dynamics results. The dashed vertical line indicates the approximate freezing density for the hard sphere fluid.

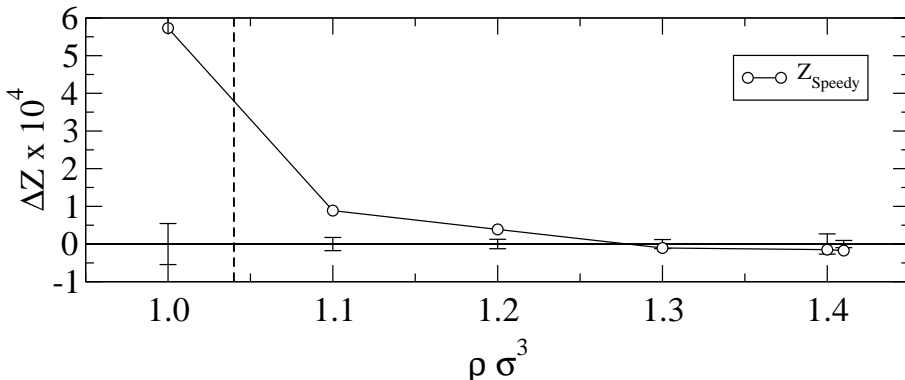


Figure 5.4: The difference between the simulation results for the compressibility and the predictions of the equations of state (Eqs. (5.2.1), (5.2.2), (5.2.3) and (5.2.5)) for the hard sphere solid. The vertical dashed line indicates the approximate melting point for the hard sphere crystal. Standard deviations in the molecular dynamics results are of the same magnitude as the symbol size.

where $A = 0.5921$, $B = 0.7072$ and $C = 0.601$ are empirical constants originally obtained by fitting to MD data. The equation performs remarkably well at high densities due to the inclusion of the exact limiting free volume EOS form $\lim_{\rho \rightarrow \infty} Z \rightarrow 3/(1 - \rho_0)$. At lower densities the equation is accurate but is showing signs of difficulties when approaching the solid metastable branch. A straightforward regression of the equation of Eq. (5.4.1) from the original coefficients to the current data yields revised coefficients of $A = 0.620735$, $B = 0.708194$, and $C = 0.591663$. The EOS predicted from these revised coefficients is indistinguishable from the MD simulation results for the densities studied, even into the metastable branch.

5.5 Conclusions

Molecular dynamics simulations were performed to generate accurate compressibility data for the testing of various equations of state. The accurate results of Kolafa et al. [12] are validated against the results reported here through comparison against their suggested empirical equations of state. This semi-empirical equation is the most accurate tested here. The Padé approximants of Clisby and McCoy [14] are excellent, but the [5,4] variant is preferable to the [4,5] form. The WC2 equation of state, which uses an exponential form to close the series, performs remarkably well given the simple nature of the closure. The EOS of Speedy [17] is accurate in the solid branch and slightly revised coefficients are suggested which improve the predictions to inside the metastable solid branch.

5.6 References

- [1] L. V. Woodcock. *Virial Equation-of-State for Hard Spheres*. 2007. arXiv: 0801 . 4846v3.
- [2] M. N. Rosenbluth and A. W. Rosenbluth, “Further results on Monte Carlo equations of state”, *J. Chem. Phys.* 22, 881–884 (1954).
- [3] F. H. Ree and W. G. Hoover, “Fifth and Sixth Virial Coefficients for Hard Spheres and Hard Disks”, *J. Chem. Phys.* 40, 939–950 (1964).
- [4] F. H. Ree and W. G. Hoover, “7th virial coefficients for hard spheres and hard disks”, *J. Chem. Phys.* 46, 4181–4197 (1967).
- [5] K. W. Kratky, “Fifth virial coefficient for a system of hard disks”, *Physica A*. 85, 607–615 (1976).
- [6] K. W. Kratky, “Fifth to tenth virial coefficients of a hard-sphere fluid”, *Physica A*. 87, 584–600 (1977).
- [7] K. W. Kratky, “A new graph expansion of virial coefficients”, *J. Stat. Phys.* 27, 533–551 (1982).
- [8] K. W. Kratky, “Overlap graph representation of B6 and B7”, *J. Stat. Phys.* 29, 129–138 (1982).
- [9] E. J. J. van Rensburg and G. M. Torrie, “Estimation of multidimensional integrals: is Monte Carlo the best method?”, *J. Phys. A*. 26, 943–953 (1993).
- [10] E. J. J. van Rensburg, “Virial coefficients for hard discs and hard spheres”, *J. Phys. A*. 26, 4805–4818 (1993).
- [11] A. Y. Vlasov, X. M. You and A. J. Masters, “Monte-Carlo integration for virial coefficients re-visited: hard convex bodies, spheres with a square-well potential and mixtures of hard spheres”, *Mol. Phys.* 100, 3313–3324 (2002).
- [12] J. Kolafa, S. Labik and A. Malijevsky, “Accurate equation of state of the hard sphere fluid in stable and metastable regions”, *PCCP*. 6, 2335–2340 (2004).
- [13] N. Clisby and B. N. McCoy, “Negative Virial Coefficients and the Dominance of Loose Packed Diagrams for D-Dimensional Hard Spheres”, *J. Stat. Phys.* 114, 1361–1392 (2004).
- [14] N. Clisby and B. N. McCoy, “Ninth and Tenth Order Virial Coefficients for Hard Spheres in D Dimensions”, *J. Stat. Phys.* 122, 15–57 (2006).
- [15] N. F. Carnahan and K. E. Starling, “Equation of state for nonattracting rigid spheres”, *J. Chem. Phys.* 51, 635–636 (1969).
- [16] J. J. Erpenbeck and W. W. Wood, “Molecular Dynamics Calculations of the Hard-Sphere Equation of State”, *J. Stat. Phys.* 35, 321–340 (1984).

- [17] R. J. Speedy, “Pressure and entropy of hard-sphere crystals”, *J. Phys.:Condens. Matter.* 10, 4387–4391 (1998).
- [18] N. G. Almarza, “A cluster algorithm for Monte Carlo simulation at constant pressure”, *J. Chem. Phys.* 130, 184106 (2009).
- [19] J.-W. Hu and Y.-X. Yu, “Prediction and Refinement of High-Order Virial Coefficients for a Hard-Sphere System”, *Chin. Phys. Lett.* 26, 086404 (2009).
- [20] L. V. Woodcock. *Virial equation-of-state for the hard-disk fluid*. 2008. arXiv: 0804.0679.
- [21] L. L. Lee. *Molecular thermodynamics of nonideal fluids*. Butterworths, 1988.

CHAPTER
SIX

COLLISION STATISTICS IN SHEARED INELASTIC HARD SPHERES

This chapter has been published in Physical Review E (see Appendix A).
Authors: M. Bannerman, T. Green, P. Grassia, L. Lue

THIS work was begun by T. Green in 2002, who performed the initial simulations and writing while under the supervision of Dr L. Lue and, later, Dr P. Grassia. The work original to this PhD thesis is described below.

It was discovered that the simulations already performed were of a system size where the system began to cluster, compromising the assumption of a homogeneous system. Using the simulator developed in this work, the simulations were rerun under rectangular boundary conditions to avoid this clustering. The Enskog theory results were calculated using both direct simulation Monte-Carlo and the approximate theory of Montanero et al. [1]. With the inclusion of the theoretical predictions and updated simulation data, the paper underwent a significant rewrite before submission to Physical Review E.

6.1 Introduction

In rapid granular flows [2, 3], the mean flight time of the particles in the granular material may be large compared to the contact time between particles. Inter-particle interactions are modelled as “collisions,” which play a key role in transferring momentum and other properties through the system. Granular materials in this flow regime can then be represented by a collection of inelastic hard spheres [4, 5].

The simplicity of the inelastic hard sphere model lends itself well to theoretical analysis. In particular, the methods developed for the kinetic theory of equilibrium gases have been applied to rapidly sheared inelastic hard sphere systems. The seminal paper by Lun et al. [6] marked the start of “complete” kinetic theories capable of predicting both the kinetic and collisional properties. The Boltzmann equation has featured predominantly in the theory of granular gases due to its simpler form (e.g., see Ref. [7]); however, the most successful molecular kinetic theory to date is the revised Enskog theory [8], an extension to the Boltzmann equation for dense systems. Enskog theory assumes uncorrelated

particle velocities and currently relies on a static structural correlation factor from elastic fluids [9]. Approximate theories beyond the Enskog theory, such as ring theory [10], have been developed and applied to granular systems, however, due to their complexity, their use has been limited (e.g., cooling, rare granular gases).

Common to most kinetic theory solutions is the assumption of a steady state, spatially uniform distribution function. Provided scale separation exists, as is the case for elastic fluids, fluctuations from this steady state can be accounted for using the Chapman-Enskog expansion [11]. To solve the Enskog equation, approximations typically begin by taking moments of the kinetic equation with respect to the density, velocity, and products of the velocity. These moment equations are used to solve for the parameters of an expansion or model. Typically, only terms up to the granular “temperature”, or isotropic stress and rotation terms [12], are included as field variables. Anisotropic stresses can still be predicted from such a theory [13]; indeed, attempts have been made to include the full second order velocity moment [14] as a hydrodynamic variable to improve theoretical predictions.

Grad’s method [15] solves Enskog theory using an expansion of the distribution function about a reference state. This has been applied to poly-disperse granular systems [5] and, unlike perturbative solutions, does not require assumptions on the strength of the shear. Kinetic models are a powerful method of generating simplified kinetic equations which retain key features of the original. Montanero et al. [1] solved an improved Bhatnagar-Gross-Krook (BGK) kinetic model [16, 17] for inelastic systems. The improved BGK model approximates the collisional term of the kinetic equation using the first two velocity moments, which correspond to the collisional stress and energy loss, and a general relaxation term. This leads to a simplified kinetic equation. The solution in the low dissipation limit is particularly attractive, as it provides estimates for the system properties without requiring numerical solution and compares favourably to Direct Simulation Monte Carlo (DSMC) results.

DSMC [18] is a numerical simulation technique to directly solve the Boltzmann equation without requiring further approximations. This can then be used to rapidly test solutions of the kinetic equation. The method has already been extended to the Enskog equation for homogeneously sheared inelastic systems [1, 19, 20].

While kinetic theories do offer insight into the behavior of granular materials, they are necessarily approximate. The Boltzmann and Enskog kinetic theories do not include velocity or dynamic structural correlations. Ring theory [10] is capable of including particle correlations; however, further approximations are required to make the resulting theory tractable. These correlations are present in moderately dense to dense systems of elastic particles, but they are enhanced by the clustering in inelastic systems [21, 22]. The failure of Boltzmann and Enskog theories at high densities is therefore expected, even for elastic hard sphere systems. On the other hand, non-equilibrium molecular dynamics (NEMD) simulations [4, 23] can, in principle, give “exact” results for driven inelastic-hard-sphere systems [24, 25]. These simulations can be used to validate kinetic theories against the

underlying model. Initial studies of sheared granular systems used moving boundaries [4, 26], such as rough walls, to introduce energy into the system. Due to the computational limitations, the wall separation is typically of the order of a few particle diameters, and wall effects dominate the simulation results. For large system sizes, shear instability is observed [27]. Consequently, the results for wall driven simulations are strongly dependent on system size.

Another manner to introduce shear in non-equilibrium molecular dynamics is the Lees-Edwards [28] or “sliding brick” boundary conditions. Simulations of inelastic hard-sphere systems using Lees-Edwards boundary conditions [23, 29–32] lessen the influence of wall effects, by elimination of the surface of the system, but these simulations still introduce shear in an inhomogenous manner, which leads to clustering instabilities [33] for larger systems.

While there are many interesting similarities between elastic hard-sphere fluids and driven inelastic hard-sphere systems, there are key differences. One is the tendency of inelastic hard spheres to form clusters and patterns, while elastic hard sphere fluids tend to remain isotropic. Another example is the velocity distribution. The velocity of elastic hard spheres is governed by the Maxwell distribution, which is isotropic and Gaussian. The velocity distribution of flowing inelastic hard spheres is, in general anisotropic [34], and can show significant deviations from the Gaussian distribution, especially when there is clustering.

In this work, we examine the properties of sheared inelastic-hard-sphere systems using non-equilibrium event-driven molecular dynamics simulations with the SLLOD algorithm combined with Lees-Edwards boundary conditions. Part of the purpose of this work is to investigate, at a particle level, the differences between the behavior of inelastic and elastic (equilibrium) hard sphere systems. Another purpose of this work is to provide simulation data which can be used to test kinetic theory predictions for the properties of these systems. A previous study by Montanero et al. [35] has already compared 2D and 3D simulations of binary inelastic hard spheres against DSMC simulations of Enskog theory. They find good agreement over the range of mass ratio, size ratio and inelasticity studied; however, the clustering instability present in systems of large numbers of highly inelastic particles appears to limit the range of inelasticity studied. As mentioned previously, kinetic theories for sheared granular materials are typically developed for the case where the system is spatially uniform and homogeneously sheared. One of the difficulties with comparing the predictions of the kinetic theory with the simulation data for sheared granular materials is the formation of clusters, which makes comparison between the two problematic. As a consequence, care is taken in this work to ensure that the systems remain homogeneous and strongly inelastic systems can be accessed. In these simulations, we investigate the collision statistics, such as velocity distributions, collision angles, time between collisions and mean free paths, of sheared inelastic hard spheres. In addition, we examine the variation of various bulk properties of the system, such as the viscosity, mean

kinetic energy, and stress, with the packing fraction and coefficient of restitution of the particles. We also investigate the correlations between the collisions, which are neglected in most kinetic theory approaches. The remainder of this paper is organized as follows. In Section 6.2, we describe the details of the granular dynamics simulations. In Section 6.3, we describe the details of the DSMC simulations. In Section 6.4, we present the results of our simulation work, including a comparison with the predictions of Enskog theory. Finally, a summary of the main findings is provided in Section 6.5.

6.2 Simulation Details

Non-equilibrium granular dynamics simulations were performed on systems of inelastic hard spheres of diameter σ and mass m . The system is sheared in the y -plane in the x -direction with a constant strain rate of $\dot{\gamma}$ using the SLLOD algorithm [36]. In this method, shear is applied through the use of the Lees-Edwards sliding brick boundary conditions [28, 36] and the velocity is transformed relative to a linear velocity profile. The equations of motion are

$$\frac{d\mathbf{r}_i}{dt} = \bar{\mathbf{v}}_i + y_i \dot{\gamma} \hat{\mathbf{e}}_x \quad (6.2.1)$$

$$\frac{d\bar{\mathbf{v}}_i}{dt} = \frac{\mathbf{F}_i}{m} - \bar{v}_{y,i} \dot{\gamma} \hat{\mathbf{e}}_x \quad (6.2.2)$$

where \mathbf{F}_i is the force acting on particle i , \mathbf{r}_i is the position of particle i , $\bar{\mathbf{v}}_i$ is the so called peculiar velocity of particle i , y_i is the y -coordinate of particle i , $\bar{v}_{y,i}$ is the y -component of the peculiar velocity of particle i , $\hat{\mathbf{e}}_x$ is a unit vector pointing in the positive x -direction, and $\dot{\gamma}$ is the strain rate.

The peculiar velocity of a particle i is defined as the difference between its lab velocity \mathbf{v}_i and the local streaming velocity (the velocity of the local streamline). For simple shear, it is given by the linear transformation

$$\bar{\mathbf{v}}_i = \mathbf{v}_i - y_i \dot{\gamma}_i \hat{\mathbf{e}}_x$$

The peculiar velocity is related to the dispersion of the particles from the average streamlines of the flow. The SLLOD equations of motion are particularly convenient as the peculiar velocity is naturally recovered without the need for a separate co-ordinate transformation. They allow the possibility of thermostating the system [37] and the study of time dependent shear flows.

In a hard-sphere system, the spheres do not experience any force between collisions. The equations of motion can then be solved analytically for the trajectories of the spheres between collisions. The evolution of the position and peculiar velocity of particle i in the

system between collisions is

$$\begin{aligned}\mathbf{r}_i(t) &= \mathbf{r}_i(t_0) + [\bar{\mathbf{v}}_i(t_0) + y_i(t_0)\dot{\gamma}\hat{\mathbf{e}}_x](t - t_0) \\ &= \mathbf{r}_i(t_0) + \mathbf{v}_i(t_0)(t - t_0) \\ \bar{\mathbf{v}}_i(t) &= \bar{\mathbf{v}}_i(t_0) - \bar{v}_{y,i}(t_0)\dot{\gamma}(t - t_0)\hat{\mathbf{e}}_x\end{aligned}\quad (6.2.3)$$

When a particle undergoes a collision, it experiences an impulse which alters its velocity. These collisions are instantaneous and only occur between pairs of spheres (i.e., there are no three or higher body collisions). The inelasticity of the hard spheres is characterized by the coefficient of restitution α . This is defined through the amount of kinetic energy ΔE lost on collision

$$\Delta E = \frac{m}{4}(1 - \alpha^2) (\hat{\mathbf{r}}_{ij} \cdot \mathbf{v}_{ij})^2 \quad (6.2.4)$$

where \mathbf{v}_i is the velocity of particle i immediately before collision, $\mathbf{v}_{ij} = \mathbf{v}_i - \mathbf{v}_j$, and $\hat{\mathbf{r}}_{ij} = \mathbf{r}_{ij}/|\mathbf{r}_{ij}|$ is the unit vector pointing from the center of particle j to the center of particle i .

Each collision preserves the total momentum of the particles involved; therefore, the change of velocities for a colliding pair of spheres i and j is given by

$$\begin{aligned}\mathbf{v}'_i &= \mathbf{v}_i - \frac{1}{2}(1 + \alpha) (\hat{\mathbf{r}}_{ij} \cdot \mathbf{v}_{ij}) \hat{\mathbf{r}}_{ij} \\ \mathbf{v}'_j &= \mathbf{v}_j + \frac{1}{2}(1 + \alpha) (\hat{\mathbf{r}}_{ij} \cdot \mathbf{v}_{ij}) \hat{\mathbf{r}}_{ij}\end{aligned}\quad (6.2.5)$$

where the primes denote post collision values of the particle velocities.

The coefficient of restitution α is, in general, a function of the relative velocity on collision. Viscoelastic models that incorporate this have been very successful in describing real systems such as steel spheres [38]. A common approximation in kinetic theory is to assume a constant coefficient of inelasticity, as this greatly simplifies the collision integrals while the basic physics is not significantly altered. A constant coefficient of restitution is used in this work to facilitate comparison against kinetic theory results.

One concern for a system with a constant coefficient of restitution is the phenomenon of inelastic collapse, where an infinite number of collisions occur between several spheres in a finite interval of time. Event-driven simulations will fail in the event of a single collapse event. In two dimensional, freely cooling, inelastic hard sphere systems under [39] inelastic collapse with coefficient of restitution as high as 0.59.

Inelastic collapse is rare in sheared systems [40] and is increasingly rare in higher dimensions; however, a near collapse situation can still cause a simulation to break down if the machine precision is not sufficiently high to resolve a rapid series of successive collisions. In the simulations performed in this work, no partial or full collapse events were found, even for dense and highly inelastic systems.

The simulation algorithm that we employ is a generalization of the standard event-

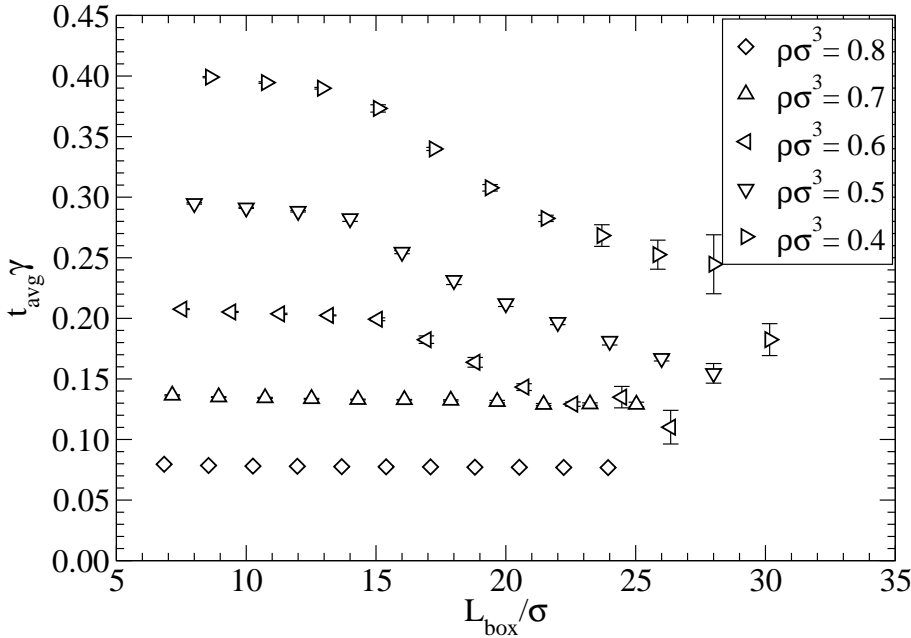


Figure 6.1: The system size dependence of the mean free time between collisions t_{avg} for simulations of a sheared, inelastic hard-sphere system with $\alpha = 0.4$ in a cubic box with sides of length L_{box} . The number of particles is $N = 256$ in the smallest system and $N = 10,976$ in the largest.

driven molecular dynamics algorithm for hard spheres [41] (see Ref. [42]). The main modifications are the use of the sliding brick boundary conditions [28] and the SLLOD equations of motion.

Unlike the elastic hard sphere system, the inelastic hard-sphere system has no intrinsic time scale. The applied strain rate $\dot{\gamma}$ sets the time scale of the system. Therefore, there are only two relevant dimensionless parameters: the density $\rho\sigma^3$ and the coefficient of restitution α . In this work, the density is varied from $\rho\sigma^3 = 0.4$ to 0.9, and the coefficient of restitution is varied from $\alpha = 0.4$ to 0.9.

Because the shear is imposed through the boundary conditions, the strain rate is only fixed at two points, separated by the entire height of the simulation box. In low density systems with large numbers of particles, clustering occurs [27]. This leads to a local variation of the strain rate in the system, and, consequently, the system will not be homogeneously sheared. At the onset of clustering, the size dependence of the system properties changes from the typical N^{-1} scaling to a different behavior. To illustrate this, the mean free time of sheared inelastic-hard-spheres with $\alpha = 0.4$ is shown in Fig. 6.1. These simulations were performed in a cubic simulation box where the system size was varied while holding the density constant. The “break” in the curves for the lower densities indicates the presence of cluster formation in the larger systems. The same general behavior manifests in all system properties and is relatively easy to detect.

Kinetic theory studies of sheared inelastic systems typically assume that the system is homogeneous and uniformly sheared, with a linear velocity profile. This makes the comparison between granular dynamics simulations and the kinetic theory problematic.

To allow comparison with these theories, we ensure that the systems remain homogeneous during the course of the simulations. In order to avoid the clustering regime while still maintaining a large system size to provide proper statistics, the x -, y -, and z -dimensions of the simulation box are set to the ratio $14.4 : 1 : 1$ and there are a total $N = 7200$ spheres. This ensured that the systems remained homogeneous for all conditions (i.e. number of particles, coefficient of restitution, and density) that were examined in this work.

At the beginning of the simulations for each set of conditions, the spheres are arranged in a face centered cubic lattice at the appropriate density. The velocities of the spheres are initially assigned from a Maxwell-Boltzmann distribution. The simulations are then run for an “equilibration” period of 10^7 collisions. Afterwards, system property data are collected over at least 10 production runs, each lasting 10^7 collisions. The uncertainties of the data are estimated from the standard deviations of the results from these separate runs. In the next section, we describe the DSMC simulations performed.

6.3 DSMC Simulations

The DSMC method was used to numerically solve the Enskog equation. This technique has been described in detail previously [1, 19] and is only covered briefly here. The peculiar velocity distribution function f is represented by using a collection of N sample velocities or “simulated” particles:

$$f(\bar{\mathbf{v}}, t) = N^{-1} \sum_{i=1}^N \delta^3 (\bar{\mathbf{v}} - \bar{\mathbf{v}}_i(t)), \quad (6.3.1)$$

where $\bar{\mathbf{v}}_i(t)$ is the peculiar velocity of sample i at time t . At each time step Δt , the samples are evolved according to the SLLOD dynamics (see Eq. (6.2.2)). The samples are then tested for collisional updates. At each time step, $\frac{1}{2}NP_{\max}^{(B)}$ pairs of samples in the collection are selected, where $P_{\max}^{(B)}$ is a parameter of the DSMC simulation. The probability that a collision between a pair of samples i and j will be executed is proportional to

$$P_{ij}^{(B)} = 4\pi\sigma^2\chi\rho \left(\hat{\mathbf{k}} \cdot \mathbf{v}_{ij} \right) \Theta \left(\hat{\mathbf{k}} \cdot \mathbf{v}_{ij} \right) \Delta t \quad (6.3.2)$$

where $\hat{\mathbf{k}}$ is a randomly generated unit vector, $\mathbf{v}_{ij} = \bar{\mathbf{v}}_i - \bar{\mathbf{v}}_j - \sigma\dot{\gamma}\hat{k}_y\hat{\mathbf{e}}_x$ is the relative lab velocity, Θ is the Heaviside step function, and χ is the radial distribution function at contact. In this work, the value of χ is taken from the Carnahan-Starling [9] equation of state for elastic hard spheres, which is given by

$$\chi = \frac{1 - \nu/2}{(1 - \nu)^3} \quad (6.3.3)$$

where $\nu = \rho\pi\sigma^3/6$ is the solid fraction.

To optimize the simulation, the quantity $P_{\max}^{(B)}$ is chosen to be the maximum observed

value of $P_{ij}^{(B)}$. This is estimated and updated during a simulation if $P_{ij}^{(B)}$ exceeds $P_{max}^{(c)}$. The probability that a collision between samples i and j is executed is $P_{ij}^{(B)} / P_{max}^{(B)}$, and, if the collision is accepted, the velocities are updated using Eq. (6.2.5) with $\mathbf{r}_{ij} = -\sigma \hat{\mathbf{k}}$.

For the results presented here, $N = 1372$ and Δt is selected such that $\frac{1}{2} N P_{max}^{(B)} < 5$. The distribution functions are equilibrated for 10^6 collisions, and then results are collected and averaged over 10 runs of 10^7 collisions.

6.4 Results and Discussion

In this section, we present our simulation results for the properties of homogeneously sheared inelastic hard sphere systems. These results are compared against DSMC simulation of the Enskog equation to test the Enskog approximation. We also include the results from the kinetic model solved by Montanero et al. [1, 43]. This theory is particularly interesting as it provides analytical results in the limit of small strain rates, along with simple expressions that approximate DSMC results. Without the small strain rate approximation, a more accurate numerical solution of the model is available [1]; however, the DSMC simulations already provide accurate Enskog theory results without further approximation.

6.4.1 Velocity Distribution

The kinetic energy of the system is defined through the fluctuations of the velocity of the particles from their respective local streaming velocity

$$E = \frac{1}{2} \sum_{k=1}^N m \bar{v}_k^2. \quad (6.4.1)$$

The mean kinetic energy is therefore a measure of the velocity dispersion present in the system. In analogy with elastic (equilibrium) hard sphere fluids, a kinetic (or “granular”) temperature T is typically introduced through the relation

$$\frac{3}{2} N k_B T \equiv \langle E \rangle, \quad (6.4.2)$$

where N is the number of particles in the system, and k_B is the Boltzmann constant. Although the physical significance of the “granular temperature” has been a subject of some controversy [13], the concept has proved effective in the theoretical modelling of the properties of granular materials.

The granular temperature of the sheared inelastic hard sphere system at steady state is plotted in Fig. 6.2. The symbols are the results of our molecular dynamics simulations, the dotted lines are the suggested expressions of Montanero et al. [1], and the solid lines are the DSMC simulation results. From the figure, it can be seen that the granular temperature of the system decreases with decreasing values of the coefficient of restitution. The

particles in a strongly inelastic system rebound less from collisions; therefore, collisions in the direction of shear can quickly settle a particle to the velocity of the streamline. In addition, the motion of the particles off the streamline (in the y - and z -directions) are more quickly dissipated by collisions with particles on neighboring streamlines. Consequently, strongly inelastic systems have a greater tendency to follow the streamlines of a flow.

At low densities, the granular temperature increases with decreasing particle densities. The collisions between particles transmit information regarding the mean velocity of the flow. For very low density systems, the collisions are relatively rare events, and between collisions a particle will generally travel on trajectories that deviate from the streamlines, thus contributing to the granular temperature. With increasing density, a particle will become increasingly “caged” by surrounding particles, experiencing more collisions that will keep it on a particular streamline. Therefore, one expects that the temperature should generally decrease with increasing particle density. However, the simulation data indicate that the temperature of the system does not depend monotonically with the density, and a minimum is observed at a relatively high density for all the systems considered. The minimum becomes more pronounced as the coefficient of restitution decreases.

We note that in dense experimental granular systems, particles mainly remain in contact with each other and interact by rolling or sliding past one another, rather than through collisions. In this regime, soft sphere models [44], as opposed to hard sphere models, are more representative. Consequently, the applicability of the simulation results for the inelastic hard sphere system at high densities to experimental granular systems should be considered with care.

In general, Enskog theory and the solution of Montanero et al. provides a fairly accurate description of the simulation results; however, there is a large discrepancy for high values of the inelasticity and density. In addition, Enskog theory does not capture the presence of the minimum in the temperature with respect to the density.

Equilibrium fluids obey the equipartition theorem: energy is, on average, distributed evenly between all degrees of freedom. In driven granular systems, however, this has been shown to not be the case [45]. Figure 6.3a shows the variation of $\langle \bar{v}_y^2 \rangle / \langle \bar{v}_x^2 \rangle$ with density, and Fig. 6.3b shows the variation of $\langle \bar{v}_z^2 \rangle / \langle \bar{v}_y^2 \rangle$. The symbols are the results of our molecular dynamics simulations, the dotted lines are the predictions of the theory of Montanero et al. [1], and the solid lines are the DSMC simulation results. If the system obeyed the equipartition function, then both these ratios would be equal to one. The dispersion of the velocity parallel to the direction of shear (i.e. the x -direction) is consistently larger than that perpendicular to the shear, which is unsurprising as this is the direction in which energy is inputted to the system. The asymmetry increases with decreasing density and with decreasing values of the coefficient of restitution. It is interesting to note, however, that the fluctuations in the velocity in the y - and z -directions are nearly equal.

The low dissipation theory of Montanero et al. strongly under predicts the anisotropy in the velocity dispersion. DSMC results provide a better description but still deviate

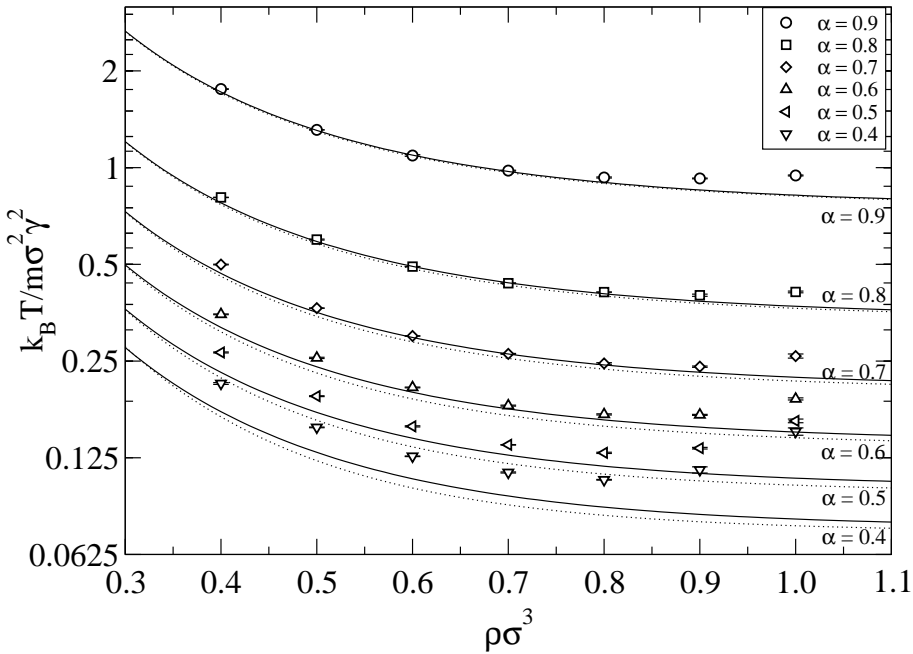


Figure 6.2: Variation of the mean kinetic energy per particle with density for (i) $\alpha = 0.4$ (circles), (ii) $\alpha = 0.5$ (squares), (iii) $\alpha = 0.6$ (diamonds), (iv) $\alpha = 0.7$ (triangles-up), (v) $\alpha = 0.8$ (triangles-left), and (vi) $\alpha = 0.9$ (triangles-down). The dotted lines are the suggested expressions of Ref. [1] and the solid lines are DSMC results.

significantly from the simulation results at low values of the elasticity.

Montanero et al.'s theory truncates terms within the second velocity moment of the collision integral and all higher terms. The full second moment could be included to improve predictions; however, as this is primarily a collision term it is unlikely to improve the predictions of the velocity anisotropy.

The kinetic model could be expanded by relaxing to a generalized Gaussian distribution, as in the ellipsoidal statistical model. The extra degrees of freedom in the model would then be solved for by the inclusion of a full second velocity moment balance. This might still prove tractable and improve the predictions for the velocity dispersion anisotropy.

For equilibrium systems, such as elastic-hard-sphere fluids, the velocity distribution is exactly given by the Maxwell-Boltzmann distribution; however, granular materials have been shown to deviate from this distribution [34, 46, 47]. The simulation data for the distributions of the single particle x -, y -, and z -component of the peculiar velocity are shown in Fig. 6.4. The peculiar velocities are reduced by their mean squared values ($v_i^* = \bar{v}_i / \langle \bar{v}_i^2 \rangle^{1/2}$, for $i = x, y$, and z). The distributions are, in general, well described by an anisotropic Gaussian distribution. For the highly inelastic systems, the distributions display a slightly enhanced high velocity tail. This is most evident in the direction of shear (i.e. the x -direction).

For simulations in a *cubic* box at the onset of clustering in the system, the peculiar velocity distributions in the y - and z -directions can be shown to develop strong high velocity tails. In this case, the bulk of the particles are within a dense low strain rate zone,

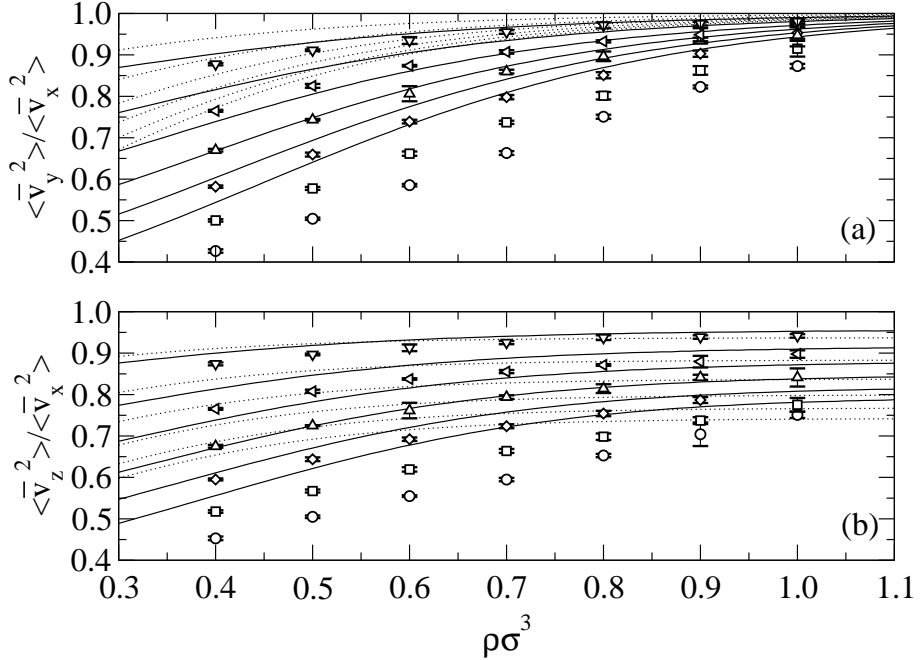


Figure 6.3: The ratio of the mean-squared-velocity (a) in the y - and x -directions and (b) in the z - and x -directions for sheared inelastic hard sphere systems with (i) $\alpha = 0.4$ (circles), (ii) $\alpha = 0.5$ (squares), (iii) $\alpha = 0.6$ (diamonds), (iv) $\alpha = 0.7$ (triangles-up), (v) $\alpha = 0.8$ (triangles-left), and (vi) $\alpha = 0.9$ (triangles-down). The dotted lines are the suggested expressions of Ref. [1], and the solid lines are the DSMC results.

while the remainder reside in a rare, high strain rate and granular temperature region. The particles in the high strain rate region lead to a high velocity tail. Further studies on clustering effects are currently underway.

6.4.2 Stress Tensor

In this section, we examine the stress tensor. The time averaged value of the stress tensor $\langle \mathbf{P} \rangle$ for a hard-sphere system is given by [48]

$$\langle \mathbf{P} \rangle = \frac{1}{V\tau} \sum_{\text{collisions}}^{\tau} \left[\Delta t_c \sum_{k=1}^N m \bar{\mathbf{v}}_k \bar{\mathbf{v}}_k + \sigma \hat{\mathbf{r}}_{ij} m \Delta \mathbf{v}_i \right] \quad (6.4.3)$$

where Δt_c is the time interval between two consecutive collisions, $\Delta \mathbf{v}_i$ is the change of velocity of sphere i on collision, τ is the time over which the stress tensor is averaged, and V is the total volume of the system. The first summation runs over all collisions that occur during the time τ , and the indexes i and j refer to the spheres undergoing the collision; the index k runs over all particles in the system.

The pressure p of the system, which is defined as

$$p \equiv \frac{1}{3} (\langle P_{xx} \rangle + \langle P_{yy} \rangle + \langle P_{zz} \rangle),$$

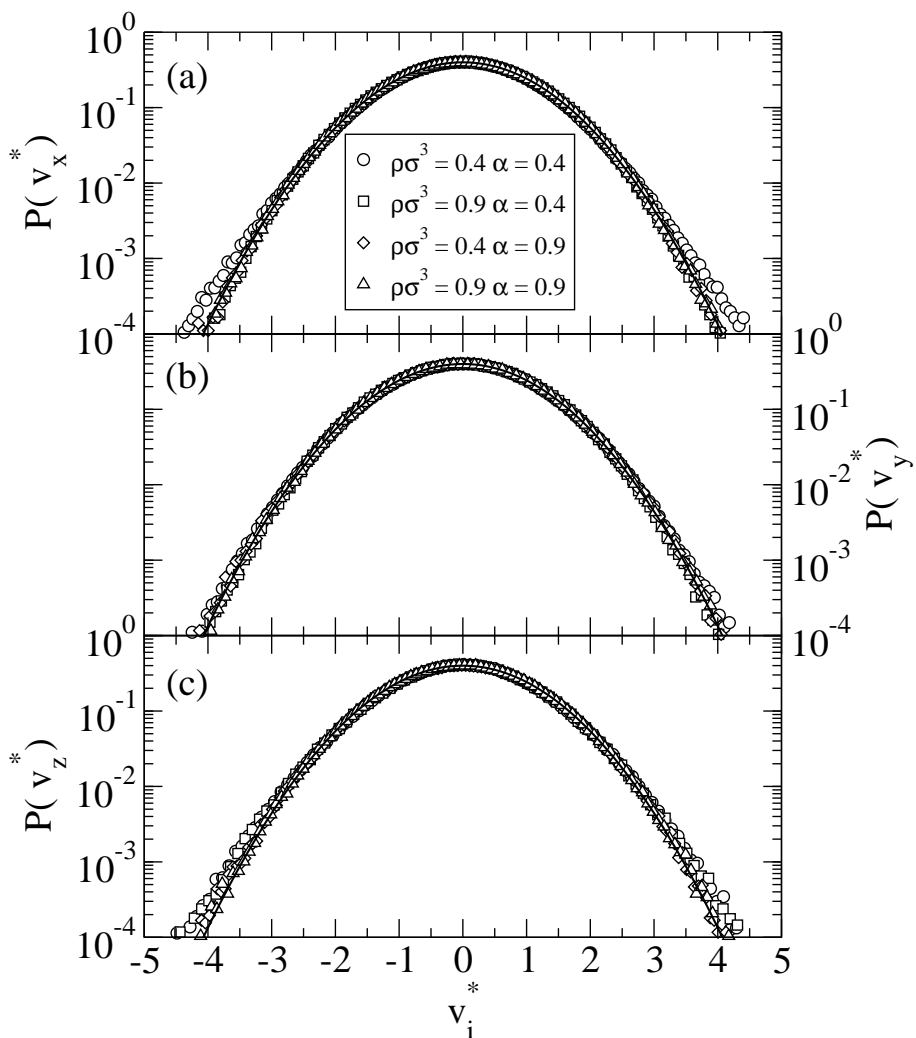


Figure 6.4: The peculiar velocity distribution in the (a) x -direction, (b) y -direction, and (c) z -direction in sheared inelastic hard sphere systems with (i) $\rho\sigma^3 = 0.4$ and $\alpha = 0.4$ (circles), (ii) $\rho\sigma^3 = 0.9$ and $\alpha = 0.4$ (squares), (iii) $\rho\sigma^3 = 0.4$ and $\alpha = 0.9$ (diamonds), and (iv) $\rho\sigma^3 = 0.9$ and $\alpha = 0.9$ (triangles). The solid line is a Gaussian distribution.

is plotted in Fig. 6.5a. As expected, the pressure increases as the density of the system increases. It also increases with increasing coefficient of restitution due to the rise in granular temperature. The Enskog theory requires, as input, the collision rate between particles as a function of the density. This is typically given by the equation of state for elastic hard sphere fluids through the compressibility factor. The compressibility factor Z , defined as

$$Z \equiv \frac{p}{\rho k_B T},$$

is plotted for the shear inelastic-hard-sphere system in Fig. 6.5b. The symbols represent the results of the simulations, and the line is the Carnahan-Starling equation of state [9] for the elastic hard sphere fluid. With the exception of the highest density, the compressibility factor for homogeneously sheared inelastic spheres is quite similar to that for elastic hard spheres. The predictions of Enskog theory and Montanero et al. for the pressure (see

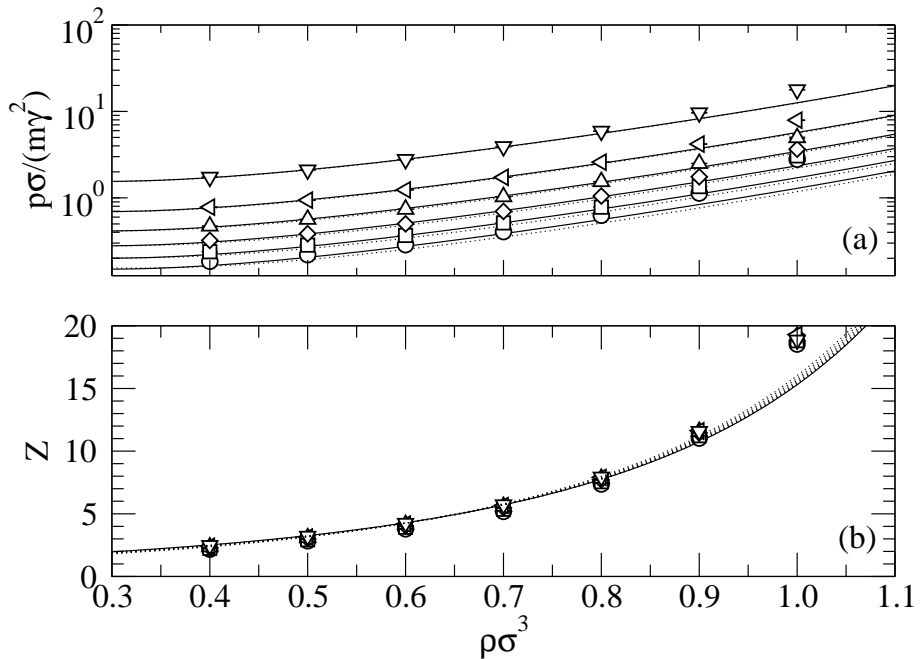


Figure 6.5: The (a) dimensionless pressure $p\sigma/(m\dot{\gamma}^2)$ and (b) the compressibility factor Z for inelastic hard-sphere systems with (i) $\alpha = 0.4$ (circles), (ii) $\alpha = 0.5$ (squares), (iii) $\alpha = 0.6$ (diamonds), (iv) $\alpha = 0.7$ (triangles-up), (v) $\alpha = 0.8$ (triangles-left), and (vi) $\alpha = 0.9$ (triangles-down). The uncertainty is smaller than the symbol size. The dotted lines are the suggested expressions of Ref. [1], and the solid lines are DSMC results. The solid line in (b) is the Carnahan-Starling equation of state for elastic hard sphere fluids, and the dotted lines are DSMC results for various α .

Fig. 6.5a) agree fairly well with the simulation data. The main source of the discrepancy is due to the mis-prediction of the kinetic contribution to the pressure.

The shear viscosity of a granular material is perhaps the most important design parameter in fast flows, quantifying the power lost per unit volume. The shear viscosity of the inelastic hard-sphere system was computed by two means. The first method is via the definition of the shear viscosity η for simple Couette flow

$$\eta \equiv - \frac{\langle P_{xy} \rangle}{\dot{\gamma}} \quad (6.4.4)$$

An alternative method is to perform an energy balance. The work of shearing inputs energy into the system. Collisions between the inelastic spheres continuously dissipate kinetic energy. At steady-state, the average rate of energy input is equal to the average rate of energy dissipation [49]:

$$\eta \dot{\gamma}^2 V = - \langle \dot{E} \rangle \quad (6.4.5)$$

where $\langle \dot{E} \rangle$ is the average rate of kinetic energy dissipation. The rate of energy dissipation is directly related to the mean time between collisions t_{avg} for a sphere by

$$\langle \dot{E} \rangle = \frac{N}{2t_{\text{avg}}} \langle \Delta E \rangle$$

Table 6.1: Dimensionless viscosity $\eta\sigma/(m\dot{\gamma})$ of sheared inelastic hard-sphere systems at various densities ρ and coefficients of restitution α . The upper value is determined from the stress tensor (see Eq. (6.4.3)), and the lower value is determined from the kinetic energy dissipation rate (see Eq. (6.4.5)). The value in brackets is the standard deviation of the last digit over all of the runs.

$\rho\sigma^3 \backslash \alpha$	0.4	0.5	0.6	0.7	0.8	0.9
0.4	0.1054(3)	0.1294(4)	0.1625(6)	0.2134(5)	0.2970(4)	0.480(2)
	0.1054(3)	0.1294(4)	0.1625(6)	0.2134(5)	0.2969(4)	0.480(2)
0.5	0.1300(3)	0.1582(2)	0.1979(7)	0.2585(3)	0.361(1)	0.583(2)
	0.1300(3)	0.1582(2)	0.1979(7)	0.2585(3)	0.361(1)	0.583(1)
0.6	0.1722(5)	0.2078(3)	0.2606(7)	0.3416(9)	0.4785(5)	0.779(6)
	0.1722(5)	0.2078(3)	0.2606(7)	0.3417(9)	0.4785(7)	0.779(7)
0.7	0.2445(4)	0.2909(8)	0.364(1)	0.4801(8)	0.677(2)	1.117(5)
	0.2446(3)	0.2909(8)	0.364(1)	0.4801(9)	0.677(2)	1.117(5)
0.8	0.371(1)	0.4375(2)	0.545(1)	0.716(3)	1.020(2)	1.722(8)
	0.371(1)	0.4375(2)	0.545(1)	0.716(3)	1.020(2)	1.722(8)
0.9	0.643(7)	0.731(1)	0.885(2)	1.141(4)	1.64(1)	2.86(1)
	0.643(8)	0.731(2)	0.885(2)	1.141(4)	1.64(1)	2.856(10)
1.0	1.42(1)	1.52(2)	1.73(2)	2.15(3)	3.01(3)	5.30(4)
	1.42(1)	1.52(2)	1.73(2)	2.15(3)	3.01(4)	5.30(3)

where N is the total number of spheres in the system, and $\langle \Delta E \rangle$ is the average amount of kinetic energy lost per collision.

The simulation results for the viscosity of sheared inelastic hard-sphere systems are summarized in Table 6.1. The upper entries are the values obtained from the stress tensor (see Eq. (6.4.3)), and the lower entries are the values obtained from the dissipation of kinetic energy (see Eq. (6.4.5)). For all the simulation runs, the two agree within the statistical uncertainties of the simulations. Figure 6.6a shows the dependence of the shear viscosity on the reduced density of the system, for various values of the coefficient of restitution. The viscosity increases with packing fraction and coefficient of restitution (remembering that the shear rate is equal to one). The theory of Montanero et al. captures the full Enskog behaviour and predicts the viscosity well. Enskog theory deviates at low values of α and high densities where the predictions for the temperature begin to deviate from the simulation results (see Fig. 6.2).

In addition to the shear viscosity, we also monitor the in-plane normal stress coefficient η_- and the out-of-plane normal stress coefficient η_0 , which are defined as [36]

$$\begin{aligned}\eta_- &= -\frac{1}{2\dot{\gamma}}(\langle P_{xx} \rangle - \langle P_{yy} \rangle) \\ \eta_0 &= -\frac{1}{2\dot{\gamma}} \left[\langle P_{zz} \rangle - \frac{1}{2}(\langle P_{xx} \rangle + \langle P_{yy} \rangle) \right]\end{aligned}$$

The in-plane normal stress coefficient is plotted in Fig. 6.6b, and the out-of-plane normal

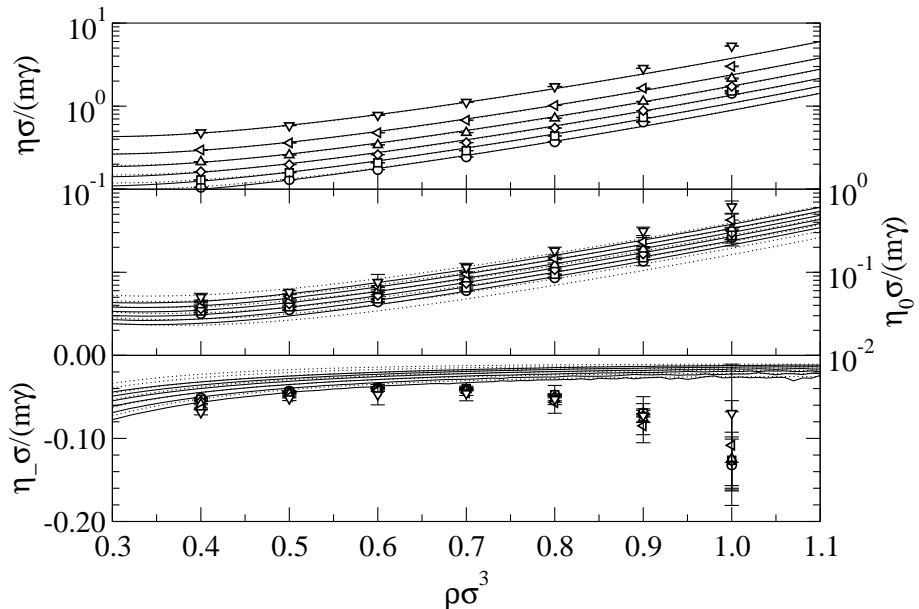


Figure 6.6: The viscosity for a homogeneously sheared inelastic-hard-sphere system with (i) $\alpha = 0.4$ (circles), (ii) $\alpha = 0.5$ (squares), (iii) $\alpha = 0.6$ (diamonds), (iv) $\alpha = 0.7$ (triangles-up), (v) $\alpha = 0.8$ (triangles-left), and (vi) $\alpha = 0.9$ (triangles-down). The dotted lines are the suggested expressions of Ref. [1], and the solid lines are DSMC results.

stress coefficient is plotted in Fig. 6.6c. The simulation values deviate significantly from the predictions of Enskog theory; however, this is unsurprising as the velocity dispersion predictions deviate significantly from the simulation results (see Fig. 6.3).

6.4.3 Collision Statistics

In this section, we examine the statistics of the collisions experienced by the spheres. The mean time between collision t_{avg} provides a characteristic time scale for the sheared inelastic hard sphere system. Figure 6.7 shows the variation of the mean time between collisions with the density of the system at various values of the coefficient of restitution. The time between collision decreases with increasing density, which is expected; increasing the coefficient of restitution decreases the mean time between collision. The variation of t_{avg} with the coefficient of restitution is given in the inset of Fig. 6.7. At densities roughly below $\rho\sigma^3 = 0.6$, the mean time between collision decreases monotonically with increasing values of the coefficient of restitution. However, at higher densities, there is a maximum in t_{avg} . The Enskog theory results describe the results qualitatively well for low density systems but fail at high densities.

For an elastic fluid, the velocities of different particles are, in general, uncorrelated. Consequently, the velocity statistics of the individual collisions can be determined exactly. On the other hand, the particle velocities in a driven granular system can be strongly correlated, and their on-collision statistics are not exactly known.

The distribution of the angle θ between the relative velocity and the relative position

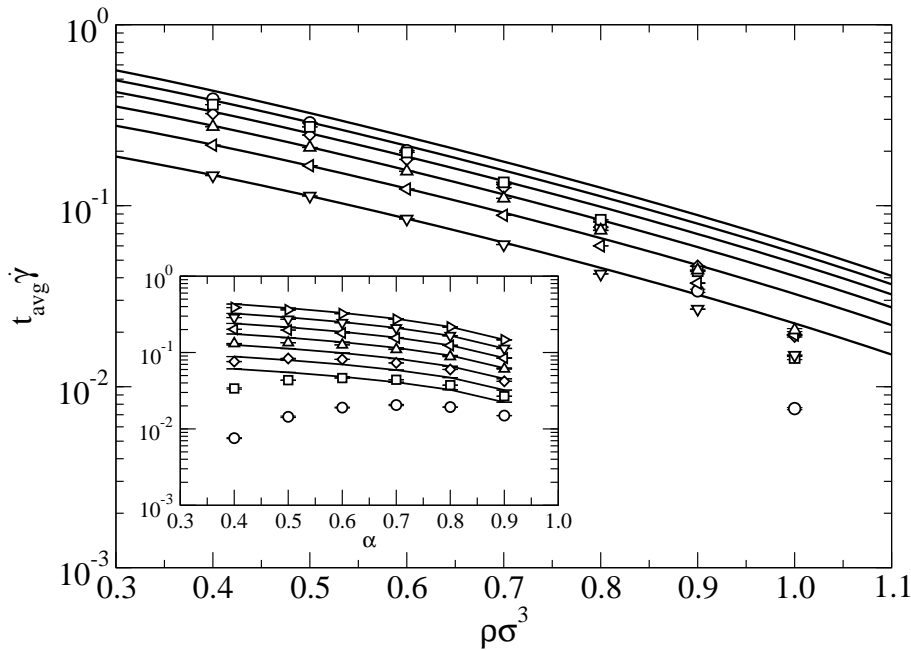


Figure 6.7: Mean time between collisions for sheared inelastic hard spheres with: (i) $\alpha = 0.4$ (circles), (ii) $\alpha = 0.5$ (squares), (iii) $\alpha = 0.6$ (diamonds), (iv) $\alpha = 0.7$ (triangles-up), (v) $\alpha = 0.8$ (triangles-left), and (vi) $\alpha = 0.9$ (triangles-down). Inset: variation of the mean time between collisions with the coefficient of restitution for (i) $\rho\sigma^3 = 1.0$ (circles), (ii) $\rho\sigma^3 = 0.9$ (squares), (iii) $\rho\sigma^3 = 0.8$ (diamonds), (iv) $\rho\sigma^3 = 0.7$ (triangles-up), (v) $\rho\sigma^3 = 0.6$ (triangles-left), (vi) $\rho\sigma^3 = 0.5$ (triangles-down), and (vii) $\rho\sigma^3 = 0.4$ (triangles-right). The solid lines are the DSMC simulation results.

of two spheres on collision ($\cos \theta = \mathbf{r}_{ij} \cdot \mathbf{v}_{ij} / |\mathbf{r}_{ij}| |\mathbf{v}_{ij}|$) is given in Fig. 6.8. The solid line denotes an isotropic collision distribution (as is the case for elastic, elastic-hard-sphere systems). The symbols are the simulation data for sheared inelastic hard spheres, and the solid line is the DSMC result for $\rho\sigma^3 = 0.9$ and $\alpha = 0.4$. For weakly inelastic systems, the distribution of the collisional angle is close to that for the elastic hard-sphere system. As the inelasticity and density of the particles increases, however, there is a gradual increase of the frequency of “glancing” collisions (where $\cos \theta$ is near 0) at the expense of more “head-on” collisions (where $\cos \theta$ is close to -1). This is in agreement with the two-dimensional shearing simulation of Tan and Goldhirsch [32] and Campbell and Brennen [4]. The Enskog theory does not capture this effect, as the DSMC simulations only display a small increased bias towards glancing collisions even in the dense, highly inelastic system.

The increase in glancing collisions for strongly inelastic systems (see Fig. 6.8) results primarily from collisions between pairs of particles orientated in the x - y plane. This occurs when the change of the streaming velocity over the diameter of a particle becomes significant in comparison to the average relative peculiar velocity [21]. Particles separated in the y -plane then have a significantly increased relative velocity which increases their probability of collision. Both the DSMC and granular dynamics simulation results support this; however, DSMC does not exhibit the large increase in collisions with a very large

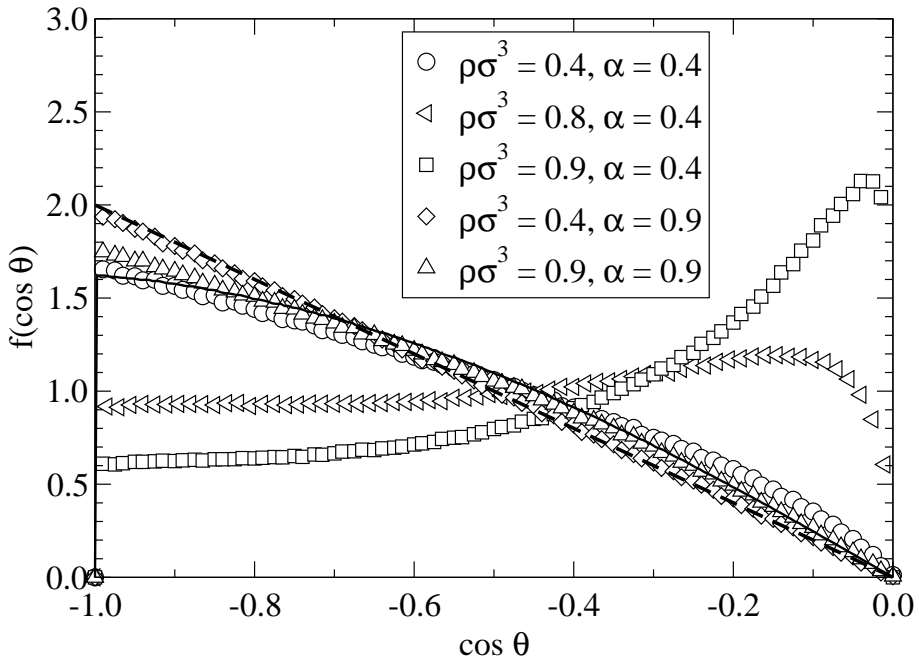


Figure 6.8: The distribution of collisional angles for (i) $\rho\sigma^3 = 0.4$ and $\alpha = 0.4$ (circles), (ii) $\rho\sigma^3 = 0.8$ and $\alpha = 0.4$ (triangles-left), (iii) $\rho\sigma^3 = 0.9$ and $\alpha = 0.4$ (squares), (iv) $\rho\sigma^3 = 0.4$ and $\alpha = 0.9$ (diamonds), and (v) $\rho\sigma^3 = 0.9$ and $\alpha = 0.9$ (triangles-up). The dashed line is for elastic hard spheres and the solid line is from a DSMC simulation of $\rho\sigma^3 = 0.9$ and $\alpha = 0.4$.

collision angle.

In the inelastic hard sphere system, every collision results in a loss of kinetic energy. The simulation results for the distribution of the loss of kinetic energy on collision is given in Fig. 6.9. If the velocity distribution of the spheres were Gaussian (e.g., Maxwell-Boltzmann distribution), then the kinetic energy loss on collision would be distributed according to a Poisson distribution:

$$f(\Delta E) = \frac{1}{\langle \Delta E \rangle} \exp\left(-\frac{\Delta E}{\langle \Delta E \rangle}\right)$$

This is given by the solid line in Fig. 6.9. At high values of α , the distribution of the change of kinetic energy on collision is nearly exponential; for these systems, density does not significantly affect the results.

As α decreases, there is a greater frequency of collisions that result in a very slight loss of kinetic energy (i.e. the initial peak in Fig. 6.9). This corresponds to the increase in the glancing collisions in the systems. This enhancement of relatively elastic collisions is accompanied by an increase in collisions that result in large losses of kinetic energy (i.e. the long tail in Fig. 6.9). These result from “head-on” collisions, which occur between particles oriented primarily in the x -direction where the velocity dispersion is the greatest. While these “head-on” collisions occur less frequently than glancing collisions in the highly inelastic systems, they are more violent. Increasing the density enhances these

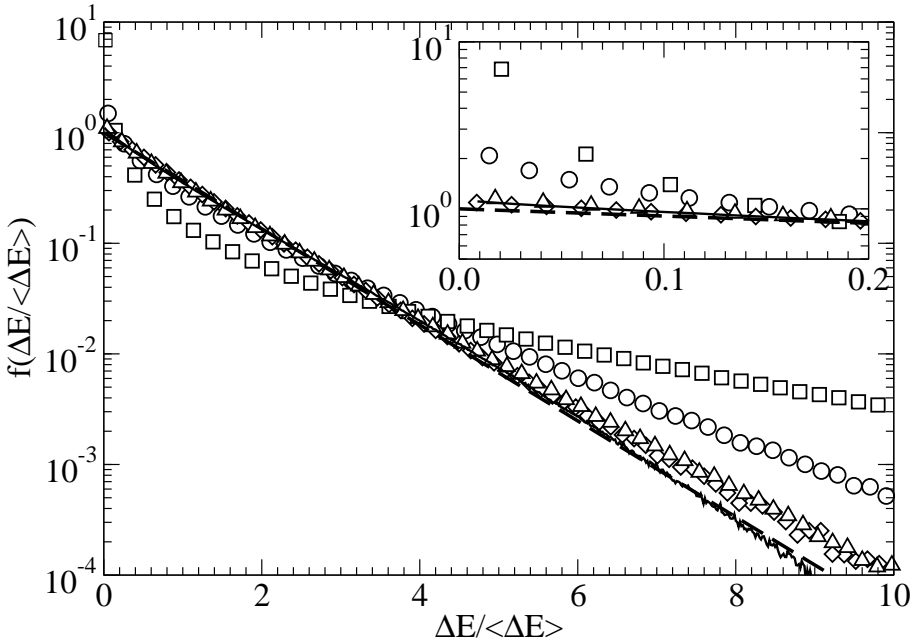


Figure 6.9: The change of kinetic energy on collision for sheared inelastic hard sphere systems with (i) $\rho\sigma^3 = 0.4$ and $\alpha = 0.4$ (circles), (ii) $\rho\sigma^3 = 0.9$ and $\alpha = 0.4$ (squares), (iii) $\rho\sigma^3 = 0.4$ and $\alpha = 0.9$ (diamonds), and (iv) $\rho\sigma^3 = 0.9$ and $\alpha = 0.9$ (triangles). The dashed line represents the kinetic energy loss on collision if the velocity were given by the Maxwell-Boltzmann distribution, and the solid line is from a DSMC simulation at $\rho\sigma^3 = 0.9$ and $\alpha = 0.4$. The inset highlights the frequency of collisions that result in low energy losses.

effects.

Thus far, we have only studied the statistics of single collisions. One common assumption in many kinetic theories is that the individual collisions experienced by a particle are statistically independent. We now study the correlation between collisions by examining the time required for a particle to undergo a number of collisions. If the various collisions experienced by a particle can be considered to arrive at random times in an independent manner, then the time t required for a particle to undergo n collisions is given by a Poisson process. The probability density function $p_n(t)$ that a particle experiences n collisions in a period of time t is

$$p_n(t) = \frac{(t/t_{\text{avg}})^{n-1}}{t_{\text{avg}}\Gamma(n)} \exp\left(-\frac{t}{t_{\text{avg}}}\right) \quad (6.4.6)$$

where $\Gamma(n)$ is the Gamma function. Deviations from this distribution are an indication of correlations between collisions. For elastic hard-sphere fluids, the Poisson process describes the collision time distribution fairly well, however, there are noticeable deviations, even at low densities, which increase with increasing density [50–52].

The collision time distributions for homogeneously sheared inelastic hard sphere systems are shown in Fig. 6.10. The solid lines denote the Poisson distribution, given by Eq. (6.4.6). At high values of the coefficient of restitution, the distributions are similar to those of elastic hard spheres and are fairly well described by a Poisson process. As

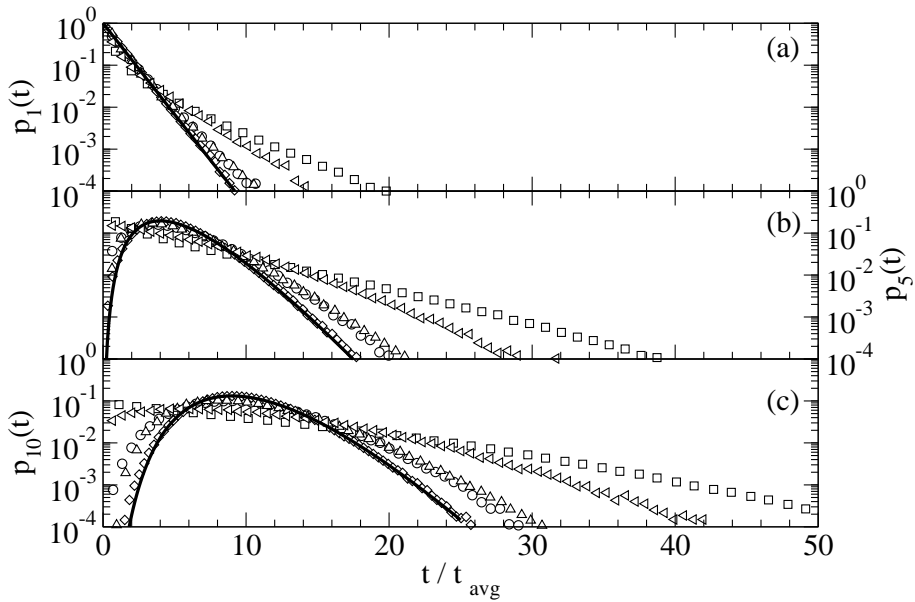


Figure 6.10: Distribution of time between (a) one collision, (b) five collisions, and (c) ten collisions in sheared inelastic hard spheres with (i) $\rho\sigma^3 = 0.4$ and $\alpha = 0.4$ (circles), (ii) $\rho\sigma^3 = 0.9$ and $\alpha = 0.4$ (squares), (iii) $\rho\sigma^3 = 0.4$ and $\alpha = 0.9$ (diamonds), and (iv) $\rho\sigma^3 = 0.9$ and $\alpha = 0.9$ (triangles). The solid line is for a Poisson process.

the coefficient of restitution decreases, however, the simulation data deviate significantly from the Poisson process, indicating very strong correlations between collisions. Qualitatively, the deviations are similar to that observed for elastic hard sphere systems: there is an enhancement of very short and very long wait-times between collisions. However, these differences are much more pronounced for the inelastic hard sphere systems.

6.5 Conclusions

We have performed non-equilibrium molecular dynamics simulations of sheared inelastic-hard-systems using the SLLOD algorithm combined with Lees-Edwards boundary conditions. In these simulations, care was taken to ensure that the systems remain homogeneous and the shear was uniform across the system. As a consequence, these simulations may prove a useful reference to compare with the predictions of kinetic theory.

DSMC simulations of the Enskog equation were performed to provide a solution to the kinetic theory without further approximation. These compared favorably with the simulation results except for dense, strongly inelastic systems. The velocity anisotropy effect can be very strong even in homogeneous systems, and kinetic theory solutions must take this into account in their approximations.

Results were presented for the velocity statistics of individual particles in the system. The velocity distributions were, in general, well described by an anisotropic Gaussian. Theories based on the anisotropic Gaussian and the full second moment balance (e.g., see Ref. [53]) are well suited to these systems. Sheared, inelastic-hard-sphere systems

do not obey the equipartition theorem. Fluctuations of the velocity in the x -direction (the direction of shear) were greater than those in the y - and z -directions, which were both similar to each other. In addition, the granular temperature, which characterizes the overall fluctuation of the velocity, was observed to possess a minimum with respect to the density. This minimum becomes more pronounced as the coefficient of restitution of the spheres decreases.

The variation of the stress in the system was also examined. The compressibility factor of the sheared inelastic-hard-sphere system was quite similar to that of elastic hard spheres, as estimated by the Carnahan-Starling equation of state. The shear viscosity of the systems was computed in two different manners: from the average of the stress tensor and from the rate of dissipation of kinetic energy. The value of the viscosity from both these methods agree to within the statistical uncertainty of the simulations. The predictions of the Enskog equation and the kinetic theory of Montanero et al. [1] were in fairly good agreement with the simulation data. The in-plane and out-of-plane stress coefficients were also computed, but the kinetic theory predictions for these quantities were not as accurate.

Finally, the collision statistics of particles in the sheared inelastic hard sphere system were studied. The mean time between collision was found to decrease monotonically with increasing density; however, at fixed density, it displays a maximum at intermediate values of the coefficient of restitution. Examination of the collision time distributions indicated the presence of strong correlations between collisions. Including these correlations within a kinetic theory will be important in developing an accurate description of high density, sheared inelastic-hard-sphere systems.

6.6 References

- [1] J. M. Montanero et al., “Kinetic theory of simple granular shear flows of smooth hard spheres”, *J. Fluid Mech.* 389, 391–411 (1999).
- [2] C. S. Campbell, “Rapid Granular Flows”, *Ann. Rev. Fluid Mech.* 22, 57–92 (1990).
- [3] I. Goldhirsch, “Rapid Granular Flows”, *Annu. Rev. Fluid Mech.* 35, 267–293 (2003).
- [4] C. S. Campbell and C. E. Brennen, “Computer simulation of granular shear flows”, *J. Fluid Mech.* 151, 167–188 (1985).
- [5] J. F. Lutsko, “Rheology of dense polydisperse granular fluids under shear”, *Phys. Rev. E.* 70, 061101 (2004).
- [6] C. K. K. Lun et al., “Kinetic Theories For Granular Flow — Inelastic Particles In Couette-Flow And Slightly Inelastic Particles In A General Flowfield”, *J. Fluid Mech.* 140, 223–256 (1984).

- [7] A. Santos and A. Astillero, “System of Elastic Hard Spheres which Mimics the Transport Properties of a Granular Gas”, *Phys. Rev E.* 72, 031308 (2005).
- [8] H. van Beijeren and M. H. Ernst, “Modified Enskog Equation”, *Physica.* 68, 437–456 (1973).
- [9] N. F. Carnahan and K. E. Starling, “Equation of state for nonattracting rigid spheres”, *J. Chem. Phys.* 51, 635–636 (1969).
- [10] T. P. C. van Noije, M. H. Ernst and R. Brito, “Ring kinetic theory for an idealized granular gas”, *Physica A.* 251, 266–283 (1998).
- [11] N. Sela and I. Goldhirsch, “Hydrodynamic equations for rapid flows of smooth inelastic spheres, to Burnett order ”, *J. Fluid Mech.* 361, 41–74 (1998).
- [12] C. K. K. Lun, “Kinetic theory for granular flow of dense, slightly inelastic, slightly rough spheres”, *J. Fluid Mech.* 233, 539–559 (1991).
- [13] I. Goldhirsch, “Introduction to granular temperature”, *Powder Tech.* 182, 130–136 (2008).
- [14] J. T. Jenkins and M. W. Richman, “Plane Simple Shear of Smooth Inelastic Circular Disks. The Anisotropy of the 2nd Moment in the Dilute and Dense Limits ”, *J. Fluid Mech.* 192, 313–328 (1988).
- [15] J. T. Jenkins and M. W. Richman, “Kinetic-Theory For Plane Flows Of A Dense Gas Of Identical, Rough, Inelastic, Circular Disks”, *Physics Of Fluids.* 28, 3485–3494 (1985).
- [16] A. Santos et al., “Kinetic model for the hard-sphere fluid and solid”, *Phys. Rev. E.* 57, 1644–1660 (1998).
- [17] J. J. Brey, J. W. Dufty and A. Santos, “Kinetic Models for Granular Flow”, *J. Stat. Phys.* 97, 281–322 (1999).
- [18] G. A. Bird. *Molecular gas dynamics and the direct simulation of gas flows*. Oxford: Oxford University Press, 1994.
- [19] M. A. Hopkins and H. H. Shen, “A Monte Carlo solution for rapidly shearing granular flows based on the kinetic theory of dense gases”, *J. Fluid Mech.* 244, 477–491 (1992).
- [20] J. M. Montanero and A. Santos, “Simulation of the Enskog equation a la Bird”, *Phys. Fluids.* 9, 2057–2060 (1997).
- [21] M. Alam and S. Luding, “First normal stress difference and crystallization in a dense sheared granular fluid”, *Phys. Fluids.* 15, 2298–2312 (2003).
- [22] M. Alam and S. Luding, “Energy nonequipartition, rheology, and microstructure in sheared bidisperse granular mixtures”, *Phys. Fluids.* 17, 063303 (2005).
- [23] C.S. Campbell, “The stress tensor for simple shear flow of a granular material”, *J. Fluid Mech.* 203, 449–473 (1989).

- [24] O. Herbst et al., “Local equation of state and velocity distributions of a driven granular gas”, *Phys. Rev. E*. 70, 051313 (2004).
- [25] Hans J. Herrmann, S. Luding and R. Cafiero, “Dynamics of granular systems”, *Physica A*. 295, 93–100 (2001).
- [26] S. L. Conway and B. J. Glasser, “Density waves and coherent structures in granular Couette flows”, *Phys. Fluids*. 16, 509–529 (2004).
- [27] M. Alam et al., “Instability-induced ordering, universal unfolding and the role of gravity in granular Couette flow”, *J. Fluid. Mech.* 523, 277–306 (2005).
- [28] A. W. Lees and S. F. Edwards, “The Computer Study of Transport Processes Under Extreme Conditions”, *J. Phys. C*. 5, 1921–1929 (1972).
- [29] O. R. Walton and R. L. Braun, “Viscosity, Granular-Temperature, and stress calculations for shearing assemblies of inelastic, frictional disks”, *J. Rheol.* 30, 949–980 (1986).
- [30] M. A. Hopkins and M. Y. Louge, “Inelastic microstructure in rapid granular flows of smooth disks”, *Phys. Fluids A*. 3, 47–57 (1991).
- [31] I. Goldhirsch and M.-L. Tan, “The single-particle distribution function for rapid granular shear flows of smooth inelastic disks”, *Phys. Fluids*. 8, 1752–1763 (1996).
- [32] M-L. Tan and I. Goldhirsch, “Intercluster interactions in rapid granular shear flows”, *Phys. Fluids*. 9, 856–869 (1997).
- [33] J. F. Lutsko. *Spontaneous development of 3-D structure in sheared granular flows*. 2004. arXiv: cond-mat/0403551v1.
- [34] W. Losert et al., “Velocity statistics in excited granular media ”, *Chaos*. 9, 682–690 (1999).
- [35] J. M. Montanero et al., “Rheology of Two- and Three-dimensional Granular Mixtures Under Uniform Shear Flow: Enskog Kinetic Theory Versus Molecular Dynamics Simulations”, *Gran. Matt.* 8, 103–115 (2006).
- [36] D. J. Evans and G. P. Morris. *Statistical Mechanics of Nonequilibrium Liquids*. London: Academic Press, 1990.
- [37] J. Petracic and O. G. Jepps, “Homogeneous shear flow of a hard-sphere fluid: Analytic solutions”, *Phys. Rev. E*. 67, 021105 (2003).
- [38] S. McNamara and E. Falcon. “Vibrated Granular Media as Experimentally Realizable Granular Gases”. In: *Granular Gas Dynamics*. Springer, 2003, pp. 347–366.
- [39] S. McNamara and W. R. Young, “Dynamics of a freely evolving, two-dimensional granular medium”, *Phys. Rev. E*. 53, 5089–5100 (1996).
- [40] M. Alam and C.M. Hrenya, “Inelastic collapse in simple shear flow of a granular medium”, *Phys. Rev. E*. 63, 061308 (2001).

-
- [41] B. J. Alder and T. E. Wainwright, “Studies in molecular dynamics. 1. General method”, *J. Chem. Phys.* 31, 459–466 (1959).
 - [42] M. Bannerman and L. Lue. *DYNAMics of discrete Objects (DYNAMO)*. <http://www.marcusbannerman.co.uk/dynamo>. 2008.
 - [43] J. W. Dufty, J. J. Brey and A. Santos, “Kinetic models for hard sphere dynamics”, *Physica A*. 240, 212–220 (1997).
 - [44] C. S. Campbell, “Granular shear flows at the elastic limit”, *J. Fluid Mech.* 465, 261–291 (2002).
 - [45] T. A. Knight and L. V. Woodcock, “Test of the equipartition principle for granular spheres in a saw-tooth shaker”, *J. Phys. A*. 29, 4365–4386 (1996).
 - [46] J. S. Olafsen and J. S. Urbach, “Velocity distributions and density fluctuations in a granular gas”, *Phys. Rev. E*. 60, R2468–R2471 (1999).
 - [47] F. Rouyer and N. Menon, “Velocity fluctuations in a homogeneous 2D granular gas in steady state”, *Phys. Rev. Lett.* 85, 3676–3679 (2000).
 - [48] B. J. Alder, D. M. Gass and T. E. Wainwright, “Studies in Molecular Dynamics. VIII. The Transport Coefficients for a Hard-Sphere Fluid”, *J. Chem. Phys.* 53, 3813–3826 (1970).
 - [49] M.C. Turner and L.V. Woodcock, “Scaling laws for rapid granular flow”, *Powder Technology*. 60, 47–60 (1990).
 - [50] L. Lue, “Collision statistics, thermodynamics, and transport coefficients of hard hyperspheres in three, four, and five dimensions”, *J. Chem. Phys.* 122, 044513 (2005).
 - [51] P. Visco, F. van Wijland and E. Trizac, “Non-Poissonian statistics in a low-density fluid”, *J. Phys. Chem. B*. 112, 5412–5415 (2008).
 - [52] P. Visco, F. van Wijland and E. Trizac, “Collisional statistics of the hard sphere-gas”, *Phys. Rev. E*. 77, 041117 (2008).
 - [53] Chuen-Shii Chou and Mark W. Richman, “Constitutive theory for homogeneous granular shear flows of highly inelastic spheres”, *Physica A: Statistical and Theoretical Physics*. 259, 430–448 (1998).

CHAPTER
SEVEN

TRANSPORT PROPERTIES OF HIGHLY ASYMMETRIC HARD SPHERE MIXTURES

This chapter has been published in The Journal of Chemical Physics (see Appendix B).
Authors: M. Bannerman, L. Lue

7.1 Introduction

Excluded volume interactions between molecules play a major role in determining the structure and properties of most fluids and colloidal systems. The hard sphere model, which captures the essence of these interactions, has played a central role in our understanding of the properties of fluids, serving as a starting point of perturbation theories for the description of real fluids [1]. Recently, there has been interest in binary hard sphere mixtures, where the diameters of the two components are very different. These systems serve as models for nanoparticle suspensions and colloid-polymer mixtures. In these systems, an entropically driven depletion force [2, 3] drives the larger particles to cluster. While there have been many studies on the structural (e.g., radial distribution function) and thermodynamic properties (e.g., equation of state) of these mixtures [4–14], there have been relatively few studies on their dynamical properties.

Much of the previous simulation work for the dynamical properties of binary mixtures has focused on tracer particle studies [15–17], the velocity auto correlation functions, or the self-diffusion coefficients [18, 19], as these are relatively computationally inexpensive to determine. These studies have revealed that the dynamics of the larger particles deviates significantly from both the theoretical predictions of Brownian particles and of Enskog theory. Lue and Woodcock [7, 9] examined the self-diffusion coefficients of size asymmetric binary mixtures of hard spheres. They found a “fines effect” at high densities, where the addition of smaller spheres enhances the mobility of the larger spheres.

Significantly less data are available for other dynamical properties. Easteal and Woolf [20] have investigated the tracer diffusion coefficient for binary hard sphere mixtures. They observe an inverse isotopic mass effect, where heavier tracer particles diffuse faster beyond a certain solvent density than lighter tracer particles. Due to the computational

cost of simulating highly size asymmetric systems, past studies have focused on small size disparity and/or moderate mole fractions of colloidal particles.

Erpenbeck [21–23] provided the first complete transport study, comparing predictions from Enskog theory and molecular dynamics results for binary hard sphere mixtures approximating a Helium-Xenon gas mixture. The mutual diffusion, thermal diffusion, thermal conductivity and shear viscosity are given over a range of state points. Enskog theory was found to provide a fairly good description of the transport properties for the conditions studied. Yeganegi and Zolfaghari [24] have investigated the thermal diffusion coefficient of binary hard spheres (for moderate size ratios) using non-equilibrium molecular dynamics. They observe a minimum in the thermal diffusion with density and good agreement with Enskog theory. Recently, Bastea [25] has investigated the viscosity and thermal conductivity of highly asymmetric “soft-sphere” mixtures at very low volume fractions of the larger spheres. Enskog theory was only able to qualitatively describe the results in that study.

In the present work, we perform event driven molecular dynamics simulations to study the static and transport properties of binary hard sphere mixtures with a diameter ratio of 0.1 and a mass ratio of 0.001. One of the motivations of this work is to further explore the “fines effect” revealed in these systems in a previous study by Lue and Woodcock [9]. Another aim of this work is to quantitatively test the predictive ability of the revised Enskog theory [26] for these binary hard sphere systems over a broad range of conditions. The remainder of this paper is organized as follows. Details of the hard sphere mixture model and the relation of the transport coefficients to the microscopic dynamics of the system are discussed in Section 7.2. The details of the molecular dynamics calculations and the direct simulation Monte Carlo solution of the Enskog equation are provided in Section 7.3. The simulation data for the static and the transport properties of the binary hard sphere mixtures are presented in Section 7.4, and the results are compared against the predictions of the Enskog theory. Finally, the main findings of this work are summarized in Section 7.5.

7.2 Theoretical Background

We consider systems consisting of additive hard spheres with differing diameters and masses. Spheres of type a have a diameter σ_a and a mass m_a . The spheres are not permitted to overlap, and so the interaction potential u_{ab} between a sphere of type a and a sphere of type b is given by

$$u_{ab}(r) = \begin{cases} \infty & \text{if } r \leq \sigma_{ab} \\ 0 & \text{if } r > \sigma_{ab} \end{cases} \quad (7.2.1)$$

where r is the distance between the centers of the two spheres, and $\sigma_{ab} = (\sigma_a + \sigma_b)/2$. Due to the simple nature of this interaction potential, all properties of hard sphere mixtures

have a trivial dependence on the temperature.

One major advantage of the hard sphere model is the simplicity of its dynamics. The dynamics of hard sphere systems is driven by collisions between spheres. Between collisions, the spheres travel at constant velocity. The solution of the trajectory of the system then reduces to determining the sequence of collisions between the spheres. These collisions alter the velocities of the spheres but conserve their energy and momentum. After a collision between a sphere i of type a and a sphere j of type b , the velocities of the spheres become \mathbf{v}'_i and \mathbf{v}'_j

$$\begin{aligned}\mathbf{v}'_i &= \mathbf{v}_i - \frac{2\mu_{ab}}{m_a} (\mathbf{v}_{ij} \cdot \hat{\mathbf{r}}_{ij}) \hat{\mathbf{r}}_{ij} \\ \mathbf{v}'_j &= \mathbf{v}_j + \frac{2\mu_{ab}}{m_b} (\mathbf{v}_{ij} \cdot \hat{\mathbf{r}}_{ij}) \hat{\mathbf{r}}_{ij}\end{aligned}\quad (7.2.2)$$

where \mathbf{v}_i and \mathbf{v}_j are the velocities of the spheres immediately before collision, $\hat{\mathbf{r}}_{ij}$ is a unit vector pointing from the center of sphere i to the center of sphere j , $\mathbf{v}_{ij} = \mathbf{v}_i - \mathbf{v}_j$ is their relative velocity, and $\mu_{ab} = m_a m_b / (m_a + m_b)$ is the reduced mass.

7.2.1 Static Properties

The pair correlation functions give an indication of the average local environment of the particles in a system. For hard sphere systems, the values of the pair correlation functions at contact $g_{ab}(\sigma_{ab}^+)$ play an important role. In particular, they are directly related to the collision rates between the spheres:

$$g_{ab}(\sigma_{ab}^+) = (4\pi\rho_b\sigma_{ab}^2 t_{ab})^{-1} (2\pi\beta\mu_{ab})^{1/2} \quad (7.2.3)$$

where ρ_b is the number density of spheres of type b , $\beta = (k_B T)^{-1}$, k_B is the Boltzmann constant, T is the absolute temperature, and t_{ab} is the mean time between which a sphere of type a undergoes collisions with a sphere of type b . The quantity t_{ab} can be calculated from the number of a - b collisions $N_{ab}^{(\text{coll})}$ that occur in a simulation of duration t

$$t_{ab} = \frac{N_a t}{2N_{ab}^{(\text{coll})}} \quad (7.2.4)$$

where N_a is the number of spheres of type a in the system. An advantage of molecular dynamics simulations over Monte Carlo simulations is that the contact values of the pair correlation functions can be directly calculated from the times t_{ab} and does not require the extrapolation of the pair correlation to contact.

The contact values of the pair correlation functions are also directly related to the equation of state of the hard sphere system:

$$\frac{\beta p}{\rho} = 1 + \frac{2\pi\rho}{3} \sum_{a,b} x_a x_b \sigma_{ab}^3 g_{ab}(\sigma_{ab}^+) \quad (7.2.5)$$

where p is the system pressure, ρ is the total number density of spheres, x_a is the mole fraction of spheres of type a , and the lowercase Latin indexes run over all species (i.e. A and B for a binary mixture) present in the system.

Due to the fundamental importance of the contact values of the pair correlation functions for hard sphere systems, there have been many efforts to develop expressions to describe them [5, 6, 8, 27]. One of the most popular is the Boublik-Mansoori-Carnahan-Starling (BMCSL) equation of state [28, 29], which is an interpolation between the virial and compressibility expressions of the Percus-Yevick theory [30]. This is given by

$$g_{ab}^{\text{BMCSL}}(\sigma_{ab}^+) = \frac{1}{1 - \xi_3} + \frac{3\xi_2}{2(1 - \xi_3)^2} \frac{\sigma_a \sigma_b}{\sigma_{ab}} + \frac{\xi_2^2}{2(1 - \xi_3)^3} \frac{\sigma_a^2 \sigma_b^2}{\sigma_{ab}^2} \quad (7.2.6)$$

where ξ_n is defined by

$$\xi_n = \frac{\pi \rho}{6} \sum_a x_a \sigma_a^n \quad (7.2.7)$$

Note that the solid fraction occupied by the spheres is given by $\phi = \xi_3$.

The BMCSL equation yields predictions that are generally in good agreement with simulation data for hard sphere mixtures over a broad range of diameters and compositions [4]. However, for highly size asymmetric binary systems at small mole fractions of the larger spheres (often referred to as the colloidal limit), the BMCSL significantly underpredicts the contact value of the pair correlation function between the larger spheres, as compared to simulation results [4, 7, 31].

Recently, there have been several efforts to correct this. Viduna and Smith [32, 33] have suggested a new expression, based on an empirical equation of state

$$g_{ab}^{\text{VS}}(\sigma_{ab}^+) = \frac{1}{1 - \xi_3} + \frac{3 - \xi_3 + \xi_3^2/2}{2(1 - \xi_3)^2} \xi_2 \frac{\sigma_a \sigma_b}{\sigma_{ab}} + \frac{2 - \xi_3 - \xi_3^2/2}{6(1 - \xi_3)^3} (2\xi_2^2 + \xi_1 \xi_3) \frac{\sigma_a^2 \sigma_b^2}{\sigma_{ab}^2} \quad (7.2.8)$$

This compact expression appears to compare well with simulation results. In the case of binary hard sphere mixtures, Henderson et al. [10] have suggested further modifications to the BMCSL and VS equations so that the contact value of the pair correlation function between the larger spheres yield the correct limiting behavior as the diameters of the larger spheres become infinite [31]. Their expressions for the pair correlation functions (which we denote as HC2) are given by

$$g_{BB}^{\text{HC2}}(\sigma_{ab}^+) = g_{BB}^{\text{BMCSL}}(\sigma_{BB}^+) \text{ or } g_{BB}^{\text{VS}}(\sigma_{BB}^+) \quad (7.2.9)$$

$$g_{AB}^{\text{HC2}}(\sigma_{ab}^+) = g_{AB}^{\text{BMCSL}}(\sigma_{AB}^+) + \frac{\xi_2^2 \sigma_{BB}^2}{(1 - \xi_3)^3 (1 + R)^2} - \frac{\xi_2^3 \sigma_{BB}^3}{(1 - \xi_3)^3 (1 + R)^3} \quad (7.2.10)$$

$$g_{AA}^{\text{HC2}}(\sigma_{ab}^+) = g_{AA}^{\text{VS}}(\sigma_{BB}^+) + e^x - 1 - x - x^2/2 \quad (7.2.11)$$

where A refers to the larger spheres, B refers to the smaller spheres, $R = \sigma_B/\sigma_A$ is the diameter ratio, and $x = 3(\xi_2 \sigma_{AA} - \xi_3)/2$.

7.2.2 Calculation of Transport Coefficients

In the continuum description of fluids [34], balance equations are typically used to relate the conserved properties of the system (e.g., energy, momentum, and mass) to their fluxes. To close these equations, constitutive relations are required. These relations link the diffusive fluxes to gradients in the thermodynamic properties of the system. Transport coefficients are defined through the assumption that the diffusive fluxes depend linearly on the thermodynamic driving forces, which are gradients of local thermodynamic properties of the system.

There are several possible choices [34] for the thermodynamic forces \mathbf{X} and the diffusive fluxes \mathbf{J} . For NVE molecular dynamics simulations, the most convenient [21] choice is the “mainstream” (or “unprimed” [21, 34]) definition of the fluxes. These are defined as

$$\mathbf{X}_a = -T\boldsymbol{\nabla} \left(\frac{\mu_a}{T} \right) \quad \mathbf{X}_\lambda = -\frac{1}{T}\boldsymbol{\nabla} T \quad (7.2.12a)$$

$$\mathbf{J}_a = L_{a\lambda}\mathbf{X}_\lambda + \sum_b L_{ab}\mathbf{X}_b \quad \mathbf{J}_\lambda = L_{\lambda\lambda}\mathbf{X}_\lambda + \sum_a L_{\lambda a}\mathbf{X}_a \quad (7.2.12b)$$

where μ_a is the chemical potential, and \mathbf{J}_a is the diffusive flux of species a , \mathbf{J}_λ is the energy flux, $L_{\lambda\lambda}$ is the thermal conductivity, L_{ab} is the mutual diffusion coefficient, and $L_{a\lambda}$ is the thermal diffusivity. The transport coefficients are defined through Eqs. (7.2.12).

The relationship between stress tensor $\boldsymbol{\tau}$ and the strain rate in the fluid is defined in the standard manner:

$$\boldsymbol{\tau} = p\mathbf{1} + \left(\frac{2}{3}\eta - \kappa \right) (\boldsymbol{\nabla} \cdot \mathbf{u}) \mathbf{1} - \eta \left[\boldsymbol{\nabla} \mathbf{u} + (\boldsymbol{\nabla} \mathbf{u})^T \right] \quad (7.2.13)$$

where η is the shear viscosity, κ is the bulk viscosity, and \mathbf{u} is the streamline velocity of the fluid. The quantity $\mathbf{1}$ represents the unit matrix, and the superscript T indicates the transpose of a matrix.

The Onsager reciprocity relations ($L_{ab} = L_{ba}$ and $L_{a\lambda} = L_{\lambda a}$), combined with the requirement that $\sum_a \mathbf{J}_a = 0$ (due to the definition of the diffusive flux) which implies $L_{aa} = -\sum_{b \neq a} L_{ab}$, reduce the number of independent transport coefficients to $L_{\lambda\lambda}$, $L_{A\lambda}$, L_{AA} , η , and κ . In the following section, we discuss how these transport coefficients can be determined from equilibrium molecular dynamics simulations.

7.2.3 Einstein Forms of the Green-Kubo Relations

The Green-Kubo formulas relate the time correlation functions of the microscopic fluxes directly to the transport coefficients [1]. However, the Green-Kubo relations are an unpopular method for obtaining the transport coefficients from molecular dynamics simulations, as they require long simulation times to obtain good statistics. This is not a significant issue in hard sphere systems, as long simulation times are more easily acces-

Table 7.1: Displacement functions for an isotropic system required to evaluate the Einstein form of the Green-Kubo relationships, see Eq. (7.2.14).

\overline{W}_ψ	
\mathbf{W}_a	$\sum_{\Delta t_c}^t \sum_k^{N_a} m_k \mathbf{v}_k \Delta t_c - c_a \sum_k^N m_k \mathbf{v}_k \Delta t_c$
\mathbf{W}_λ	$\sum_{\Delta t_c}^t \left(\sum_k^N \frac{1}{2} m_k v_k^2 \mathbf{v}_k \Delta t_c + \frac{1}{2} m_i \Delta v_i^2 \mathbf{v}_{ij} \right)$
\mathbf{W}_η	$\sum_{\Delta t_c}^t \left(\sum_k^N m_k \mathbf{v}_k \mathbf{v}_k \Delta t_c + m_i \mathbf{r}_{ij} \Delta \mathbf{v}_i - 1 p V \Delta t_c \right)$

The first summation runs over all time intervals between collisions Δt_c that occur during the simulation time t . The indexes i and j denote the pair of spheres that undergo collision at the end of this time interval. Note that c_a is the mass fraction of sphere of type a .

sible. For systems with particles interacting with discontinuous potentials, the Einstein form of the Green-Kubo relations must be used, due to the impulsive nature of the interaction potential. The full derivation of the these formulas are already available [1, 21], and, therefore, only the final expressions are presented here for completeness.

The Einstein relations have the general form

$$\psi(t) = \frac{\beta}{2Vt} \langle W_{\psi_1}(t) W_{\psi_2}(t) \rangle \quad (7.2.14)$$

where $\psi(t)$ is a time dependent transport coefficient, V is the volume of the system, and W_{ψ_1} and W_{ψ_2} are displacement functions corresponding to time integrals of the microscopic fluxes. The displacement functions for a system with zero total momentum in the microcanonical ensemble are given in Table 7.1. The pair of displacement functions that correspond to each of the transport coefficients are summarized in Table 7.2. In hydrodynamic regime, the transport coefficients are given by the infinite time limit of Eq. (7.2.14)

$$\psi = \lim_{t \rightarrow \infty} \psi(t) \quad (7.2.15)$$

A sample of reduced correlators for a single molecular dynamics simulation run is plotted in Fig. 7.1. The function $t\psi(t)$ typically displays transient behavior for short times before changing to the linear, long-time regime. All the transport properties, with the exception of the bulk viscosity, rapidly transition to the linear regime within a few mean free times. The bulk viscosity, however, only slowly approaches the linear regime, and, consequently, the limiting values are difficult to extract. As a result, we do not present data for the bulk viscosity.

A time correlation function of a finite sized simulation is only representative of a bulk system for a limited duration. Beyond the time a sound wave takes to traverse the simulation box, the system size begins to affect the correlation function. The sound wave traversal time is determined directly from the speed of sound, c . For a hard sphere system

Table 7.2: Transport coefficients and the corresponding displacement functions. The right hand columns indicate which rows of Table 7.1 are used.

ψ	W_{ψ_1}	W_{ψ_2}
L_{ab}	$W_{a,x}$	$W_{b,x}$
$L_{a\lambda}$	$W_{a,x}$	$W_{\lambda,x}$
$L_{\lambda\lambda}$	$W_{\lambda,x}$	$W_{\lambda,x}$
η	$W_{\eta,xy}$	$W_{\eta,xy}$
$\frac{4}{3}\eta + \kappa$	$W_{\eta,xx}$	$W_{\eta,xx}$

As the system is isotropic, the transport coefficients are averaged over all components $x \neq y$ of the displacement functions.

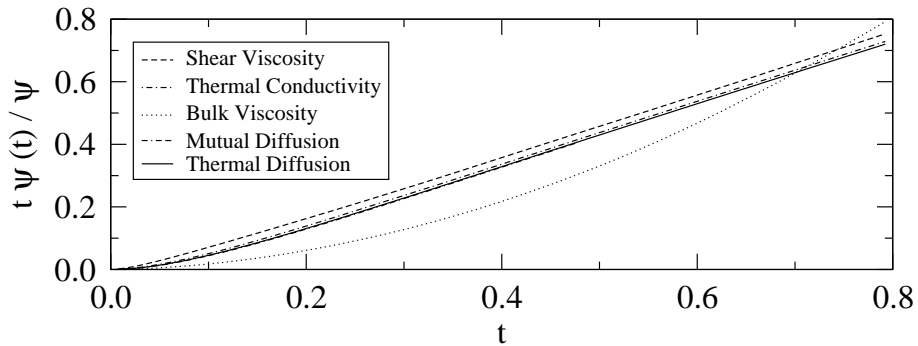


Figure 7.1: Time dependent transport coefficients (see Eq. (7.2.14)), reduced by their infinite time result, from a single simulation run for a binary hard sphere system with $x_A = 0.01$ and solid fraction $\phi = 0.1$. The time is presented in units of $(\beta m_A \sigma_A^2)^{1/2}$; the mean free time is roughly $0.015(\beta m_A \sigma_A^2)^{1/2}$.

the speed of sound is given by

$$c^2 = m^{-1} k_B T \left[\frac{2Z^2}{3} + \frac{\partial \rho Z}{\partial \rho} \right] \quad (7.2.16)$$

where $Z = \beta p / \rho$ is the compressibility factor, and $m = \sum_a x_a m_a$ is the mean particle mass. The HC2 equation of state (see Eqs. (7.2.5), (7.2.9), (7.2.10), and (7.2.11)) is used to estimate the speed of sound, via Eq. (7.2.16). Data for the time correlation functions are only collected for a duration of time shorter than the sound wave traversal time.

7.2.4 Enskog Theory Predictions for the Transport Coefficients

Revised Enskog theory (RET) [26, 35–37] is an extension of the highly successful Enskog theory to mixtures. This is the most widely applied kinetic theory of moderately dense fluids. In the Enskog approximation, all pre-collision correlations between particles are ignored, save for a single static structural correlation function. In a homogeneous system, this reduces to the values of the various pair correlation functions at contact, which govern the collision rates. Given these as input, Enskog theory yields predictions

for the transport properties through the Chapman-Enskog expansion [38].

The standard method to solve to the Enskog equation is to expand the one-particle distribution function in a series of Sonine polynomials. Erpenbeck [21] has compiled the (corrected) Enskog expressions for all transport properties, excluding the bulk viscosity, of hard sphere mixtures. These expressions have been combined with the table of integrals given by Ferziger and Kaper [39] and a linear equation solver to evaluate Enskog theory to the third order in the Sonine expansion. We present results calculated from the BMCSL and HC2 equations to determine the effect of improved values for $g_{ab}(\sigma_{ab}^+)$ on the predictions of the transport properties.

7.2.5 DSMC Solution of the Enskog Equation

Another method for obtaining solutions to the Enskog equations is through the use of the direct simulation Monte Carlo (DSMC) method. This technique was originally developed for the Boltzmann equation but has recently been extended to the Enskog equation [40–42]. In this work, DSMC of the Enskog equation, in the style of Bird’s NTC method [43], is used to provide results. In this approach, the velocity distribution of each species is approximated using a set of samples

$$f_a(\mathbf{v}, t) = \mathcal{N}_a^{-1} \sum_{i=1}^{\mathcal{N}_a} \delta(\mathbf{v} - \mathbf{v}_i(t)) \quad (7.2.17)$$

where \mathcal{N}_a is the number of samples of the velocity distribution of species a . For simplicity, in the following expressions we assume each sample represents a single sphere. Other choices are possible; however, the difference merely affects the relative sample collision testing rates and time scale of the simulation.

The probability that a sample i of species a undergoes a collision event with species b after a time step Δt_{ab} is [44]

$$\omega_{ib} = 4g_{ab}(\sigma_{ab}^+) \pi \rho_b \sigma_{ab}^2 (\mathbf{v}_{ij} \cdot \hat{\mathbf{k}}) \Theta(\mathbf{v}_{ij} \cdot \hat{\mathbf{k}}) \Delta t_{ab} \quad (7.2.18)$$

where j is a randomly chosen sample from species b , $\hat{\mathbf{k}}$ is a randomly chosen relative orientation between the samples on collision, $\mathbf{v}_{ij} = \mathbf{v}_i - \mathbf{v}_j$ is the relative velocity, and Θ is the Heaviside step function. The time step Δt_{ab} describes the rate at which samples in species a are tested for collisions with a sample of species b . For a DSMC calculation of a binary mixture, there are four rates, one for each pairing of the species (AA , AB , BA , and BB).

The simplest DSMC algorithm proceeds by incrementing time to the next test for collisions between species a and b . Each sample i of species a is tested for an event with another sample j , which is randomly selected. A collision is executed with a probability given by Eq. (7.2.18). This collision only affects sample i and not the collision partner j . This method is simple but inefficient because properties that are conserved on collision

(e.g., momentum and energy) are only conserved on average. In addition, all samples in species a are tested at each time step, which is computationally expensive, even though Δt_{ab} is selected to yield only a few events per time step.

An improved algorithm, based on Bird's NTC method, executes symmetric species-species collision events simultaneously, and, therefore, there are three independent test rates for the binary system (Δt_{AA} , $\Delta t_{AB} = \Delta t_{BA}$, and Δt_{BB}). For a given time step, we assume there are a maximum of $N_{ab}^{pairs} = \mathcal{N}_a \omega_{ab}^{(max)} = \mathcal{N}_b \omega_{ba}^{(max)}$ events that may occur for each species; the quantity $\omega_{ba}^{(max)}$ is the maximum observed value of ω_{ba} , which is updated, if required, during the course of a simulation. N_{ab}^{pairs} pairs of a and b samples are randomly selected at each time step. The probability of collision is then scaled to

$$\frac{1}{2}(2 - \delta_{ab})\omega_{ab} \frac{\mathcal{N}_a}{N_{pairs}} \quad (7.2.19)$$

where δ_{ab} is the Kronecker delta. If the collision is accepted, then the velocities of both samples are updated according to the collision rule (see Eq. (7.2.2)). This conserves energy and momentum at all times and greatly improves the statistics of the simulation. Like Enskog theory, the DSMC calculations require g_{ab} (σ_{ab}^+) as input, however, DSMC requires no polynomial expansion to make the problem tractable.

The transport coefficients are obtained through the use of the appropriate time correlation functions, as in the full molecular dynamics simulations (see Section 7.2.2). DSMC provides an attractive method of numerically solving a kinetic equation, especially as computing power increases. Its results are still, however, limited by the approximations of the underlying kinetic equation.

7.3 Simulation Details

In this work, we examine the static and transport properties of highly asymmetric binary hard sphere mixtures. The larger A spheres have a diameter σ_A and mass m_A , and the smaller B spheres have a diameter σ_B and mass m_B . We consider systems with $\sigma_B/\sigma_A = 0.1$ and $m_B/m_A = 0.001$, consistent with particles of the same density.

Discrete potentials, such as the hard sphere model, have an important advantage over more complex “soft” potentials. Between collisions the spheres or molecules experience no forces and travel on ballistic trajectories. The dynamics can be solved analytically, and the integration of the equations of motion is processed as a sequence of events. Current event driven molecular dynamics algorithms are now quite advanced and allow the simulation of large systems for the long times required to extract accurate transport properties.

7.3.1 MD Simulations

The basic event driven algorithm used in this work to perform the molecular dynamics simulations is fundamentally the same as the one originally described by Alder and

Wainwright [45]. Neighbor lists and the delayed states algorithm [46] are included to optimize the calculations. These methods are combined with a new bounded priority queue, suggested by Paul [47], to remove the system size dependence of sorting the event queue. Finally, the interactions between the largest spheres are removed from the neighbor list and processed separately [12] to allow the use of a smaller cell size and reduced number of collision tests. This removal is restricted to low mole fractions of the larger spheres as the overhead of these removed interactions is of order $O(N^2)$ in the number of large spheres.

A total of $N = 13500$ spheres in a cubic box of volume V with standard periodic boundary conditions were used in all the simulations. The volume of the system and the relative number of large and small spheres (i.e., N_A and N_B) were adjusted to obtain the required packing fraction and composition, respectively. For each of the systems examined, the initial configurations were equilibrated over a period of 10^7 collisions and then run for 20 trajectories of 10^8 collisions to collect the collision statistics and time correlation functions.

The time correlation functions for the various transport properties were collected over approximately 100 intervals of a mean free time, using the start time averaging method [48]. The last 50 values of the correlator were fitted to a line to extract the long time limit of the transport coefficient.

7.3.2 DSMC Simulations

DSMC simulations were performed using a total of $\mathcal{N}_A + \mathcal{N}_B = 13500$ samples of the velocity distribution. Each of the simulations was initially equilibrated for 10^7 collisions. The time correlation functions were then collected over 8 separate trajectories, each consisting of 10^8 collisions, using 100 intervals of a mean free time. The statistical uncertainty of the shorter DSMC calculations are smaller than the uncertainties of the MD simulations because Enskog theory neglects dynamical correlations.

7.4 Results and Discussion

In this section, we present the results of the molecular dynamics simulations for the contact value of the pair correlation functions and the transport coefficients of binary hard sphere mixtures. A comparison of the predictions of the revised Enskog theory is also provided. All quantities are reported in reduced units, where the unit of mass is m_A , the unit of length is σ_A , and the unit of energy is $k_B T$.

7.4.1 Static Properties

The variation of the pressure of the binary hard sphere mixtures with packing fraction and composition is shown in Fig. 7.2. The symbols are the data from the molecular

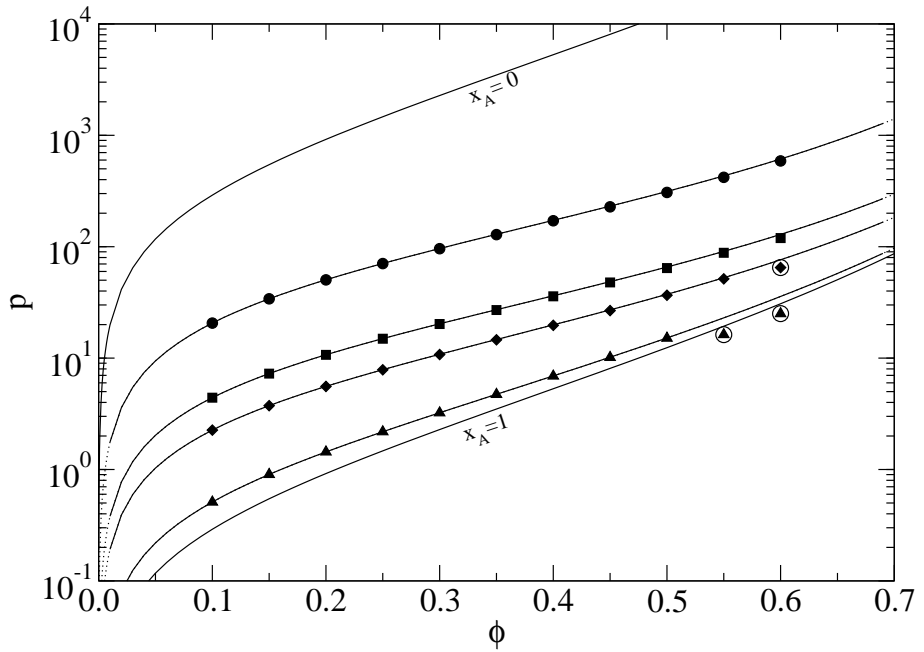


Figure 7.2: Pressure p as a function of solid fraction ϕ for binary hard sphere mixtures with $\sigma_B/\sigma_A = 0.1$, $m_B/m_A = 0.001$, and (i) $x_A = 0.01$ (circles), (ii) $x_A = 0.05$ (squares), (iii) $x_A = 0.1$ (diamonds), and (iv) $x_A = 0.5$ (triangles). The filled symbols are from molecular dynamics simulations, the lines are the predictions of the BMCSL (solid) and HC2 (dotted) equations of state. Data points are circled where the system shows signs of freezing.

dynamics simulations, and the lines are the predictions of the BMCSL (solid) and HC2 (dotted) equations of state. These equations of state provide an excellent description of the simulation data, with the exception of the very highest packing fractions where they overpredict the pressure. These deviations, however, are due to the onset of freezing of the larger spheres; the single component hard sphere fluid begins to freeze at a packing fraction of 0.494 [49].

The contact values of the AA , AB , and BB pair correlation functions are plotted in Fig. 7.3 as a function of the total volume fraction of spheres for different mole fractions of the larger A spheres x_A . The simulation results for g_{BB} are well described by the BMCSL theory. This is in agreement with previous simulation studies of binary hard spheres mixtures [7, 13]. The VS predictions (not shown) provide equally accurate predictions for g_{BB} .

The BMCSL predictions for g_{AB} lie above the simulation results at high density for the lowest mole fraction studied. The HC2 predictions are higher still, however, the error is within a few percent. The corrections of Henderson et al. [10] to g_{AB} are small for the systems studied. The VS predictions (not shown) lie between the HC2 and the BMCSL results.

For the contact value of pair correlation function between the larger spheres, the BMCSL predictions fall significantly below the simulation results at high density for the low-

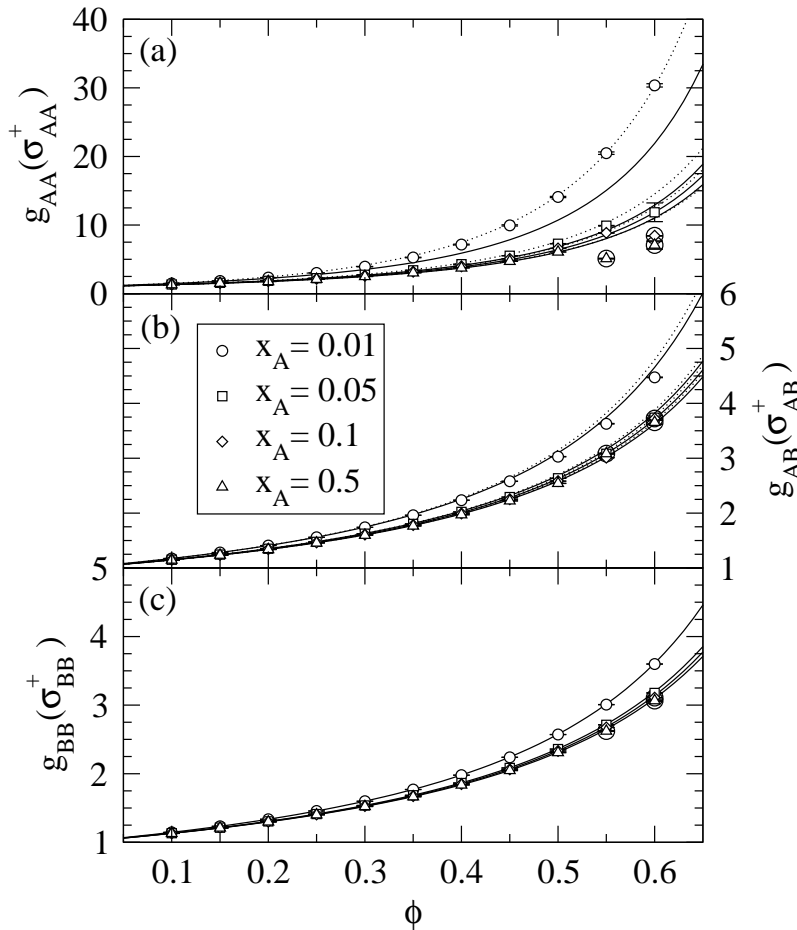


Figure 7.3: Contact value of the pair correlation function $g_{ab}(\sigma_{ab}^+)$ between the large-large (a), large-small (b), and small-small (c) sphere species as a function of solid fraction ϕ for binary hard sphere mixtures with $\sigma_B/\sigma_A = 0.1$, $m_B/m_A = 0.001$, and (i) $x_A = 0.01$ (circles), (ii) $x_A = 0.05$ (squares), (iii) $x_A = 0.1$ (diamonds), and (iv) $x_A = 0.5$ (triangles). The solid lines are the predictions of the BMCSEL equation (see Eq. (7.2.6)), and the dotted lines are the predictions of the HC2 equation (see Eq. (7.2.11)). Simulation data points are circled where the system shows signs of freezing.

est mole fraction studied. The HC2 predictions are exceptionally accurate, even for the smallest mole fractions of the larger spheres. This is due to the success of the underlying VS equation (not shown), which give results that are nearly indistinguishable from the HC2 equation. At $\phi \approx 0.55$, $g_{AA}(\sigma_{AA}^+)$ for the $x_A = 0.5$ system decreases significantly. This also occurs in the $x_A = 0.1$ system at a higher packing fraction of $\phi = 0.6$. It appears that the larger component has frozen while the smaller spheres remain fluid.

Overall, the HC2 expression is accurate and provides excellent estimates for the contact values of the pair correlation functions for all the conditions studied in this work.

7.4.2 Thermal Conductivity

The thermal conductivity of the binary hard sphere mixtures is plotted in Fig. 7.4a with respect to the packing fraction and in Fig. 7.4b with respect to the pressure. The molecu-

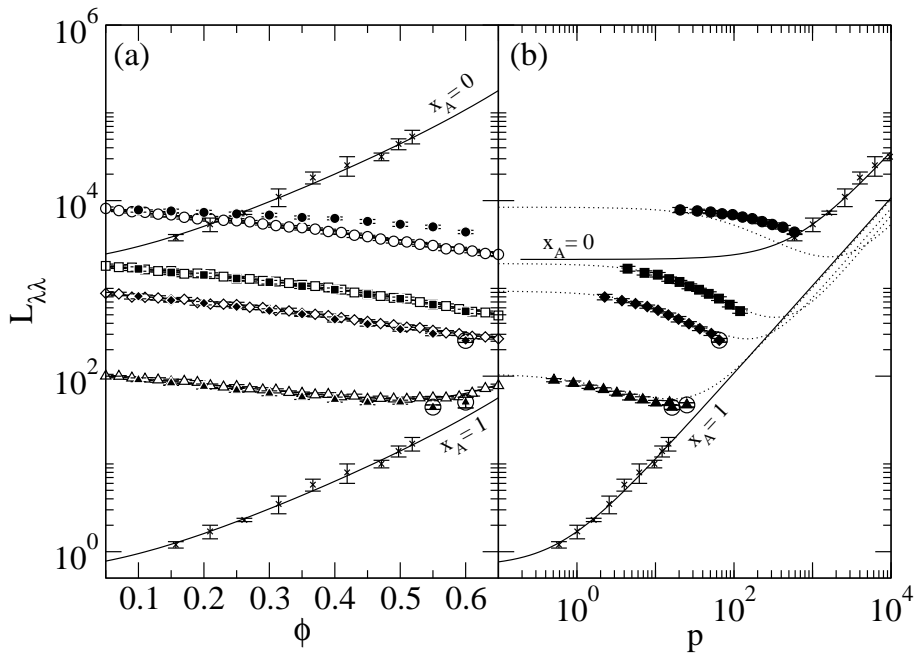


Figure 7.4: Thermal conductivity $L_{\lambda\lambda}$ as a function of solid fraction ϕ (a) and pressure p (b) for binary hard sphere mixtures with $\sigma_B/\sigma_A = 0.1$, $m_B/m_A = 0.001$, and (i) $x_A = 0.01$ (circles), (ii) $x_A = 0.05$ (squares), (iii) $x_A = 0.1$ (diamonds), and (iv) $x_A = 0.5$ (triangles). The filled symbols are from molecular dynamics simulations, and the open symbols are the DSMC results for the Enskog theory. The crosses are molecular dynamics simulations for single component hard spheres, taken from Ref. [50]. The lines are third order Enskog theory predictions using BMCSL (solid) and HC2 (dotted) values of $g_{ab}(\sigma_{ab}^+)$. Simulation data points are circled where systems show signs of freezing.

lar dynamics simulation data are given by the filled symbols. The crosses are molecular simulation data for single component hard spheres, taken from Ref. [50]. For single component hard sphere systems, the thermal conductivity increases with increasing packing fraction and pressure. The initial addition of smaller spheres to a system of larger spheres (i.e. decreasing x_A) significantly increases the thermal conductivity of the mixture. At the same packing fraction, a system with a lower mole fraction of larger spheres will have many more particles than a system with a higher mole fraction of larger spheres. These additional particles enhance the ability of system to transport energy. With the addition of smaller spheres to the large sphere system, we observe that the thermal conductivity no longer increases monotonically with the packing fraction (or the pressure). Rather, the thermal conductivity initially decreases with increasing packing fraction down to a minimum value, and then it increases. The packing fraction at the minimum increases as the fraction of smaller spheres increases.

Interestingly, at packing fractions below $\phi \approx 0.25$, the thermal conductivity of pure B spheres (i.e., $x_A = 0$) is lower than the thermal conductivity for the $x_A = 0.01$ system, while for $\phi > 0.25$ it is higher. This implies that at sufficiently low packing fraction (or pressure) the thermal conductivity of the system must have a maximum with respect to x_A . Physically, this would correspond to a situation where the addition of larger spheres

to a fluid of smaller hard spheres would enhance its thermal conductivity.

The solid lines in Fig. 7.4 are the predictions of Enskog theory within the third order Sonine approximation with the BMCSL expressions for the collision rates, while the dotted lines are the third order Enskog predictions with the HC2 expressions. The difference between using the BMCSL and HC2 expressions in Enskog theory is negligible, as the collisional contribution to the thermal conductivity is dominated by the *BB* and *BA* interactions (see Figs. 7.3b and c). The open symbols in Fig. 7.4 are from DSMC calculations using the HC2 expressions for the collision rates. These results are nearly identical to the third order Sonine approximation, indicating the accuracy of the approximation and validating the DSMC code.

The simulation results are well described by Enskog theory for the pure hard sphere systems (i.e. $x_A = 0$ and 1), as well as for mixtures with relatively high mole fractions of the larger spheres ($x_A \geq 0.05$). At high packing fractions, the Enskog predictions deviate slightly for the case $x_A = 0.5$; however, this occurs at the conditions where component *A* appears to freeze (see Fig. 7.3a), and the BMCSL and HC2 expressions for g_{ab} (σ_{ab}^+) are not applicable for solid phases.

For $x_A = 0.01$, Enskog theory significantly underpredicts the thermal conductivity of the system. This deviation may be related to the enhanced mobility of the system due to the fines effect [9] and is a result of a dynamic process not captured by Enskog theory. Note, however, that Enskog theory provides good predictions for the thermal conductivity of one component hard sphere systems [50], so one expects that for vanishing amounts of the larger spheres (i.e. the limit where $x_A \rightarrow 0$), Enskog theory should again provide a fairly good description of the simulation data.

7.4.3 Shear Viscosity

The shear viscosity is plotted in Fig. 7.5. The viscosity of all the mixtures increases monotonically with the packing fraction of the spheres and the pressure of the system (see Fig. 7.5a-c). Unlike for the thermal conductivity, the Enskog theory predictions for the shear viscosity using the HC2 expression for the collision rates noticeably differ from the BMCSL results (see Fig. 7.5a); however, this only occurs in regions where Enskog theory poorly describes the simulation results (see Fig. 7.5b and c). Enskog theory captures the low density behavior of the viscosity quite well. For single component hard sphere systems, Enskog theory is known to underpredict the viscosity at high densities [51], due to its inability to account for correlated collisions resulting from the caging of spheres at these conditions. For the binary hard sphere mixtures that we study here, the Enskog theory underpredicts the viscosity, in general. However, the case $x_A = 0.01$ is an exception, where Enskog theory actually overpredicts the viscosity at high packing fractions.

An interesting “fines” effect occurs in the viscosity of these systems. At low overall packing fractions (or pressures), the addition of smaller spheres to a system of larger spheres (i.e. decreasing x_A) increases the viscosity of the system. However, above a

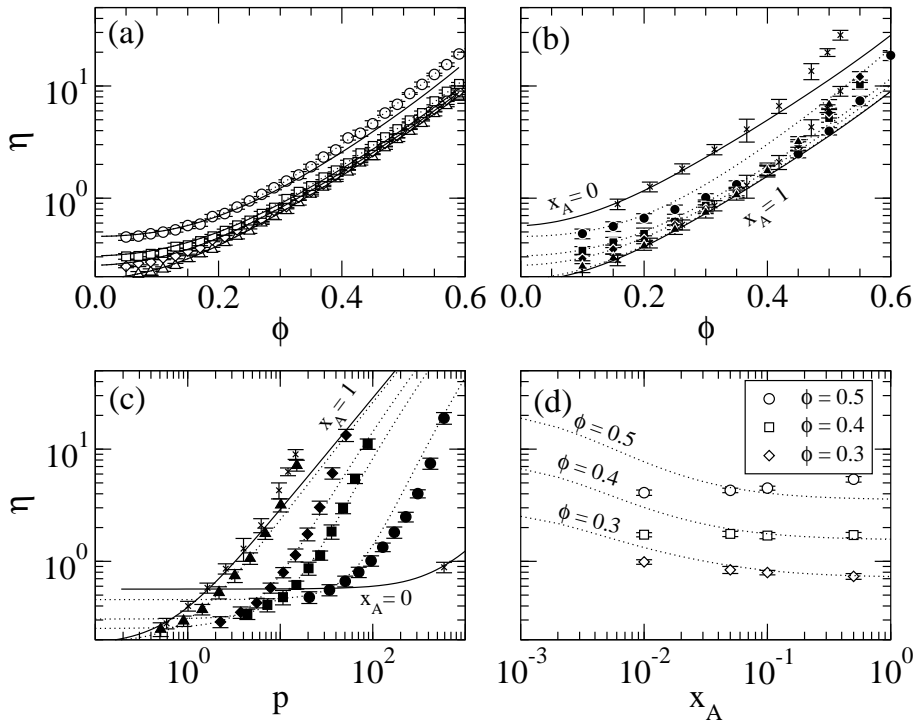


Figure 7.5: Shear viscosity η as a function of solid fraction ϕ (a-b), pressure p (c), and mole fraction x_A (d) for binary hard sphere mixtures with $\sigma_B/\sigma_A = 0.1$ and $m_B/m_A = 0.001$. With the exception of (d), the symbols indicate a mole fraction of (i) $x_A = 0.01$ (circles), (ii) $x_A = 0.05$ (squares), (iii) $x_A = 0.1$ (diamonds), and (iv) $x_A = 0.5$ (triangles). The filled symbols are from molecular dynamics simulations, and the open symbols are the DSMC results for the Enskog theory. The crosses are molecular dynamics simulations for single component hard spheres, taken from Ref. [50]. The lines are third order Enskog theory predictions using the BMCSL (solid) and HC2 (dotted) predictions for $g_{ab}(\sigma_{ab}^+)$.

packing fraction of about $\phi = 0.4$, the curves for the viscosity crossover, and the addition of smaller spheres to a system of larger spheres *decreases* the viscosity of the system. This is highlighted in Fig. 7.5d where the viscosity is almost independent of composition at a packing fraction of $\phi = 0.4$. The “fines” effect is not captured by Enskog theory, which indicates its origin is in dynamical correlations between particles. In these systems, the presence of the smaller spheres leads to an attractive depletion force [2, 3] between the larger spheres, which is entropically driven. This force may disrupt the caging of larger spheres [9] by forcing them into closer contact, thereby creating a more open network and increasing the mobility of both species.

7.4.4 Thermal Diffusion Coefficient

Figure 7.6 presents the thermal diffusivity of the larger spheres over a range of packing fractions and pressures. Because $L_{A\lambda}$ is negative, the larger species tends to move towards regions of higher temperature. Increasing the packing fraction, the pressure, or the fraction of larger spheres in the system decreases the magnitude of the thermal diffusivity.

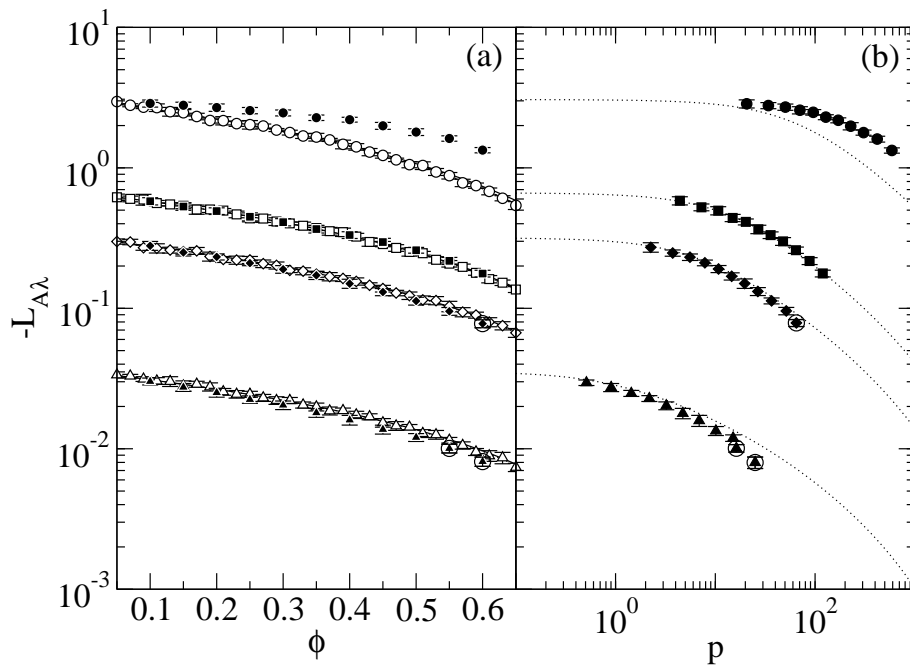


Figure 7.6: Thermal diffusivity $L_{A\lambda}$ as a function of solid fraction ϕ (a) and pressure p (b) for binary hard sphere mixtures with $\sigma_B/\sigma_A = 0.1$, $m_B/m_A = 0.001$, and (i) $x_A = 0.01$ (circles), (ii) $x_A = 0.05$ (squares), (iii) $x_A = 0.1$ (diamonds), and (iv) $x_A = 0.5$ (triangles). The filled symbols are from molecular dynamics simulations, and the open symbols are the DSMC results for the Enskog theory. The lines are third order Enskog theory predictions using the BMCSL (solid) and HC2 (dotted) predictions for $g_{ab}(\sigma_{ab}^+)$. Simulation data points are circled where the system shows signs of freezing.

This general trend is in agreement with previous NEMD simulations [24].

The use of the HC2 expressions with Enskog theory offers no significant improvement on the BMCSL predictions, again due to the dominance of the small spheres in the energy transport. Enskog theory is in quantitative agreement with the simulation data over a broad range of conditions examined in this work. However, the main exception is for the composition $x_A = 0.01$, where it substantially underpredicts the $L_{A\lambda}$ at the higher packing fractions.

7.4.5 Mutual Diffusion Coefficient

The mutual diffusion coefficient of the binary hard sphere mixtures is plotted in Fig. 7.7. The mutual diffusion coefficient behaves similarly to the thermal diffusivity. The displacement functions required to calculate this transport coefficient contain no potential terms, and therefore, they do not contain a collisional component of the flux (see Tables 7.1 and 7.2). Consequently, Enskog theory performs equally well with HC2 or BMCSL contact radial distribution values. Similar to the results for the thermal diffusivity, Enskog theory is in quantitative agreement with the simulation data over most of the conditions examined, with the exception of the $x_A = 0.01$ systems, where it significantly underpredicts the diffusion coefficient.

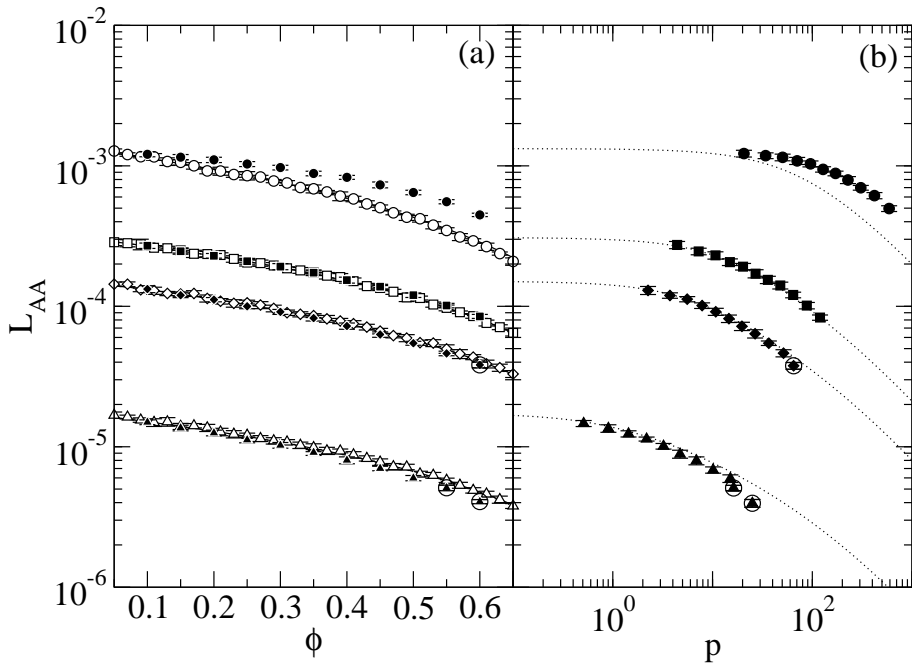


Figure 7.7: Mutual diffusion coefficient L_{AA} as a function of solid fraction ϕ (a) and pressure p (b) for binary hard sphere mixtures with $\sigma_B/\sigma_A = 0.1$, $m_B/m_A = 0.001$, and (i) $x_A = 0.01$ (circles), (ii) $x_A = 0.05$ (squares), (iii) $x_A = 0.1$ (diamonds), and (iv) $x_A = 0.5$ (triangles). The filled symbols are from molecular dynamics simulations, and the open symbols are the DSMC results for the Enskog theory. The lines are third order Enskog theory predictions using the BMCSL (solid) and HC2 (dotted) predictions for $g_{ab}(\sigma_{ab}^+)$. Simulation data points are circled where the system shows signs of freezing.

7.5 Conclusions

In this work, we examined the properties of binary mixtures of hard spheres with a diameter ratio of $\sigma_B/\sigma_A = 0.1$ and a mass ratio of $m_B/m_A = 0.001$. The BMCSL equation of state is able to accurately describe the pressure for all the conditions that we investigated where the system did not freeze. However, it underpredicts the value of g_{AB} and g_{AA} , especially at high packing fractions and low mole fractions of the larger spheres. The recently developed HC2 equation, however, is able to quantitatively predict these quantities.

Enskog theory provides fairly accurate predictions for the transport coefficients of the systems that we studied in this work. The third order Sonine approximation and the DSMC results agree well with one another, both validating the DSMC code and demonstrating that the third order solution is sufficiently accurate over the conditions studied. At low mole fractions of the larger hard spheres, Enskog theory fails to capture the behavior of the transport properties, especially the shear viscosity. This may be due to the increased correlations in the collisions between the larger spheres caused by the depletion forces due to the presence of the smaller spheres.

DSMC provides a speed benefit over traditional molecular dynamics simulations where large size asymmetries and low mole fractions are computationally expensive. Unfortu-

nately, this is where Enskog theory begins to break down in predicting the transport properties of the fluid. Extension of DSMC to other kinetic theories, such as ring theory, is necessary to capture this behavior, however, these techniques are yet to be developed.

We find a “fines” effect where the addition of smaller spheres to a larger hard sphere fluid decreases the viscosity of the system, which occurs at packing fractions greater than about 0.4. This effect is not captured by Enskog theory. With the addition of fines, the thermal conductivity of the mixture no longer monotonically increases with the packing fraction but instead initially decreases with increasing packing fraction to a minimum value and then increases. In addition, at low to moderate packing fractions, there is a region in x_A where the thermal conductivity of the mixture is higher than thermal conductivity of either pure species.

7.6 References

- [1] J. Pierre Hansen and I. R. McDonald. *Theory of Simple Liquids*. 2nd. London: Academic Press, 1986.
- [2] F. Oosawa and S. Asakura, “On Interaction between Two Bodies Immersed in a Solution of Macromolecules”, *J. Chem. Phys.* 22, 1255–1256 (1954).
- [3] A. Vrij, “Polymers at Interfaces and the Interactions in Colloidal Dispersions”, *Pure Appl. Chem.* 48, 471–483 (1976).
- [4] G. Jackson, J. S. Rowlinson and F. van Swol, “Computer Simulation of Mixtures of Hard Spheres”, *J. Phys. Chem.* 91, 4907–4912 (1987).
- [5] D. H. L. Yau, K.-Y. Chan and D. Henderson, “A further test of the Boublik et al equations for binary hard sphere mixtures”, *Mol. Phys.* 88, 1237–1248 (1996).
- [6] D. H. L. Yau, K.-Y. Chan and D. Henderson, “Pair correlation functions for a hard sphere mixture in the colloidal limit”, *Mol. Phys.* 91, 1137–1142 (1997).
- [7] L. Lue and L. V. Woodcock, “Depletion effects and gelation in a binary hard-sphere fluid”, *Mol. Phys.* 96, 1435–1443 (1999).
- [8] K.-Y. Chan and D. Henderson, “Equation of State and Correlation Function Contact Values of a Hard Sphere Mixture”, *Mol. Phys.* 98, 1005–1010 (2000).
- [9] L. Lue and L. V. Woodcock, “Depletion and “fines” effects on transport in hard-sphere colloids”, *Int. J. Thermophys.* 23, 937–947 (2002).
- [10] D. Henderson et al., “Simulation and approximate formulae for the radial distribution functions of highly asymmetric hard sphere mixtures”, *Mol. Phys.* 103, 667–674 (2005).
- [11] A. Santos and M. L. López de Haro, “Contact values of the particle-particle and wall-particle correlation functions in a hard-sphere polydisperse fluid”, *J. Chem. Phys.* 123, 234512 (2005).

- [12] A. Vrabecz and G. Tóth, “Simulation of binary hard-sphere systems with 1 : 5 and 1 : 10 size ratios”, *Mol. Phys.* 104, 1843–1853 (2006).
- [13] M. Alawneh and D. Henderson, “Molecular dynamics results for the radial distribution functions of highly asymmetric hard sphere mixtures”, *Mol. Phys.* 106, 607–614 (2008).
- [14] M. Alawneh and D. Henderson, “Molecular dynamics results for the radial distribution functions of highly asymmetric hard sphere mixtures (vol 106, pg 607, 2008)”, *Mol. Phys.* 106, 2407–2408 (2008).
- [15] P. T. Herman and B. J. Alder, “Studies in molecular dynamics. 11. Correlation-functions of a hard-sphere test particle”, *J. Chem. Phys.* 56, 987–991 (1972).
- [16] G. Subramanian, D. Levitt and H. T. Davis, “Computer studies of the onset of Brownian motion in a hard sphere fluid”, *J. Chem. Phys.* 60, 591–594 (1974).
- [17] B. J. Alder, W. E. Alley and J. H. Dymond, “Studies in molecular-dynamics. 14. Mass and size dependence of the binary diffusion coefficient”, *J. Chem. Phys.* 61, 1415–1420 (1974).
- [18] V. Y. Rudyak, G. V. Kharlamov and A. A. Belkin, “The velocity autocorrelation function of nanoparticles in a hard-sphere molecular system”, *Tech. Phys. Let.* 26, 553–556 (2000).
- [19] V. Y. Rudyak, G. V. Kharlamov and A. A. Belkin, “Diffusion of nanoparticles and macromolecules in dense gases and liquids”, *High Temp.* 39, 264–271 (2001).
- [20] A. J. Easteal and L. A. Woolf, “Tracer diffusion in hard-sphere liquids from molecular-dynamics simulations”, *Chem. Phys. Lett.* 167, 329–333 (1990).
- [21] J. J. Erpenbeck, “Transport-coefficients of hard-sphere mixtures theory and Monte-Carlo molecular-dynamics calculations for an isotopic mixture”, *Phys. Rev. A.* 39, 4718–4731 (1989).
- [22] J. J. Erpenbeck, “Transport-coefficients of hard-sphere mixtures. 2. Diameter ratio 0.4 and mass ratio 0.03 at low-density”, *Phys. Rev. A.* 45, 2298–2307 (1992).
- [23] J. J. Erpenbeck, “Transport-coefficients of hard-sphere mixtures. 3. Diameter ratio 0.4 and mass-ratio 0.03 at high fluid density”, *Phys. Rev. E.* 48, 223–232 (1993).
- [24] S. Yeganegi and M. Zolfaghari, “Non-equilibrium molecular dynamics calculation of thermal diffusion factor in binary mixtures of hard spheres”. English, *Fluid Phase Equilibria.* 243, 161–165 (2006).
- [25] S. Bastea, “Transport in a highly asymmetric binary fluid mixture”, *Phys. Rev. E.* 75, 031201 (2007).
- [26] M. López de Haro, E. G. D. Cohen and J. M. Kincaid, “The Enskog Theory for Multicomponent Mixtures. 1. Linear Transport-Theory”, *J. Chem. Phys.* 78, 2746–2759 (1983).

- [27] D. V. Matyushov and B. Ladanyi, “Cavity Formation Energy in Hard Sphere Fluids: An Asymptotically Correct Expression”, *J. Chem. Phys.* 107, 5815–5820 (1997).
- [28] T. Boublik, “Hard-Sphere Equation of State”, *J. Chem. Phys.* 53, 471–472 (1970).
- [29] G. A. Mansoori et al., “Equilibrium thermodynamic properties of mixtures of hard spheres”, *J. Chem. Phys.* 54, 1523–1525 (1971).
- [30] J. K. Percus and G. J. Yevick, “Analysis of classical statistical mechanics by means of collective coordinates”, *Phys. Rev.* 110, 1–13 (1958).
- [31] B. Götzemann, R. Evans and S. Dietrich, “Depletion forces in fluids”, *Phys. Rev. E* 57, 6785–6800 (2000).
- [32] D. Viduna and W. R. Smith, “Calculation of binary hard-sphere mixture radial distribution functions at contact from an equation of state”, *J. Chem. Phys.* 117, 1214–1219 (2002).
- [33] D. Viduna and W. R. Smith, “New accurate binary hard sphere mixture radial distribution functions at contact and a new equation of state”, *Mol. Phys.* 100, 2903–2905 (2002).
- [34] S. de Groot and P. Mazur. *Non-Equilibrium Thermodynamics*. New York: Dover, 1984.
- [35] J. M. Kincaid, M. López de Haro and E. G. D. Cohen, “The Enskog Theory for Multicomponent Mixtures. 2. Mutual Diffusion”, *J. Chem. Phys.* 79, 4509–4521 (1983).
- [36] M. L. López de Haro and E. G. D. Cohen, “The Enskog Theory for Multicomponent Mixtures. 3. Transport-properties of dense binary-mixtures with one tracer component”, *J. Chem. Phys.* 80, 408–415 (1984).
- [37] J. M. Kincaid, E. G. D. Cohen and M. López de Haro, “The Enskog Theory for Multicomponent Mixtures. 4. Thermal-Diffusion”, *J. Chem. Phys.* 86, 963–975 (1987).
- [38] S. Chapman and T. G. Cowling. *The Mathematical Theory of Non-Uniform Gases*. 3rd. Cambridge: Cambridge, 1970.
- [39] J. H. Ferziger and H. G. Kaper. *Mathematical Theory of Transport Processes in Gases*. London: North-Holland, 1972.
- [40] J. M. Montanero and A. Santos, “Monte Carlo simulation method for the Enskog equation”, *Phys. Rev. E* 54, 438–444 (1996).
- [41] J. M. Montanero and A. Santos, “Simulation of the Enskog equation a la Bird”, *Phys. Fluids*. 9, 2057–2060 (1997).
- [42] A. Frezzotti, “A particle scheme for the numerical solution of the Enskog equation”, *Phys. Fluids*. 9, 1329–1335 (1997).

-
- [43] G. A. Bird. *Molecular gas dynamics and the direct simulation of gas flows*. Oxford: Oxford University Press, 1994.
 - [44] M. A. Hopkins and H. H. Shen, “A Monte Carlo solution for rapidly shearing granular flows based on the kinetic theory of dense gases”, *J. Fluid Mech.* 244, 477–491 (1992).
 - [45] B. J. Alder and T. E. Wainwright, “Studies in molecular dynamics. 1. General method”, *J. Chem. Phys.* 31, 459–466 (1959).
 - [46] M. Marin, D. Risso and P. Cordero, “Efficient Algorithms for Many-Body Hard Particle Molecular Dynamics”, *J. Comp. Phys.* 109, 306–317 (1993).
 - [47] G. Paul, “A Complexity O(1) priority queue for event driven molecular dynamics simulations”, *J. Comp. Phys.* 221, 615–625 (2007).
 - [48] J. M. Haile. *Molecular Dynamics Simulation - Elementary Methods*. New York: Wiley-Interscience, 1997.
 - [49] W. G. Hoover and F. H. Ree, “Melting Transition and Communal Entropy for Hard Spheres”, *J. Chem. Phys.* 49, 3609–3617 (1968).
 - [50] L. Lue, “Collision statistics, thermodynamics, and transport coefficients of hard hyperspheres in three, four, and five dimensions”, *J. Chem. Phys.* 122, 044513 (2005).
 - [51] L. Lue and Marvin Bishop, “Molecular dynamics study of the thermodynamics and transport coefficients of hard hyperspheres in six and seven dimensions”, *Phys. Rev. E* 74, 021201 (2006).

CHAPTER
EIGHT

STRUCTURE AND STABILITY OF HELICES IN SQUARE-WELL HOMOPOLYMERS

This chapter has been published in Physical Review E (see Appendix C).

Authors: M. Bannerman, J. E. Magee, L. Lue

THIS chapter is primarily the work of M. Bannerman. J. E. Magee played an advisory role during the establishment of the replica exchange simulation code.

8.1 Introduction

One of the fascinating features of proteins is their ability to lock into a specific, folded structure. This feature is often crucial to their function. A key structural unit which frequently appears in proteins is the helix. Helical structures also appear in other molecules, such as in DNA, homopolypeptides (e.g., polyalanine), as well as in some synthetic polymers. Consequently, there has been a lot of interest in the helix-coil transition as a starting point to understanding the more general issue of protein folding.

Many detailed computer simulations on “realistic” interaction potential models have been conducted, to better understand the formation of helices in polypeptides and proteins (e.g., see Refs. [1–4]). In these systems, the formation of hydrogen bond interactions between different amino acid groups is principally responsible for the formation of the helix. Helices also spontaneously form in simplified interaction models that have short-ranged, directional interactions between their constituent monomers [5, 6]. Many theories have been developed to describe the helix-coil transition in homopolypeptides and other biological molecules, starting with the pioneering work of Zimm and Bragg [7] and later followed by many others [8–12]. The key feature of these theories is the characterization of a distinct helix and coil state for each residue in the peptide chain. This is justified for these systems because of the specific arrangement of the residues in the helix conformation and the large energies due to the formation of the hydrogen bonds. While these approaches have led to keen insights for helix formation in polypeptide and protein molecules, they are dependent on the fact that short-ranged, directional interactions drive the formation

of the helix structure. In these molecules, one can argue that the helix structure has been “built” in.

Can the helix structure occur in molecules without these specific interactions, and if so, what then controls its geometry? It has been suggested that the helix is a stationary configuration for semi-flexible chains [13], and the optimal shape of flexible [14] and closely packed, compact [15, 16] strings. This hints at a more general driving force for helix formation in real proteins and may explain why the structure is so prolific in nature. In order to gain some more general understanding of the mechanisms behind helix formation, we examine the square-well homopolymer model. This is a simple polymer model composed of linearly bonded, hard spheres that interact with each other through an isotropic square-well attraction. Isolated square-well homopolymers exhibit the typical coil to globule transition observed in many polymers as the temperature is decreased below the theta point; however, they also freeze into compact, crystal-like structures [17, 18] at sufficiently low temperatures. Interestingly, Magee et al. [19] have demonstrated that, by introducing stiffness, the square-well homopolymer model can fold into a helix structure. This is a remarkable result, as the model is achiral and yet it spontaneously breaks symmetry and folds into left or right handed helices. This is merely a result of the polymer being stiff, having an excluded volume and an attractive self interaction. An exact analysis of the density of states of square-well tetramers and pentamers was performed [20] to examine the relationship between the distributions and correlations of the torsional angles in these fragments to the stability of the helix in longer length chains. However, the question still remains as to what controls the geometry and the stability of the helical structures formed by these molecules.

In this work, we use molecular dynamics, combined with the replica exchange method, to explore the behavior of square-well homopolymers to better understand the link between the interactions between the monomers of the chain and the overall structure of the molecule. In particular, we are interested in the range of conditions over which the helix structure is stable. The remainder of this paper is organized as follows. Section 8.2 describes the details of the square-well homopolymer model that we investigate in this work. In addition, it provides background information on the simulation methods we employed and outlines the procedures used to generate and analyze the resulting simulation data. The results of the simulations are presented in Section 8.3. This section begins with an overview of the general behavior exhibited by the square-well homopolymers. Then, it continues by analyzing and discussing the influence of the bond length (or equivalently monomer size), the range of attraction between monomers, and the total number of monomers in the polymer on the structure and thermodynamic behavior of the homopolymer. Finally, the major findings of this work are summarized in Section 8.4.

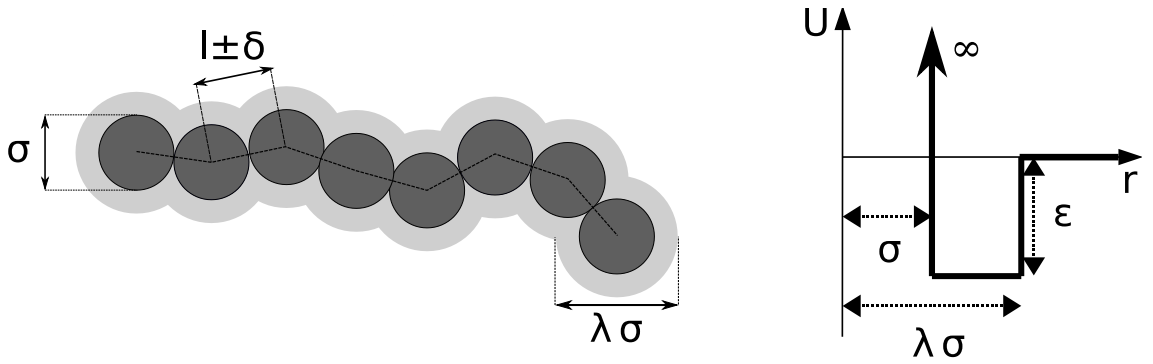


Figure 8.1: Polymer model with bond length $l \pm \delta$, well energy ϵ , well width $\lambda\sigma$, and monomer diameter σ . The interaction energy between two non-bonded monomers separated by a distance r is given on the right.

8.2 Simulation Details

The polymer model that we study in this work is a chain of linearly bonded monomers. Monomers that are not directly bonded together interact with each other through the potential

$$u(r) = \begin{cases} \infty & \text{for } r < \sigma \\ -\epsilon & \text{for } \sigma < r < \lambda\sigma \\ 0 & \text{for } \lambda\sigma < r \end{cases} \quad (8.2.1)$$

where r is the distance between the centers of the monomers. Each monomer is a hard sphere of diameter σ , surrounded by an attractive square well of diameter $\lambda\sigma$. When two monomers are within a distance $\lambda\sigma$, they feel an attractive interaction energy of magnitude ϵ . Monomers that are directly bonded together interact with each other through the potential

$$u_{\text{bond}}(r) = \begin{cases} \infty & \text{for } r < l - \delta \\ 0 & \text{for } l - \delta < r < l + \delta \\ \infty & \text{for } l + \delta < r \end{cases} \quad (8.2.2)$$

The bond length is nominally equal to l but is allowed to fluctuate between $l - \delta$ and $l + \delta$. If $\sigma/l > 1$, then directly bonded monomers in the chain overlap. Monomers that are not directly bonded together other are not allowed to overlap each other. This induces a stiffness in the polymer, due to the restrictions on the allowed bond angles imposed by the excluded volume interaction between monomers separated by two bonds. In the limit that σ/l approaches $2(1 + \delta/l)$, the chain becomes completely rigid. For all the simulations presented here, $\delta/\sigma = 0.1$, and so the bond length is allowed to vary by $\pm 10\%$. A schematic drawing of the polymer model is given in Fig. 8.1.

We use constant temperature molecular dynamics (MD) to investigate the structural and thermodynamic properties of the square-well polymer chains over a range of temperatures. The temperature of the simulations was maintained with the Andersen thermostat [21]. The basic algorithm that we employ to perform the MD simulations is based on the one originally developed by Alder and Wainwright [22]. Several subsequent advances

have significantly improved the computational speed of this original algorithm. These include the use of overlapping cells [23, 24], the delayed states algorithm [25], and calendar event queues [26]. We have incorporated these advances in order to construct a code where the computational cost of the simulation is independent of the number of particles N in the system.

One shortcoming of molecular dynamics is that it is prone to becoming trapped in local energy minima, especially at low temperatures. In particular for conditions where helical or other “frozen” structures are formed, the homopolymer may become locked within a specific configuration. Using only molecular dynamics, the helices formed by the square-well polymers are stable over the length of accessible simulation times and rarely transform between the left and right handed forms. This makes the study of the equilibrium behavior of these systems at low temperatures extremely formidable.

To overcome this difficulty, the MD simulations are coupled with the replica exchange/parallel tempering method [27]. In this technique, several molecular dynamics simulations, each at a different temperature, are run simultaneously; a Monte Carlo move is added to exchange chain configurations between simulations at different temperatures. A configuration that is locked at a low temperature may then move up in temperature, unfold, and drop in temperature to sample another configuration. This enables the systems to rapidly overcome local energy minima and better explore the full range of available configurations.

The effectiveness of the replica exchange method depends on the choice of the temperatures of the individual simulations. In order to determine the optimal values of these temperatures, we use an approach recently developed by Katzgraber et al. [28]. This maximizes the number of configurations that travel between the lowest and highest temperature simulations, as modeled by a one-dimensional diffusion process. A typical optimal distribution of system temperatures is presented in Fig. 8.2, along with the resulting exchange rates. The optimization procedure clusters the simulation temperatures near conditions where the polymer undergoes structural changes with significant topological differences. The optimal distribution of system temperatures does not correspond to a constant acceptance ratio [28], as is commonly presumed.

A series of NVT molecular dynamics simulations, combined with the replica exchange method, is performed to examine the properties of square-well homopolymers over a range of values for σ/l , λ , and N . For each particular chain, 51 temperatures are used, and the systems are equilibrated for 10^4 attempted replica exchange moves. The replica exchange move consists of selecting 5×51 random pairs and attempting to swap the configuration between each pair. Between each replica exchange move, the dynamics of the isolated polymers is run for a few hundred mean free times. Following an initial equilibration period, data are collected over 5×10^4 attempted replica exchange moves. The collected data are then interpolated using multiple histogram reweighting [29] to obtain smooth heat capacity curves as a function of the temperature.

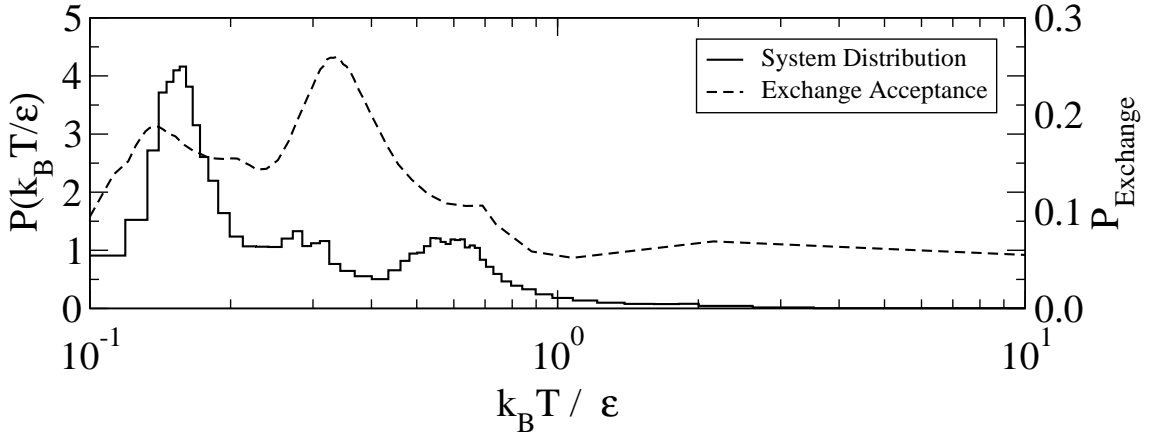


Figure 8.2: Replica exchange simulations for an isolated square-well homopolymer with $N = 20$, $\sigma/l = 1.6$, and $\lambda = 1.5$. Optimal distribution of system temperatures is given by the solid line, and the acceptance ratio of the replica exchange move for adjacent temperature systems is given by the dashed line.

8.3 Results and Discussion

8.3.1 Overview

To illustrate the general behavior of the square-well homopolymers, we present results from MD simulations in Fig. 8.3 for a chain consisting of $N = 20$ monomers with $\sigma/l = 1.6$ and $\lambda = 1.5$. The solid line in the plot shows the variation of the excess heat capacity C_v with temperature. The peaks of the heat capacity typically indicate transitions between different structural states of the polymer.

To characterize the rigidity (i.e., “frozen” vs. flexible) of the structure of the homopolymer at a particular temperature, we collect N_{ss} configurations of the polymer at regular intervals in time during the course of the simulation (here we choose 10 replica exchange times). For each sampled configuration α , we then determine the average R_α of the root mean square difference (RMSD) against all other collected configurations, which is given by

$$R_\alpha = N_{ss}^{-1} \sum_{\alpha'=1}^{N_{ss}} \text{RMSD}(\alpha, \alpha'), \quad (8.3.1)$$

where the RMSD between two configurations α and α' is defined as

$$\text{RMSD}(\alpha, \alpha') = \left[N^{-1} \sum_{i=1}^N \left| \mathbf{r}_i^{(\alpha)} - \mathbf{r}_i^{(\alpha')} \right|^2 \right]^{1/2}. \quad (8.3.2)$$

and $\mathbf{r}_i^{(\alpha)}$ is the position of monomer i in the polymer of configuration α . The reported value of the RMSD between a pair of configurations is the minimum value obtained by rotating [30] and reflecting the configurations, as well as reversing the numbering se-

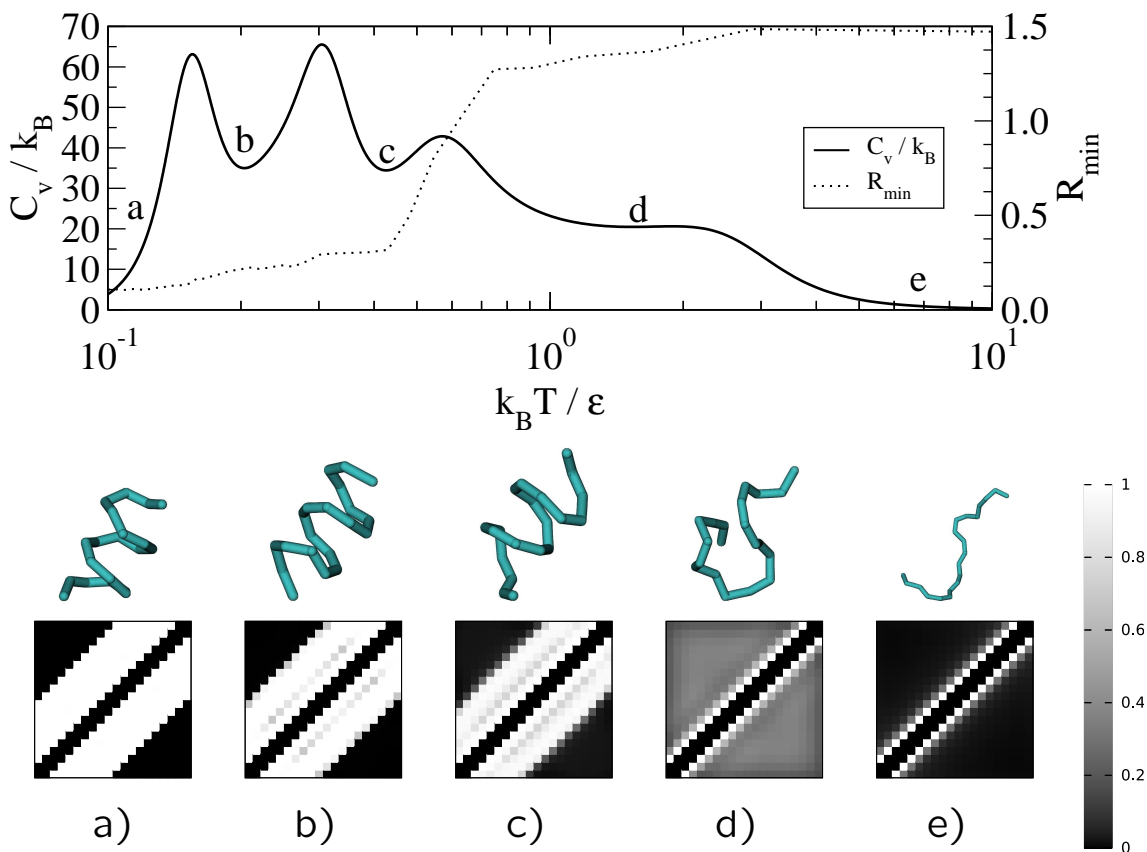


Figure 8.3: The heat capacity, the optimal configuration RMSD, sample configurations, and contact maps at various temperatures (*a*–*e*) of an isolated helix homopolymer with $N = 20$, $\sigma/l = 1.6$, and $\lambda = 1.5$.

quence of the monomers. We consider the configuration with the lowest value of R_α as the most representative of the entire set of sampled configurations of the homopolymer. The average RMSD of this configuration, denoted by R_{\min} , is used to indicate how rigid the polymer structure is at a given temperature (i.e., $R_{\min} = \min_\alpha R_\alpha$). Low values of R_{\min} suggest that the homopolymer remains “frozen” within same structural configuration. High values of R_{\min} indicate that the homopolymer is not well characterized by a single structure. This can imply that the homopolymer is in a rather flexible state, such as a coil or a molten globule. However, high values of R_{\min} could also result if the homopolymer can be “frozen” into several distinct configurations, such as in a glassy state. Using cluster analysis of the distance matrix formed by the RMSD’s of every pair of sample configurations, it is possible to estimate the number of stable states and thereby distinguish between these two situations. This issue will be discussed further in Sec. 8.3.4, where the effect of polymer length is explored.

The variation of R_{\min} with temperature is given by the dotted line in the plot in Fig. 8.3. Beneath the plot are sample configurations of the homopolymer at several different representative temperatures. Underneath each of these configurations is the corresponding contact map of the average structure, which details the proximity of pairs of monomers in the polymer. The positions along the ordinate and abscissa of the contact maps denote each of the monomers along the chain. The locations within the con-

tact map are shaded according to how often two monomers interact with each other (i.e. within a distance $\lambda\sigma$). Black denotes no interaction, white denotes continuous interaction, and gray denotes intermittent interaction. For monomers that are bonded together (along the diagonal), we have shaded the entries in the contact map black. For the case where $\sigma/l = 1.6$ and $\lambda = 1.5$, monomers that are separated by two bonds are always in each others attractive well due to the overlap and result in two off-diagonal white bands.

At higher temperatures (point *e*), the polymer is extended, and the contact map indicates that the monomers of the polymer are rarely in contact with each other. The optimal configuration RMSD (R_{\min}) also indicates that the typical configuration is not locked but, instead, is quite flexible. Upon decreasing the temperature, a shoulder in the heat capacity marks the transition from an extended coil to a globule state *d*. The contact map indicates that while monomers do interact significantly with each other, they do not remain in continuous contact with the same monomers, and, therefore, the contact map is primarily gray. Although the polymer has collapsed into a compact structure, it contains no regular structure and R_{\min} remains high.

Decreasing the temperature still further (point *c*), we see that the polymer changes from an unstructured globule to a more ordered helical structure. The contact map shows the stripe pattern that is characteristic of a spiral or helical structure. Two more helical structures are present at lower temperatures (points *b* and *a*) which possess a slightly different pitch and radius. The value of R_{\min} decreases sharply over the first helix transition as the polymer forms a regular structure. This decreases further, indicating that the structures become more rigid. This is in agreement with the contact maps, where intermittent contacts become permanently “on” at low temperatures. Points *c* and *b* correspond to the helix 1 and 2 structures in the diagram of states presented by Magee et al. [19]. We will refer to the structure at point *a* as the helix 3 structure. The transitions between the three helical structures are not visible in R_{\min} as the structures are very similar but the transition to a folded state is strongly marked.

In the following, we examine how the structure of square-well homopolymers is affected by the monomer size (σ/l), the range of the attractive interaction (λ), and the length of the polymer chain (N). In particular, we are interested in understanding the range of parameters where helical structures are stable.

8.3.2 Ratio of Monomer Size to Bond Length

In this section, we study the influence of monomer size, or equivalently the bond length, on the structure of square-well homopolymers. We limit our attention to homopolymers with $N = 20$ and $\lambda = 1.5$. The main effect of changing the monomer size is to alter the local stiffness of the polymer chain. Decreasing the size of the monomers (or increasing the bond length) increases the flexibility of the homopolymer. The stiffness of a polymer chain can be characterized by the bond correlation function, which is defined

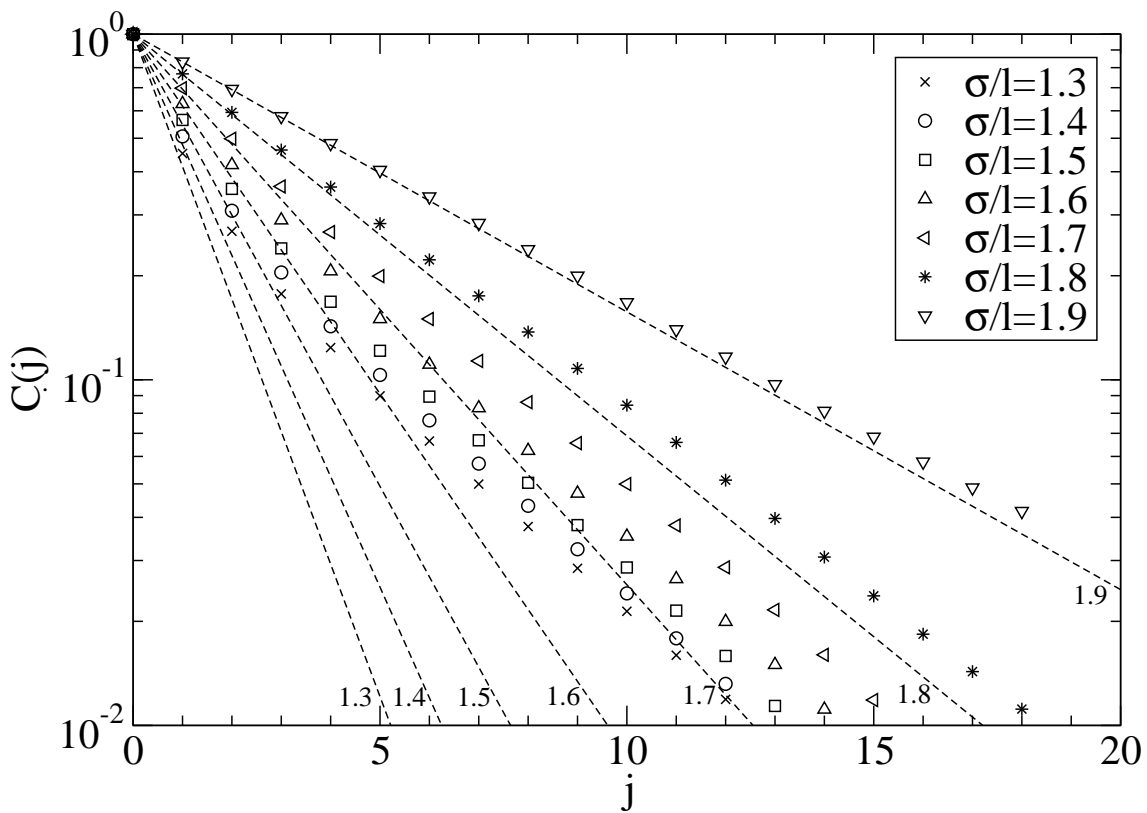


Figure 8.4: Average bond angle correlations for athermal overlapping chains as a function of separation in a $N = 20$ chain. The dotted lines correspond to neglecting the influence of long range excluded volume interactions between the monomers.

as

$$C(j) = \frac{1}{N-j-1} \sum_{k=1}^{N-j-1} \frac{\langle \Delta\mathbf{r}_k \cdot \Delta\mathbf{r}_{k+j} \rangle}{\langle \Delta\mathbf{r}_k \cdot \Delta\mathbf{r}_k \rangle} \quad (8.3.3)$$

where $\Delta\mathbf{r}_k = \mathbf{r}_{k+1} - \mathbf{r}_k$ is the orientation of the k^{th} bond in the polymer, and \mathbf{r}_k is the position of the k^{th} monomer. This function describes the degree to which the orientations of two bonds are correlated to each other. The more flexible the chain, the more rapidly the bond correlation function decays with the distance j between the bonds.

Figure 8.4 presents the bond correlation functions for athermal chains (i.e. $\epsilon = 0$) with $N = 20$ for various values of σ/l . The symbols are the results obtained from MD simulations. The dotted lines are the corresponding exponential decays for the athermal chains where excluded volume interactions are neglected, with the exception to those between monomers separated by two bonds, which give rise to the local stiffness. At very low values of σ/l (not shown), there are no correlations between the bonds, and the polymer behaves essentially as a random walk. At intermediate values of the overlap parameter, the excluded volume interactions between monomers separated by several bonds enhance the correlations between the bonds, and the correlation function decays algebraically, rather than exponentially. For $\sigma/l > 1.8$, the decay is nearly exponential because the chain is too stiff for there to be significant excluded volume interactions between the monomers.

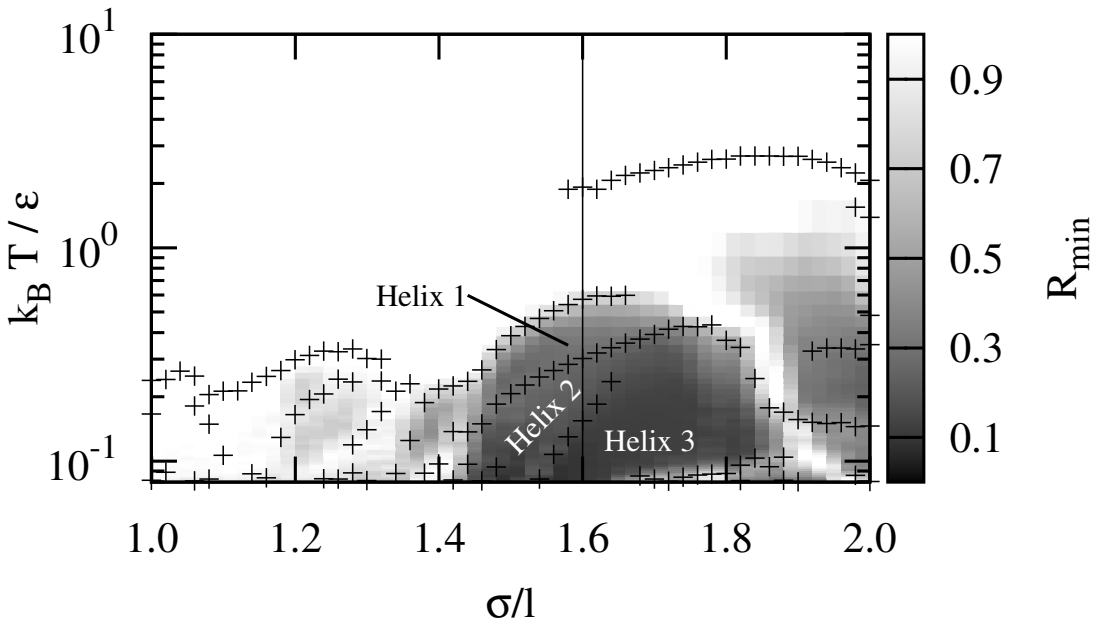


Figure 8.5: Diagram of states for isolated square-well homopolymers with $N = 20$ and $\lambda = 1.5$. The graph is shaded according to R_{\min} .

A diagram of states for homopolymers with $N = 20$ and $\lambda = 1.5$ is given in Figure 8.5, which explores the effect of the monomer overlap parameter (σ/l). The crosses mark the locations of peaks in the heat capacity, and the diagram is shaded according to the value of R_{\min} . The data in Fig. 8.3 correspond to the vertical line at $\sigma/l = 1.6$ in Fig. 8.5.

There are what at first appear to be discontinuities in the heat capacity maxima in the diagram. These peaks are generally weak maxima in the heat capacity which are hidden behind the rapid increase in C_v due to the presence of sharper peaks at another temperature. The highest temperature maximum in C_v typically corresponds to the coil-globule collapse or “theta point” (see point *d* in Fig. 8.3).

Homopolymers with $\sigma/l \lesssim 1.1$ crystallize into compact, nearly spherical, regularly packed structures at low temperatures [17, 18]. The comparatively high value of the RMSD for these polymers, however, indicates that the structures that they freeze into are not unique. There may be several arrangements of the bonds of the polymer for a given “crystalline” packing of the monomers. Consequently, these polymers are like glasses at low temperatures.

When $\sigma/l \gtrsim 1+\delta/l = 1.1$, directly bonded monomers always overlap one another. At low temperatures, homopolymers with $1.1 \lesssim \sigma/l \lesssim 1.4$ (see Fig. 8.5) exhibit a “freezing” transition, but, similarly to the polymers with $\sigma/l \lesssim 1.1$, they do not lock into a single, stable conformation. The high value of the RMSD indicates that many folded configurations exist. On visual inspection of these configurations, helical features are visible within some other structure. For example, the ends of the polymer may be wrapped around the outside of a helical core. These “loose ends” increase the number of possible frozen states

and therefore increase the value of R_{\min} .

For homopolymers with a well width of $\lambda = 1.5$, monomers separated by two bonds are permanently within each others attractive wells when $\sigma/l > 2(1 + \delta/l)/\lambda \approx 1.47$. This coincides with the onset of the region of low values for R_{\min} , where homopolymers fold into the helix 1, 2, and 3 structures. Here, the homopolymers fold into a single, helical conformation (neglecting the distinction between the left and right handed configurations). A significant portion of the folded parameter space is occupied by the helix 3 structure, which is the most rigid of the helix structures.

At high overlaps, the values of R_{\min} are on average lower due to the stiffness of the chain limiting the range of motion of the monomers. There is a sharp transition at $\sigma/l \approx 1.8$ with an increase in R_{\min} along the line of the heat capacity peaks. For polymers with a well width of $\lambda = 1.5$, two monomers separated by 4 bonds cannot interact with each other when $\sigma/l > \sqrt{7/2} \approx 1.87$ [20]. If we account for the fact that in the simulations the bonds can stretch by 10%, then this would occur at $\sigma/l \gtrsim 1.70$, which coincides with loss of the helix 1 structure.

It appears that the observed helix structures are closely related to the constraint of interactions between monomers in the chain. The values at which certain interactions become prohibited depends on the well width λ , and the effect of this parameter is explored in the next section.

8.3.3 Range of Attractive Interaction

Now, we examine the influence of the range of the attractive interaction, which is characterized by the parameter λ . In this section, we limit the analysis to square-well homopolymers with $N = 20$ and $\sigma/l = 1.6$. A diagram of states is provided in Fig. 8.6. Several sample configurations are presented in Fig. 8.7 at various values of λ . From the diagram and the associated configurations, we see that a series of distinct, helical structures are formed at low temperatures. The range of the attractive interaction appears to control the radius of the helix: smaller well widths lead to helical structures with a smaller radius and a larger pitch.

At low values of the well width ($\lambda \lesssim 1.3$), helical structures appear with structural variations, much like what occurs at low values of the overlap parameter σ/l . For high values of λ , the helix structure begins to degrade. It still retains the spiral structure, however, it no longer has a constant radius. Interestingly, for the structure shown in Fig. 8.7d, the monomers appear to be packed in a fairly spherical crystalline arrangement. If the well width becomes too large, then the helix structure will completely vanish, replaced by another structure.

For an overlap of $\sigma/l = 1.6$ and a well width of $\lambda \geq 1.375$, monomers separated by two bonds are permanently within each others attractive well. This again coincides with a large decrease in R_{\min} , indicating a single stable structure. As with the diagram of states in the overlap parameter σ/l (see Fig. 8.5), it is easy to distinguish certain helical

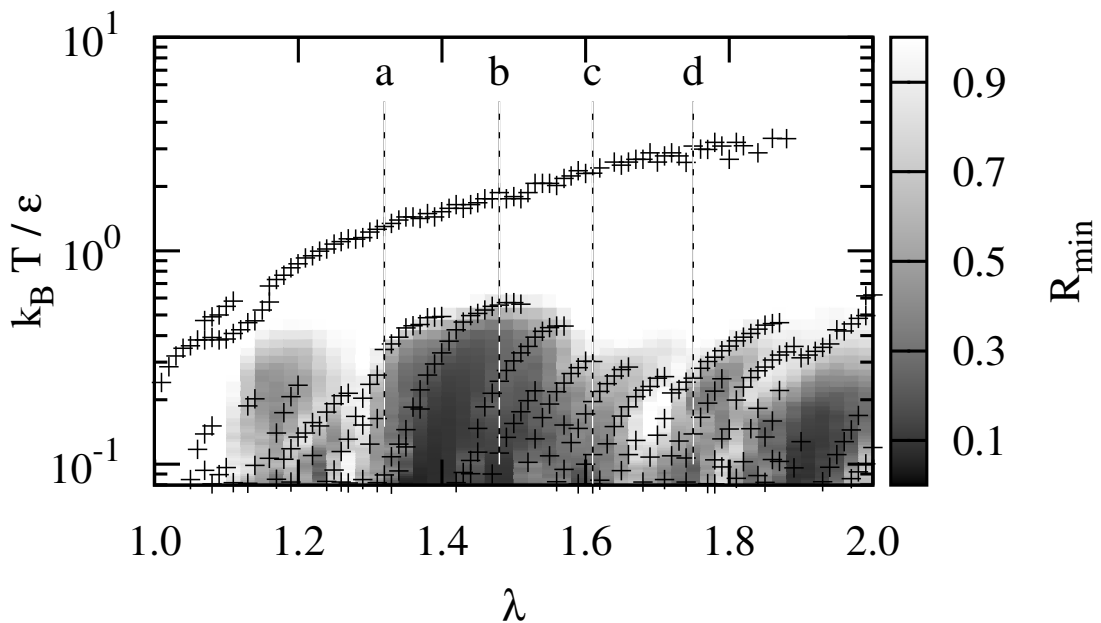


Figure 8.6: Diagram of states for isolated square-well homopolymers with $N = 20$ and $\sigma/l = 1.6$. The graph is shaded according to R_{\min} . The letters and dashed lines correspond to the configurations shown in Fig. 8.7.

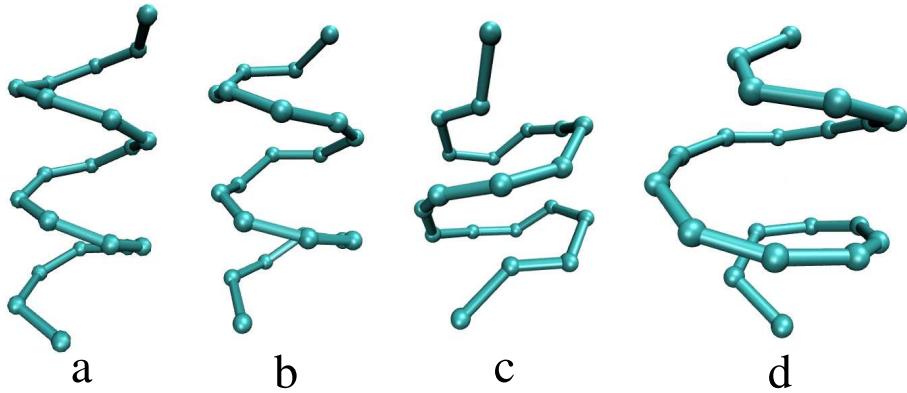


Figure 8.7: Representative configurations at the state points indicated in Fig. 8.6.

structures using R_{\min} .

It is interesting to note that the helices observed here all have a much higher monomer per turn count than the alpha helix commonly found in nature. There are 4 residues per turn of the alpha helix, whereas the wider helices presented here contain 7 for the tightest helix observed (Fig. 8.6a). Maritan et al. [15] characterized their compact string helices using a parameter f , related to the helix radius and monomer spacing in consecutive turns of the helix. Applying their analysis, the values of f exhibited by our helices are consistently above the value of $f \approx 1$ (e.g., Fig. 8.6a-d $f \approx 1.2, 1.1, 1.3$, and 1.1 , respectively) reported by Maritan for compact strings and naturally occurring alpha helices. These larger values of f may be due to the manner in which we introduce stiffness (i.e., overlapping spheres).

Unlike the overlap parameter, the transitions between the various helical states are typically marked by peaks and large changes in R_{\min} , as the well width parameter λ has a significant effect on the structure of the folded state. In the following section, we explore the structure as a function of chain length.

8.3.4 Chain Length

For the square-well homopolymer, the main driving force for the formation of the helix is the tendency of the polymer to recover interaction energy through the contacts of its constituent monomers. This energetic driving force is balanced against the loss of entropy encountered in restricting the polymer to the helical structure (to maintain the necessary contacts). If the polymer chain is too short, then the energy recovered will not be sufficient to overcome the entropy loss, and the helix will not be stable. If the polymer chain is too long, then structures other than the helix are expected to be stable. Therefore, we expect the helix to appear only within a window of chain lengths. In this section, we examine the range of N where the helical structure is stable.

The diagram of states for square-well polymers with $\lambda = 1.5$ and $\sigma/l = 1.6$ is presented in Fig. 8.8. For small chain lengths ($N \lesssim 12$) the RMSD is, on average, a low value. This is due to the short distance that monomers can actually be separated in space. This can be accounted for by reducing R_{\min} by the chain length; however, similar structures at different chain lengths typically exhibit the same value of R_{\min} and this data would be lost. The conditions where helical structures are formed are still well defined by the heat capacity peaks and areas where the value of R_{\min} is low. For this system, the chain must consist of at least $N = 10$ monomers before helices can form. The helix 3 structure does not appear until $N = 14$, and the largest chain length at which the helix structure is stable is $N = 22$.

At low temperatures, homopolymers with $N > 22$ appear to freeze into rigid structures, yet the high values of R_{\min} indicate that the homopolymer does not freeze into a single, repeatable, folded structure. In fact, these folded states are no longer unique, and several distinct structures exist with comparable free energies. These longer homopolymers arrange themselves into regularly packed structures with a spherical shape. Figure 8.9 provides several snapshots of configurations for square-well homopolymers with $N = 34$ at a temperature $k_B T/\epsilon = 1.35$ (see also Fig. 8.8). These chiral structures have the same interaction energy, and they are all stable over long times. They appear to be variations on a similar structural theme: a core of a few monomers with a chiral outer core.

The RMSD's of the different folded structures in Fig. 8.9 lie between 0.86σ and 1.05σ , which is a relatively high value. Thus, the RMSD can discriminate between distinct folded structures, provided that the configurations within each of the structures have a low average RMSD. If we perform a quality threshold (QT) cluster analysis [31] of the RMSD between all pairs of sample configurations using a cutoff value of $< 0.25\sigma$ to

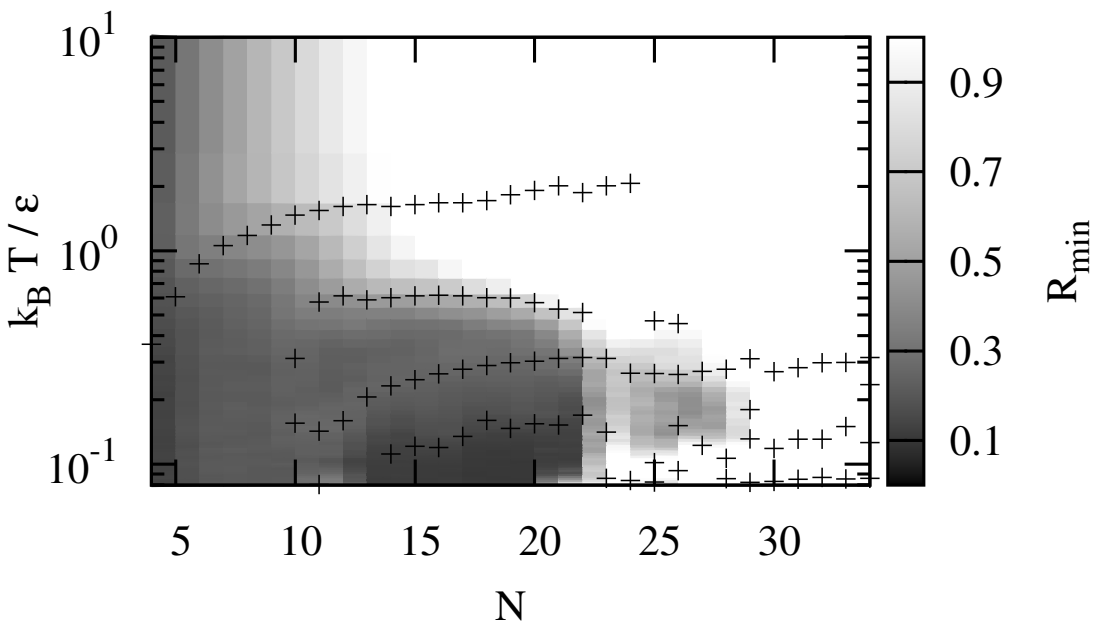


Figure 8.8: Diagram of states for isolated square-well homopolymers with $\sigma/l = 1.6$ and $\lambda = 1.5$ as a function of the chain length N . The graph is shaded according to R_{\min} .

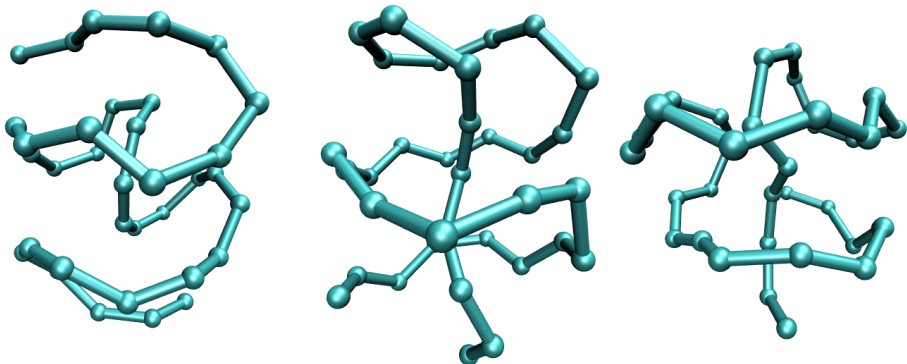


Figure 8.9: Samples of stable configurations for square-well homopolymers with $\sigma/l = 1.6$, $\lambda = 1.5$, and $N = 34$ at $k_B T/\epsilon = 0.13741$.

group the data and a threshold of 1% to eliminate intermediates, we can attempt to count the number of distinct structures formed. We perform this counting at the heat capacity minima, as the heat capacity maxima tend to occur at transitions between structures. For $N = 22$, only one cluster is apparent, which indicates that the homopolymer folds into a unique structure at low temperatures; in this case, it is a helix. In contrast, for $N = 23$, a single helix occupies approximately 50% of the simulation snapshots. The remainder are a large number of variations on the helix with “loose” ends wrapped around the central coil.

In fact, once the single helix structure is no longer dominant the number of distinct folded structures rapidly increases with the length of the homopolymer. These polymers will behave similarly to a glass at low temperatures, becoming trapped into one of these

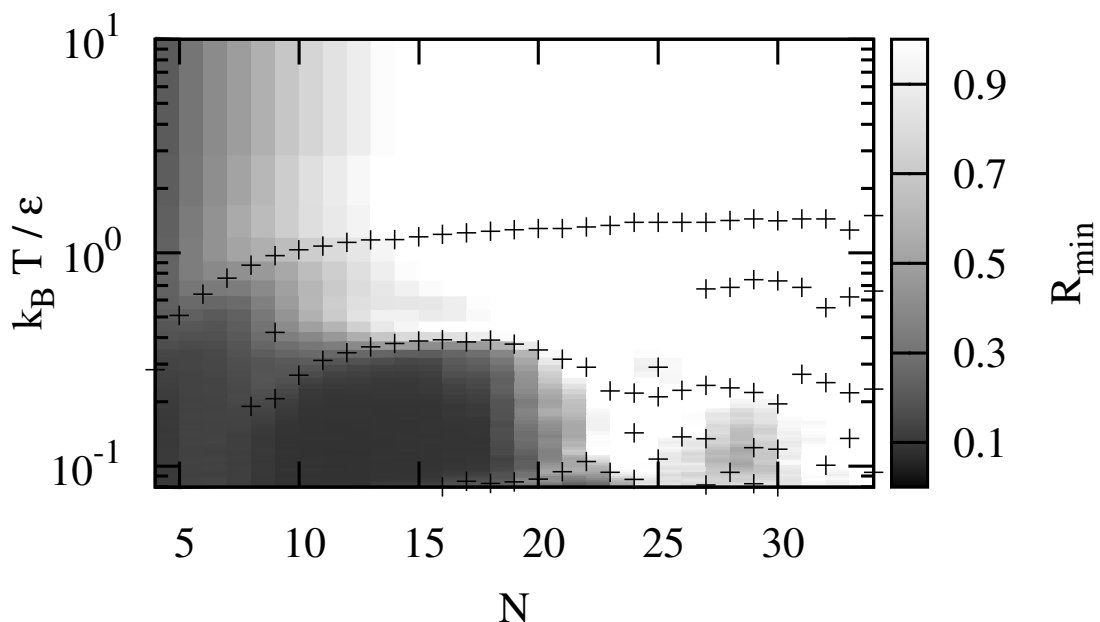


Figure 8.10: Diagram of states for isolated square-well homopolymers with $\sigma/l = 1.6$ and $\lambda = 1.32$ as a function of the chain length N . The graph is shaded according to R_{\min} .

many structures.

To understand how the range of the attractive interactions affects the window of chain lengths where the helix is stable, we examine square-well homopolymer chains with $\lambda = 1.32$ and $\sigma/l = 1.6$. The diagram of states is presented in Fig. 8.10. These polymers tend to form helices at shorter chain lengths than polymers with a wider well widths (cf. Fig. 8.8 for $\lambda = 1.5$). The helices formed by the $\lambda = 1.32$ polymers have a tighter radius and are more rigid (lower value of R_{\min}) than the helices formed by the $\lambda = 1.5$ polymers. The shortest homopolymer that forms a helix ($N = 8$) appears to be correlated to the number of monomers in a single turn of the helix. The helix structure vanishes for chain lengths greater than $N = 22$, which is similar to what is found for homopolymers with $\lambda = 1.5$. At longer chain lengths, the system again exhibits multiple folded states, and the structures formed are similar to those displayed in Fig. 8.9.

To investigate the influence of the monomer size (or bond length) on the window of chain lengths where the helix is formed, we examine square-well homopolymers with $\sigma/l = 1.8$ and $\lambda = 1.5$. The diagram of states for these systems is given in Fig. 8.11, which shows a rich range of structural behavior. The minimum chain length for helix formation is larger ($N = 11$) than for polymers with a monomer size of $\sigma/l = 1.6$. The increased stiffness of the chain is limiting the curvature of the helix formed, thus requiring more monomers per turn of the helix. It appears that the typical “glassy” behavior of the longer polymers has been eliminated for the examined chain lengths. Therefore, the maximum chain length displaying a helical structure must be determined using QT analysis and visual inspection. The last chain length where a single helix structure is stable is $N = 22$, yet for the longer chain lengths ($23 \leq N \leq 34$), the folded structures remain

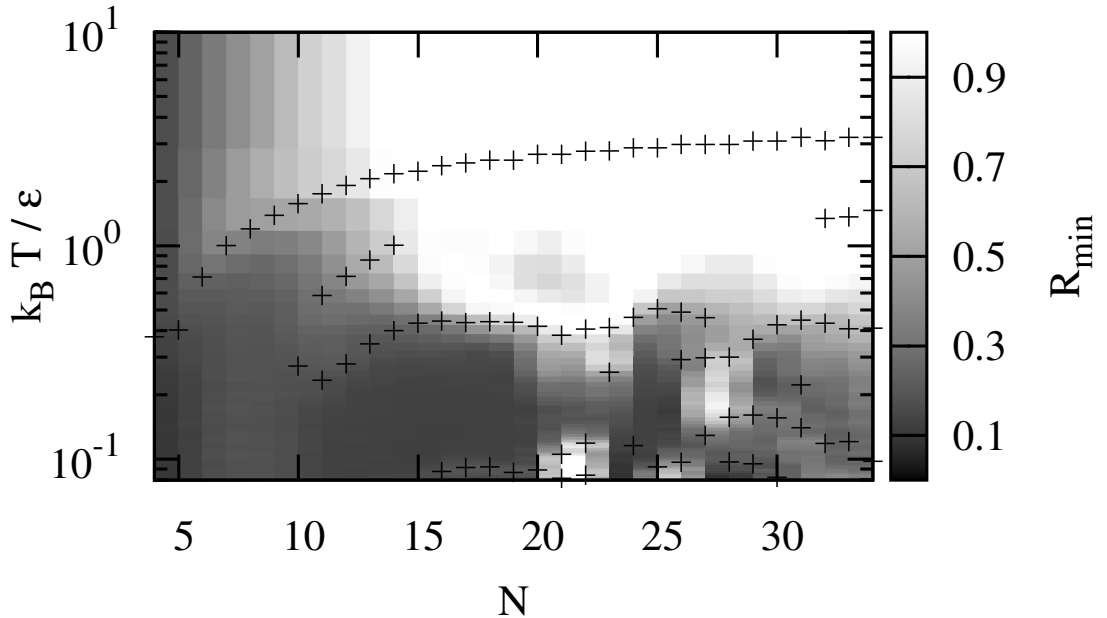


Figure 8.11: Diagram of states for isolated square-well homopolymers with $\sigma/l = 1.8$ and $\lambda = 1.5$ as a function of the chain length N . The graph is shaded according to R_{\min} .

unique and not glassy. A single structure, which we refer to as the “barbers pole” structure, is observed over these chain lengths and is similar to the two rightmost structures of Fig. 8.9. This structure was first observed by Magee et al. (See Fig. 2 of Ref. [19]). Unlike the configurations of Fig. 8.9, the polymer is too stiff to allow the reversal of direction or doubling back of the outer spiral in the “barbers pole”. It appears that the increased stiffness has reduced the number of possible low energy permutations, which manifest in more flexible chains as the doubling back of the outer spiral, to a single configuration. The small regions of high R_{\min} at low temperatures in Fig. 8.11 correspond to broad peaks in the heat capacity where transitions between different “barbers pole” structures occur.

Chains with a higher value of σ/l appear to favor a single folded structure at longer chain lengths than compared to more flexible chains. This is understandable as in the limit of a rigid chain there is only one possible physical configuration. As the chain becomes stiffer the number of low energy permutations on a structural theme are limited until only one configuration becomes optimal.

8.4 Conclusions

In this work, we have used event-driven molecular dynamics, coupled with the replica exchange and histogram reweighting techniques, to explore the behavior of isolated, square-well homopolymers. The structural properties of these polymers were characterized through a combination of configurational snapshots, monomer contact maps, and the root mean square deviation of the configuration, combined with QT cluster analysis. The

RMSD is able distinguishing between the unfolded and folded helix states. QT cluster analysis of the RMSD allows the estimate of the number of folded states, which reflects the “variability” of the state.

The homopolymer model studied here exhibits complex behavior. The stability of the helix structure is related to the constriction/elimination of interactions between monomers separated by a number of bonds in the chain. This is affected by the chain stiffness, which controlled by the monomer overlap parameter σ/l . The pitch and curvature of a helix is governed mainly by the range of the attractive interaction λ . Helices form with a higher curvature for short-range attractive wells. For larger values of λ , the monomers pack into a more spherical arrangement while still retaining a spiral bond structure.

Helices are only stable within a window of the chain length N . The lower limit appears to be related to the number of monomers in a single turn of the stable helix structure. Above a critical chain length, the isolated homopolymer folds into a rapidly increasing number of stable states, displaying characteristics reminiscent of a glass transition. These structures are more compact and spherical than their lower N counterparts, result from a minimization of the surface area to volume ratio of the polymer.

Finally, as the stiffness of the homopolymer is increased ($\sigma/l \rightarrow 2(1 + \delta/l)$) the number of observed folded states in longer chain lengths is reduced. At an overlap of $\sigma/l = 1.9$, we only observe unique folded states for the range of polymer lengths studied ($4 \leq N \leq 34$).

8.5 References

- [1] Y. Okamoto and U. Hansmann, “Thermodynamics of helix-coil transitions studied by multicanonical alorithms”, *J. Phys. Chem.* 99, 11276–11287 (1995).
- [2] C. L. Brooks, “Protein and Peptide folding explored with molecular simulations”, *Acc. Chem. Res.* 35, 447–454 (2002).
- [3] H. D. Nguyen, A. J. Marchut and C. K. Hall, “Solvent effects on the conformational transition of a model polyalanine peptide”, *Protein Sci.* 13, 2909–2924 (2004).
- [4] H. A. Scheraga, M. Khalili and A. Liwo, “Protein-folding dynamics: Overview of molecular simulation techniques”, *Ann. Rev. Phys. Chem.* 58, 57–83 (2007).
- [5] Josh P. Kemp and Zheng Yu Chen, “Formation of helical states in wormlike polymer chains”, *Phys. Rev. Lett.* 81, 3880–3883 (1998).
- [6] Josh P. Kemp and Jeff Z. Y. Chen, “Helical structures in proteins”, *Biomacromol.* 2, 389–401 (2001).
- [7] B. H. Zimm and J. K. Bragg, “Theory of the phase transition between helix and random coil in polypeptide chains”, *J. Chem. Phys.* 31, 526–535 (1959).
- [8] J. A. Schellman, “The factors affecting the stability of hydrogen bonded polypeptide structures in solution”, *J. Chem. Phys.* 62, 1485–1494 (1958).

- [9] S. Lifson and A. Roig, “On the theory of helix-coil transition in polypeptides”, *J. Chem. Phys.* 34, 1963–1974 (1961).
- [10] V. Munoz and L. Serrano, “Elucidating the folding problem of helical peptides using empiric parameters”, *Nature Struct. Biol.* 1, 399–409 (1994).
- [11] A. J. Doig, “Recent advances in helix-coil theory”, *Biophys. Chem.* 101–102, 281–293 (2002).
- [12] Vikas Varshney et al., “A minimal model for the helix-coil transition of wormlike polymers. Insights from Monte Carlo simulations and theoretical implications”, *Macromolecules.* 37, 8794–8804 (2004).
- [13] A. Kholodenko, M. Ballauff and M. A. Granados, “Conformal statistics of semiflexible polymers: Comparison between different models”, *Physica A.* 260, 267–293 (1998).
- [14] T. Vogel et al., “Thickness-dependent secondary structure formation of tubelike polymers”, *Europhys. Lett.* 85, 10003 (2009).
- [15] A. Maritan et al., “Optimal shapes of compact strings”, *Nature.* 406, 287–290 (2000).
- [16] D Marenduzzo et al., “Physics of Thick Polymers”, *J. Polym. Sci. B.* 43, 650–679 (2005).
- [17] Y. Zhou, C. K. Hall and M Karplus, “First-Order Disorder-to-Order Transition in an Isolated Homopolymer Model”, *Phys. Rev. Lett.* 77, 2822–2825 (1996).
- [18] Y. Zhou et al., “Equilibrium thermodynamics of homopolymers and clusters: Molecular dynamics and Monte Carlo simulations of systems with square well interactions”, *J. Chem. Phys.* 107, 10691–10708 (1997).
- [19] J. E. Magee, V. R. Vasquez and L. Lue, “Helical structures from an isotropic homopolymer model”, *Phys. Rev. Lett.* 96, 207802 (2006).
- [20] James E. Magee, Leo Lue and Robin A. Curtis, “Density of states for a short overlapping-bead polymer: Clues to a mechanism for helix formation?”, *Phys. Rev. E.* 78, 031803 (2008).
- [21] H. C. Andersen, “Molecular dynamics simulations at constant pressure and/or temperature”, *J. Chem. Phys.* 72, 2384–2393 (1980).
- [22] B. J. Alder and T. E. Wainwright, “Studies in molecular dynamics. 1. General method”, *J. Chem. Phys.* 31, 459–466 (1959).
- [23] D. C. Rapaport, “Event Scheduling Problem in Molecular Dynamics Simulation”, *J. Comp. Phys.* 34, 184–201 (1980).
- [24] Alan T. Krantz, “Analysis of an efficient algorithm for the hard-sphere problem”, *TOMACS.* 6, 185–209 (1996).

- [25] M. Marin, D. Risso and P. Cordero, “Efficient Algorithms for Many-Body Hard Particle Molecular Dynamics”, *J. Comp. Phys.* 109, 306–317 (1993).
- [26] G. Paul, “A Complexity O(1) priority queue for event driven molecular dynamics simulations”, *J. Comp. Phys.* 221, 615–625 (2007).
- [27] R. H. Swendsen and J. Wang, “Replica Monte Carlo Simulation of Spin-Glasses”, *Phys. Rev. Lett.* 57, 2607–2609 (1986).
- [28] H. G. Katzgraber et al., “Feedback-optimized parallel tempering Monte Carlo”, *J. Stat. Mech.* 2006, P03018 (2006).
- [29] A. M. Ferrenberg and R. H. Swendsen, “Optimized Monte Carlo data analysis”, *Phys. Rev. Lett.* 63, 1195–1198 (1989).
- [30] W. Kabsch, “A solution for the best rotation to relate two sets of vectors”, *Acta Cryst. A* 32, 922–923 (1976).
- [31] Laurie J. Heyer, Semyon Kruglyak and Shibu Yooseph, “Exploring expression data: Identification and analysis of coexpressed genes”, *Genome Res.* 9, 1106–1115 (1999).

CONCLUSIONS AND FUTURE WORK

THE discrete potential models used in this work approximate systems from the macroscopic scale (granular materials), down to the molecular scale (nano-colloidal fluids or isolated polymer). These systems are simulated using DYNAMO, a versatile, object oriented program for the simulation of event-driven dynamics. This chapter will first summarise the conclusions drawn from the development of DYNAMO and each of the studies performed with it, and then suggests some promising future directions for further study.

9.1 Conclusions

In this thesis, the properties of several discrete potential systems are examined. Event driven simulations are performed to generate numerical results for these model systems using DYNAMO. DYNAMO, the general event-driven simulator developed for this work, achieves its design goals of speed, accuracy and flexibility (see Chap. 4). DYNAMO exhibits the theoretical optimum linear scaling of the calculation cost with system size, once memory architecture effects are taken into account (see Fig. 4.5). Morton-ordered neighbour lists (see Sec. 4.3.3) are developed to combat some of these memory effects and are proven to be efficient for simulations at the larger system sizes (see Fig. 4.6). Simulations of the hard sphere fluid (see Chap. 5) validate the program's accuracy and confirm the stability of the algorithm for the larger system sizes and long run times performed.

The DSMC techniques implemented in DYNAMO are utilised in Chaps. 6 and 7 to provide predictions from Enskog theory without further approximation. This technique is generalised in Chap. 3 to attempt to include pre-collision correlations. The resulting $f^{(2)}$ -DSMC technique is moderately successful, and its predictions of the dynamical properties, with the exception of the diffusion coefficient, are only slightly improved compared to those of Enskog theory; however, $f^{(2)}$ -DSMC and higher provide a starting point from which new approximations or phenomenological theories for dynamical behaviour may be used. For example, a simple phenomenological correction for the re-collision rate leads to greatly improved predictions of the diffusion coefficient for hard spheres (see Sec. 3.5.1). The range of models and simulation methods employed in the studies con-

tained in this thesis highlight the flexibility of the modular design of DYNAMO and its suitability in facilitating rapid extension and generalisation (see Sec. 4.4). The conclusions drawn from each of these studies are summarised in the remainder of this section.

The calculation speed of DYNAMO is utilised in Chap. 5 to calculate accurate ($\gtrsim 5$ s.f.) pressures for the hard sphere system when approaching the thermodynamic limit. These are then used to assess recent equations of state and predictions from a novel exponential closure of the reduced virial series. As expected, the semi-empirical fitted equations of Kolafa et al. [1] agree to within the uncertainty of the simulation results. The exponential closure also performs surprisingly well given its simple form, with only one form of the Padé approximants of Clisby and McCoy [2] faring better.

Collision statistics in homogeneously sheared granular materials are investigated in Chap. 6 to evaluate the fundamental differences between elastic and inelastic systems and to test Enskog theory predictions for a steady state granular system. Anisotropies in the kinetic energy are under-predicted by the approximate Enskog theory of Montanero et al. [3], and also by Enskog DSMC to a lesser degree. $f^{(2)}$ -DSMC yields improved predictions (see Sec. 3.6), indicating this anisotropy is related to the repeated re-collisions between clustered particles. Enskog theory generally performs well (see Sec. 6.4), but begins to deviate at low densities for strongly inelastic particles. The effects of strong correlations are observed in the mean free times leading to an enhancement of the number of collision sequences at both short and long times (see Fig. 6.10).

Highly asymmetric binary hard spheres are explored in Chap. 7 to determine the effect of extreme size disparities on the transport properties. A “fines” effect not captured by Enskog theory is found at sufficiently high densities, where the addition of smaller spheres lowers the fluid viscosity. The thermal conductivity is also severely under-predicted for dense systems with a low mole fraction of large spheres. The low mole fraction systems are found which exhibit thermal conductivities above that of the pure component fluids at the same density or pressure. Therefore a maximum exists in the fluid thermal conductivity for a given mole fraction of larger spheres.

Finally, the control parameters of a simple model for helix formation are fully characterised in Chap. 8. Replica exchange simulations, along with histogram re-weighting and cluster analysis techniques, have allowed the determination of diagrams of states for the homopolymer in terms of the well width, overlap parameter and chain length. Increasing the overlap parameter σ/l from 1 first stabilises, and then destabilises, the helix structure by restricting and removing interactions between monomers separated by an increasing number of bonds in the chain (see Sec. 8.3.2). The well width is found to control the pitch of the helix (see Sec. 8.3.3), with smaller well widths leading to higher curvatures and larger well widths generating almost spherical helices (see Fig. 8.7). The helix structure is only stable for a window of polymer lengths, with the minimum length close to the number of monomers in a single turn of the stable helix. At larger polymer lengths, the number of possible folded states increases rapidly, displaying characteristics reminiscent

of a glass transition (see Sec. 8.3.4).

9.2 Future Work

The possible directions for further study are tremendous, and so the items proposed here are by no means exhaustive. There are many algorithmic developments which could be implemented in DYNAMO and many interesting systems which DYNAMO can already explore. Some avenues of research are already ongoing, either by the author or other researchers. In this section, a selection of the possible systems for future study are first outlined, then the possible algorithmic improvements are proposed.

9.2.1 Future Systems for Study

There are some simple discrete potentials which can allow different approximations in kinetic theory to be tested in isolation, to reveal possible shortcomings and suggest new approximations. The thin needle system of Frenkel and Maguire [4] is an ideal gas, yet it exhibits complex time dependent behaviour and non-trivial transport coefficients. This allows the dynamical predictions of theories to be tested independently of the treatment of the static behaviour, which is known exactly. Thanks to the efforts of R. Sargent (see Chap. 4), this model is now available in DYNAMO and simulations of sheared granular needles are currently underway.

The parallel hard-cube model [5] is another example of a simple model, yet the nature of its phase transitions are still uncertain. A fluid and an ordered phase are evident, but the conclusive determination of the order of the transition has so far eluded researchers. Preliminary results, calculated using DYNAMO on large systems of parallel cubes, have already been published by Hoover et al. [6] and further simulations are underway.

Using slightly more complex models, the fundamental behaviour of realistic systems can be studied. The homopolymers of Chap. 8 are by definition comprised of monomers of only a single type. However, real proteins and polymers are comprised of several monomer types, and the sequence of these groups determines the folded structure which is key to the functional behaviour. DYNAMO has already been extended to heteropolymers to study the effects of sequencing, and simulations are being performed by several researchers. The speed of the event driven technique allows previous results [7] gathered using Monte Carlo techniques to be expanded upon. The differences in the number and quality of the folded states between sequences which are random and those which are correlated may lead to a better understanding of the nature of protein folding.

Finally, test simulations of 32×10^6 particles at a density of $\rho \sigma^3 = 0.5$ have already been performed using 64 bit processors. DYNAMO currently utilises around 500 bytes of memory per particle, and reducing the memory usage of the event list would allow significantly larger systems to be studied. These system sizes are rapidly approaching the scales where the hydrodynamic description of fluids could be directly tested. Inversely,

real systems modelled using hydrodynamics are becoming smaller as microfluidics devices approach the femtolitre scale. As these scales converge, large MD systems could provide another method for the analysis of the theoretical descriptions for microfluidics.

The following section will now deal with more general improvements to DYNAMO itself, which will allow a wider range of systems to be studied.

9.2.2 Event Driven Algorithms

A few key suggestions for future directions of DYNAMO are already outlined in Sec. 4.6, but there are some important additional areas which are included here.

At present, DYNAMO is not applicable to systems with general asymmetric potentials; however, DYNAMO is flexible enough for these systems to be implemented. The asymmetric potential framework of van Zon and Schofield [8] requires a numerical root finding routine to determine the time of the next event. This is computationally expensive and, as the stepped potentials can be quite long ranged, a limiting step in the speed of the simulation. The root finding technique itself takes as input only a few variables (e.g., relative positions, velocities and rotational data) and returns whether an event occurs and the time of the event. This step could be replaced by an artificial neural net which had been trained to the inputs and outputs of this root finding step. Benedict and Maguire [9] have already utilised artificial neural nets in the simulation of a 2D fluid of triangles, and they report an increase in computational speed by several orders of magnitude. Leveraging this technique could greatly increase the speed of the stepped potentials making them increasingly attractive over their continuous potential counterparts.

In the simulations of homopolymers (Chap. 8), the replica exchange technique is used to try and ensure the full phase-space of the system is explored. In larger or more complex systems this technique alone is not sufficient to guarantee ergodicity. Multicanonical or “blue moon” simulations are a technique which introduces a bias into the Hamiltonian of the system to increase the probability of the system exploring rare or inaccessible states. These techniques are well established in continuous potential systems [10], and the generalisation to discrete potentials is straightforward. This should allow the rapid characterisation of homopolymers and heteropolymers and facilitate the study of secondary structure in proteins and sequence effects.

Finally, the direct simulation Monte Carlo (DSMC) technique offers a relatively computationally inexpensive method to explore systems over large length and time scales (hydrodynamics), while still providing an approximate description of the smallest length scales of a simulation. Donev [11] proposed using DSMC in a hybrid MD-DSMC algorithm to approximate solvent-solvent interactions in dissolved polymers. This is particularly interesting as the entire algorithm remains event-driven, and the boundary conditions of the polymer particles are a natural part of the DSMC approximation. Coupled hydro-molecular dynamics simulations are notoriously difficult but this algorithm is relatively straightforward and could be used at larger scales to simulate interstitial gases in granular

flows.

9.3 References

- [1] J. Kolafa, S. Labik and A. Malijevsky, “Accurate equation of state of the hard sphere fluid in stable and metastable regions”, *PCCP*. 6, 2335–2340 (2004).
- [2] N. Clisby and B. N. McCoy, “Ninth and Tenth Order Virial Coefficients for Hard Spheres in D Dimensions”, *J. Stat. Phys.* 122, 15–57 (2006).
- [3] J. M. Montanero et al., “Kinetic theory of simple granular shear flows of smooth hard spheres ”, *J. Fluid Mech.* 389, 391–411 (1999).
- [4] D. Frenkel and J. F. Maguire, “Molecular dynamics study of the dynamical properties of an assembly of infinitely thin hard rods”, *Mol. Phys.* 49, 503–541 (1983).
- [5] R. W. Zwanzig, “Virial Coefficients of “Parallel Square” and “Parallel Cube” Gases”, *J. Chem. Phys.* 24, 855–856 (1956).
- [6] W. G. Hoover, C. G. Hoover and M. N. Bannerman, “Single-Speed Molecular Dynamics of Hard Parallel Squares and Cubes”, *J. Stat. Phys.* (2009).
- [7] J. E. Magee, J. Warwicker and L. Lue, “Freezing and folding behavior in simple off-lattice heteropolymers”, *J. Chem. Phys.* 120, 11285–11291 (2004).
- [8] R. van Zon and J. Schofield, “Event-driven dynamics of rigid bodies interacting via discretized potentials”, *J. Chem. Phys.* 128, 154119 (2008).
- [9] M. Benedict and J. F. Maguire, “Molecular dynamics simulation of nanomaterials using an artificial neural net”, *Phys. Rev. B*. 70, 174112 (2004).
- [10] N. Nakajima, H. Nakamura and A. Kidera, “Multicanonical Ensemble Generated by Molecular Dynamics Simulation for Enhanced Conformational Sampling of Peptides ”, *J. Phys. Chem. B*. 101, 817–824 (1997).
- [11] A. Donev, “Asynchronous Event-Driven Particle Algorithms”, *Simulation*. 85, 229–242 (2009).

APPENDIX
A

**REPRINT: COLLISION STATISTICS IN SHEARED
INELASTIC HARD SPHERES**

Collision statistics in sheared inelastic hard spheres

Marcus N. Bannerman, Thomas E. Green, Paul Grassia, and Leo Lue*

School of Chemical Engineering and Analytical Science, The University of Manchester, P.O. Box 88, Sackville Street, Manchester M60 1QD, United Kingdom

(Received 9 December 2008; published 22 April 2009)

The dynamics of sheared inelastic-hard-sphere systems is studied using nonequilibrium molecular-dynamics simulations and direct simulation Monte Carlo. In the molecular-dynamics simulations Lees-Edwards boundary conditions are used to impose the shear. The dimensions of the simulation box are chosen to ensure that the systems are homogeneous and that the shear is applied uniformly. Various system properties are monitored, including the one-particle velocity distribution, granular temperature, stress tensor, collision rates, and time between collisions. The one-particle velocity distribution is found to agree reasonably well with an anisotropic Gaussian distribution, with only a slight overpopulation of the high-velocity tails. The velocity distribution is strongly anisotropic, especially at lower densities and lower values of the coefficient of restitution, with the largest variance in the direction of shear. The density dependence of the compressibility factor of the sheared inelastic-hard-sphere system is quite similar to that of elastic-hard-sphere fluids. As the systems become more inelastic, the glancing collisions begin to dominate over more direct, head-on collisions. Examination of the distribution of the times between collisions indicates that the collisions experienced by the particles are strongly correlated in the highly inelastic systems. A comparison of the simulation data is made with direct Monte Carlo simulation of the Enskog equation. Results of the kinetic model of Montanero *et al.* [J. Fluid Mech. **389**, 391 (1999)] based on the Enskog equation are also included. In general, good agreement is found for high-density, weakly inelastic systems.

DOI: [10.1103/PhysRevE.79.041308](https://doi.org/10.1103/PhysRevE.79.041308)

PACS number(s): 45.70.-n, 47.57.Gc, 05.20.Dd

I. INTRODUCTION

In rapid granular flows [1,2], the mean flight time of the particles in the granular material may be large compared to the contact time between particles. Interparticle interactions are modeled as “collisions,” which play a key role in transferring momentum and other properties through the system. Granular materials in this flow regime can then be represented by a collection of inelastic hard spheres [3,4].

The simplicity of the inelastic-hard-sphere model lends itself well to theoretical analysis. In particular, the methods developed for the kinetic theory of equilibrium gases have been applied to rapidly sheared inelastic-hard-sphere systems. The seminal paper by Lun *et al.* [5] marked the start of “complete” kinetic theories capable of predicting both the kinetic and collisional properties. The Boltzmann equation has featured predominantly in the theory of granular gases due to its simpler form (e.g., see Ref. [6]). However, the most successful molecular kinetic theory to date is the revised Enskog theory [7], an extension to the Boltzmann equation for dense systems. The Enskog theory assumes uncorrelated particle velocities and currently relies on a static structural correlation factor from elastic fluids [8]. Approximate theories beyond the Enskog theory, such as ring theory [9], have been developed and applied to granular systems. However, due to their complexity, their use has been limited (e.g., cooling, rare granular gases).

Common to most kinetic-theory solutions is the assumption of a steady-state spatially uniform distribution function. Provided scale separation exists, as in the case of elastic

fluids, fluctuations from this steady state can be accounted for using the Chapman-Enskog expansion [10]. To solve the Enskog equation, approximations typically begin by taking moments of the kinetic equation with respect to the density, velocity, and products of the velocity. These moment equations are used to solve for the parameters of an expansion or model. Typically, only terms up to the granular “temperature,” or isotropic stress and rotation terms [11], are included as field variables. Anisotropic stresses can still be predicted from such a theory [12]. Indeed, attempts have been made to include the full second-order velocity moment [13] as a hydrodynamic variable to improve theoretical predictions.

Grad’s method [14] solves Enskog theory using an expansion of the distribution function about a reference state. This has been applied to polydisperse granular systems [4] and, unlike perturbative solutions, does not require assumptions on the strength of the shear. Kinetic models are a powerful method of generating simplified kinetic equations which retain key features of the original. Montanero *et al.* [15] solved an improved Bhatnagar-Gross-Krook (BGK) kinetic model [16,17] for inelastic systems. The improved BGK model approximates the collisional term of the kinetic equation using the first two velocity moments, which correspond to the collisional stress and energy loss, and a general relaxation term. This leads to a simplified kinetic equation. The solution in the low-dissipation limit is particularly attractive, as it provides estimates for the system properties without requiring numerical solution and compares favorably to direct simulation Monte Carlo (DSMC) results.

DSMC [18] is a numerical simulation technique used to directly solve the Boltzmann equation without requiring further approximations. This can then be used to rapidly test solutions of the kinetic equation. The method has already

*leo.lue@manchester.ac.uk

been extended to the Enskog equation for homogeneously sheared inelastic systems [15,19,20].

While kinetic theories do offer insight into the behavior of granular materials, they are necessarily approximate. The Boltzmann and Enskog kinetic theories do not include velocity or dynamic structural correlations. Ring theory [9] is capable of including particle correlations. However, further approximations are required to make the resulting theory tractable. These correlations are present in moderately dense to dense systems of elastic particles, but they are enhanced by the clustering in inelastic systems [21,22]. The failure of Boltzmann and Enskog theories at high densities is therefore expected, even for elastic-hard-sphere systems. On the other hand, nonequilibrium molecular-dynamics (NEMD) simulations [3,23] can, in principle, give “exact” results for driven inelastic-hard-sphere systems [24,25]. These simulations can be used to validate kinetic theories against the underlying model. Initial studies of sheared granular systems used moving boundaries [3,26], such as rough walls, to introduce energy into the system. Due to the computational limitations, the wall separation is typically on the order of a few particle diameters, and wall effects dominate the simulation results. For large system sizes, shear instability is observed [27]. Consequently, the results for wall-driven simulations are strongly dependent on system size.

Another manner by which to introduce shear in nonequilibrium molecular dynamics is the Lees-Edwards [28] or “sliding-brick” boundary conditions. Simulations of inelastic-hard-sphere systems using Lees-Edwards boundary conditions [23,29–32] lessen the influence of wall effects, by eliminating the surface of the system, but these simulations still introduce shear in an inhomogeneous manner, which may lead to clustering instabilities [33] for larger systems.

While there are many interesting similarities between elastic-hard-sphere fluids and driven inelastic-hard-sphere systems, there are key differences. One is the tendency of inelastic hard spheres to form clusters and patterns, while elastic-hard-sphere fluids tend to remain isotropic. Another example is the velocity distribution. The velocity of elastic hard spheres is governed by the Maxwell distribution, which is isotropic and Gaussian. The velocity distribution of flowing inelastic hard spheres is, in general, anisotropic [34] and can show significant deviations from the Gaussian distribution, especially when there is clustering.

In this work, we examine the properties of sheared inelastic-hard-sphere systems using nonequilibrium event-driven molecular-dynamics simulations with the Sllod algorithm combined with Lees-Edwards boundary conditions. Part of the purpose of this work is to investigate, at a particle level, the differences between the behavior of inelastic and elastic (equilibrium) hard-sphere systems. Another purpose of this work is to provide simulation data which can be used to test kinetic-theory predictions for the properties of these systems. A previous study by Montanero *et al.* [35] already compared two-dimensional (2D) and three-dimensional (3D) simulations of binary inelastic hard spheres against DSMC simulations of Enskog theory. They found good agreement over the range of mass ratio, size ratio, and inelasticity studied. However, the clustering instability present in systems of large numbers of highly inelastic particles appears to limit

the range of inelasticity studied. As mentioned previously, kinetic theories for sheared granular materials are typically developed for the case where the system is spatially uniform and homogeneously sheared. One of the difficulties with comparing the predictions of the kinetic theory with the simulation data for sheared granular materials is the formation of clusters, which makes comparison between the two problematic. As a consequence, care is taken in this work to ensure that the systems remain homogeneous, and strongly inelastic systems can be accessed. In these simulations, we investigate the collision statistics, such as velocity distributions, collision angles, time between collisions, and mean free paths, of sheared inelastic hard spheres. In addition, we examine the variation in various bulk properties of the system, such as the viscosity, mean kinetic energy, and stress, with the packing fraction and coefficient of restitution of the particles. We also investigate the correlations between the collisions, which are neglected in most kinetic-theory approaches. The remainder of this paper is organized as follows. In Sec. II, we describe the details of the granular-dynamics simulations. In Sec. III, we describe the details of the DSMC simulations. In Sec. IV, we present the results of our simulation work, including a comparison with the predictions of Enskog theory. Finally, a summary of the main findings is provided in Sec. V.

II. SIMULATION DETAILS

Nonequilibrium granular-dynamics simulations were performed on systems of inelastic hard spheres of diameter σ and mass m . The system is sheared in the y plane in the x direction with a constant strain rate of $\dot{\gamma}$ using the Sllod algorithm [36]. In this method, shear is applied through the use of the Lees-Edwards sliding-brick boundary conditions [28,36] and the velocity is transformed relative to a linear velocity profile. The equations of motion are

$$\frac{d\mathbf{r}_i}{dt} = \bar{\mathbf{v}}_i + y_i \dot{\gamma} \hat{\mathbf{e}}_x, \quad (1)$$

$$\frac{d\bar{\mathbf{v}}_i}{dt} = \frac{\mathbf{F}_i}{m} - \bar{v}_{y,i} \dot{\gamma} \hat{\mathbf{e}}_x, \quad (2)$$

where \mathbf{F}_i is the force acting on particle i , \mathbf{r}_i is the position of particle i , $\bar{\mathbf{v}}_i$ is the so-called peculiar velocity of particle i , y_i is the y coordinate of particle i , $\bar{v}_{y,i}$ is the y component of the peculiar velocity of particle i , $\hat{\mathbf{e}}_x$ is a unit vector pointing in the positive x direction, and $\dot{\gamma}$ is the strain rate.

The peculiar velocity of a particle i is defined as the difference between its laboratory velocity \mathbf{v}_i and the local streaming velocity (the velocity of the local streamline). For simple shear, it is given by the linear transformation

$$\bar{\mathbf{v}}_i = \mathbf{v}_i - y_i \dot{\gamma} \hat{\mathbf{e}}_x.$$

The peculiar velocity is related to the dispersion of the particles from the average streamlines of the flow. The Sllod equations of motion are particularly convenient as the peculiar velocity is naturally recovered without the need for a separate coordinate transformation. They allow the possibil-

ity of thermostating the system [37] and the study of time dependent shear flows.

In a hard-sphere system, the spheres do not experience any force between collisions. The equations of motion can then be solved analytically for the trajectories of the spheres between collisions. The evolution of the position and peculiar velocity of particle i in the system between collisions is

$$\begin{aligned}\mathbf{r}_i(t) &= \mathbf{r}_i(t_0) + [\bar{\mathbf{v}}_i(t_0) + y_i(t_0) \dot{\gamma} \hat{\mathbf{e}}_x](t - t_0) \\ &= \mathbf{r}_i(t_0) + \mathbf{v}_i(t_0)(t - t_0), \\ \bar{\mathbf{v}}_i(t) &= \bar{\mathbf{v}}_i(t_0) - \bar{v}_{y,i}(t_0) \dot{\gamma}(t - t_0) \hat{\mathbf{e}}_x.\end{aligned}\quad (3)$$

When a particle undergoes a collision, it experiences an impulse which alters its velocity. These collisions are instantaneous and only occur between pairs of spheres (i.e., there are no three- or higher-body collisions). The inelasticity of the hard spheres is characterized by the coefficient of restitution α . This is defined through the amount of kinetic energy ΔE lost on collision,

$$\Delta E = \frac{m}{4}(1 - \alpha^2)(\hat{\mathbf{r}}_{ij} \cdot \mathbf{v}_{ij})^2, \quad (4)$$

where \mathbf{v}_i is the velocity of particle i immediately before collision, $\mathbf{v}_{ij} = \mathbf{v}_i - \mathbf{v}_j$, and $\hat{\mathbf{r}}_{ij} = \mathbf{r}_{ij}/|\mathbf{r}_{ij}|$ is the unit vector pointing from the center of particle j to the center of particle i .

Each collision preserves the total momentum of the particles involved. Therefore, the change in velocities for a colliding pair of spheres i and j is given by

$$\begin{aligned}\mathbf{v}'_i &= \mathbf{v}_i - \frac{1}{2}(1 + \alpha)(\hat{\mathbf{r}}_{ij} \cdot \mathbf{v}_{ij})\hat{\mathbf{r}}_{ij}, \\ \mathbf{v}'_j &= \mathbf{v}_j + \frac{1}{2}(1 + \alpha)(\hat{\mathbf{r}}_{ij} \cdot \mathbf{v}_{ij})\hat{\mathbf{r}}_{ij},\end{aligned}\quad (5)$$

where the primes denote postcollision values of the particle velocities.

The coefficient of restitution α is, in general, a function of the relative velocity on collision. Viscoelastic models that incorporate this have been very successful in describing real systems such as steel spheres [38]. A common approximation in kinetic theory is to assume a constant coefficient of inelasticity, as this greatly simplifies the collision integrals while the basic physics is not significantly altered. A constant coefficient of restitution is used in this work to facilitate comparison against kinetic-theory results.

One concern for a system with a constant coefficient of restitution is the phenomenon of inelastic collapse, where an infinite number of collisions occur between several spheres in a finite interval of time. Event-driven simulations will fail in the event of a single collapse event. In two dimensions, freely cooling inelastic-hard-sphere systems undergo [39] inelastic collapse with coefficient of restitution as high as 0.59.

Inelastic collapse is rare in sheared systems [40] and is increasingly rare in higher dimensions. However, a near-collapse situation can still cause a simulation to break down if the machine precision is not sufficiently high to resolve a rapid series of successive collisions. In the simulations performed in this work, no partial or full collapse events were found, even for dense and highly inelastic systems.

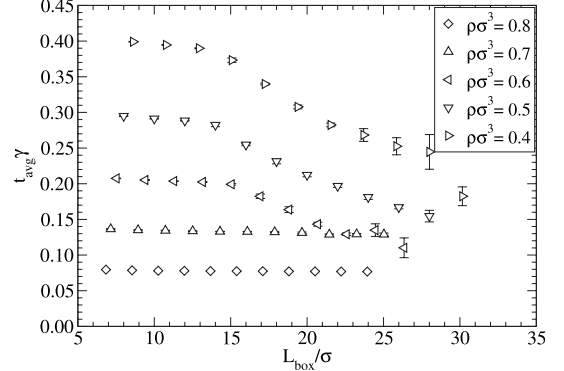


FIG. 1. The system size dependence of the mean free time between collisions, t_{avg} , for simulations of a sheared inelastic-hard-sphere system with $\alpha=0.4$ in a cubic box with sides of length L_{box} . The number of particles is $N=256$ in the smallest system, and $N=10\,976$ in the largest.

The simulation algorithm that we employ is a generalization of the standard event-driven molecular-dynamics algorithm for hard spheres [41] (for more details, see Ref. [42]). The main modifications are the use of the sliding-brick boundary conditions [28] and the Sllod equations of motion.

Unlike the elastic-hard-sphere system, the inelastic-hard-sphere system has no intrinsic time scale. The applied strain rate $\dot{\gamma}$ sets the time scale of the system. Therefore, there are only two relevant dimensionless parameters: the density $\rho\sigma^3$ and the coefficient of restitution α . In this work, the density is varied from $\rho\sigma^3=0.4$ to 0.9, and the coefficient of restitution is varied from $\alpha=0.4$ to 0.9.

Because the shear is imposed through the boundary conditions, the strain rate is only fixed at two points, separated by the entire height of the simulation box. In low-density systems with large numbers of particles, clustering occurs [27]. This leads to a local variation in the strain rate in the system, and, consequently, the system will not be homogeneously sheared. At the onset of clustering, the size dependence of the system properties changes from the typical N^{-1} scaling to a different behavior. To illustrate this, the mean free time of sheared inelastic hard spheres with $\alpha=0.4$ is shown in Fig. 1. These simulations were performed in a cubic simulation box where the system size was varied while holding the density constant. The “break” in the curves for the lower densities indicates the presence of cluster formation in the larger systems. The same general behavior manifests in all system properties and is relatively easy to detect.

Kinetic-theory studies of sheared inelastic systems typically assume that the system is homogeneous and uniformly sheared, with a linear velocity profile. This makes the comparison between granular-dynamics simulations and the kinetic theory problematic. To allow comparison with these theories, we ensure that the systems remain homogeneous during the course of the simulations. In order to avoid the clustering regime while still maintaining a sufficiently large system size to provide proper statistics, the x , y , and z dimensions of the simulation box are set to the ratio of 14.4:1:1, and a total of $N=7200$ spheres are used. This ensured that the systems remained homogeneous for all condi-

tions (i.e., number of particles, coefficient of restitution, and density) that were examined in this work.

At the beginning of the simulations for each set of conditions, the spheres are arranged in a face-centered cubic lattice at the appropriate density. The velocities of the spheres are initially assigned from a Maxwell-Boltzmann distribution. The simulations are then run for an “equilibration” period of 10^7 collisions. Afterward, system property data are collected over at least ten production runs, each lasting 10^7 collisions. The uncertainties of the data are estimated from the standard deviations of the results from these separate runs. In Sec. III, we describe the DSMC simulations performed.

III. DSMC SIMULATIONS

The DSMC method was used to numerically solve the Enskog equation. This technique has been described in detail previously [15,19] and is only covered briefly here. The peculiar velocity distribution function f is represented by using a collection of N sample velocities or “simulated” particles:

$$f(\bar{\mathbf{v}}, t) = N^{-1} \sum_{i=1}^N \delta^3[\bar{\mathbf{v}} - \bar{\mathbf{v}}_i(t)], \quad (6)$$

where $\bar{\mathbf{v}}_i(t)$ is the peculiar velocity of sample i at time t . At each time step Δt , the samples are evolved according to the Sllod dynamics [see Eq. (2)]. The samples are then tested for collisional updates. At each time step, $\frac{1}{2}NP_{\max}^{(c)}$ pairs of samples in the collection are selected, where $P_{\max}^{(c)}$ is a parameter of the DSMC simulation. The probability that a collision between a pair of samples i and j will be executed is proportional to

$$P_{ij}^{(c)} = 4\pi\sigma^2\chi\rho(\hat{\mathbf{k}} \cdot \mathbf{v}_{ij})\Theta(\hat{\mathbf{k}} \cdot \mathbf{v}_{ij})\Delta t, \quad (7)$$

where $\hat{\mathbf{k}}$ is a randomly generated unit vector, $\mathbf{v}_{ij} = \bar{\mathbf{v}}_i - \bar{\mathbf{v}}_j - \sigma\hat{k}_y\hat{\mathbf{e}}_x$ is the relative laboratory velocity, Θ is the Heaviside step function, and χ is the radial distribution function at contact. In this work, the value of χ is taken from the Carnahan-Starling [8] equation of state for elastic hard spheres, which is given by

$$\chi = \frac{1 - \nu/2}{(1 - \nu)^3}, \quad (8)$$

where $\nu = \rho\pi\sigma^3/6$ is the solid fraction.

To optimize the simulation, the quantity $P_{\max}^{(c)}$ is chosen to be the maximum observed value of $P_{ij}^{(c)}$. This is estimated and updated during a simulation if $P_{ij}^{(c)}$ exceeds $P_{\max}^{(c)}$. The probability that a collision between samples i and j is executed is $P_{ij}^{(c)}/P_{\max}^{(c)}$, and, if the collision is accepted, the velocities are updated using Eq. (5) with $\mathbf{r}_{ij} = -\sigma\hat{\mathbf{k}}$.

For the results presented here, $N=1372$ and Δt is selected such that $\frac{1}{2}NP_{\max}^{(c)} < 5$. The distribution functions are equilibrated for 10^6 collisions, and then results are collected and averaged over ten runs of 10^7 collisions.

IV. RESULTS AND DISCUSSION

In this section, we present our simulation results for the properties of homogeneously sheared inelastic-hard-sphere

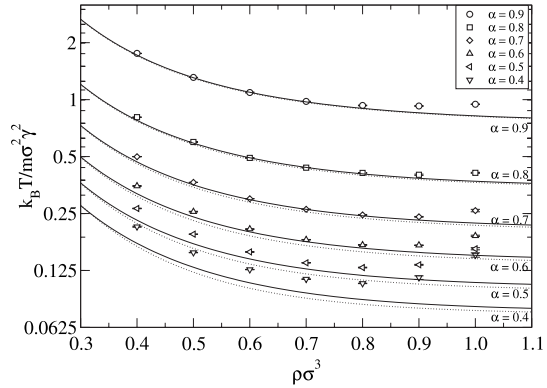


FIG. 2. Variations in the mean kinetic energy per particle with density for (i) $\alpha=0.4$ (circles), (ii) $\alpha=0.5$ (squares), (iii) $\alpha=0.6$ (diamonds), (iv) $\alpha=0.7$ (up triangles), (v) $\alpha=0.8$ (left triangles), and (vi) $\alpha=0.9$ (down triangles). The dotted lines are the suggested expressions of Ref. [15] and the solid lines are DSMC results.

systems. These results are compared against DSMC simulation of the Enskog equation to test the Enskog approximation. We also include the results from the kinetic model solved by Montanero *et al.* [15,43]. This theory is particularly interesting as it provides analytical results in the limit of small strain rates, along with simple expressions that approximate DSMC results. Without the small-strain-rate approximation, a more accurate numerical solution of the model is available [15]. However, the DSMC simulations already provide accurate Enskog theory results without further approximation.

A. Velocity distribution

The kinetic energy of the system is defined through the fluctuations of the velocity of the particles from their respective local streaming velocity,

$$E = \frac{1}{2} \sum_{k=1}^N m\bar{v}_k^2. \quad (9)$$

The mean kinetic energy is therefore a measure of the velocity dispersion present in the system. In analogy with elastic (equilibrium) hard-sphere fluids, a kinetic (or “granular”) temperature T is typically introduced through the relation

$$\frac{3}{2}Nk_B T \equiv \langle E \rangle, \quad (10)$$

where N is the number of particles in the system, and k_B is the Boltzmann constant. Although the physical significance of the granular temperature has been a subject of some controversy [12], the concept has proved effective in the theoretical modeling of the properties of granular materials.

The granular temperature of the sheared inelastic-hard-sphere system at steady state is plotted in Fig. 2. The symbols are the results of our molecular-dynamics simulations, the dotted lines are the suggested expressions of Montanero *et al.* [15], and the solid lines are the DSMC simulation results. From the figure, it can be seen that the granular temperature of the system decreases with decreasing values of

the coefficient of restitution. The particles in a strongly inelastic system rebound less from collisions. Therefore, collisions in the direction of shear can quickly settle a particle to the velocity of the streamline. In addition, the motion of the particles off the streamline (in the y and z directions) are more quickly dissipated by collisions with particles on neighboring streamlines. Consequently, strongly inelastic systems have a greater tendency to follow the streamlines of a flow.

At low densities, the granular temperature increases with decreasing particle densities. The collisions between particles transmit information regarding the mean velocity of the flow. For very-low-density systems, the collisions are relatively rare events, and between collisions a particle will generally travel on trajectories that deviate from the streamlines, thus contributing to the granular temperature. With increasing density, a particle will become increasingly “caged” by surrounding particles, experiencing more collisions that will keep it on a particular streamline. Therefore, one expects that the temperature should generally decrease with increasing particle density. However, the simulation data indicate that the temperature of the system does not depend monotonically with the density, and a minimum is observed at a relatively high density for all the systems considered. The minimum becomes more pronounced as the coefficient of restitution decreases.

We note that in dense experimental granular systems, particles mainly remain in contact with each other and interact by rolling or sliding past one another, rather than through collisions. In this regime, soft-sphere models [44], as opposed to hard-sphere models, are more representative. Consequently, the applicability of the simulation results for the inelastic-hard-sphere system at high densities to experimental granular systems should be considered with care.

In general, Enskog theory and the solution of Montanero *et al.* [15] provides a fairly accurate description of the simulation results. However, there is a large discrepancy for high values of the inelasticity and density. In addition, Enskog theory does not capture the presence of the minimum in the temperature with respect to the density.

Equilibrium fluids obey the equipartition theorem: energy is, on average, distributed evenly between all degrees of freedom. In driven granular systems, however, this has been shown to not be the case [45]. Figure 3(a) shows the variation in $\langle \bar{v}_y^2 \rangle / \langle \bar{v}_x^2 \rangle$ with density, and Fig. 3(b) shows the variation in $\langle \bar{v}_z^2 \rangle / \langle \bar{v}_y^2 \rangle$. The symbols are the results of our molecular-dynamics simulations, the dotted lines are the predictions of the theory of Montanero *et al.* [15], and the solid lines are the DSMC simulation results. If the system obeyed the equipartition function, then both these ratios would be equal to 1. The dispersion of the velocity parallel to the direction of shear (i.e., the x direction) is consistently larger than that perpendicular to the shear, which is unsurprising as this is the direction in which energy is inputted to the system. The asymmetry increases with decreasing density and with decreasing values of the coefficient of restitution. It is interesting to note, however, that the fluctuations in the velocity in the y and z directions are nearly equal.

The low-dissipation theory of Montanero *et al.* [15] strongly underpredicts the anisotropy in the velocity disper-

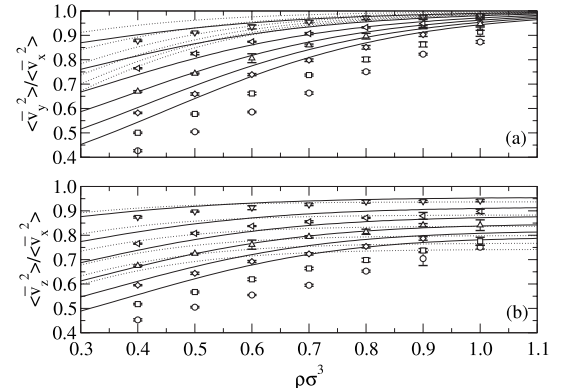


FIG. 3. The ratios of the mean-square velocity (a) in the y and x directions and (b) in the z and x directions for sheared inelastic-hard-sphere systems with (i) $\alpha=0.4$ (circles), (ii) $\alpha=0.5$ (squares), (iii) $\alpha=0.6$ (diamonds), (iv) $\alpha=0.7$ (up triangles), (v) $\alpha=0.8$ (left triangles), and (vi) $\alpha=0.9$ (down triangles). The dotted lines are the suggested expressions of Ref. [15], and the solid lines are the DSMC results.

sion. DSMC results provide a better description but still deviate significantly from the simulation results at low values of the elasticity.

The theory of Montanero *et al.* [15] truncates terms within the second velocity moment of the collision integral and all higher terms. The full second moment could be included to improve predictions. However, as this is primarily a collision term it is unlikely to improve the predictions of the velocity anisotropy.

The kinetic model could be expanded by relaxing to a generalized Gaussian distribution, as in the ellipsoidal statistical model. The extra degrees of freedom in the model would then be solved for by the inclusion of a full second velocity moment balance. This might still prove tractable and improve the predictions for the velocity-dispersion anisotropy.

For equilibrium systems, such as elastic-hard-sphere fluids, the velocity distribution is exactly given by the Maxwell-Boltzmann distribution. However, granular materials have been shown to deviate from this distribution [34,46,47]. The simulation data for the distributions of the single-particle x , y , and z components of the peculiar velocity are shown in Fig. 4. The peculiar velocities are reduced by their mean-square values ($v_i^* = \bar{v}_i / \langle \bar{v}_i^2 \rangle^{1/2}$, for $i=x, y$, and z). The distributions are, in general, well described by an anisotropic Gaussian distribution. For the highly inelastic systems, the distributions display a slightly enhanced high-velocity tail. This is most evident in the direction of shear (i.e., the x direction).

For simulations in a cubic box at the onset of clustering in the system, the peculiar velocity distributions in the y and z directions can be shown to develop strong high-velocity tails. In this case, the bulk of the particles are within a dense low-strain-rate zone, while the remainder reside in a rare high-strain-rate and granular-temperature region. The particles in the high-strain-rate region lead to a high-velocity tail. Further studies on clustering effects are currently underway.

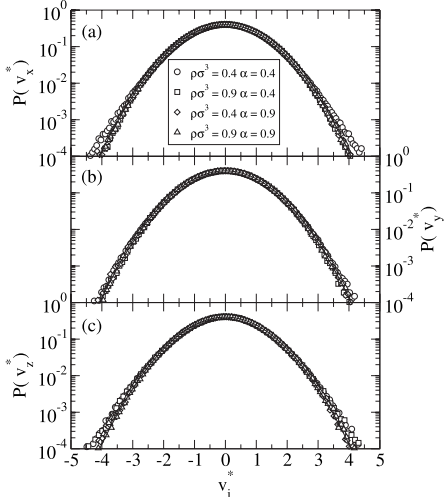


FIG. 4. The peculiar velocity distributions in the (a) x direction, (b) y direction, and (c) z direction in sheared inelastic-hard-sphere systems with (i) $\rho\sigma^3=0.4$ and $\alpha=0.4$ (circles), (ii) $\rho\sigma^3=0.9$ and $\alpha=0.4$ (squares), (iii) $\rho\sigma^3=0.4$ and $\alpha=0.9$ (diamonds), and (iv) $\rho\sigma^3=0.9$ and $\alpha=0.9$ (triangles). The solid line is a Gaussian distribution.

B. Stress tensor

In this section, we examine the stress tensor. The time-averaged value of the stress tensor $\langle \mathbf{P} \rangle$ for a hard-sphere system is given by [48]

$$\langle \mathbf{P} \rangle = \frac{1}{V\tau} \sum_{\text{collisions}}^{\tau} \left[\Delta t_c \sum_{k=1}^N m \bar{\mathbf{v}}_k \bar{\mathbf{v}}_k + \sigma \hat{\mathbf{r}}_{ij} m \Delta \mathbf{v}_i \right], \quad (11)$$

where Δt_c is the time interval between two consecutive collisions, $\Delta \mathbf{v}_i$ is the change in velocity of sphere i on collision, τ is the time over which the stress tensor is averaged, and V is the total volume of the system. The first summation runs over all collisions that occur during the time τ , and the indexes i and j refer to the spheres undergoing the collision. The index k runs over all particles in the system.

The pressure p of the system, which is defined as

$$p \equiv \frac{1}{3} (\langle P_{xx} \rangle + \langle P_{yy} \rangle + \langle P_{zz} \rangle),$$

is plotted in Fig. 5(a). As expected, the pressure increases as the density of the system increases. It also increases with increasing coefficient of restitution due to the rise in granular temperature. The Enskog theory requires, as input, the collision rate between particles as a function of the density. This is typically given by the equation of state for elastic-hard-sphere fluids through the compressibility factor. The compressibility factor Z , defined as

$$Z \equiv \frac{p}{\rho k_B T},$$

is plotted for the sheared inelastic-hard-sphere system in Fig. 5(b). The symbols represent the results of the simulations, and the line is the Carnahan-Starling equation of state [8] for the elastic-hard-sphere fluid. With the exception of the highest density, the compressibility factor for homogeneously

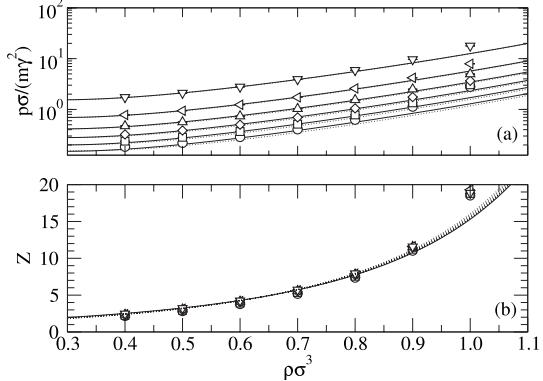


FIG. 5. (a) The dimensionless pressures $p\sigma/m\gamma^2$ and (b) the compressibility factors Z for inelastic-hard-sphere systems with (i) $\alpha=0.4$ (circles), (ii) $\alpha=0.5$ (squares), (iii) $\alpha=0.6$ (diamonds), (iv) $\alpha=0.7$ (up triangles), (v) $\alpha=0.8$ (left triangles), and (vi) $\alpha=0.9$ (down triangles). The uncertainty is smaller than the symbol size. The dotted lines are the suggested expressions of Ref. [15], and the solid lines are DSMC results. The solid line in (b) is the Carnahan-Starling equation of state for elastic-hard-sphere fluids, and the dotted lines are DSMC results for various α .

sheared inelastic spheres is quite similar to that for elastic hard spheres. The predictions of Enskog theory and Montanero *et al.* [15] for the pressure [see Fig. 5(a)] agree fairly well with the simulation data. The main source of the discrepancy is due to the misprediction of the kinetic contribution to the pressure.

The shear viscosity of a granular material is perhaps the most important design parameter in fast flows, quantifying the power lost per unit volume. The shear viscosity of the inelastic-hard-sphere system was computed by two means. The first method is via the definition of the shear viscosity η for simple Couette flow,

$$\eta \equiv - \frac{\langle P_{xy} \rangle}{\dot{\gamma}}. \quad (12)$$

An alternative method is to perform an energy balance. The work of shearing inputs energy into the system. Collisions between the inelastic spheres continuously dissipate kinetic energy. At steady state, the average rate of energy input is equal to the average rate of energy dissipation [49]

$$\eta \dot{\gamma}^2 V = - \langle \dot{E} \rangle, \quad (13)$$

where $\langle \dot{E} \rangle$ is the average rate of kinetic-energy dissipation. The rate of energy dissipation is directly related to the mean time between collisions, t_{avg} , for a sphere by

$$\langle \dot{E} \rangle = \frac{N}{2t_{\text{avg}}} \langle \Delta E \rangle,$$

where N is the total number of spheres in the system, and $\langle \Delta E \rangle$ is the average amount of kinetic energy lost per collision.

The simulation results for the viscosity of sheared inelastic-hard-sphere systems are summarized in Table I. The upper entries are the values obtained from the stress tensor

TABLE I. Dimensionless viscosities $\eta\sigma/m\dot{\gamma}$ of sheared inelastic-hard-sphere systems at various densities ρ and coefficients of restitution α . The upper value is determined from the stress tensor [see Eq. (11)], and the lower value is determined from the kinetic-energy dissipation rate [see Eq. (13)]. The value in brackets is the standard deviation over all of the runs.

$\rho\sigma^3$	α					
	0.4	0.5	0.6	0.7	0.8	0.9
0.4	0.1054(0.0003)	0.1294(0.0004)	0.1625(0.0006)	0.2134(0.0005)	0.2970(0.0004)	0.480(0.002)
	0.1054(0.0003)	0.1294(0.0004)	0.1625(0.0006)	0.2134(0.0005)	0.2969(0.0004)	0.480(0.002)
0.5	0.1300(0.0003)	0.1582(0.0002)	0.1979(0.0007)	0.2585(0.0003)	0.361(0.001)	0.583(0.002)
	0.1300(0.0003)	0.1582(0.0002)	0.1979(0.0007)	0.2585(0.0003)	0.361(0.001)	0.583(0.001)
0.6	0.1722(0.0005)	0.2078(0.0003)	0.2606(0.0007)	0.3416(0.0009)	0.4785(0.0005)	0.779(0.006)
	0.1722(0.0005)	0.2078(0.0003)	0.2606(0.0007)	0.3417(0.0009)	0.4785(0.0007)	0.779(0.007)
0.7	0.2445(0.0004)	0.2909(0.0008)	0.364(0.001)	0.4801(0.0008)	0.677(0.002)	1.117(0.005)
	0.2446(0.0003)	0.2909(0.0008)	0.364(0.001)	0.4801(0.0009)	0.677(0.002)	1.117(0.005)
0.8	0.371(0.001)	0.4375(0.0002)	0.545(0.001)	0.716(0.003)	1.020(0.002)	1.722(0.008)
	0.371(0.001)	0.4375(0.0002)	0.545(0.001)	0.716(0.003)	1.020(0.002)	1.722(0.008)
0.9	0.643(0.007)	0.731(0.001)	0.885(0.002)	1.141(0.004)	1.64(0.01)	2.86(0.01)
	0.643(0.008)	0.731(0.002)	0.885(0.002)	1.141(0.004)	1.64(0.01)	2.856(0.010)
1.0	1.42(0.01)	1.52(0.02)	1.73(0.02)	2.15(0.03)	3.01(0.03)	5.30(0.04)
	1.42(0.01)	1.52(0.02)	1.73(0.02)	2.15(0.03)	3.01(0.04)	5.30(0.03)

[see Eq. (11)], and the lower entries are the values obtained from the dissipation of kinetic energy [see Eq. (13)]. For all the simulation runs, the two agree within the statistical uncertainties of the simulations. Figure 6(a) shows the dependence of the shear viscosity on the reduced density of the system, for various values of the coefficient of restitution. The viscosity increases with packing fraction and coefficient of restitution (remembering that the shear rate is equal to 1). The theory of Montanero *et al.* [15] captures the full Enskog behavior and predicts the viscosity well. Enskog theory deviates at low values of α and high densities where the predictions for the temperature begin to deviate from the simulation results (see Fig. 2).

In addition to the shear viscosity, we also monitor the in-plane normal stress coefficient η_- and the out-of-plane

normal stress coefficient η_0 , which are defined as [36]

$$\eta_- = -\frac{1}{2\dot{\gamma}}(\langle P_{xx} \rangle - \langle P_{yy} \rangle),$$

$$\eta_0 = -\frac{1}{2\dot{\gamma}} \left[\langle P_{zz} \rangle - \frac{1}{2}(\langle P_{xx} \rangle + \langle P_{yy} \rangle) \right].$$

The in-plane normal stress coefficient is plotted in Fig. 6(b), and the out-of-plane normal stress coefficient is plotted in Fig. 6(c). The simulation values deviate significantly from the predictions of Enskog theory. However, this is unsurprising as the velocity-dispersion predictions deviate significantly from the simulation results (see Fig. 3).

C. Collision statistics

In this section, we examine the statistics of the collisions experienced by the spheres. The mean time between collision, t_{avg} , provides a characteristic time scale for the sheared inelastic-hard-sphere system. Figure 7 shows the variation in the mean time between collisions with the density of the system at various values of the coefficient of restitution. The time between collision decreases with increasing density, which is expected. Increasing the coefficient of restitution decreases the mean time between collision. The variation in t_{avg} with the coefficient of restitution is given in the inset of Fig. 7. At densities roughly below $\rho\sigma^3=0.6$, the mean time between collision decreases monotonically with increasing values of the coefficient of restitution. However, at higher densities, there is a maximum in t_{avg} . The Enskog theory results describe the results qualitatively well for low-density systems but fail at high densities.

For an elastic fluid, the velocities of different particles are, in general, uncorrelated. Consequently, the velocity statistics

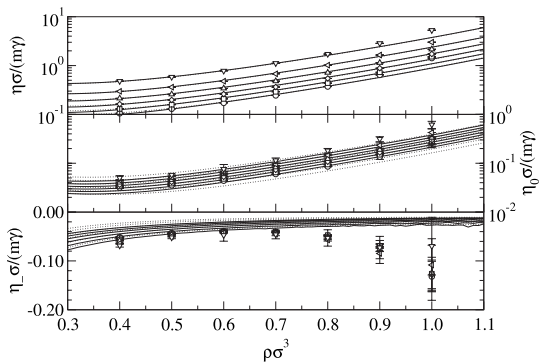


FIG. 6. The viscosities for a homogeneously sheared inelastic-hard-sphere system with (i) $\alpha=0.4$ (circles), (ii) $\alpha=0.5$ (squares), (iii) $\alpha=0.6$ (diamonds), (iv) $\alpha=0.7$ (up triangles), (v) $\alpha=0.8$ (left triangles), and (vi) $\alpha=0.9$ (down triangles). The dotted lines are the suggested expressions of Ref. [15], and the solid lines are DSMC results.

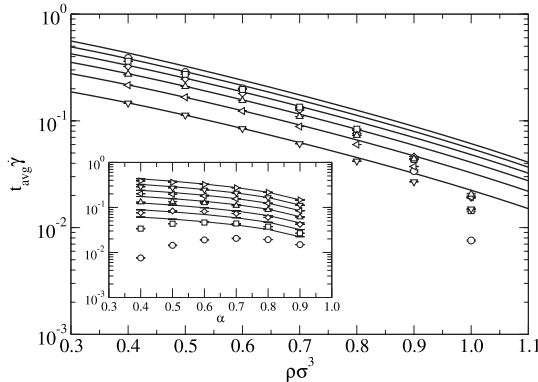


FIG. 7. Mean times between collisions for sheared inelastic hard spheres with (i) $\alpha=0.4$ (circles), (ii) $\alpha=0.5$ (squares), (iii) $\alpha=0.6$ (diamonds), (iv) $\alpha=0.7$ (up triangles), (v) $\alpha=0.8$ (left triangles), and (vi) $\alpha=0.9$ (down triangles). Inset: variations in the mean time between collisions with the coefficient of restitution for (i) $\rho\sigma^3=1.0$ (circles), (ii) $\rho\sigma^3=0.9$ (squares), (iii) $\rho\sigma^3=0.8$ (diamonds), (iv) $\rho\sigma^3=0.7$ (up triangles), (v) $\rho\sigma^3=0.6$ (left triangles), (vi) $\rho\sigma^3=0.5$ (down triangles), and (vii) $\rho\sigma^3=0.4$ (right triangles). The solid lines are the DSMC simulation results.

of the individual collisions can be determined exactly. On the other hand, the particle velocities in a driven granular system can be strongly correlated, and their on-collision statistics are not exactly known.

The distribution of the angle θ between the relative velocity and the relative position of two spheres on collision ($\cos \theta = \mathbf{r}_{ij} \cdot \mathbf{v}_{ij} / |\mathbf{r}_{ij}| |\mathbf{v}_{ij}|$) is given in Fig. 8. The solid line denotes an isotropic collision distribution (as is the case for elastic-hard-sphere systems). The symbols are the simulation data for sheared inelastic hard spheres, and the solid line is the DSMC result for $\rho\sigma^3=0.9$ and $\alpha=0.4$. For weakly inelastic systems, the distribution of the collisional angle is close to that for the elastic-hard-sphere system. As the inelasticity and density of the particles increases, however, there is a gradual increase in the frequency of “glancing” collisions (where $\cos \theta$ is near 0) at the expense of more “head-on”

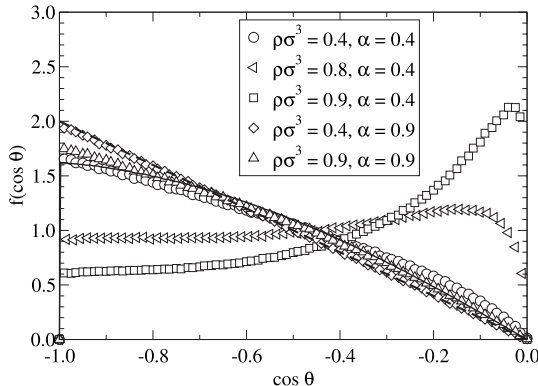


FIG. 8. The distributions of collisional angles for (i) $\rho\sigma^3=0.4$ and $\alpha=0.4$ (circles), (ii) $\rho\sigma^3=0.8$ and $\alpha=0.4$ (left triangles), (ii) $\rho\sigma^3=0.9$ and $\alpha=0.4$ (squares), (iii) $\rho\sigma^3=0.4$ and $\alpha=0.9$ (diamonds), and (iv) $\rho\sigma^3=0.9$ and $\alpha=0.9$ (up triangles). The dashed line is for elastic hard spheres and the solid line is from a DSMC simulation of $\rho\sigma^3=0.9$ and $\alpha=0.4$.

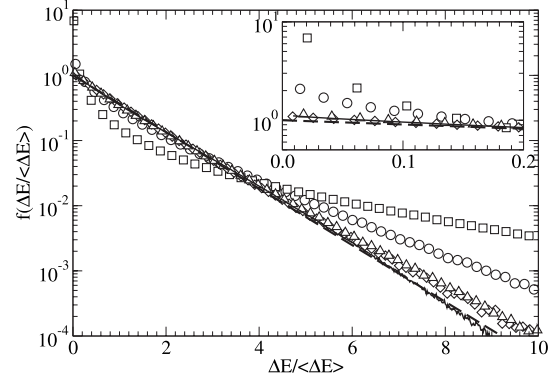


FIG. 9. The changes in kinetic energy on collision for sheared inelastic-hard-sphere systems with (i) $\rho\sigma^3=0.4$ and $\alpha=0.4$ (circles), (ii) $\rho\sigma^3=0.9$ and $\alpha=0.4$ (squares), (iii) $\rho\sigma^3=0.4$ and $\alpha=0.9$ (diamonds), and (iv) $\rho\sigma^3=0.9$ and $\alpha=0.9$ (triangles). The dashed line represents the kinetic-energy loss on collision if the velocity were given by the Maxwell-Boltzmann distribution, and the solid line is from a DSMC simulation at $\rho\sigma^3=0.9$ and $\alpha=0.4$. The inset highlights the frequency of collisions that result in low-energy losses.

collisions (where $\cos \theta$ is close to -1). This is in agreement with the two-dimensional shearing simulation of Tan and Goldhirsch [32] and Campbell and Brennen [3]. The Enskog theory does not capture this effect, as the DSMC simulations only display a small increased bias toward glancing collisions even in the dense, highly inelastic system.

The increase in glancing collisions for strongly inelastic systems (see Fig. 8) results primarily from collisions between pairs of particles orientated in the x - y plane. This occurs when the change in the streaming velocity over the diameter of a particle becomes significant in comparison to the average relative peculiar velocity [21]. Particles separated in the y plane then have a significantly increased relative velocity, which increases their probability of collision. Both the DSMC and granular-dynamics simulation results support this. However, DSMC does not exhibit the large increase in collisions with a very large collision angle.

In the inelastic-hard-sphere system, every collision results in a loss of kinetic energy. The simulation results for the distribution of the loss of kinetic energy on collision are given in Fig. 9. If the velocity distribution of the spheres were Gaussian (e.g., Maxwell-Boltzmann distribution), then the kinetic-energy loss on collision would be distributed according to a Poisson distribution:

$$f(\Delta E) = \frac{1}{\langle \Delta E \rangle} \exp\left(-\frac{\Delta E}{\langle \Delta E \rangle}\right).$$

This is given by the solid line in Fig. 9. At high values of α , the distribution of the change in kinetic energy on collision is nearly exponential. For these systems, density does not significantly affect the results.

As α decreases, there is a greater frequency of collisions that results in a very slight loss of kinetic energy (i.e., the initial peak in Fig. 9). This corresponds to the increase in the glancing collisions in the systems. This enhancement of relatively elastic collisions is accompanied by an increase in col-

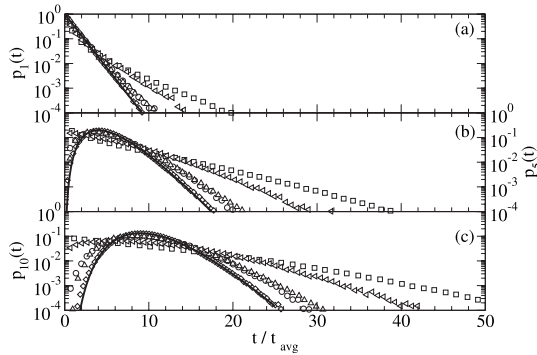


FIG. 10. Distributions of time between (a) one collision, (b) five collisions, and (c) ten collisions in sheared inelastic hard spheres with (i) $\rho\sigma^3=0.4$ and $\alpha=0.4$ (circles), (ii) $\rho\sigma^3=0.9$ and $\alpha=0.4$ (squares), (iii) $\rho\sigma^3=0.4$ and $\alpha=0.9$ (diamonds), and (iv) $\rho\sigma^3=0.9$ and $\alpha=0.9$ (triangles). The solid line is for a Poisson process.

lisions that results in large losses of kinetic energy (i.e., the long tail in Fig. 9). These result from head-on collisions, which occur between particles oriented primarily in the x direction where the velocity dispersion is the greatest. While these head-on collisions occur less frequently than glancing collisions in the highly inelastic systems, they are more violent. Increasing the density enhances these effects.

Thus far, we have only studied the statistics of single collisions. One common assumption in many kinetic theories is that the individual collisions experienced by a particle are statistically independent. We now study the correlation between collisions by examining the time required for a particle to undergo a number of collisions. If the various collisions experienced by a particle can be considered to arrive at random times in an independent manner, then the time t required for a particle to undergo n collisions is given by a Poisson process. The probability density function $p_n(t)$ that a particle experiences n collisions in a period of time t is

$$p_n(t) = \frac{(t/t_{\text{avg}})^{n-1}}{t_{\text{avg}}\Gamma(n)} \exp\left(-\frac{t}{t_{\text{avg}}}\right), \quad (14)$$

where $\Gamma(n)$ is the gamma function. Deviations from this distribution are an indication of correlations between collisions. For elastic-hard-sphere fluids, the Poisson process describes the collision time distribution fairly well. However, there are noticeable deviations, even at low densities, which increase with increasing density [50–52].

The collision time distributions for homogeneously sheared inelastic-hard-sphere systems are shown in Fig. 10. The solid lines denote the Poisson distribution, given by Eq. (14). At high values of the coefficient of restitution, the distributions are similar to those of elastic hard spheres and are fairly well described by a Poisson process. As the coefficient of restitution decreases, however, the simulation data deviate significantly from the Poisson process, indicating very strong correlations between collisions. Qualitatively, the deviations are similar to that observed for elastic-hard-sphere systems: there is an enhancement of very short and very long wait times between collisions. However, these differences are

much more pronounced for the inelastic-hard-sphere systems.

V. CONCLUSIONS

We have performed nonequilibrium molecular-dynamics simulations of sheared inelastic-hard-sphere systems using the Slod algorithm combined with Lees-Edwards boundary conditions. In these simulations, care was taken to ensure that the systems remain homogeneous and the shear was uniform across the system. As a consequence, these simulations may prove a useful reference to compare with the predictions of kinetic theory.

DSMC simulations of the Enskog equation were performed to provide a solution to the kinetic theory without further approximation. These compared favorably with the simulation results except for dense, strongly inelastic systems. The velocity-anisotropy effect can be very strong even in homogeneous systems, and kinetic-theory solutions must take this into account in their approximations.

Results were presented for the velocity statistics of individual particles in the system. The velocity distributions were, in general, well described by an anisotropic Gaussian. Theories based on the anisotropic Gaussian and the full second moment balance (e.g., see Ref. [53]) are well suited to these systems. Sheared inelastic-hard-sphere systems do not obey the equipartition theorem. Fluctuations of the velocity in the x direction (the direction of shear) were greater than those in the y and z directions, which were both similar to each other. In addition, the granular temperature, which characterizes the overall fluctuation of the velocity, was observed to possess a minimum with respect to the density. This minimum becomes more pronounced as the coefficient of restitution of the spheres decreases.

The variation in the stress in the system was also examined. The compressibility factor of the sheared inelastic-hard-sphere system was quite similar to that of elastic hard spheres, as estimated by the Carnahan-Starling equation of state. The shear viscosity of the systems was computed in two different manners: from the average of the stress tensor and from the rate of dissipation of kinetic energy. The values of the viscosity from both these methods agree to within the statistical uncertainty of the simulations. The predictions of the Enskog equation and the kinetic theory of Montanero *et al.* [15] were in fairly good agreement with the simulation data. The in-plane and out-of-plane stress coefficients were also computed, but the kinetic-theory predictions for these quantities were not as accurate.

Finally, the collision statistics of particles in the sheared inelastic-hard-sphere system was studied. The mean time between collisions was found to decrease monotonically with increasing density. However, at fixed density, it displays a maximum at intermediate values of the coefficient of restitution. Examination of the collision time distributions indicated the presence of strong correlations between collisions. Including these correlations within a kinetic theory will be important in developing an accurate description of high-density, sheared inelastic-hard-sphere systems.

- [1] C. S. Campbell, *Annu. Rev. Fluid Mech.* **22**, 57 (1990).
- [2] I. Goldhirsch, *Annu. Rev. Fluid Mech.* **35**, 267 (2003).
- [3] C. S. Campbell and C. E. Brennen, *J. Fluid Mech.* **151**, 167 (1985).
- [4] J. F. Lutsko, *Phys. Rev. E* **70**, 061101 (2004).
- [5] C. K. K. Lun, S. B. Savage, D. J. Jeffrey, and N. Chepurniy, *J. Fluid Mech.* **140**, 223 (1984).
- [6] A. Santos and A. Astillero, *Phys. Rev. E* **72**, 031308 (2005).
- [7] H. van Beijeren and M. H. Ernst, *Physica (Amsterdam)* **68**, 437 (1973).
- [8] N. F. Carnahan and K. E. Starling, *J. Chem. Phys.* **51**, 635 (1969).
- [9] T. P. C. van Noije, M. H. Ernst, and R. Brito, *Physica A* **251**, 266 (1998).
- [10] N. Sela and I. Goldhirsch, *J. Fluid Mech.* **361**, 41 (1998).
- [11] C. K. K. Lun, *J. Fluid Mech.* **233**, 539 (1991).
- [12] I. Goldhirsch, *Powder Technol.* **182**, 130 (2008).
- [13] J. T. Jenkins and M. W. Richman, *J. Fluid Mech.* **192**, 313 (1988).
- [14] J. T. Jenkins and M. W. Richman, *Phys. Fluids* **28**, 3485 (1985).
- [15] J. M. Montanero, V. Garzo, A. Santos, and J. J. Brey, *J. Fluid Mech.* **389**, 391 (1999).
- [16] A. Santos, J. M. Montanero, J. W. Dufty, and J. J. Brey, *Phys. Rev. E* **57**, 1644 (1998).
- [17] J. J. Brey, J. W. Dufty, and A. Santos, *J. Stat. Phys.* **97**, 281 (1999).
- [18] G. A. Bird, *Molecular Gas Dynamics and the Direct Simulation of Gas Flows* (Oxford Science, Oxford, 1994).
- [19] M. A. Hopkins and H. H. Shen, *J. Fluid Mech.* **244**, 477 (1992).
- [20] J. M. Montanero and A. Santos, *Phys. Fluids* **9**, 2057 (1997).
- [21] M. Alam and S. Luding, *Phys. Fluids* **15**, 2298 (2003).
- [22] M. Alam and S. Luding, *Phys. Fluids* **17**, 063303 (2005).
- [23] C. Campbell, *J. Fluid Mech.* **203**, 449 (1989).
- [24] O. Herbst, P. Müller, M. Otto, and A. Zippelius, *Phys. Rev. E* **70**, 051313 (2004).
- [25] H. J. Herrmann, S. Luding, and R. Cafiero, *Physica A* **295**, 93 (2001).
- [26] S. L. Conway and B. J. Glasser, *Phys. Fluids* **16**, 509 (2004).
- [27] M. Alam, V. H. Arakeri, P. R. Nott, J. D. Goddard, and H. J. Herrman, *J. Fluid Mech.* **523**, 277 (2005).
- [28] A. W. Lees and S. F. Edwards, *J. Phys. C* **5**, 1921 (1972).
- [29] O. R. Walton and R. L. Braun, *J. Rheol.* **30**, 949 (1986).
- [30] M. A. Hopkins and M. Y. Louge, *Phys. Fluids A* **3**, 47 (1991).
- [31] I. Goldhirsch and M.-L. Tan, *Phys. Fluids* **8**, 1752 (1996).
- [32] M.-L. Tan and I. Goldhirsch, *Phys. Fluids* **9**, 856 (1997).
- [33] J. F. Lutsko, e-print arXiv:cond-mat/0403551.
- [34] W. Losert, D. Cooper, J. Delour, A. Kudrolli, and J. Gollub, *Chaos* **9**, 682 (1999).
- [35] J. M. Montanero, V. Garzó, M. Alam, and S. Luding, *Granular Matter* **8**, 103 (2006).
- [36] D. J. Evans and G. P. Morris, *Statistical Mechanics of Non-equilibrium Liquids* (Academic, London, 1990).
- [37] J. Petracic and O. G. Jepps, *Phys. Rev. E* **67**, 021105 (2003).
- [38] S. McNamara and E. Falcon, *Granular Gas Dynamics* (Springer, New York, 2003), pp. 347–366.
- [39] S. McNamara and W. R. Young, *Phys. Rev. E* **53**, 5089 (1996).
- [40] M. Alam and C. M. Hrenya, *Phys. Rev. E* **63**, 061308 (2001).
- [41] B. J. Alder and T. E. Wainwright, *J. Chem. Phys.* **31**, 459 (1959).
- [42] M. Bannerman and L. Lue, Dynamics of discrete objects (DYNAMO), 2008, <http://www.marcusbannerman.co.uk/dynamo>
- [43] J. W. Dufty, J. J. Brey, and A. Santos, *Physica A* **240**, 212 (1997).
- [44] C. S. Campbell, *J. Fluid Mech.* **465**, 261 (2002).
- [45] T. A. Knight and L. V. Woodcock, *J. Phys. A* **29**, 4365 (1996).
- [46] J. S. Olafsen and J. S. Urbach, *Phys. Rev. E* **60**, R2468 (1999).
- [47] F. Rouyer and N. Menon, *Phys. Rev. Lett.* **85**, 3676 (2000).
- [48] B. J. Alder, D. M. Gass, and T. E. Wainwright, *J. Chem. Phys.* **53**, 3813 (1970).
- [49] M. Turner and L. Woodcock, *Powder Technol.* **60**, 47 (1990).
- [50] L. Lue, *J. Chem. Phys.* **122**, 044513 (2005).
- [51] P. Visco, F. van Wijland, and E. Trizac, *J. Phys. Chem. B* **112**, 5412 (2008).
- [52] P. Visco, F. van Wijland, and E. Trizac, *Phys. Rev. E* **77**, 041117 (2008).
- [53] C.-S. Chou and M. W. Richman, *Physica A* **259**, 430 (1998).

APPENDIX
B

REPRINT: TRANSPORT PROPERTIES OF HIGHLY
ASYMMETRIC HARD-SPHERE MIXTURES

Transport properties of highly asymmetric hard-sphere mixtures

Marcus N. Bannerman^{a)} and Leo Lue^{b)}

*School of Chemical Engineering and Analytical Science, The University of Manchester,
P.O. Box 88 Sackville Street, Manchester M60 1QD, United Kingdom*

(Received 12 February 2009; accepted 27 March 2009; published online 23 April 2009)

The static and dynamic properties of binary mixtures of hard spheres with a diameter ratio of $\sigma_B/\sigma_A=0.1$ and a mass ratio of $m_B/m_A=0.001$ are investigated using event driven molecular dynamics. The contact values of the pair correlation functions are found to compare favorably with recently proposed theoretical expressions. The transport coefficients of the mixture, determined from simulation, are compared to the predictions of the revised Enskog theory using both a third-order Sonine expansion and direct simulation Monte Carlo. Overall, the Enskog theory provides a fairly good description of the simulation data, with the exception of systems at the smallest mole fraction of larger spheres ($x_A=0.01$) examined. A “fines effect” was observed at higher packing fractions, where adding smaller spheres to a system of large spheres decreases the viscosity of the mixture; this effect is not captured by the Enskog theory. © 2009 American Institute of Physics. [DOI: 10.1063/1.3120488]

I. INTRODUCTION

Excluded volume interactions between molecules play a major role in determining the structure and properties of most fluids and colloidal systems. The hard-sphere model, which captures the essence of these interactions, has played a central role in our understanding of the properties of fluids, serving as a starting point of perturbation theories for the description of real fluids.¹ Recently, there has been interest in binary hard-sphere mixtures, where the diameters of the two components are very different. These systems serve as models for nanoparticle suspensions and colloid-polymer mixtures. In these systems, an entropically driven depletion force^{2,3} drives the larger particles to cluster. While there have been many studies on the structural (e.g., radial distribution function) and thermodynamic properties (e.g., equation of state) of these mixtures,^{4–14} there have been relatively few studies on their dynamical properties.

Much of the previous simulation work for the dynamical properties of binary mixtures has focused on tracer particle studies,^{15–17} the velocity autocorrelation functions, or the self-diffusion coefficients,^{18,19} as these are relatively computationally inexpensive to determine. These studies have revealed that the dynamics of the larger particles deviates significantly from both the theoretical predictions of Brownian particles and of the Enskog theory. Lue and Woodcock^{7,9} examined the self-diffusion coefficients of size asymmetric binary mixtures of hard spheres. They found a “fines effect” at high densities, where the addition of smaller spheres enhances the mobility of the larger spheres.

Significantly less data are available for other dynamical properties. Easteal and Woolf²⁰ investigated the tracer diffusion coefficient for binary hard-sphere mixtures. They observed an inverse isotopic mass effect, where heavier tracer

particles diffuse faster beyond a certain solvent density than lighter tracer particles. Due to the computational cost of simulating highly size asymmetric systems, past studies have focused on small size disparity and/or moderate mole fractions of colloidal particles.

Erpenbeck^{21–23} provided the first complete transport study, comparing predictions from the Enskog theory and molecular dynamics results for binary hard-sphere mixtures approximating a helium-xenon gas mixture. The mutual diffusion, thermal diffusion, thermal conductivity, and shear viscosity are given over a range of state points. The Enskog theory was found to provide a fairly good description of the transport properties for the conditions studied. Yeganegi and Zolfaghari²⁴ investigated the thermal diffusion coefficient of binary hard spheres (for moderate size ratios) using nonequilibrium molecular dynamics. They observed a minimum in the thermal diffusion with density and good agreement with the Enskog theory. Recently, Bastea²⁵ investigated the viscosity and thermal conductivity of highly asymmetric “soft-sphere” mixtures at very low volume fractions of the larger spheres. The Enskog theory was only able to qualitatively describe the results in that study.

In the present work, we perform event driven molecular dynamics simulations to study the static and transport properties of binary hard-sphere mixtures with a diameter ratio of 0.1 and a mass ratio of 0.001. One of the motivations of this work is to further explore the fines effect revealed in these systems in a previous study by Lue and Woodcock.⁹ Another aim of this work is to quantitatively test the predictive ability of the revised Enskog theory²⁶ (RET) for these binary hard-sphere systems over a broad range of conditions. The remainder of this paper is organized as follows. Details of the hard-sphere mixture model and the relation of the transport coefficients to the microscopic dynamics of the system are discussed in Sec. II. The details of the molecular dynamics calculations and the direct simulation Monte Carlo (DSMC) solution of the Enskog equation are provided in Sec. III. The

^{a)}Electronic mail: m.bannerman@postgrad.manchester.ac.uk.

^{b)}Electronic mail: leo.lue@manchester.ac.uk.

simulation data for the static and the transport properties of the binary hard-sphere mixtures are presented in Sec. IV, and the results are compared against the predictions of the Enskog theory. Finally, the main findings of this work are summarized in Sec. V.

II. THEORETICAL BACKGROUND

We consider systems consisting of additive hard spheres with differing diameters and masses. Spheres of type a have a diameter σ_a and a mass m_a . The spheres are not permitted to overlap, and so the interaction potential u_{ab} between a sphere of type a and a sphere of type b is given by

$$u_{ab}(r) = \begin{cases} \infty & \text{if } r \leq \sigma_{ab} \\ 0 & \text{if } r > \sigma_{ab}, \end{cases} \quad (1)$$

where r is the distance between the centers of the two spheres, and $\sigma_{ab} = (\sigma_a + \sigma_b)/2$. Due to the simple nature of this interaction potential, all properties of hard-sphere mixtures have a trivial dependence on the temperature.

One major advantage of the hard-sphere model is the simplicity of its dynamics. The dynamics of hard-sphere systems is driven by collisions between spheres. Between collisions, the spheres travel at constant velocity. The solution of the trajectory of the system then reduces to determining the sequence of collisions between the spheres. These collisions alter the velocities of the spheres but conserve their energy and momentum. After a collision between a sphere i of type a and a sphere j of type b , the velocities of the spheres become \mathbf{v}'_i and \mathbf{v}'_j ,

$$\begin{aligned} \mathbf{v}'_i &= \mathbf{v}_i - \frac{2\mu_{ab}}{m_a}(\mathbf{v}_{ij} \cdot \hat{\mathbf{r}}_{ij})\hat{\mathbf{r}}_{ij}, \\ \mathbf{v}'_j &= \mathbf{v}_j + \frac{2\mu_{ab}}{m_b}(\mathbf{v}_{ij} \cdot \hat{\mathbf{r}}_{ij})\hat{\mathbf{r}}_{ij}, \end{aligned} \quad (2)$$

where \mathbf{v}_i and \mathbf{v}_j are the velocities of the spheres immediately before collision, $\hat{\mathbf{r}}_{ij}$ is a unit vector pointing from the center of sphere i to the center of sphere j , $\mathbf{v}_{ij} = \mathbf{v}_i - \mathbf{v}_j$ is their relative velocity, and $\mu_{ab} = m_a m_b / (m_a + m_b)$ is the reduced mass.

A. Static properties

The pair correlation functions give an indication of the average local environment of the particles in a system. For hard-sphere systems, the values of the pair correlation functions at contact $g_{ab}(\sigma_{ab}^+)$ play an important role. In particular, they are directly related to the collision rates between the spheres:

$$g_{ab}(\sigma_{ab}^+) = (4\pi\rho_b\sigma_{ab}^2 t_{ab})^{-1} (2\pi\beta\mu_{ab})^{1/2}, \quad (3)$$

where ρ_b is the number density of spheres of type b , $\beta = (k_B T)^{-1}$ (k_B is the Boltzmann constant and T is the absolute temperature), and t_{ab} is the mean time between which a sphere of type a undergoes collisions with a sphere of type b . The quantity t_{ab} can be calculated from the number of a - b collisions, $N_{ab}^{(\text{coll})}$, that occur in a simulation of duration t ,

$$t_{ab} = \frac{N_a t}{2N_{ab}^{(\text{coll})}}, \quad (4)$$

where N_a is the number of spheres of type a in the system. An advantage of molecular dynamics simulations over Monte Carlo simulations is that the contact values of the pair correlation functions can be directly calculated from the times t_{ab} and does not require the extrapolation of the pair correlation to contact.

The contact values of the pair correlation functions are also directly related to the equation of state of the hard-sphere system:

$$\frac{\beta p}{\rho} = 1 + \frac{2\pi\rho}{3} \sum_{a,b} x_a x_b \sigma_{ab}^3 g_{ab}(\sigma_{ab}^+), \quad (5)$$

where p is the system pressure, ρ is the total number density of spheres, x_a is the mole fraction of spheres of type a , and the lowercase Latin indices run over all species (i.e., A and B for a binary mixture) present in the system.

Due to the fundamental importance of the contact values of the pair correlation functions for hard-sphere systems, there have been many efforts to develop expressions to describe them.^{5,6,8,27} One of the most popular is the Boublik–Mansoori–Carnahan–Starling (BMCSL) equation of state,^{28,29} which is an interpolation between the virial and compressibility expressions of the Percus–Yevick theory.³⁰ This is given by

$$\begin{aligned} g_{ab}^{\text{BMCSL}}(\sigma_{ab}^+) &= \frac{1}{1 - \xi_3} + \frac{3\xi_2}{2(1 - \xi_3)^2} \frac{\sigma_a \sigma_b}{\sigma_{ab}} \\ &\quad + \frac{\xi_2^2}{2(1 - \xi_3)^3} \frac{\sigma_a^2 \sigma_b^2}{\sigma_{ab}^2}, \end{aligned} \quad (6)$$

where ξ_n is defined by

$$\xi_n = \frac{\pi\rho}{6} \sum_a x_a \sigma_a^n. \quad (7)$$

Note that the solid fraction occupied by the spheres is given by $\phi = \xi_3$.

The BMCSL equation yields predictions that are generally in good agreement with simulation data for hard-sphere mixtures over a broad range of diameters and compositions.⁴ However, for highly size asymmetric binary systems at small mole fractions of the larger spheres (often referred to as the colloidal limit), the BMCSL significantly underpredicts the contact value of the pair correlation function between the larger spheres, as compared to simulation results.^{4,7,31}

Recently, there have been several efforts to correct this. Viduna and Smith^{32,33} suggested a new expression, based on an empirical equation of state,

$$\begin{aligned} g_{ab}^{\text{VS}}(\sigma_{ab}^+) &= \frac{1}{1 - \xi_3} + \frac{3 - \xi_3 + \xi_3^2/2}{2(1 - \xi_3)^2} \xi_2 \frac{\sigma_a \sigma_b}{\sigma_{ab}} \\ &\quad + \frac{2 - \xi_3 - \xi_3^2/2}{6(1 - \xi_3)^3} (2\xi_2^2 + \xi_1 \xi_3) \frac{\sigma_a^2 \sigma_b^2}{\sigma_{ab}^2}. \end{aligned} \quad (8)$$

This compact expression appears to compare well with simulation results. In the case of binary hard-sphere mixtures,

Henderson *et al.*¹⁰ suggested further modifications to the BMCSL and Viduna-Smith (VS) equations so that the contact value of the pair correlation function between the larger spheres yields the correct limiting behavior as the diameters of the larger spheres become infinite.³¹ Their expressions for the pair correlation functions (which we denote as HC2) are given by

$$g_{BB}^{\text{HC2}}(\sigma_{ab}^+) = g_{BB}^{\text{BMCSL}}(\sigma_{BB}^+) \quad \text{or} \quad g_{BB}^{\text{VS}}(\sigma_{BB}^+)s, \quad (9)$$

$$\begin{aligned} g_{AB}^{\text{HC2}}(\sigma_{ab}^+) &= g_{AB}^{\text{BMCSL}}(\sigma_{AB}^+) + \frac{\xi_2^2 \sigma_{BB}^2}{(1 - \xi_3)^3 (1 + R)^2} \frac{1 - R^2}{(1 - \xi_3)^3 (1 + R)^3}, \\ &\quad (10) \end{aligned}$$

$$g_{AA}^{\text{HC2}}(\sigma_{ab}^+) = g_{AA}^{\text{VS}}(\sigma_{BB}^+) + e^x - 1 - x - x^2/2, \quad (11)$$

where A refers to the larger spheres, B refers to the smaller spheres, $R = \sigma_B/\sigma_A$ is the diameter ratio, and $x = 3(\xi_2 \sigma_{AA} - \xi_3)/2$.

B. Calculation of transport coefficients

In the continuum description of fluids,³⁴ balance equations are typically used to relate the conserved properties of the system (e.g., energy, momentum, and mass) to their fluxes. To close these equations, constitutive relations are required. These relations link the diffusive fluxes to gradients in the thermodynamic properties of the system. Transport coefficients are defined through the assumption that the diffusive fluxes depend linearly on the thermodynamic driving forces, which are gradients of local thermodynamic properties of the system.

There are several possible choices³⁴ for the thermodynamic forces \mathbf{X} and the diffusive fluxes \mathbf{J} . For NVE molecular dynamics simulations, the most convenient²¹ choice is the “mainstream” (or “unprimed”,^{21,34}) definition of the fluxes. These are defined as

$$\mathbf{X}_a = -T \nabla \left(\frac{\mu_a}{T} \right), \quad \mathbf{X}_\lambda = -\frac{1}{T} \nabla T, \quad (12a)$$

$$\mathbf{J}_a = L_{a\lambda} \mathbf{X}_\lambda + \sum_b L_{ab} \mathbf{X}_b, \quad \mathbf{J}_\lambda = L_{\lambda\lambda} \mathbf{X}_\lambda + \sum_a L_{\lambda a} \mathbf{X}_a, \quad (12b)$$

where μ_a is the chemical potential, \mathbf{J}_a is the diffusive flux of species a , \mathbf{J}_λ is the energy flux, $L_{\lambda\lambda}$ is the thermal conductivity, L_{ab} is the mutual diffusion coefficient, and $L_{\lambda a}$ is the thermal diffusivity. The transport coefficients are defined through Eq. (12).

The relationship between stress tensor τ and the strain rate in the fluid is defined in the standard manner:

$$\tau = p \mathbf{1} + \left(\frac{2}{3} \eta - \kappa \right) (\nabla \cdot \mathbf{u}) \mathbf{1} - \eta [\nabla \mathbf{u} + (\nabla \mathbf{u})^T], \quad (13)$$

where η is the shear viscosity, κ is the bulk viscosity, and \mathbf{u} is the streamline velocity of the fluid. The quantity $\mathbf{1}$ represents the unit matrix, and the superscript T indicates the transpose of a matrix.

The Onsager reciprocity relations ($L_{ab} = L_{ba}$ and $L_{a\lambda} = L_{\lambda a}$), combined with the requirement that $\sum_a \mathbf{J}_a = 0$ (due to

TABLE I. Displacement functions for an isotropic system required to evaluate the Einstein form of the Green–Kubo relationships, see Eq. (14). The first summation runs over all time intervals between collisions Δt_c that occur during the simulation time t . The indices i and j denote the pair of spheres that undergo collision at the end of this time interval. Note that c_a is the mass fraction of sphere of type a .

W_ψ	
W_a	$\sum'_{\Delta t_c} \sum_k^{N_a} m_k \mathbf{v}_k \Delta t_c - c_a \sum_k^N m_k \mathbf{v}_k \Delta t_c$
W_λ	$\sum'_{\Delta t_c} (\sum_k^N \frac{1}{2} m_k \mathbf{v}_k^2 \mathbf{v}_k \Delta t_c + \frac{1}{2} m_i \Delta v_{ij}^2 \mathbf{v}_{ij})$
W_η	$\sum'_{\Delta t_c} (\sum_k^N m_k \mathbf{v}_k \mathbf{v}_k \Delta t_c + m_i \mathbf{r}_{ij} \Delta \mathbf{v}_i - 1 p V \Delta t_c)$

the definition of the diffusive flux) which implies $L_{aa} = -\sum_{b \neq a} L_{ab}$, reduce the number of independent transport coefficients to $L_{\lambda\lambda}$, $L_{a\lambda}$, L_{AA} , η , and κ . In Sec. II C, we discuss how these transport coefficients can be determined from equilibrium molecular dynamics simulations.

C. Einstein forms of the Green–Kubo relations

The Green–Kubo formulas relate the time correlation functions of the microscopic fluxes directly to the transport coefficients.¹ However, the Green–Kubo relations are an unpopular method for obtaining the transport coefficients from molecular dynamics simulations, as they require long simulation times to obtain good statistics. This is not a significant issue in hard-sphere systems, as long simulation times are more easily accessible. For systems with particles interacting with discontinuous potentials, the Einstein form of the Green–Kubo relations must be used due to the impulsive nature of the interaction potential. The full derivation of these formulas are already available,^{1,21} and therefore, only the final expressions are presented here for completeness.

The Einstein relations have the general form

$$\psi(t) = \frac{\beta}{2Vt} \langle W_{\psi_1}(t) W_{\psi_2}(t) \rangle, \quad (14)$$

where $\psi(t)$ is a time dependent transport coefficient, V is the volume of the system, and W_{ψ_1} and W_{ψ_2} are displacement functions corresponding to time integrals of the microscopic fluxes. The displacement functions for a system with zero total momentum in the microcanonical ensemble are given in Table I. The pair of displacement functions that correspond to each of the transport coefficients are summarized in Table II. In hydrodynamic regime, the transport coefficients are given by the infinite time limit of Eq. (14),

TABLE II. Transport coefficients and the corresponding displacement functions. The right hand columns indicate which rows of Table I are used. As the system is isotropic, the transport coefficients are averaged over all components $x \neq y$ of the displacement functions.

ψ	W_{ψ_1}	W_{ψ_2}
L_{ab}	$W_{a,x}$	$W_{b,x}$
$L_{a\lambda}$	$W_{a,x}$	$W_{\lambda,x}$
$L_{\lambda\lambda}$	$W_{\lambda,x}$	$W_{\lambda,x}$
η	$W_{\eta,xy}$	$W_{\eta,xy}$
$\frac{4}{3}\eta + \kappa$	$W_{\eta,xx}$	$W_{\eta,xx}$

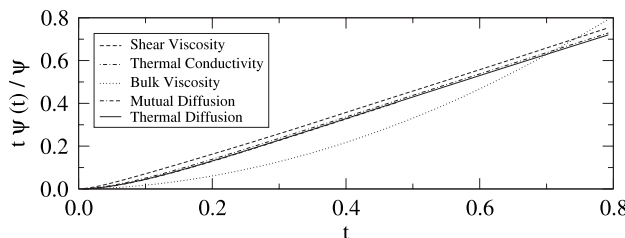


FIG. 1. Time dependent transport coefficients [see Eq. (14)], reduced by their infinite time result, from a single simulation run for a binary hard-sphere system with $x_A=0.01$ and solid fraction $\phi=0.1$. The time is presented in units of $(\beta m_A \sigma_A^2)^{1/2}$, the mean free time is roughly $0.015(\beta m_A \sigma_A^2)^{1/2}$.

$$\psi = \lim_{t \rightarrow \infty} \psi(t). \quad (15)$$

A sample of reduced correlators for a single molecular dynamics simulation run is plotted in Fig. 1. The function $t\psi(t)$ typically displays transient behavior for short times before changing to the linear, long-time regime. All the transport properties, with the exception of the bulk viscosity, rapidly change to the linear regime within a few mean free times. The bulk viscosity, however, only slowly approaches the linear regime, and consequently, the limiting values are difficult to extract. As a result, we do not present data for the bulk viscosity.

A time correlation function of a finite sized simulation is only representative of a bulk system for a limited duration. Beyond the time a sound wave takes to traverse the simulation box, the system size begins to affect the correlation function. The sound wave traversal time is determined directly from the speed of sound, c . For a hard-sphere system the speed of sound is given by

$$c^2 = m^{-1} k_B T \left[\frac{2Z^2}{3} + \frac{\partial \rho Z}{\partial \rho} \right], \quad (16)$$

where $Z=\beta p/\rho$ is the compressibility factor and $m=\sum_a x_a m_a$ is the mean particle mass. The HC2 equation of state [see Eqs. (5) and (9)–(11)] is used to estimate the speed of sound, via Eq. (16). Data for the time correlation functions are only collected for a duration of time shorter than the sound wave traversal time.

D. Enskog theory predictions for the transport coefficients

RET^{26,35–37} is an extension of the highly successful Enskog theory to mixtures. This is the most widely applied kinetic theory of moderately dense fluids. In the Enskog approximation, all precollision correlations between particles are ignored, save for a single static structural correlation function. In a homogeneous system, this reduces to the values of the various pair correlation functions at contact, which govern the collision rates. Given these as input, the Enskog theory yields predictions for the transport properties through the Chapman–Enskog expansion.³⁸

The standard method to solve to the Enskog equation is to expand the one-particle distribution function in a series of Sonine polynomials. Erpenbeck²¹ compiled the (corrected) Enskog expressions for all transport properties, excluding the

bulk viscosity, of hard-sphere mixtures. These expressions have been combined with the table of integrals given by Ferziger and Kaper³⁹ and a linear equation solver to evaluate the Enskog theory to the third order in the Sonine expansion. We present results calculated from the BMCSL and HC2 equations to determine the effect of improved values for $g_{ab}(\sigma_{ab}^+)$ on the predictions of the transport properties.

E. DSMC solution of the Enskog equation

Another method for obtaining solutions to the Enskog equations is through the use of the DSMC method. This technique was originally developed for the Boltzmann equation but has recently been extended to the Enskog equation.^{40–42} In this work, DSMC of the Enskog equation, in the style of Bird's no time counter (NTC) method,⁴³ is used to provide results. In this approach, the velocity distribution of each species is approximated using a set of samples,

$$f_a(\mathbf{v}, t) = \mathcal{N}_a^{-1} \sum_{i=1}^{\mathcal{N}_a} \delta(\mathbf{v} - \mathbf{v}_i(t)) \quad (17)$$

where \mathcal{N}_a is the number of samples of the velocity distribution of species a . For simplicity, in the following expressions we assume that each sample represents a single sphere. Other choices are possible; however, the difference merely affects the relative sample collision testing rates and time scale of the simulation.

The probability that a sample i of species a undergoes a collision event with species b after a time step Δt_{ab} is⁴⁴

$$\omega_{ib} = 4g_{ab}(\sigma_{ab}^+) \pi \rho_b \sigma_{ab}^2 (\mathbf{v}_{ij} \cdot \hat{\mathbf{k}}) \Theta(\mathbf{v}_{ij} \cdot \hat{\mathbf{k}}) \Delta t_{ab}, \quad (18)$$

where j is a randomly chosen sample from species b , $\hat{\mathbf{k}}$ is a randomly chosen relative orientation between the samples on collision, $\mathbf{v}_{ij} = \mathbf{v}_i - \mathbf{v}_j$ is the relative velocity, and Θ is the Heaviside step function. The time step Δt_{ab} describes the rate at which samples in species a are tested for collisions with a sample of species b . For a DSMC calculation of a binary mixture, there are four rates, one for each pairing of the species (AA , AB , BA , and BB).

The simplest DSMC algorithm proceeds by incrementing time to the next test for collisions between species a and b . Each sample i of species a is tested for an event with another sample j , which is randomly selected. A collision is executed with a probability given by Eq. (18). This collision only affects sample i and not the collision partner j . This method is simple but inefficient because properties that are conserved on collision (e.g., momentum and energy) are only conserved on average. In addition, all samples in species a are tested at each time step, which is computationally expensive, even though Δt_{ab} is selected to yield only a few events per time step.

An improved algorithm, based on Bird's NTC method, executes symmetric species-species collision events simultaneously, and therefore, there are three independent test rates for the binary system (Δt_{AA} , $\Delta t_{AB} = \Delta t_{BA}$, and Δt_{BB}). For a given time step, we assume that there are a maximum of $N_{ab}^{pairs} = \mathcal{N}_a \omega_{ab}^{(max)} = \mathcal{N}_b \omega_{ba}^{(max)}$ events that may occur for each species; the quantity $\omega_{ba}^{(max)}$ is the maximum observed value

of ω_{ba} , which is updated, if required, during the course of a simulation. N_{ab}^{pairs} pairs of a and b samples are randomly selected at each time step. The probability of collision is then scaled to

$$\frac{1}{2}(2 - \delta_{ab})\omega_{ab} \frac{N_a}{N_{\text{pairs}}}, \quad (19)$$

where δ_{ab} is the Kronecker delta. If the collision is accepted, then the velocities of both samples are updated according to the collision rule [see Eq. (2)]. This conserves energy and momentum at all times and greatly improves the statistics of the simulation. Like the Enskog theory, the DSMC calculations require $g_{ab}(\sigma_{ab}^+)$ as input; however, DSMC requires no polynomial expansion to make the problem tractable.

The transport coefficients are obtained through the use of the appropriate time correlation functions, as in the full molecular dynamics simulations (see Sec. II B). DSMC provides an attractive method of numerically solving a kinetic equation, especially as computing power increases. Its results are still, however, limited by the approximations of the underlying kinetic equation.

III. SIMULATION DETAILS

In this work, we examine the static and transport properties of highly asymmetric binary hard-sphere mixtures. The larger A spheres have a diameter σ_A and mass m_A , and the smaller B spheres have a diameter σ_B and mass m_B . We consider systems with $\sigma_B/\sigma_A=0.1$ and $m_B/m_A=0.001$, consistent with particles of the same density.

Discrete potentials, such as the hard-sphere model, have an important advantage over more complex “soft” potentials. Between collisions the spheres or molecules experience no forces and travel on ballistic trajectories. The dynamics can be solved analytically, and the integration of the equations of motion is processed as a sequence of events. Current event driven molecular dynamics algorithms are now quite advanced and allow the simulation of large systems for the long times required to extract accurate transport properties.

A. MD simulations

The basic event driven algorithm used in this work to perform the molecular dynamics simulations is fundamentally the same as the one originally described by Alder and Wainwright.⁴⁵ Neighbor lists and the delayed states algorithm⁴⁶ are included to optimize the calculations. These methods are combined with a new bounded priority queue, suggested by Paul,⁴⁷ to remove the system size dependence of sorting the event queue. Finally, the interactions between the largest spheres are removed from the neighbor list and processed separately¹¹ to allow the use of a smaller cell size and reduced number of collision tests. This removal is restricted to low mole fractions of the larger spheres as the overhead of these removed interactions is of order $O(N^2)$ in the number of large spheres.

A total of $N=13\,500$ spheres in a cubic box of volume V with standard periodic boundary conditions were used in all the simulations. The volume of the system and the relative number of large and small spheres (i.e., N_A and N_B) were

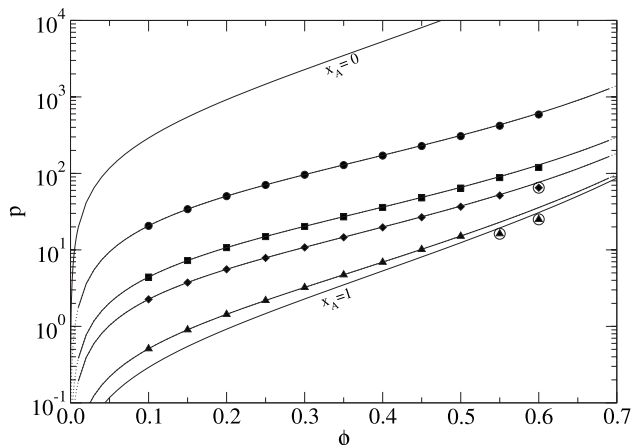


FIG. 2. Pressure p as a function of solid fraction ϕ for binary hard-sphere mixtures with $\sigma_B/\sigma_A=0.1$, $m_B/m_A=0.001$, and (i) $x_A=0.01$ (circles), (ii) $x_A=0.05$ (squares), (iii) $x_A=0.1$ (diamonds), and (iv) $x_A=0.5$ (triangles). The filled symbols are from molecular dynamics simulations, and the lines are the predictions of the BMCSL (solid) and HC2 (dotted) equations of state. Data points are circled where the system shows signs of freezing.

adjusted to obtain the required packing fraction and composition, respectively. For each of the systems examined, the initial configurations were equilibrated over a period of 10^7 collisions and then run for 20 trajectories of 10^8 collisions to collect the collision statistics and time correlation functions.

The time correlation functions for the various transport properties were collected over approximately 100 intervals of a mean free time using the start time averaging method.⁴⁸ The last 50 values of the correlator were fitted to a line to extract the long-time limit of the transport coefficient.

B. DSMC simulations

DSMC simulations were performed using a total of $N_A + N_B=13\,500$ samples of the velocity distribution. Each of the simulations was initially equilibrated for 10^7 collisions. The time correlation functions were then collected over eight separate trajectories, each consisting of 10^8 collisions, using 100 intervals of a mean free time. The statistical uncertainties of the shorter DSMC calculations are smaller than the uncertainties of the MD simulations because the Enskog theory neglects dynamical correlations.

IV. RESULTS AND DISCUSSION

In this section, we present the results of the molecular dynamics simulations for the contact value of the pair correlation functions and the transport coefficients of binary hard-sphere mixtures. A comparison of the predictions of the RET is also provided. All quantities are reported in reduced units, where the unit of mass is m_A , the unit of length is σ_A , and the unit of energy is $k_B T$.

A. Static properties

The variation of the pressure of the binary hard-sphere mixtures with packing fraction and composition is shown in Fig. 2. The symbols are the data from the molecular dynamics simulations, and the lines are the predictions of the

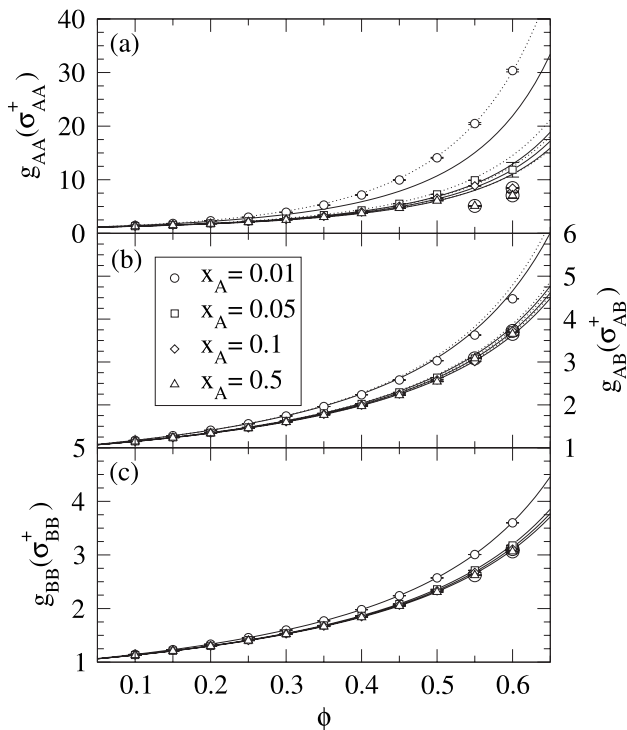


FIG. 3. Contact value of the pair correlation function $g_{ab}(\sigma_{ab}^+)$ between the (a) large-large, (b) large-small, (c) and small-small (c) sphere species as a function of solid fraction ϕ for binary hard-sphere mixtures with $\sigma_B/\sigma_A = 0.1$, $m_B/m_A = 0.001$, and (i) $x_A = 0.01$ (circles), (ii) $x_A = 0.05$ (squares), (iii) $x_A = 0.1$ (diamonds), and (iv) $x_A = 0.5$ (triangles). The solid lines are the predictions of the BMCSL equation [see Eq. (6)], and the dotted lines are the predictions of the HC2 equation [see Eq. (11)]. Simulation data points are circled where the system shows signs of freezing.

BMCSL (solid) and HC2 (dotted) equations of state. These equations of state provide an excellent description of the simulation data, with the exception of the very highest packing fractions where they overpredict the pressure. These deviations, however, are due to the onset of freezing of the larger spheres; the single component hard-sphere fluid begins to freeze at a packing fraction of 0.494.⁴⁹

The contact values of the AA, AB, and BB pair correlation functions are plotted in Fig. 3 as a function of the total volume fraction of spheres for different mole fractions of the larger A spheres x_A . The simulation results for g_{BB} are well described by the BMCSL theory. This is in agreement with previous simulation studies of binary hard-sphere mixtures.^{7,12} The VS predictions (not shown) provide equally accurate predictions for g_{BB} .

The BMCSL predictions for g_{AB} lie above the simulation results at high density for the lowest mole fraction studied. The HC2 predictions are higher still; however, the error is within a few percent. The corrections of Henderson *et al.*¹⁰ to g_{AB} are small for the systems studied. The VS predictions (not shown) lie between the HC2 and the BMCSL results.

For the contact value of pair correlation function between the larger spheres, the BMCSL predictions fall significantly below the simulation results at high density for the lowest mole fraction studied. The HC2 predictions are exceptionally accurate, even for the smallest mole fractions of

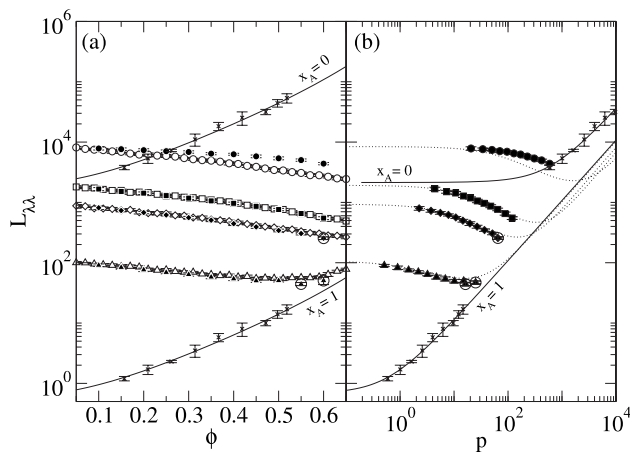


FIG. 4. Thermal conductivity $L_{\lambda\lambda}$ as a function of (a) solid fraction ϕ and (b) pressure p for binary hard-sphere mixtures with $\sigma_B/\sigma_A = 0.1$, $m_B/m_A = 0.001$, and (i) $x_A = 0.01$ (circles), (ii) $x_A = 0.05$ (squares), (iii) $x_A = 0.1$ (diamonds), and (iv) $x_A = 0.5$ (triangles). The filled symbols are from molecular dynamics simulations, and the open symbols are the DSMC results for the Enskog theory. The crosses are molecular dynamics simulations for single component hard spheres, taken from Ref. 50. The lines are third-order Enskog theory predictions using BMCSL (solid) and HC2 (dotted) values of $g_{ab}(\sigma_{ab}^+)$. Simulation data points are circled where systems show signs of freezing.

the larger spheres. This is due to the success of the underlying VS equation (not shown), which give results that are nearly indistinguishable from the HC2 equation. At $\phi \approx 0.55$, $g_{AA}(\sigma_{AA}^+)$ for the $x_A = 0.5$ system decreases significantly. This also occurs in the $x_A = 0.1$ system at a higher packing fraction of $\phi = 0.6$. It appears that the larger component has frozen while the smaller spheres remain fluid.

Overall, the HC2 expression is accurate and provides excellent estimates for the contact values of the pair correlation functions for all the conditions studied in this work.

B. Thermal conductivity

The thermal conductivity of the binary hard-sphere mixtures is plotted in Fig. 4(a) with respect to the packing fraction and in Fig. 4(b) with respect to the pressure. The molecular dynamics simulation data are given by the filled symbols. The crosses are molecular simulation data for single component hard spheres, taken from Ref. 50. For single component hard-sphere systems, the thermal conductivity increases with increasing packing fraction and pressure. The initial addition of smaller spheres to a system of larger spheres (i.e., decreasing x_A) significantly increases the thermal conductivity of the mixture. At the same packing fraction, a system with a lower mole fraction of larger spheres will have many more particles than a system with a higher mole fraction of larger spheres. These additional particles enhance the ability of a system to transport energy. With the addition of smaller spheres to the large sphere system, we observe that the thermal conductivity no longer increases monotonically with the packing fraction (or the pressure). Rather, the thermal conductivity initially decreases with increasing packing fraction down to a minimum value, and then it increases. The packing fraction at the minimum increases as the fraction of smaller spheres increases.

Interestingly, at packing fractions below $\phi \approx 0.25$, the thermal conductivity of pure B spheres (i.e., $x_A=0$) is lower than the thermal conductivity for the $x_A=0.01$ system, while for $\phi > 0.25$ it is higher. This implies that at sufficiently low packing fraction (or pressure) the thermal conductivity of the system must have a maximum with respect to x_A . Physically, this would correspond to a situation where the addition of larger spheres to a fluid of smaller hard spheres would enhance its thermal conductivity.

The solid lines in Fig. 4 are the predictions of the Enskog theory within the third-order Sonine approximation with the BMCSL expressions for the collision rates, while the dotted lines are the third-order Enskog predictions with the HC2 expressions. The difference between using the BMCSL and HC2 expressions in the Enskog theory is negligible, as the collisional contribution to the thermal conductivity is dominated by the BB and BA interactions [see Figs. 3(b) and 3(c)]. The open symbols in Fig. 4 are from DSMC calculations using the HC2 expressions for the collision rates. These results are nearly identical to the third-order Sonine approximation, indicating the accuracy of the approximation and validating the DSMC code.

The simulation results are well described by the Enskog theory for the pure hard-sphere systems (i.e., $x_A=0$ and 1), as well as for mixtures with relatively high mole fractions of the larger spheres ($x_A \geq 0.05$). At high packing fractions, the Enskog predictions deviate slightly for the case $x_A=0.5$; however, this occurs at the conditions where component A appears to freeze [see Fig. 3(a)], and the BMCSL and HC2 expressions for $g_{ab}(\sigma_{ab}^+)$ are not applicable for solid phases.

For $x_A=0.01$, the Enskog theory significantly underpredicts the thermal conductivity of the system. This deviation may be related to the enhanced mobility of the system due to the fines effect⁹ and is a result of a dynamic process not captured by the Enskog theory. Note, however, that the Enskog theory provides good predictions for the thermal conductivity of one component hard-sphere systems,⁵⁰ so one expects that for vanishing amounts of the larger spheres (i.e., the limit where $x_A \rightarrow 0$), the Enskog theory should again provide a fairly good description of the simulation data.

C. Shear viscosity

The shear viscosity is plotted in Fig. 5. The viscosity of all the mixtures increases monotonically with the packing fraction of the spheres and the pressure of the system [see Figs. 5(a)–5(c)]. Unlike for the thermal conductivity, the Enskog theory predictions for the shear viscosity using the HC2 expression for the collision rates noticeably differ from the BMCSL results [see Fig. 5(a)]; however, this only occurs in regions where the Enskog theory poorly describes the simulation results [see Figs. 5(b) and 5(c)]. The Enskog theory captures the low density behavior of the viscosity quite well. For single component hard-sphere systems, the Enskog theory is known to underpredict the viscosity at high densities⁵¹ due to its inability to account for correlated collisions resulting from the caging of spheres at these conditions. For the binary hard-sphere mixtures that we study here, the Enskog theory underpredicts the viscosity, in gen-

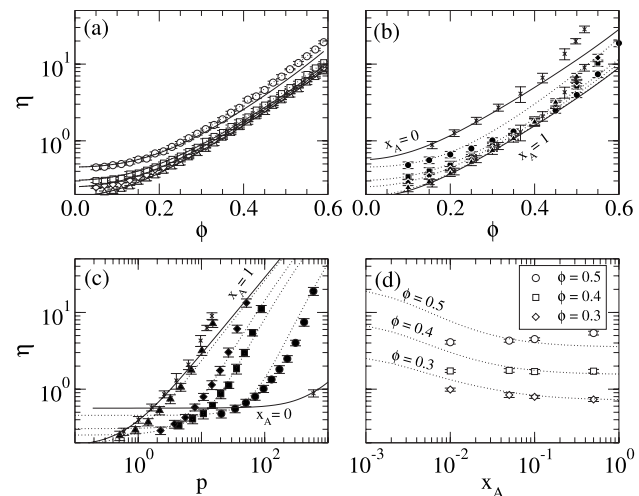


FIG. 5. Shear viscosity η as a function of [(a) and (b)] solid fraction ϕ , (c) pressure p , and (d) mole fraction x_A for binary hard-sphere mixtures with $\sigma_B/\sigma_A=0.1$ and $m_B/m_A=0.001$. With the exception of (d), the symbols indicate mole fractions of (i) $x_A=0.01$ (circles), (ii) $x_A=0.05$ (squares), (iii) $x_A=0.1$ (diamonds), and (iv) $x_A=0.5$ (triangles). The filled symbols are from molecular dynamics simulations, and the open symbols are the DSMC results for the Enskog theory. The crosses are molecular dynamics simulations for single component hard spheres, taken from Ref. 50. The lines are third-order Enskog theory predictions using the BMCSL (solid) and HC2 (dotted) predictions for $g_{ab}(\sigma_{ab}^+)$.

eral. However, the case $x_A=0.01$ is an exception, where the Enskog theory actually overpredicts the viscosity at high packing fractions.

An interesting fines effect occurs in the viscosity of these systems. At low overall packing fractions (or pressures), the addition of smaller spheres to a system of larger spheres (i.e., decreasing x_A) increases the viscosity of the system. However, above a packing fraction of about $\phi=0.4$, the curves for the viscosity crossover, and the addition of smaller spheres to a system of larger spheres *decreases* the viscosity of the system. This is highlighted in Fig. 5(d) where the viscosity is almost independent of composition at a packing fraction of $\phi=0.4$. The fines effect is not captured by the Enskog theory, which indicates that its origin is in dynamical correlations between particles. In these systems, the presence of the smaller spheres leads to an attractive depletion force^{2,3} between the larger spheres, which is entropically driven. This force may disrupt the caging of larger spheres⁹ by forcing them into closer contact, thereby creating a more open network and increasing the mobility of both species.

D. Thermal diffusion coefficient

Figure 6 presents the thermal diffusivity of the larger spheres over a range of packing fractions and pressures. Because L_{AA} is negative, the larger species tends to move toward regions of higher temperature. Increasing the packing fraction, the pressure, or the fraction of larger spheres in the system decreases the magnitude of the thermal diffusivity. This general trend is in agreement with previous non-equilibrium molecular dynamics simulations.²⁴

The use of the HC2 expressions with the Enskog theory offers no significant improvement on the BMCSL predictions, again due to the dominance of the small spheres in the

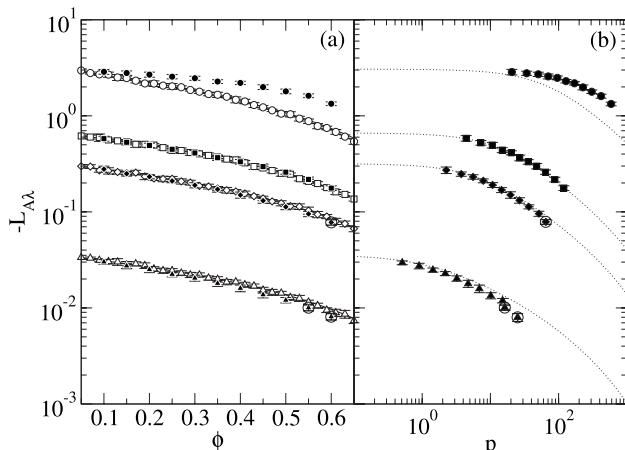


FIG. 6. Thermal diffusivity L_{AA} as a function of (a) solid fraction ϕ and (b) pressure p for binary hard-sphere mixtures with $\sigma_B/\sigma_A=0.1$, $m_B/m_A=0.001$, and (i) $x_A=0.01$ (circles), (ii) $x_A=0.05$ (squares), (iii) $x_A=0.1$ (diamonds), and (iv) $x_A=0.5$ (triangles). The filled symbols are from molecular dynamics simulations, and the open symbols are the DSMC results for the Enskog theory. The lines are third-order Enskog theory predictions using the BMCSL (solid) and HC2 (dotted) predictions for $g_{ab}(\sigma_{ab}^+)$. Simulation data points are circled where the system shows signs of freezing.

energy transport. The Enskog theory is in quantitative agreement with the simulation data over a broad range of conditions examined in this work. However, the main exception is for the composition $x_A=0.01$, where it substantially underpredicts the L_{AA} at the higher packing fractions.

E. Mutual diffusion coefficient

The mutual diffusion coefficient of the binary hard-sphere mixtures is plotted in Fig. 7. The mutual diffusion coefficient behaves similarly to the thermal diffusivity. The displacement functions required to calculate this transport coefficient contain no potential terms, and therefore, they do

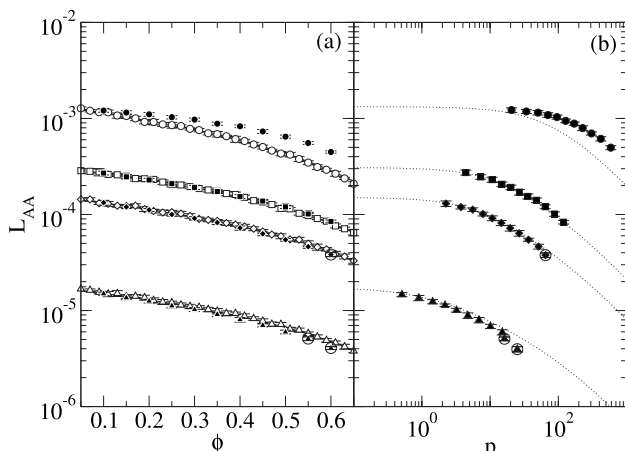


FIG. 7. Mutual diffusion coefficient L_{AA} as a function of (a) solid fraction ϕ and (b) pressure p for binary hard-sphere mixtures with $\sigma_B/\sigma_A=0.1$, $m_B/m_A=0.001$, and (i) $x_A=0.01$ (circles), (ii) $x_A=0.05$ (squares), (iii) $x_A=0.1$ (diamonds), and (iv) $x_A=0.5$ (triangles). The filled symbols are from molecular dynamics simulations, and the open symbols are the DSMC results for the Enskog theory. The lines are third-order Enskog theory predictions using the BMCSL (solid) and HC2 (dotted) predictions for $g_{ab}(\sigma_{ab}^+)$. Simulation data points are circled where the system shows signs of freezing.

not contain a collisional component of the flux (see Tables I and II). Consequently, the Enskog theory performs equally well with HC2 or BMCSL contact radial distribution values. Similar to the results for the thermal diffusivity, the Enskog theory is in quantitative agreement with the simulation data over most of the conditions examined, with the exception of the $x_A=0.01$ systems, where it significantly underpredicts the diffusion coefficient.

V. CONCLUSIONS

In this work, we examined the properties of binary mixtures of hard spheres with a diameter ratio of $\sigma_B/\sigma_A=0.1$ and a mass ratio of $m_B/m_A=0.001$. The BMCSL equation of state is able to accurately describe the pressure for all the conditions that we investigated where the system did not freeze. However, it underpredicts the values of g_{AB} and g_{AA} , especially at high packing fractions and low mole fractions of the larger spheres. The recently developed HC2 equation, however, is able to quantitatively predict these quantities.

The Enskog theory provides fairly accurate predictions for the transport coefficients of the systems that we studied in this work. The third-order Sonine approximation and the DSMC results agree well with one another, both validating the DSMC code and demonstrating that the third-order solution is sufficiently accurate over the conditions studied. At low mole fractions of the larger hard spheres, the Enskog theory fails to capture the behavior of the transport properties, especially the shear viscosity. This may be due to the increased correlations in the collisions between the larger spheres caused by the depletion forces due to the presence of the smaller spheres.

DSMC provides a speed benefit over traditional molecular dynamics simulations where large size asymmetries and low mole fractions are computationally expensive. Unfortunately, this is where the Enskog theory begins to break down in predicting the transport properties of the fluid. Extension of DSMC to other kinetic theories, such as ring theory, is necessary to capture this behavior; however, these techniques are yet to be developed.

We find a fines effect where the addition of smaller spheres to a larger hard-sphere fluid decreases the viscosity of the system, which occurs at packing fractions greater than about 0.4. This effect is not captured by the Enskog theory. With the addition of fines, the thermal conductivity of the mixture no longer monotonically increases with the packing fraction but instead initially decreases with increasing packing fraction to a minimum value and then increases. In addition, at low to moderate packing fractions, there is a region in x_A where the thermal conductivity of the mixture is higher than the thermal conductivity of either pure species.

ACKNOWLEDGMENTS

M. N. Bannerman acknowledges support from an EPSRC-GB DTA.

¹J. P. Hansen and I. R. McDonald, *Theory of Simple Liquids*, 2nd ed. (Academic, London, 1986).

²F. Oosawa and S. Asakura, J. Chem. Phys. **22**, 1255 (1954).

³A. Vrij, Pure Appl. Chem. **48**, 471 (1976).

- ⁴G. Jackson, J. S. Rowlinson, and F. van Swol, *J. Phys. Chem.* **91**, 4907 (1987).
- ⁵D. H. L. Yau, K.-Y. Chan, and D. Henderson, *Mol. Phys.* **88**, 1237 (1996).
- ⁶D. H. L. Yau, K.-Y. Chan, and D. Henderson, *Mol. Phys.* **91**, 1137 (1997).
- ⁷L. Lue and L. V. Woodcock, *Mol. Phys.* **96**, 1435 (1999).
- ⁸K.-Y. Chan and D. Henderson, *Mol. Phys.* **98**, 1005 (2000).
- ⁹L. Lue and L. V. Woodcock, *Int. J. Thermophys.* **23**, 937 (2002).
- ¹⁰D. Henderson, A. Trokhymchuk, L. V. Woodcock, and C. Kwong-Yu, *Mol. Phys.* **103**, 667 (2005).
- ¹¹A. Vrabecz and G. Tóth, *Mol. Phys.* **104**, 1843 (2006).
- ¹²M. Alawneh and D. Henderson, *Mol. Phys.* **106**, 607 (2008).
- ¹³M. Alawneh and D. Henderson, *Mol. Phys.* **106**, 2407 (2008).
- ¹⁴A. Santos and M. L. López de Haro, *J. Chem. Phys.* **123**, 234512 (2005).
- ¹⁵P. T. Herman and B. J. Alder, *J. Chem. Phys.* **56**, 987 (1972).
- ¹⁶G. Subramanian, D. Levitt, and H. T. Davis, *J. Chem. Phys.* **60**, 591 (1974).
- ¹⁷B. J. Alder, W. E. Alley, and J. H. Dymond, *J. Chem. Phys.* **61**, 1415 (1974).
- ¹⁸V. Y. Rudyak, G. V. Kharlamov, and A. A. Belkin, *Tech. Phys. Lett.* **26**, 553 (2000).
- ¹⁹V. Y. Rudyak, G. V. Kharlamov, and A. A. Belkin, *High Temp.* **39**, 264 (2001).
- ²⁰A. J. Eastal and L. A. Woolf, *Chem. Phys. Lett.* **167**, 329 (1990).
- ²¹J. J. Erpenbeck, *Phys. Rev. A* **39**, 4718 (1989).
- ²²J. J. Erpenbeck, *Phys. Rev. A* **45**, 2298 (1992).
- ²³J. J. Erpenbeck, *Phys. Rev. E* **48**, 223 (1993).
- ²⁴S. Yeganegi and M. Zolfaghari, *Fluid Phase Equilib.* **243**, 161 (2006).
- ²⁵S. Bastea, *Phys. Rev. E* **75**, 031201 (2007).
- ²⁶M. López de Haro, E. G. D. Cohen, and J. M. Kincaid, *J. Chem. Phys.* **78**, 2746 (1983).
- ²⁷D. V. Matyushov and B. Ladanyi, *J. Chem. Phys.* **107**, 5815 (1997).
- ²⁸T. Boublík, *J. Chem. Phys.* **53**, 471 (1970).
- ²⁹G. A. Mansoori, N. F. Carnahan, K. E. Starling, and T. W. Leland, *J. Chem. Phys.* **54**, 1523 (1971).
- ³⁰J. K. Percus and G. J. Yevick, *Phys. Rev.* **110**, 1 (1958).
- ³¹R. Roth, R. Evans, and S. Dietrich, *Phys. Rev. E* **57**, 6785 (2000).
- ³²D. Viduna and W. R. Smith, *J. Chem. Phys.* **117**, 1214 (2002).
- ³³D. Viduna and W. R. Smith, *Mol. Phys.* **100**, 2903 (2002).
- ³⁴S. de Groot and P. Mazur, *Non-Equilibrium Thermodynamics* (Dover, New York, 1984).
- ³⁵J. M. Kincaid, M. López de Haro, and E. G. D. Cohen, *J. Chem. Phys.* **79**, 4509 (1983).
- ³⁶M. L. López de Haro and E. G. D. Cohen, *J. Chem. Phys.* **80**, 408 (1984).
- ³⁷J. M. Kincaid, E. G. D. Cohen, and M. López de Haro, *J. Chem. Phys.* **86**, 963 (1987).
- ³⁸S. Chapman and T. G. Cowling, *The Mathematical Theory of Non-Uniform Gases*, 3rd ed. (Cambridge University Press, Cambridge, 1970).
- ³⁹J. H. Ferziger and H. G. Kaper, *Mathematical Theory of Transport Processes in Gases* (North-Holland, London, 1972).
- ⁴⁰J. M. Montanero and A. Santos, *Phys. Rev. E* **54**, 438 (1996).
- ⁴¹J. M. Montanero and A. Santos, *Phys. Fluids* **9**, 2057 (1997).
- ⁴²A. Frezzotti, *Phys. Fluids* **9**, 1329 (1997).
- ⁴³G. A. Bird, *Molecular Gas Dynamics and the Direct Simulation of Gas Flows* (Oxford University Press, Oxford, 1994).
- ⁴⁴M. A. Hopkins and H. H. Shen, *J. Fluid Mech.* **244**, 477 (1992).
- ⁴⁵B. J. Alder and T. E. Wainwright, *J. Chem. Phys.* **31**, 459 (1959).
- ⁴⁶M. Marin, D. Risso, and P. Cordero, *J. Comput. Phys.* **109**, 306 (1993).
- ⁴⁷G. Paul, *J. Comput. Phys.* **221**, 615 (2007).
- ⁴⁸J. M. Haile, *Molecular Dynamics Simulation—Elementary Methods* (Wiley-Interscience, New York, 1997).
- ⁴⁹W. G. Hoover and F. H. Ree, *J. Chem. Phys.* **49**, 3609 (1968).
- ⁵⁰L. Lue, *J. Chem. Phys.* **122**, 044513 (2005).
- ⁵¹L. Lue and M. Bishop, *Phys. Rev. E* **74**, 021201 (2006).

APPENDIX

C

REPRINT: STRUCTURE AND STABILITY OF HELICES
IN SQUARE-WELL HOMOPOLYMERS

Structure and stability of helices in square-well homopolymers

M. N. Bannerman, J. E. Magee, and L. Lue*

*School of Chemical Engineering and Analytical Science, The University of Manchester,
P.O. Box 88, Sackville Street, Manchester M60 1QD, United Kingdom*

(Received 21 May 2009; published 26 August 2009)

Recently, it has been demonstrated [Magee *et al.*, Phys. Rev. Lett. **96**, 207802 (2006)] that isolated square-well homopolymers can spontaneously break chiral symmetry and “freeze” into helical structures at sufficiently low temperatures. This behavior is interesting because the square-well homopolymer is itself achiral. In this work, we use event-driven molecular dynamics combined with an optimized parallel tempering scheme to study this polymer model over a wide range of parameters. We examine the conditions where the helix structure is stable and determine how the interaction parameters of the polymer govern the details of the helix structure. The width of the square well (proportional to λ) is found to control the radius of the helix, which decreases with increasing well width until the polymer forms a coiled sphere for sufficiently large wells. The helices are found to be stable for only a “window” of molecular weights. If the polymer is too short, the helix will not form. If the polymer is too long, the helix is no longer the minimum energy structure, and other folded structures will form. The size of this window is governed by the chain stiffness, which in this model is a function of the ratio of the monomer size to the bond length. Outside this window, the polymer still freezes into a locked structure at low temperature; however, unless the chain is sufficiently stiff, this structure will not be unique and is similar to a glassy state.

DOI: [10.1103/PhysRevE.80.021801](https://doi.org/10.1103/PhysRevE.80.021801)

PACS number(s): 61.41.+e, 33.15.Bh

I. INTRODUCTION

One of the fascinating features of proteins is their ability to lock into a specific folded structure. This feature is often crucial to their function. A key structural unit which frequently appears in proteins is the helix. Helical structures also appear in other molecules, such as in DNA, homopeptides (e.g., polyalanine), as well as in some synthetic polymers. Consequently, there has been a lot of interest in the helix-coil transition as a starting point to understanding the more general issue of protein folding.

Many detailed computer simulations on “realistic” interaction potential models have been conducted to better understand the formation of helices in polypeptides and proteins (e.g., see Refs. [1–4]). In these systems, the formation of hydrogen bond interactions between different amino acid groups is principally responsible for the formation of the helix. Helices also spontaneously form in simplified interaction models that have short-ranged directional interactions between their constituent monomers [5,6]. Many theories have been developed to describe the helix-coil transition in homopeptides and other biological molecules, starting with the pioneering work of Zimm and Bragg [7] and later followed by many others [8–12]. The key feature of these theories is the characterization of a distinct helix and coil state for each residue in the peptide chain. This is justified for these systems because of the specific arrangement of the residues in the helix conformation and the large energies due to the formation of the hydrogen bonds. While these approaches have led to keen insights for helix formation in polypeptide and protein molecules, they are dependent on the fact that short-ranged directional interactions drive the for-

mation of the helix structure. In these molecules, one can argue that the helix structure has been “built” in.

Can the helix structure occur in molecules without these specific interactions, and if so, what then controls its geometry? It has been suggested that the helix is a stationary configuration for semiflexible chains [13] and the optimal shape of flexible [14] and closely-packed compact [15,16] strings. This hints at a more general driving force for helix formation in real proteins and may explain why the structure is so prolific in nature. In order to gain some more general understanding of the mechanisms behind helix formation, we examine the square-well homopolymer model. This is a simple polymer model composed of linearly bonded hard spheres that interact with each other through an isotropic square-well attraction. Isolated square-well homopolymers exhibit the typical coil to globule transition observed in many polymers as the temperature is decreased below the theta point; however, they also freeze into compact crystal-like structures [17,18] at sufficiently low temperatures. Interestingly, Magee *et al.* [19] demonstrated that, by introducing stiffness, the square-well homopolymer model can fold into a helix structure. This is a remarkable result, as the model is achiral and yet it spontaneously breaks symmetry and folds into left- or right-handed helices. This is merely a result of the polymer being stiff, having an excluded volume and an attractive self interaction. An exact analysis of the density of states of square-well tetramers and pentamers was performed [20] to examine the relationship between the distributions and correlations of the torsional angles in these fragments to the stability of the helix in longer length chains. However, the question still remains as to what controls the geometry and the stability of the helical structures formed by these molecules.

In this work, we use molecular dynamics (MD) combined with the replica exchange method to explore the behavior of square-well homopolymers to better understand the link be-

*leo.lue@manchester.ac.uk

tween the interactions between the monomers of the chain and the overall structure of the molecule. In particular, we are interested in the range of conditions over which the helix structure is stable. The remainder of this paper is organized as follows. Section II describes the details of the square-well homopolymer model that we investigate in this work. In addition, it provides background information on the simulation methods we employed and outlines the procedures used to generate and analyze the resulting simulation data. The results of the simulations are presented in Sec. III. This section begins with an overview of the general behavior exhibited by the square-well homopolymers. Then, it continues by analyzing and discussing the influence of the bond length (or equivalently monomer size), the range of attraction between monomers, and the total number of monomers in the polymer on the structure and thermodynamic behavior of the homopolymer. Finally, the major findings of this work are summarized in Sec. IV.

II. SIMULATION DETAILS

The polymer model that we study in this work is a chain of linearly bonded monomers. Monomers that are not directly bonded together interact with each other through the potential

$$u(r) = \begin{cases} \infty & \text{for } r < \sigma \\ -\epsilon & \text{for } \sigma < r < \lambda\sigma \\ 0 & \text{for } \lambda\sigma < r, \end{cases} \quad (1)$$

where r is the distance between the centers of the monomers. Each monomer is a hard sphere of diameter σ surrounded by an attractive square well of diameter $\lambda\sigma$. When two monomers are within a distance $\lambda\sigma$, they feel an attractive interaction energy of magnitude ϵ . Monomers that are directly bonded together interact with each other through the potential

$$u_{\text{bond}}(r) = \begin{cases} \infty & \text{for } r < l - \delta \\ 0 & \text{for } l - \delta < r < l + \delta \\ \infty & \text{for } l + \delta < r. \end{cases} \quad (2)$$

The bond length is nominally equal to l but is allowed to fluctuate between $l - \delta$ and $l + \delta$. If $\sigma/l > 1$, then directly bonded monomers in the chain overlap. Monomers that are not directly bonded together other are not allowed to overlap each other. This induces a stiffness in the polymer due to the restrictions on the allowed bond angles imposed by the excluded volume interaction between monomers separated by two bonds. In the limit that σ/l approaches $2(1 + \delta/l)$, the chain becomes completely rigid. For all the simulations presented here, $\delta/\sigma = 0.1$, and so the bond length is allowed to vary by $\pm 10\%$. A schematic drawing of the polymer model is given in Fig. 1.

We use constant temperature MD to investigate the structural and thermodynamic properties of the square-well polymer chains over a range of temperatures. The temperature of the simulations was maintained with the Andersen thermostat [21]. The basic algorithm that we employ to perform the MD

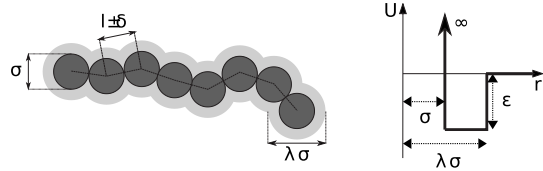


FIG. 1. Polymer model with bond length $l \pm \delta$, well energy ϵ , well width $\lambda\sigma$, and monomer diameter σ . The interaction energy between two nonbonded monomers separated by a distance r is given on the right.

simulations is based on the one originally developed by Alder and Wainwright [22]. Several subsequent advances have significantly improved the computational speed of this original algorithm. These include the use of overlapping cells [23,24], the delayed states algorithm [25], and calendar event queues [26]. We have incorporated these advances in order to construct a code where the computational cost of the simulation is independent of the number of particles N in the system.

One shortcoming of molecular dynamics is that it is prone to becoming trapped in local energy minima, especially at low temperatures. In particular for conditions where helical or other “frozen” structures are formed, the homopolymer may become locked within a specific configuration. Using only molecular dynamics, the helices formed by the square-well polymers are stable over the length of accessible simulation times and rarely transform between the left- and right-handed forms. This makes the study of the equilibrium behavior of these systems at low temperatures extremely formidable.

To overcome this difficulty, the MD simulations are coupled with the replica exchange/parallel tempering method [27]. In this technique, several molecular-dynamics simulations, each at a different temperature, are run simultaneously; a Monte Carlo move is added to exchange chain configurations between simulations at different temperatures. A configuration that is locked at a low temperature may then move up in temperature, unfold, and drop in temperature to sample another configuration. This enables the systems to rapidly overcome local energy minima and better explore the full range of available configurations.

The effectiveness of the replica exchange method depends on the choice of the temperatures of the individual simulations. In order to determine the optimal values of these temperatures, we use an approach recently developed by Katzgraber *et al.* [28]. This maximizes the number of configurations that travel between the lowest- and highest-temperature simulations, as modeled by a one-dimensional diffusion process. A typical optimal distribution of system temperatures is presented in Fig. 2, along with the resulting exchange rates. The optimization procedure clusters the simulation temperatures near conditions where the polymer undergoes structural changes with significant topological differences. The optimal distribution of system temperatures does not correspond to a constant acceptance ratio [28], as is commonly presumed.

A series of *NVT* molecular-dynamics simulations combined with the replica exchange method is performed to ex-

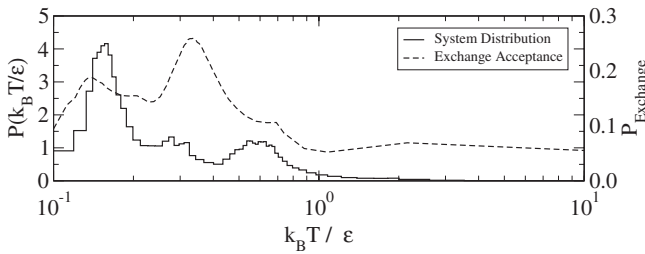


FIG. 2. Replica exchange simulations for an isolated square-well homopolymer with $N=20$, $\sigma/l=1.6$, and $\lambda=1.5$. Optimal distribution of system temperatures is given by the solid line, and the acceptance ratio of the replica exchange move for adjacent temperature systems is given by the dashed line.

amine the properties of square-well homopolymers over a range of values for σ/l , λ , and N . For each particular chain, 51 temperatures are used, and the systems are equilibrated for 10^4 attempted replica exchange moves. The replica exchange move consists of selecting 5×51 random pairs and attempting to swap the configuration between each pair. Between each replica exchange move, the dynamics of the isolated polymers is run for a few hundred mean free times. Following an initial equilibration period, data are collected over 5×10^4 attempted replica exchange moves. The collected data are then interpolated using multiple histogram reweighting [29] to obtain smooth heat-capacity curves as a function of the temperature.

III. RESULTS AND DISCUSSION

A. Overview

To illustrate the general behavior of the square-well homopolymers, we present results from MD simulations in Fig. 3 for a chain consisting of $N=20$ monomers with $\sigma/l=1.6$ and $\lambda=1.5$. The solid line in the plot shows the variation in the excess heat capacity C_v with temperature. The peaks of

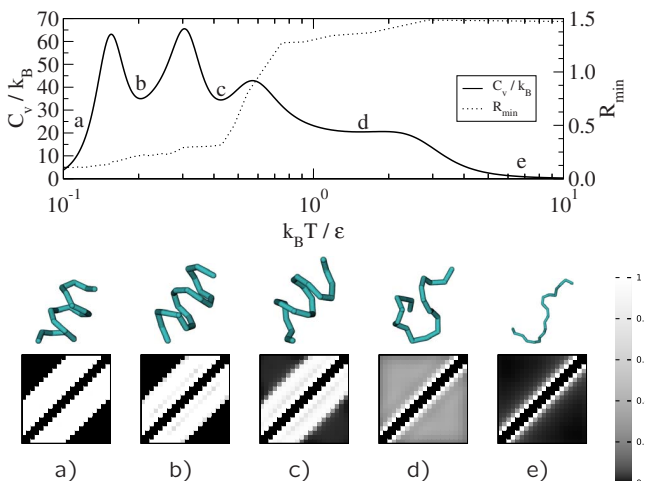


FIG. 3. (Color online) The heat capacity, the optimal configuration D_{rms} , sample configurations, and contact maps at various temperatures (a–e) of an isolated helix homopolymer with $N=20$, $\sigma/l=1.6$, and $\lambda=1.5$.

the heat capacity typically indicate transitions between different structural states of the polymer.

To characterize the rigidity (i.e., frozen vs flexible) of the structure of the homopolymer at a particular temperature, we collect N_{ss} configurations of the polymer at regular intervals in time during the course of the simulation (here we choose ten replica exchange times). For each sampled configuration α , we then determine the average R_α of the root-mean-square difference (rms, D_{rms}) against all other collected configurations, which is given by

$$R_\alpha = N_{ss}^{-1} \sum_{\alpha'=1}^{N_{ss}} D_{\text{rms}}(\alpha, \alpha'), \quad (3)$$

where the D_{rms} between two configurations α and α' is defined as

$$D_{\text{rms}}(\alpha, \alpha') = \left[N^{-1} \sum_{i=1}^N |\mathbf{r}_i^{(\alpha)} - \mathbf{r}_i^{(\alpha')}|^2 \right]^{1/2} \quad (4)$$

and $\mathbf{r}_i^{(\alpha)}$ is the position of monomer i in the polymer of configuration α . The reported value of the D_{rms} between a pair of configurations is the minimum value obtained by rotating [30] and reflecting the configurations, as well as reversing the numbering sequence of the monomers. We consider the configuration with the lowest value of R_α as the most representative of the entire set of sampled configurations of the homopolymer. The average D_{rms} of this configuration denoted by R_{\min} is used to indicate how rigid the polymer structure is at a given temperature (i.e., $R_{\min} = \min_\alpha R_\alpha$). Low values of R_{\min} suggest that the homopolymer remains frozen within the same structural configuration. High values of R_{\min} indicate that the homopolymer is not well characterized by a single structure. This can imply that the homopolymer is in a rather flexible state, such as a coil or a molten globule. However, high values of R_{\min} could also result if the homopolymer can be frozen into several distinct configurations, such as in a glassy state. Using cluster analysis of the distance matrix formed by the D_{rms} 's of every pair of sample configurations, it is possible to estimate the number of stable states and thereby distinguish between these two situations. This issue will be discussed further in Sec. III D, where the effect of polymer length is explored.

The variation in R_{\min} with temperature is given by the dotted line in the plot in Fig. 3. Beneath the plot are sample configurations of the homopolymer at several different representative temperatures. Underneath each of these configurations is the corresponding contact map of the average structure, which details the proximity of pairs of monomers in the polymer. The positions along the ordinate and abscissa of the contact maps denote each of the monomers along the chain. The locations within the contact map are shaded according to how often two monomers interact with each other (i.e., within a distance $\lambda\sigma$). Black denotes no interaction, white denotes continuous interaction, and gray denotes intermittent interaction. For monomers that are bonded together (along the diagonal), we have shaded the entries in the contact map black. For the case where $\sigma/l=1.6$ and $\lambda=1.5$,

monomers that are separated by two bonds are always in each others attractive well due to the overlap and result in two off-diagonal white bands.

At higher temperatures (point *e*), the polymer is extended, and the contact map indicates that the monomers of the polymer are rarely in contact with each other. The optimal configuration $D_{\text{rms}}(R_{\min})$ also indicates that the typical configuration is not locked but, instead, is quite flexible. Upon decreasing the temperature, a shoulder in the heat capacity marks the transition from an extended coil to a globule state (point *d*). The contact map indicates that while monomers do interact significantly with each other, they do not remain in continuous contact with the same monomers, and therefore, the contact map is primarily gray. Although the polymer has collapsed into a compact structure, it contains no regular structure and R_{\min} remains high.

Decreasing the temperature still further (point *c*), we see that the polymer changes from an unstructured globule to a more ordered helical structure. The contact map shows the stripe pattern that is characteristic of a spiral or helical structure. Two more helical structures are present at lower temperatures (points *b* and *a*) which possess a slightly different pitch and radius. The value of R_{\min} decreases sharply over the first helix transition as the polymer forms a regular structure. This decreases further, indicating that the structures become more rigid. This is in agreement with the contact maps, where intermittent contacts become permanently “on” at low temperatures. Points *c* and *b* correspond to the helix 1 and 2 structures in the diagram of states presented by Magee *et al.* [19]. We will refer to the structure at point *a* as the helix 3 structure. The transitions between the three helical structures are not visible in R_{\min} as the structures are very similar but the transition to a folded state is strongly marked.

In the following, we examine how the structure of square-well homopolymers is affected by the monomer size (σ/l), the range of the attractive interaction (λ), and the length of the polymer chain (N). In particular, we are interested in understanding the range of parameters where helical structures are stable.

B. Ratio of monomer size to bond length

In this section, we study the influence of monomer size, or equivalently the bond length, on the structure of square-well homopolymers. We limit our attention to homopolymers with $N=20$ and $\lambda=1.5$. The main effect of changing the monomer size is to alter the local stiffness of the polymer chain. Decreasing the size of the monomers (or increasing the bond length) increases the flexibility of the homopolymer. The stiffness of a polymer chain can be characterized by the bond correlation function, which is defined as

$$C(j) = \frac{1}{N-j-1} \sum_{k=1}^{N-j-1} \frac{\langle \Delta \mathbf{r}_k \cdot \Delta \mathbf{r}_{k+j} \rangle}{\langle \Delta \mathbf{r}_k \cdot \Delta \mathbf{r}_k \rangle}, \quad (5)$$

where $\Delta \mathbf{r}_k = \mathbf{r}_{k+1} - \mathbf{r}_k$ is the orientation of the k th bond in the polymer and \mathbf{r}_k is the position of the k th monomer. This function describes the degree to which the orientations of two bonds are correlated with each other. The more flexible

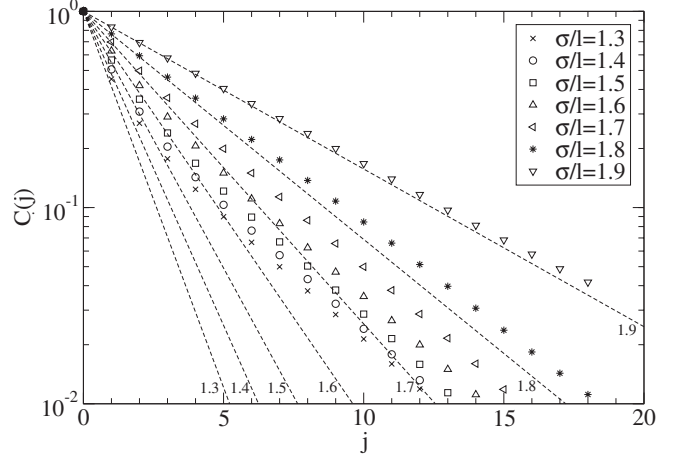


FIG. 4. Average bond angle correlations for athermal overlapping chains as a function of separation in a $N=20$ chain. The dotted lines correspond to neglecting the influence of long range excluded volume interactions between the monomers.

the chain, the more rapidly the bond correlation function decays with the distance j between the bonds.

Figure 4 presents the bond correlation functions for athermal chains (i.e., $\epsilon=0$) with $N=20$ for various values of σ/l . The symbols are the results obtained from MD simulations. The dotted lines are the corresponding exponential decays for the athermal chains where excluded volume interactions are neglected, with the exception to those between monomers separated by two bonds, which give rise to the local stiffness. At very low values of σ/l (not shown), there are no correlations between the bonds, and the polymer behaves essentially as a random walk. At intermediate values of the overlap parameter, the excluded volume interactions between monomers separated by several bonds enhance the correlations between the bonds, and the correlation function decays algebraically rather than exponentially. For $\sigma/l > 1.8$, the decay is nearly exponential because the chain is too stiff for there to be significant excluded volume interactions between the monomers.

A diagram of states for homopolymers with $N=20$ and $\lambda=1.5$ is given in Fig. 5, which explores the effect of the monomer overlap parameter (σ/l). The crosses mark the locations of peaks in the heat capacity, and the diagram is shaded according to the value of R_{\min} . The data in Fig. 3 correspond to the vertical line at $\sigma/l=1.6$ in Fig. 5.

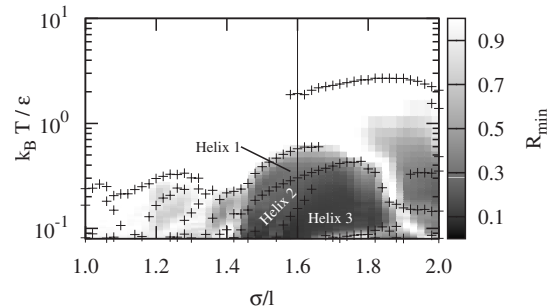


FIG. 5. Diagram of states for isolated square-well homopolymers with $N=20$ and $\lambda=1.5$. The graph is shaded according to R_{\min} .

There are what at first appear to be discontinuities in the heat-capacity maxima in the diagram. These peaks are generally weak maxima in the heat capacity which are hidden behind the rapid increase in C_v due to the presence of sharper peaks at another temperature. The highest-temperature maximum in C_v typically corresponds to the coil-globule collapse or “theta point” (see point *d* in Fig. 3).

Homopolymers with $\sigma/l \leq 1.1$ crystallize into compact, nearly spherical, regularly packed structures at low temperatures [17,18]. The comparatively high value of the D_{rms} for these polymers, however, indicates that the structures that they freeze into are not unique. There may be several arrangements of the bonds of the polymer for a given “crystalline” packing of the monomers. Consequently, these polymers are like glasses at low temperatures.

When $\sigma/l \geq 1 + \delta/l = 1.1$, directly bonded monomers always overlap one another. At low temperatures, homopolymers with $1.1 \leq \sigma/l \leq 1.4$ (see Fig. 5) exhibit a freezing transition; but, similarly to the polymers with $\sigma/l \leq 1.1$, they do not lock into a single stable conformation. The high value of the D_{rms} indicates that many folded configurations exist. On visual inspection of these configurations, helical features are visible within some other structure. For example, the ends of the polymer may be wrapped around the outside of a helical core. These “loose ends” increase the number of possible frozen states and therefore increase the value of R_{\min} .

For homopolymers with a well width of $\lambda = 1.5$, monomers separated by two bonds are permanently within each others attractive wells when $\sigma/l > 2(1 + \delta/l)/\lambda \approx 1.47$. This coincides with the onset of the region of low values for R_{\min} , where homopolymers fold into the helix 1, 2, and 3 structures. Here, the homopolymers fold into a single, helical conformation (neglecting the distinction between the left- and right-handed configurations). A significant portion of the folded parameter space is occupied by the helix 3 structure, which is the most rigid of the helix structures.

At high overlaps, the values of R_{\min} are on average lower due to the stiffness of the chain limiting the range of motion of the monomers. There is a sharp transition at $\sigma/l \approx 1.8$ with an increase in R_{\min} along the line of the heat-capacity peaks. For polymers with a well width of $\lambda = 1.5$, two monomers separated by four bonds cannot interact with each other when $\sigma/l > \sqrt{7}/2 \approx 1.87$ [20]. If we account for the fact that in the simulations the bonds can stretch by 10%, then this would occur at $\sigma/l \geq 1.70$, which coincides with loss of the helix 1 structure.

It appears that the observed helix structures are closely related to the constraint of interactions between monomers in the chain. The values at which certain interactions become prohibited depends on the well width λ , and the effect of this parameter is explored in the next section.

C. Range of attractive interaction

Now, we examine the influence of the range of the attractive interaction, which is characterized by the parameter λ . In this section, we limit the analysis to square-well homopolymers with $N=20$ and $\sigma/l=1.6$. A diagram of states is provided in Fig. 6. Several sample configurations are presented

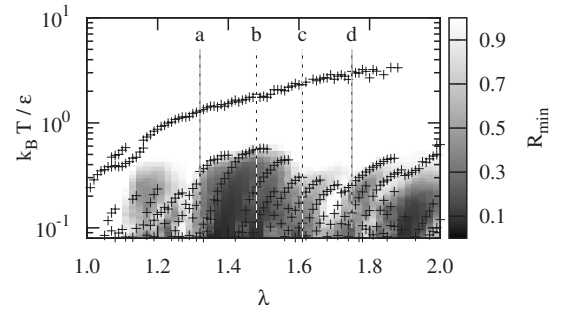


FIG. 6. Diagram of states for isolated square-well homopolymers with $N=20$ and $\sigma/l=1.6$. The graph is shaded according to R_{\min} . The letters and dashed lines correspond to the configurations shown in Fig. 7.

in Fig. 7 at various values of λ . From the diagram and the associated configurations, we see that a series of distinct helical structures are formed at low temperatures. The range of the attractive interaction appears to control the radius of the helix: smaller well widths lead to helical structures with a smaller radius and a larger pitch.

At low values of the well width ($\lambda \leq 1.3$), helical structures appear with structural variations, much like what occurs at low values of the overlap parameter σ/l . For high values of λ , the helix structure begins to degrade. It still retains the spiral structure, however, it no longer has a constant radius. Interestingly, for the structure shown in Fig. 7(d), the monomers appear to be packed in a fairly spherical crystalline arrangement. If the well width becomes too large, then the helix structure will completely vanish, replaced by another structure.

For an overlap of $\sigma/l=1.6$ and a well width of $\lambda \geq 1.375$, monomers separated by two bonds are permanently within each others attractive well. This again coincides with a large decrease in R_{\min} , indicating a single stable structure. As with the diagram of states in the overlap parameter σ/l (see Fig. 5), it is easy to distinguish certain helical structures using R_{\min} .

It is interesting to note that the helices observed here all have a much higher monomer per turn count than the alpha helix commonly found in nature. There are 4 residues per turn of the alpha helix, whereas the wider helices presented here contain 7 for the tightest helix observed [Fig. 6(a)]. Maritan *et al.* [15] characterized their compact string helices using a parameter f related to the helix radius and monomer spacing in consecutive turns of the helix. Applying their analysis, the values of f exhibited by our helices are consistently above the value of $f \approx 1$ [e.g., Figs. 6(a)–6(d)] $f \approx 1.2$,

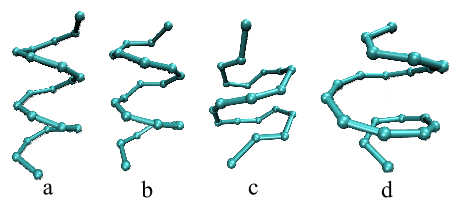


FIG. 7. (Color online) Representative configurations at the state points indicated in Fig. 6.

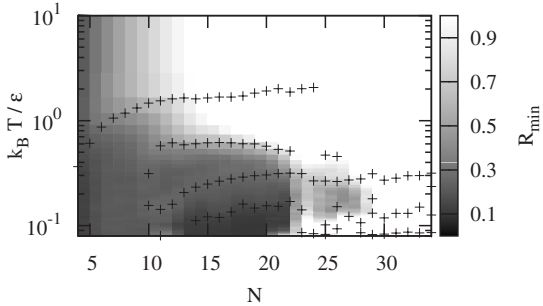


FIG. 8. Diagram of states for isolated square-well homopolymers with $\sigma/l=1.6$ and $\lambda=1.5$ as a function of the chain length N . The graph is shaded according to R_{\min} .

1.1, 1.3, and 1.1, respectively] reported by Maritan for compact strings and naturally occurring alpha helices. These larger values of f may be due to the manner in which we introduce stiffness (i.e., overlapping spheres).

Unlike the overlap parameter, the transitions between the various helical states are typically marked by peaks and large changes in R_{\min} , as the well-width parameter λ has a significant effect on the structure of the folded state. In the following section, we explore the structure as a function of chain length.

D. Chain length

For the square-well homopolymer, the main driving force for the formation of the helix is the tendency of the polymer to recover interaction energy through the contacts of its constituent monomers. This energetic driving force is balanced against the loss of entropy encountered in restricting the polymer to the helical structure (to maintain the necessary contacts). If the polymer chain is too short, then the energy recovered will not be sufficient to overcome the entropy loss, and the helix will not be stable. If the polymer chain is too long, then structures other than the helix are expected to be stable. Therefore, we expect the helix to appear only within a window of chain lengths. In this section, we examine the range of N where the helical structure is stable.

The diagram of states for square-well polymers with $\lambda=1.5$ and $\sigma/l=1.6$ is presented in Fig. 8. For small chain lengths ($N \lesssim 12$) the D_{rms} is, on average, a low value. This is due to the short distance that monomers can actually be separated in space. This can be accounted for by reducing R_{\min} by the chain length; however, similar structures at different chain lengths typically exhibit the same value of R_{\min} and these data would be lost. The conditions where helical structures are formed are still well defined by the heat-capacity peaks and areas where the value of R_{\min} is low. For this system, the chain must consist of at least $N=10$ monomers before helices can form. The helix 3 structure does not appear until $N=14$, and the largest chain length, at which the helix structure is stable, is $N=22$.

At low temperatures, homopolymers with $N > 22$ appear to freeze into rigid structures yet the high values of R_{\min} indicate that the homopolymer does not freeze into a single repeatable folded structure. In fact, these folded states are no

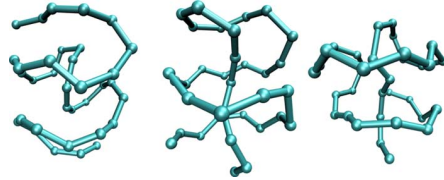


FIG. 9. (Color online) Samples of stable configurations for square-well homopolymers with $\sigma/l=1.6$, $\lambda=1.5$, and $N=34$ at $k_B T / \epsilon=0.137$.

longer unique, and several distinct structures exist with comparable free energies. These longer homopolymers arrange themselves into regularly packed structures with a spherical shape. Figure 9 provides several snapshots of configurations for square-well homopolymers with $N=34$ at a temperature $k_B T / \epsilon=1.35$ (see also Fig. 8). These chiral structures have the same interaction energy, and they are all stable over long times. They appear to be variations in a similar structural theme: a core of a few monomers with a chiral outer core.

The D_{rms} 's of the different folded structures in Fig. 9 lie between 0.86σ and 1.05σ , which is a relatively high value. Thus, the D_{rms} can discriminate between distinct folded structures provided that the configurations within each of the structures have a low average D_{rms} . If we perform a quality threshold (QT) cluster analysis [31] of the D_{rms} between all pairs of sample configurations using a cut-off value of $<0.25\sigma$ to group the data and a threshold of 1% to eliminate intermediates, we can attempt to count the number of distinct structures formed. We perform this counting at the heat-capacity minima as the heat-capacity maxima tend to occur at transitions between structures. For $N=22$, only one cluster is apparent, which indicates that the homopolymer folds into a unique structure at low temperatures; in this case, it is a helix. In contrast, for $N=23$, a single helix occupies approximately 50% of the simulation snapshots. The remainder are a large number of variations on the helix with loose ends wrapped around the central coil.

In fact, once the single helix structure is no longer dominant the number of distinct folded structures rapidly increases with the length of the homopolymer. These polymers will behave similarly to a glass at low temperatures, becoming trapped into one of these many structures.

To understand how the range of the attractive interactions affects the window of chain lengths where the helix is stable, we examine square-well homopolymer chains with $\lambda=1.32$ and $\sigma/l=1.6$. The diagram of states is presented in Fig. 10. These polymers tend to form helices at shorter chain lengths than polymers with a wider well widths (cf. Fig. 8 for $\lambda=1.5$). The helices formed by the $\lambda=1.32$ polymers have a tighter radius and are more rigid (lower value of R_{\min}) than the helices formed by the $\lambda=1.5$ polymers. The shortest homopolymer that forms a helix ($N=8$) appears to be correlated with the number of monomers in a single turn of the helix. The helix structure vanishes for chain lengths greater than $N=22$, which is similar to what is found for homopolymers with $\lambda=1.5$. At longer chain lengths, the system again exhibits multiple folded states, and the structures formed are similar to those displayed in Fig. 9.

To investigate the influence of the monomer size (or bond length) on the window of chain lengths where the helix is

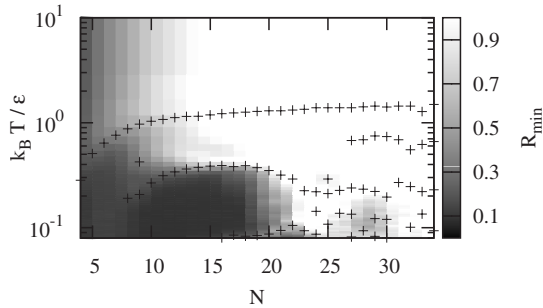


FIG. 10. Diagram of states for isolated square-well homopolymers with $\sigma/l=1.6$ and $\lambda=1.32$ as a function of the chain length N . The graph is shaded according to R_{\min} .

formed, we examine square-well homopolymers with $\sigma/l=1.8$ and $\lambda=1.5$. The diagram of states for these systems is given in Fig. 11, which shows a rich range of structural behavior. The minimum chain length for helix formation is larger ($N=11$) than for polymers with a monomer size of $\sigma/l=1.6$. The increased stiffness of the chain is limiting the curvature of the helix formed, thus requiring more monomers per turn of the helix. It appears that the typical “glassy” behavior of the longer polymers has been eliminated for the examined chain lengths. Therefore, the maximum chain length displaying a helical structure must be determined using QT analysis and visual inspection. The last chain length where a single helix structure is stable is $N=22$, yet for the longer chain lengths ($23 \leq N \leq 34$), the folded structures remain unique and not glassy. A single structure, which we refer to as the “barbers pole” structure, is observed over these chain lengths and is similar to the two rightmost structures of Fig. 9. This structure was first observed by Magee *et al.* (see Fig. 2 of Ref. [19]). Unlike the configurations of Fig. 9, the polymer is too stiff to allow the reversal of direction or doubling back of the outer spiral in the barbers pole. It appears that the increased stiffness has reduced the number of possible low-energy permutations, which manifest in more flexible chains as the doubling back of the outer spiral, to a single configuration. The small regions of high R_{\min} at low temperatures in Fig. 11 correspond to broad peaks in the heat capacity where transitions between different barbers pole structures occur.

Chains with a higher value of σ/l appear to favor a single-folded structure at longer chain lengths than compared to more flexible chains. This is understandable as in the limit of a rigid chain there is only one possible physical configuration. As the chain becomes stiffer the number of low-energy permutations on a structural theme are limited until only one configuration becomes optimal.

IV. CONCLUSIONS

In this work, we have used event-driven molecular dynamics, coupled with the replica exchange and histogram

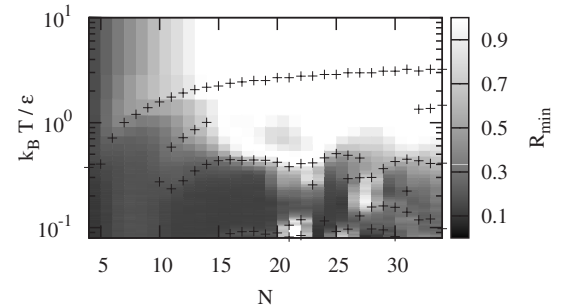


FIG. 11. Diagram of states for isolated square-well homopolymers with $\sigma/l=1.8$ and $\lambda=1.5$ as a function of the chain length N . The graph is shaded according to R_{\min} .

reweighting techniques, to explore the behavior of isolated square-well homopolymers. The structural properties of these polymers were characterized through a combination of configurational snapshots, monomer contact maps, and the root-mean-square deviation of the configuration combined with QT cluster analysis. The D_{rms} is able distinguishing between the unfolded and folded helix states. QT cluster analysis of the D_{rms} allows the estimate of the number of folded states, which reflects the “variability” of the state.

The homopolymer model studied here exhibits complex behavior. The stability of the helix structure is related to the constriction/elimination of interactions between monomers separated by a number of bonds in the chain. This is affected by the chain stiffness, which controlled by the monomer overlap parameter σ/l . The pitch and curvature of a helix is governed mainly by the range of the attractive interaction λ . Helices form with a higher curvature for short-range attractive wells. For larger values of λ , the monomers pack into a more spherical arrangement while still retaining a spiral bond structure.

Helices are only stable within a window of the chain length N . The lower limit appears to be related to the number of monomers in a single turn of the stable helix structure. Above a critical chain length, the isolated homopolymer folds into a rapidly increasing number of stable states, displaying characteristics reminiscent of a glass transition. These structures are more compact and spherical than their lower N counterparts, result from a minimization of the surface area to volume ratio of the polymer.

Finally, as the stiffness of the homopolymer is increased [$\sigma/l \rightarrow 2(1 + \delta/l)$] the number of observed folded states in longer chain lengths is reduced. At an overlap of $\sigma/l=1.9$, we only observe unique folded states for the range of polymer lengths studied ($4 \leq N \leq 34$).

ACKNOWLEDGMENT

M.N.B. acknowledges support from an EPSRC DTA.

- [1] Y. Okamoto and U. Hansmann, *J. Phys. Chem.* **99**, 11276 (1995).
- [2] C. L. Brooks, *Acc. Chem. Res.* **35**, 447 (2002).
- [3] H. D. Nguyen, A. J. Marchut, and C. K. Hall, *Protein Sci.* **13**, 2909 (2004).
- [4] H. A. Scheraga, M. Khalili, and A. Liwo, *Annu. Rev. Phys. Chem.* **58**, 57 (2007).
- [5] J. P. Kemp and Z. Y. Chen, *Phys. Rev. Lett.* **81**, 3880 (1998).
- [6] J. P. Kemp and J. Z. Y. Chen, *Biomacromolecules* **2**, 389 (2001).
- [7] B. H. Zimm and J. K. Bragg, *J. Chem. Phys.* **31**, 526 (1959).
- [8] S. Lifson and A. Roig, *J. Chem. Phys.* **34**, 1963 (1961).
- [9] V. Varshney, T. E. Dirama, T. Z. Sen, and G. A. Carri, *Macromolecules* **37**, 8794 (2004).
- [10] J. A. Schellman, *J. Chem. Phys.* **62**, 1485 (1958).
- [11] V. Munoz and L. Serrano, *Nat. Struct. Biol.* **1**, 399 (1994).
- [12] A. J. Doig, *Biophys. Chem.* **101-102**, 281 (2002).
- [13] A. Kholodenko, M. Ballauff, and M. A. Granados, *Physica A* **260**, 267 (1998).
- [14] T. Vogel, T. Neuhaus, M. Bachmann, and W. Janke, *EPL* **85**, 10003 (2009).
- [15] A. Maritan, C. Micheletti, A. Trovato, and J. Banavar, *Nature (London)* **406**, 287 (2000).
- [16] D. Marenduzzo, A. Flammini, A. Trovato, J. Banavar, and A. Maritan, *J. Polym. Sci., Part B: Polym. Phys.* **43**, 650 (2005).
- [17] Y. Zhou, C. K. Hall, and M. Karplus, *Phys. Rev. Lett.* **77**, 2822 (1996).
- [18] Y. Zhou, M. Karplus, J. Wichert, and C. Hall, *J. Chem. Phys.* **107**, 10691 (1997).
- [19] J. E. Magee, V. R. Vasquez, and L. Lue, *Phys. Rev. Lett.* **96**, 207802 (2006).
- [20] J. E. Magee, L. Lue, and R. A. Curtis, *Phys. Rev. E* **78**, 031803 (2008).
- [21] H. C. Andersen, *J. Chem. Phys.* **72**, 2384 (1980).
- [22] B. J. Alder and T. E. Wainwright, *J. Chem. Phys.* **31**, 459 (1959).
- [23] D. C. Rapaport, *J. Comput. Phys.* **34**, 184 (1980).
- [24] A. T. Krantz, *ACM Trans. Model. Comput. Simul.* **6**, 185 (1996).
- [25] M. Marin, D. Risso, and P. Cordero, *J. Comput. Phys.* **109**, 306 (1993).
- [26] G. Paul, *J. Comput. Phys.* **221**, 615 (2007).
- [27] R. H. Swendsen and J. S. Wang, *Phys. Rev. Lett.* **57**, 2607 (1986).
- [28] H. G. Katzgraber, S. Trebst, D. A. Huse, and M. Troyer, *J. Stat. Mech.: Theory Exp.* (2006), P03018.
- [29] A. M. Ferrenberg and R. H. Swendsen, *Phys. Rev. Lett.* **63**, 1195 (1989).
- [30] W. Kabsch, *Acta Crystallogr., Sect. A: Cryst. Phys., Diff., Theor. Gen. Crystallogr.* **32**, 922 (1976).
- [31] L. J. Heyer, S. Kruglyak, and S. Yoosiph, *Genome Res.* **9**, 1106 (1999).

APPENDIX
D

PRE TO POST COLLISION JACOBIAN

For the derivation of the distribution interaction operators, the Jacobian J for the variable change $d\mathbf{v}'_1 d\mathbf{v}'_2 dr'_1 dr'_2 = J d\mathbf{v}_1 d\mathbf{v}_2 dr_1 dr_2$ is required, given that

$$\begin{aligned}\mathbf{v}'_i &= \mathbf{v}_i - (1 + \alpha) \frac{\mu}{m_i} (\hat{\mathbf{r}}_{ij} \cdot \mathbf{v}_{ij}) \hat{\mathbf{r}}_{ij} \\ \mathbf{v}'_j &= \mathbf{v}_j + (1 + \alpha) \frac{\mu}{m_j} (\hat{\mathbf{r}}_{ij} \cdot \mathbf{v}_{ij}) \hat{\mathbf{r}}_{ij} \\ \mathbf{r}'_i &= \mathbf{r}_i\end{aligned}$$

Using a coordinate frame rotated such that one axis is along \mathbf{r}_{ij} greatly simplifies the problem. The solutions are equivalent as a rotation has a Jacobian of 1. This results in

$$\begin{aligned}\frac{\partial v'_1}{\partial v_1} &= 1 - (1 + \alpha) \frac{\mu}{m_1} \\ \frac{\partial v'_1}{\partial v_1} &= 1 - (1 + \alpha) \frac{\mu}{m_2} \\ \frac{\partial r_i}{\partial r'_j} &= \delta_{ij}\end{aligned}\quad \begin{aligned}\frac{\partial v'_1}{\partial v_2} &= (1 + \alpha) \frac{\mu}{m_1} \\ \frac{\partial v'_2}{\partial v_1} &= (1 + \alpha) \frac{\mu}{m_2}\end{aligned}$$

The determinant is then

$$\begin{aligned}J &= \begin{vmatrix} \frac{\partial v'_1}{\partial v_1} & \frac{\partial v'_1}{\partial v_2} & \frac{\partial v'_1}{\partial r_1} & \frac{\partial v'_1}{\partial r_2} \\ \frac{\partial v'_1}{\partial v_2} & \frac{\partial v'_2}{\partial v_2} & \frac{\partial v'_2}{\partial r_1} & \frac{\partial v'_2}{\partial r_2} \\ \frac{\partial r'_1}{\partial v_1} & \frac{\partial v_2}{\partial v_2} & \frac{\partial r'_1}{\partial r_1} & \frac{\partial r'_1}{\partial r_2} \\ \frac{\partial r'_1}{\partial v_2} & \frac{\partial v_2}{\partial v_2} & \frac{\partial r'_1}{\partial r_1} & \frac{\partial r'_2}{\partial r_2} \\ \frac{\partial r'_2}{\partial v_1} & \frac{\partial r'_2}{\partial v_2} & \frac{\partial r'_2}{\partial r_1} & \frac{\partial r'_2}{\partial r_2} \end{vmatrix} \\ &= \left| [1 - (1 + \alpha) \frac{\mu}{m_1}] [1 - (1 + \alpha) \frac{\mu}{m_2}] - (1 + \alpha)^2 \frac{\mu^2}{m_1 m_2} \right| \\ &= \left| 1 - (1 + \alpha) \mu \left(\frac{1}{m_1} + \frac{1}{m_2} \right) \right| \\ &= \alpha\end{aligned}$$

APPENDIX
E

STREAMING OPERATOR BBGKY HIERARCHY

The streaming operator hierarchy derivation is analogous to the derivation of the BBGKY hierarchy. This derivation is presented here in full for convenience. Starting with the Dyson equation for the evolution of the full N particle distribution (see Eq. (2.5.4b)), integrating over $N - n$ variables, and multiplying by $N!/(N - n)!$ gives

$$\begin{aligned} \frac{N!}{(N - n)!} \int d\Gamma_n, \dots \Gamma_N \mathcal{S}_t F &= \frac{N!}{(N - n)!} \int d\Gamma_n, \dots \Gamma_N \mathcal{S}_t^0 F \\ &\quad + \frac{N!}{(N - n)!} \int d\Gamma_n, \dots \Gamma_N \int_0^t dt' \mathcal{S}_{t-t'}^0 \sum_{j,k>j}^N \mathcal{T}(j,k) \mathcal{S}_{t'} F \end{aligned} \quad (\text{E.0.1})$$

The left hand side becomes $f^{(n)}(t)$, as the full distribution function F obeys Eq. 2.5.1 for all times. The integration over the $N - n$ variables also passes through the free streaming operator \mathcal{S}_t^0 . This can be directly shown by examining the Taylor expansion of \mathcal{S}_t^0 .

$$\mathcal{S}_t^0 \approx 1 - t \sum_j^N \mathcal{L}_j^0 + \frac{t}{2} \left[\sum_j^N \mathcal{L}_j^0 \right]^2 + \dots$$

The integration passes through terms where it does not share a common particle index with the Liouvillean operator. Where there is a common particle index, the free streaming Liouvillean operator generates a derivative in the particle position. As the distribution function and all of its derivatives vanish at the extremes of the system these terms are zero. Regrouping the terms that survive shows that the integration can travel through the free streaming operator \mathcal{S}^0 , but that this changes to the n -particle free streaming operator $\exp(-t \sum_j^n \mathcal{L}_j^0)$. The full free streaming operator may be used in place of the n -particle free streaming operator as it is functionally equivalent. Equation E.0.1 therefore becomes

$$f^{(n)}(t) = \mathcal{S}_t^0 f^{(n)} + \frac{N!}{(N - n)!} \int_0^t dt' \mathcal{S}_{t-t'}^0 \int d\Gamma_n, \dots \Gamma_N \sum_{j,k>j}^N \mathcal{T}(j,k) \mathcal{S}_{t'} F \quad (\text{E.0.2})$$

For the interaction operators, if $j > n$ and $k > n$ then the corresponding term is zero. This is a result of the conservation of members of the ensemble, or a conservation of particle number or mass which can be easily proven if the adjoint interaction operator is used. If $j < n$ and $k < n$ then the integration passes through unaffected giving

$$f^{(n)}(t) = \mathcal{S}_t^0 f^{(n)} + \int_0^t dt' \mathcal{S}_{t-t'}^0 \sum_{j,k>j}^n \mathcal{T}(j,k) f^{(n)}(t') \\ + \frac{N!}{(N-n)!} \int_0^t dt' \mathcal{S}_{t-t'}^0 \int d\Gamma_n, \dots \Gamma_N \sum_j^n \sum_{k=n+1}^N \mathcal{T}(j,k) \mathcal{S}_{t'} F \quad (\text{E.0.3})$$

Finally, the k variable in the final sum of Eq. (E.0.3) may be relabelled for every term ($k \rightarrow n+1$), all other integration variables will pass through and reduce the F to give the final result

$$f^{(n)}(t) = \mathcal{S}_t^0 f^{(n)} + \int_0^t dt' \mathcal{S}_{t-t'}^0 \sum_{j,k>j}^n \mathcal{T}(j,k) f^{(n)}(t') \\ + \int_0^t dt' \mathcal{S}_{t-t'}^0 \int d\Gamma_{n+1} \sum_j^n \mathcal{T}(j,n+1) f^{(n+1)}(t') \quad (\text{E.0.4})$$